KU Leuven

Biomedical Sciences Group

Faculty of Medicine

Department of Imaging & Pathology

Fluorine-19 Magnetic Resonance Imaging as a Potential Tool in Preclinical Research

With Focus on Diabetes

Sayuan Liang

Jury:

Promoter: Prof. Dr. Uwe Himmelreich

Co-promoter: Prof. Dr. Hauke Kolster

Chair: Prof. Dr. Tania Roskams

Secretary: Prof. Dr. Christophe Deroose

Jury members: Prof. Dr. Philippe Demaerel

Prof. Dr. Christophe Deroose

Prof. Dr. Mangala Srinivas

Dr. Philipp Boehm-Sturm

Dissertation presented in partial fulfilment of the requirements for the degree of Doctor in Biomedical Science

November 2017

Acknowledgements

Finally, here we are! It has been definitely a too looooooong journey for getting this thesis done, I could not imagine how I could get through it without people I encountered over the years.

First of all, I own my deepest gratitude to my promoter Prof. Uwe Himmelreich. He granted me this great opportunity to pursue my doctoral degree at the end of 2010. Thanks for his patience by giving me the freedom to try, fail, try again, fail again till some results. Thanks for his understanding by encouraging me to follow my ideas and decisions. Thanks for his supports by willing to share his experience not only in scientific domain but also daily life. As Chinese says, day as a teacher, life fatherhood.

I would also like to thank my co-promoter Prof. Hauke Kolster, who taught me all the tricks of how to make a working and reliable RF coil. It is really a pity that he could not stay longer and I missed so much of his critical scientific thinking. My sincere thanks go to all my jury members for their precious time in evaluation of this thesis and giving constructive comments to make it significantly improved. Prof. Philippe Demaerel and Prof. Christophe Deroose, thanks for their patience over the years to be present in my formal presentations to discuss my PhD progress with many meaningful suggestions and inputs. My external juries, Prof. Mangala Srinivas and Dr. Philipp Boehm-Sturm, both pioneers in fluorine-19 MRI field, it is my great honor that both of them accept to become my jury members. Not only the tremendous efforts they have made towards my thesis, but also the plenty useful information they published in their papers really helped me during my PhD. I am happy that I could be part of the 19F MRI family with a little bit own contribution at last.

It would be not fair if I don't mention Prof. Patrick Dupont and Dr. Dimiter Prodanov. Patrick is a super promoter when he mentored my master thesis. He was always willing to have a meeting with me whenever I have problems. As a professor, he not only taught me how to do research, but also he acted like a friend, listen to my concerns and try to resolve them for me. Dimiter was my supervisor during my intern at IMEC. Although I only stayed there for couple of months, he did show me the imageJ world with a very ambitious project. Without their influence and recommendation, I wound not be able to start my PhD journey.

Along this journey, I met lots of wonderful colleagues and built close friendship with them. Bryan, my BLI master and loyal Man-Utd fan, beyond colleague, has been a fantastic friend. We share very similar hobby (football) and value, which is not easy considering our very different culture background. I am really grateful for all his helps (like all the Dutch context in this thesis translated by him) and the moments we shared. I wish him very successful salesman career in a Japanese company. Shweta, another "victim" of 19F MRI, very traditional India woman. If I can, I would consider her as my "only student", eager to learn and always have many questions (sometimes, same ones). Nevertheless, so happy to see how she grow as a researcher gradually under all kinds of pressures. Jennifer, a typical warm hearted Belgian girl, I still remember during my preparation of final doctoral plan defense in MoSAIC meeting room back to 3 years ago, she helped me write down all the comments from the audiences and passed it to me afterwards with 4 pages of A4. I was so impressed just like when she heard that I managed how to cycle in half day! Kristof, true scientific nerd in the lab, I enjoyed our time in Toronto, I have to say though we have different interests, I am proud that I could eventually persuaded him to enjoy baseball game together and cheered up for Blue Jay (if he still remembers the name of the team). Rita, Portuguese chemist, sorry that I have to occupy

much of Uwe's time to correct my thesis while she was preparing her paper. Don't worry too much and I guess she will do her defense soon. Greetje, I still remember during one trip back from ISMRMB meeting, I showed a small conjuring, while others were still wondering, she could immediate point out the tricks behind. I was then totally convinced how smart she is! I would also like to thank Peter, Ann and Tinne for their help over the years regarding all kinds of administration issues (finance, keys, lab supplies and etc.). Sorry for any kinds of inconvenience I brought to you. For all other current lab members (Stefaan, Bella, Willy, Liesbeth, Sarah, Akila and more), it is a pity that I did not stay in the lab for longer, but I do wish you like this family and be very successful in the future.

There are also many members who left the lab to mention. Tom, previous MRI hotline, the first person Uwe introduced me, we met each other in the 9.4T room, immediately after the introduction, he started to show me PV5.0 and the system in details. This truly reflected his personality and responsibility. He treated MoSAIC as his family and the system as his baby. I guess people in MoSAIC miss him very much. Karim, my mentor of cell culture and islets isolation, he gave me lots of useful instructions, inspired me with many new ideas. Every time when I had questions regarding cells/ islets, I know he will be there for me. He also trusted me by letting me choose what to do, I will definitely miss the mornings we did experiments together. All previous graduated PhD students from NMR unit have set good examples for me. Jesse, presentation master, always remember the street of Blackbergen on a Monday evening, three guys hanged around with a mission of a bar; Ashiwini, another warm hearted India woman, I was so jealous when we went for taking pictures for US visa application together, she told me that US normally issued 10 years for Indian citizens. Thank for all her smiles when I asked for help. Sophie, the real radiologist, I admire her so much that once she left one of her technical books about MRI in the meeting room, full of her remarks. Cindy, a rigorous scientist, I have to admit I was a bit afraid of her at the beginning as I made many stupid mistakes. Antoine, our nanostar, his fast and successful transformation to a businessman after his PhD demonstrates that a good scientist could also do good business. Nevertheless, I feel honored now to be officially part of this family tree.

From July 2015 to couple of months ago, I also have been working in Bio-Imaging Lab Antwerpen for two fantastic years. I have my fully respect towards Prof. Annemie Van der Linden and Prof. Marleen Verhoye. Thanks for offering this wonderful opportunity to work for BIL. I appreciate all their support and understanding no matter I got ill for hospitalization or decided to come back to China. Working for BIL will always be an unforgettable memory for me. Johan, backbone in the lab, he won everyone's respect in the lab. It is my pleasure to first met him in our coil building course and then worked with him. The attitude, the passion and responsibility he passed to me during every day work is numerous assets for me. I will always miss the time we shared the big office together at the corner of Uc building. Changhong, like my little brother in Antwerpen, I know it was never an easy decision for him to leave the lab and make a new start. However, everything would be fine and I am sure he will learn from it and be stronger. Rukun and Lore, thank them for introducing their family and neighborhood. We had many great moments all over the city of Antwerpen, if possible I would very happy to show them the city of Shanghai too. Micheal, a very sensitive boy, who is very dedicated to his research topic, so happy to see that he could get exchange program funding and meetup his girlfriend in the US. Disha, a super PhD with already many high impact papers published, we had many talks and shared many funny things. I wish her very good luck with her PhD and future scientific career. Other BIL members (Julie, Maarten, Cynthia, Stephan, Ines, Annelien), thanks for the great time we have been together, all the best to your PhD and future.

Research could not live without collaborations. I also like to take this opportunity to thank all my collaborators both inside and outside of KU Leuven. Yipeng, it was a coincidence I met him during a symposium but it ended up with a nice paper thanks to his Matlab codes. Dominiek, we were both a bit upset before our project started but it went so smoothly that ensured our degrees. Ranhua, another crazy scientific nerd, kept on asking for experimental results and very efficient in terms of performing experiments and writing papers, there is no doubt why he had so many excellence publications. Rein and Heleen, thank them for the fast deliver of 19F compounds all the time, no compounds, no experiments.

Chinese are used to gathering together. Indeed, I have made lots of Chinese friends over the years. Kan, we shared our first year abroad experience together, the sweets and bitters. I always remember the word "gratis" he taught me which proven to be really useful all the time. Chun, my old sister, we met by chance during the Spring Festival 2007, however I felt so lucky that the ten years' journey in Belgium, I have Yu and she accompanied. Congratulation on their recent great news, I wish she become a happy mum soon. Xu, another name on my emergency contact, she is very reliable and I always trust her, every time when I encountered general problems, I always ringed her. Yang, our friendship started from a mis-sent letter. She enlightened me dark first years' life in Leuven by bringing me to different restaurants. Unitl now, my favorite restaurant is still the first one your brought me to "Timory". Liang, a big brother to me, thank him so much for taking care of me during our time in CSAL and my trip in Seoul. Dan, she was a super-girl both in study and organizing activity, she gave lots of assistance during my presidency in CSAL and it was a great New Year gala 2011, all the credits should go to her. Yu, a typical Shaanxi girl, so glad to be the first one she got to know in our faculty and further became a really tight friend for our PhD journeys. Yanyan and Hong, my best roommates ever, thanks for tolerating all my weaknesses. I really missed the time we shared food, played poker, did sports and went for shopping together. Yewei, my officemate, although she is often shy, whenever I need her help or assistance, she will always be there without any doubts. There are many more friends I would like to mention. Friends in Leuven: Feng, Ling, Lei, Yaojuan, Tina, Jingjing, Lin, Hang, Yuanbo, Junjie, Ting, Xiaolan, Liqun, Zengjing, Xiaowen, Xiaocheng, Guangda, Xinwu, Hui, Zhe, Yejun, Tiannan, Juncheng, Zhenyu, Xiaowei, Chen, Biyuan, Doingqing, Yuwei, Shinan…Friends in Brussels and Antwerpen: Yijia, Jie, James, You, Dan, Emily, Meng, Xuan, Xiaodi, Yijun, Changsheng, Jun, Jiaying, Rui, Le, Wei, Hua, Siqi, Xiayang, Tianhong, Rongrong, Sihan, Yuqian, Zhiyi, Lu….Old friends in China: Yi, Wangting, Tianyu, Jiujiu, You, Ying, Lingqing, Tuo, Jing, Yu, Dian…For auld lang syne, we will take a cup o' kindness yet.

I have list lots of names, well, actually, I would also like to thanks the initial program brought me to this great country. Over eleven years' education and stay, I realize I become almost half Belgian. I support red devils with their up and downs; I start to miss my favorite French fries, Hoegaarden beer after I got back to China just for one week; when I jumped on my plane back to China I got similar feeling as first time I left China for Belgium. I will forever treasure my time and memories in Belgium.

At last but not least, I have to say thank my parents for being my strongest backing and warmest harbor. From my childhood, they always respect my opinions, grant me freedom and give all the supports they can. I love them so much and after this long journey seeing the western world, now, I am home.

Summary

Diabetes remains one of the increasing threats to human health with over 422 million people suffering from the disease all over the world. Despite the advancements in understanding the disease and improvements in treatment, diagnosis and early prevention, effective monitoring the status of the disease is still urgently needed. Hereby, the function and mass of pancreatic islets (PIs) and in particular their beta cells play an important role for monitoring the progression of the disease. Efforts have been made to stimulate researchers to track them in a quantitative way. Hereby, magnetic resonance imaging (MRI) is considered as a safe (no ionizing radiation) prime aid with excellent soft tissue contrast and high-resolution with detailed anatomical information. In order to further enhance the sensitivity of MRI for cellular imaging, contrast agents are often utilized to label the targeted cells either by *in situ* labelling after systemic injection or *ex vivo* pre-labelling with subsequent transplantation. Recently, due to its unique feature of being background free, fluorine based contrast agents together with ^{19}F MRI techniques have attracted attention, with first successful applications in immune cell tracking like dendritic cells and T cells in immunotherapy. This might also open new perspectives for diabetes research. The main aim of this PhD thesis was to contribute to the development and validation of PI and beta cell labelling with different fluorine-based contrast agents to follow their fate *in vivo* using ^{19}F MRI. Based on the properties of the contrast agents, both *in situ* and *ex vivo* labelling strategy have been explored.

In the context of *in situ* labelling, fluorine labelled D-mannoheptulose (^{19}FMH) was tested for its high specificity towards GLUT-2 transporters, which are highly expressed by beta cells and hepatocytes. With the establishment of an in-house built, double-tuned radio-frequency coil, we can assess the distribution of ^{19}FMH *in vivo*. Due to the quick clearance of the compound and relative low sensitivity of ^{19}F MRI, limited *in vivo* signal was detected in the liver and potentially from the pancreas. Nevertheless, *ex vivo* ^{19}F MR spectroscopy (MRS) confirmed the preferential uptake of ^{19}FMH in tissue with high expression of the GLUT-2 transporter. These results suggest that synthesis of ^{18}F-labeled FMH and detection by highly sensitive PET could be a potential alternative solution for the future to overcome the sensitivity limitations of ^{19}F MRI. *Ex vivo* labelling was applied to isolated PIs and INS-1E cells using liposomal particles containing a DiD fluorescent dye and perfluoro-5-crown-ether (PFCE) for both ^{19}F MRI and fluorescence imaging (FLI) detection. In addition, lentiviral vector (LV) transduction of PIs and INS-1E cells was also performed for bioluminescent imaging (BLI). The PFCE labelling and LV transduction protocols were optimized for PIs and cells *in vitro* to be sufficient for *in vivo* imaging purposes without affecting the viability and functionality of PIs and INS-1E cells. Longitudinal multimodal *in vivo* imaging of transplanted PIs and cells at subcutaneous sites demonstrated the feasibility of longitudinal cell tracking for several months with PFCE labels. This presented imaging approach addresses a potential solution to overcome limitations in sensitivity, resolution and specificity of individual imaging techniques using a multimodal approach.

The inherent sensitivity limitation of ^{19}F MRI was also tackled by implementation of data analysis tools like the compressed sensing (CS) technique with a focus on low signal-to-noise ratio (SNR) images of PFCE labelled PIs and INS-1E cells. Both, offline simulation and CS acquisition with different reconstruction algorithms showed a three- to fourfold increase of SNR per time. These preliminary results not only demonstrated again that the CS technique together with appropriate reconstruction algorithms is useful to reduce the scan time for ^{19}F MRI application with low SNR, but also provides evidence that by using the CS techniques, extra signal of interest could be detected,

which might be missed otherwise by using conventional ^{19}F MRI acquisition schemes within the same scan time.

In this thesis, ^{19}F MRI was also applied for a controlled release study from a pH-sensitive capsule. By combining ^{19}F MRI and CT with fluoro-deoxyglucose (^{19}FDG) and $BaSO_4$ as contrast agents, respectively, information on early permeability of capsule material to water, the capsule's integrity and its exact anatomical location of the site of release could be obtained both *in vitro* and *in vivo* in a hamster model. This novel imaging approach could serve as a valuable tool for understanding and evaluation of different models of controlled release mechanisms.

This PhD work has added knowledge to the further understanding, improvement and validation of ^{19}F MRI as a preclinical imaging tool for cell tracking and controlled release. The future of ^{19}F MRI remains bright due to its versatile applications in different biomedical fields. This work will hopefully contribute to a solid basis not only for its future applications and development in preclinical research, but also for the translation of the studied technique towards the clinic.

Samenvatting

Diabetes blijft een van de toenemende risico's voor de gezondheid van de mens, meer dan 422 miljoen mensen hebben namelijk deze ziekte wereldwijd. Ondanks de toenemende kennis over de ziekte, preventie, vroegtijdige diagnose en verbeterde therapieën blijft het opvolgen van de ziekte voor en na toedienen van de therapie zeer noodzakelijk. Het is hierbij belangrijk om de functie en de massa van de eilandjes van Langerhans (PIs) en specifiek de bètacellen op te volgen, aangezien zij een belangrijke rol spelen in ziekteprogressie. Daarom is er veel onderzoek gebeurd om deze cellen te volgen op een kwantitatieve manier. Beeldvorming met magnetische resonantie (MRI) wordt beschouwd als een veilige (geen ioniserende straling) methode met uitstekend zacht weefselcontrast en gedetailleerde anatomische informatie. Om de sensitiviteit van MRI te verbeteren wordt er vaak een contraststof aan de cellen toegediend zodat deze gevisualiseerd kunnen worden. Dit kan *in situ* gebeuren na het systemisch toedienen van de contraststof of *ex vivo* door de cellen vooraf te labelen met een contraststof gevolgd door het transplanteren van de cellen. Recentelijk hebben fluorine gebaseerde contraststoffen de aandacht getrokken voor ^{19}F MRI aangezien ze geen achtergrond signaal geven. Dit heeft geleid tot de eerste succesvolle toepassing van het visualiseren van immuuncellen, zoals dendritische en T cellen, voor immunotherapie. Deze vooruitgang opent ook nieuwe perspectieven voor het onderzoek naar diabetes. Het belangrijkste doel van deze PhD thesis was om bij te dragen tot de ontwikkeling en validatie van PI en bètacel labeling met verschillende fluorine-gebaseerde contraststoffen om de bestemming van deze cellen *in vivo* te kunnen visualiseren gebruikmakende van ^{19}F MRI. Op basis van de eigenschappen van de contrastagentia is zowel een *in situ* en *ex vivo* labelingstrategie onderzocht.

Om de cellen in situ te labelen werd het fluorine-gelabeld D-mannoheptulose (^{19}FMH) geëvalueerd voor zijn specificiteit voor de GLUT-2 transporter. Deze transporter komt hoog tot expressie op bètacellen en hepatocyten. Door de eigen ontwikkeling van een dubbel getunede radiofrequentie spoel konden we de distributie van 19FMH onderzoeken in vivo. Beperkt fluorine signaal werd gedetecteerd in de lever en mogelijks ook in de pancreas omdat de contraststof snel werd uitgescheiden en ^{19}F MRI een relatief lage sensitiviteit heeft. Desondanks heeft ex vivo ^{19}F MR-spectroscopie (MRS) aangetoond dat de contraststof voornamelijk werd opgenomen in de weefsels met hoge expressie van de GLUT-2 transporter. Deze resultaten tonen aan dat de ontwikkeling van een ^{18}F-gelabeld FMH als een mogelijks alternatief kan dienen aangezien PET een beeldvormingsmodaliteit is met een hoge sensitiviteit. PIs en INS-1E cellen werden ex vivo gelabeld met liposomale partikels die een DiD fluorescente kleurstof en een perfluoro-5-kroonether (PFCE) bevatten voor respectievelijk fluorescentie beeldvorming en ^{19}F MRI. Verder werden de PIs en de INS-1E cellen ook getransduceerd door een lentivirale vector (LV) om bioluminescente beeldvorming toe te laten. De protocollen voor PFCE labeling en LV transductie werden in vitro geoptimaliseerd voor PIs en INS-1E cellen om in vivo beeldvorming toe te laten zonder de levensvatbaarheid en functionaliteit van de PIs en INS-1E cellen aan te tasten. Na onderhuidse transplantatie van PIs en INS-1E konden de cellen langdurig worden opgevolgd door bovenvermelde beeldvormingsmodaliteiten en werd de haalbaarheid van het longitudinaal opvolgen van cellen door een PFCE-contraststof aangetoond. Deze multimodale beeldvormingsaanpak brengt een mogelijke oplossing om de limitaties in sensitiviteit, resolutie en specificiteit van de individuele beeldvormingstechnieken te overkomen.

De limitatie in sensitiviteit die inherent is aan ^{19}F MRI werd ook aangepakt aan de hand van het implementeren van data-analyse tools zoals de gecomprimeerde sensing (CS) techniek, waarbij we

ons focusten op de laag signaal ruis (SNR) beelden van PFCE gelabelde PIs en INS-1E cellen. Zowel offline simulaties en CS acquisities met verschillende reconstructiealgoritmes toonden een drie- tot viervoud toename in SNR per tijdstip. Deze voorlopige resultaten tonen niet enkel aan dat de CS techniek, samen met de juiste reconstructiealgoritmes, nuttig is om de scantijd te reduceren voor ^{19}F MRI toepassingen met lage SNR, maar bewijst ook dat door de CS techniek toe te passen een verhoogde sensitiviteit kon worden behaald ten opzichte van de conventionele ^{19}F MRI acquisitie schema's voor dezelfde scantijden.

In deze thesis werd ^{19}F MRI ook gebruikt voor een studie over gecontroleerde vrijgave van een pH sensitieve capsule. Door combinatie van ^{19}F MRI en CT met fluoro-deoxyglucose (^{19}FDG) en BaSO4 als respectievelijke contraststoffen werd informatie over de vroegtijdige permeabiliteit, integriteit en exacte anatomische locatie van de capsule verkregen zowel in vitro als in vivo in een hamstermodel. Deze nieuwe beeldvormingsaanpak kan hiervoor dienen als een nuttige tool voor het begrijpen en evalueren van verschillende modellen van gecontroleerde vrijgave mechanismen.

Deze PhD heeft bijgedragen aan het beter begrijpen, optimaliseren en valideren van ^{19}F MRI als een preklinische beeldvormingstool voor het visualiseren van cellen en evalueren van gecontroleerde vrijgave capsules. De toekomst van ^{19}F MRI blijft rooskleurig door zijn veelzijdigheid aan applicaties in verschillende domeinen van biomedische wetenschappen. Dit werk zal hopelijk bijdragen als solide basis voor verdere applicaties en ontwikkelingen in preklinisch onderzoek, maar ook voor de translatie van deze techniek naar het ziekenhuis.

Abbreviations

1-^{19}FMH	1-deoxy-1-fluoro-D-manno-hept-2-ulose
^{1}H-MRI	Proton Images
^{19}FDG	2-fluoro-2-deoxy-D-glucose
^{19}FMH	^{19}F-deoxyfluoromannoheptuloses
^{19}F NMR	Fluorine nuclear magnetic resonance
2D	Two dimension
3-^{19}FMH	3-deoxy-3-fluoro-D-manno-hept-2-ulose
3D	Three-dimensional
3flagFluc	Triple flag tagged firefly luciferase
5-FC	5-fluorocytosine
5-FU	5-fluorouracil
ADC	Apparent diffusion coefficient
B_0	Static magnetic field
$BaSO_4$	Barium sulphate
BBB	Blood-brain barrier
BCM	β cell mass
BLI	Bioluminescence Imaging
BOLD	Blood oxygenation level dependent
bSSFP	Balanced steady-state free precession
CCD	Charge-coupled device
CF_4	Tetrafluoromethane
COPD	Chronic obstructive pulmonary disease
CoSaMP	Compressive sampling matching pursuit
CS	Compressed Sensing
CSI	Chemical Shift Imaging
CT	X-ray based Computer Tomography
DC	Dendritic Cell
DMH	D-mannoheptulose
DOPE	1,2-dioleoyl-sn-glycero-3-phosphoethanolamine
DOTAP	1,2-dioleoyl-3-trimethylammonium-propane
Dp	Proton (spin) density

DSPE-PEG(2000)	1,2-distearoyl-sn-glycero-3-phosphoethanolamine-N-[amino(polyethylene glycol)-2000]
DTBZ	Dihydrotetrabenazine
ELISA	Enzyme-linked immunosorbent assay
FA	Flip angle
FBS	Fetal bovine serum
FDG	2-fluoro-2-deoxy-D-glucose
FDK	Metal-binding beta-diketones
FLASH	Gradient echo
FLI	Fluorescence Imaging
Fluc	Firefly luciferase
FID	Free induction decay
FOV	Field of View
G	Gradient field
GE	Gradient echo
Gd	Gadolinium
GI	Gastrointestinal
GLP-1	Glucagon-like peptide-1
GSIS	Glucose stimulated insulin secretion
HBSS	Hanks' Balanced Salt Solution
HP	Hyperpolarized
IP	Intraperitoneal
IPGTT	Intraperitoneal (IP) glucose tolerance test
IRWL1	Iterative reweighted L1 minimization
KPF6	Hexaflorophosphate
LV	Lentiviral vector
M	Magnetization vector
MRI	Magnetic Resonance Imaging
MRS	NMR Spectroscopy
MRT	Magnetic resonance tomography
M_{xy}	Transversal component
M_z	Longitudinal component
NA	Number of Average

NaF	Sodium fluoride
NMR	Nuclear magnetic resonance
NMRI	Nuclear magnetic resonance imaging
NP	Nanoparticle
OI	Optical imaging
OMP	Orthogonal Matching Pursuit
OMMP	Orthogonal multi-matching pursuit
p	Polynomial power
PBS	Phosphate buffered saline
PET	Positron emission tomography
PFC	Perfluorocarbons
PFCE	Perfluoro-15-crown-5-ether
PFOB	Perfluorooctylbromide
PFPE	Perfluoropolyethers
PFTA	Perfluorotributylamine
PIs	Pancreatic islets
pO_2	Partial pressure of dissolved O2
PuroR	Puromycin resistance gene
QDs	Quantum Dots
RARE	Rapid spin echo
rBW	Receiver bandwidth
RF	Radiofrequency
RIP-GFP	Rat insulin-1 promoter
ROI	Region of Interests
SE	Spin echo
SNR	Signal-to-Noise Ratio
SPECT	Single photon emission computed tomography
SPIO	Super-paramagnetic iron oxide
SOIs	Signals of Interest
T1	Pin-Lattice Relaxation
T1D	Type 1 Diabetes
T2	Spin- Spin Relaxation
TE	Echo Time

R	Repetition Time
TV	Total Variation
Two-level	Two-level L1 minimization
UF	Under sampling Factors
US	Ultrasound
UTE	Ultra-short Echo Time
VMAT2	Vesicular monoamine transporter type 2
V/Q	Ventilation/ perfusion ratio
ZTE	Zero Echo Time

Table of contents

ACKNOWLEDGEMENTS ..... **III**

SUMMARY ..... **VII**

SAMENVATTING ..... **IX**

ABBREVIATIONS ..... **XI**

TABLE OF CONTENTS ..... **XV**

CHAPTER 1. GENERAL INTRODUCTION **1**

1.1. DIABETES MELLITUS 1

1.2. NON-INVASIVE IMAGING TECHNIQUES 2

1.2.1. Optical Imaging (OI) *3*

1.2.2. Ultrasound (US) *4*

1.2.3. Computed Tomography (CT) *4*

1.2.4. Nuclear Medicine: PET/SPECT *5*

1.3. MAGNETIC RESONANCE IMAGING (MRI) 6

1.3.1. MRI scanner *7*

1.3.2. MR endogenous contrast *8*

1.3.2.1. Spin-Lattice relaxation 8

1.3.2.2. Spin-Spin relaxation 8

1.3.3. MR exogenous contrast *10*

1.4. FLUORINE MAGNETIC RESONANCE IMAGING AND SPECTROSCOPY 11

1.4.1. Introduction of ^{19}F MRI *11*

1.4.2. Applications of ^{19}F MRI/ MRS *12*

1.4.2.1. Assessment of pharmacological compounds 12

1.4.2.2. ^{19}F magnetic resonance as a novel pulmonary imaging platform 13

1.4.2.3. Assessment of physiological parameters using fluorine-containing probes 14

1.4.2.4. In vivo cell tracking 16

1.4.3. Limitations of ^{19}F MRI/MRS *17*

1.4.4. Improving the Sensitivity of ^{19}F MRI/ MRS *17*

1.4.4.1. Probe/ contrast agent design 17

1.4.4.2. Cell labelling strategies 20

1.4.4.3. MRI hardware 21

1.4.4.3.1. Static magnetic field 21

1.4.4.3.2. Magnetic field gradient system 21

1.4.4.3.3. Radio frequency (RF) system 22

1.4.4.4. Software 23

1.4.4.4.1. Choice of the MR sequence 24

1.4.4.4.2. Acquisition parameters 25

1.4.4.4.3. Post processing methods 26

1.5. MAIN OBJECTIVES 27

1.6. OUTLINE OF RESEARCH 29

CHAPTER 2. *IN VIVO* AND *EX VIVO* 19-FLUORINE MAGNETIC RESONANCE IMAGING AND SPECTROSCOPY OF BETA-CELLS AND PANCREATIC ISLETS USING GLUT-2 SPECIFIC CONTRAST AGENTS **31**

2.1 INTRODUCTION 31

2.2 RESULTS 32

2.2.1 Hardware considerations *32*

2.2.2 Uptake of ^{19}F-deoxymannoheptulose by isolated pancreatic islets *33*

2.2.3 In vivo results *34*

2.2.4 Ex vivo ^{19}F MRS measurements *35*

2.2.5 IPGTT results *36*

2.3 DISCUSSION....36
2.4 CONCLUSIONS....38
2.5 EXPERIMENTS....38
2.5.1 ^{19}FMH and ^{19}FDG....38
2.5.2 In vitro uptake of ^{19}FMH and ^{19}FDG by isolated pancreatic islets....38
2.5.3 Study design of the in vivo experiments....38
2.5.4 Magnetic resonance imaging....39
2.5.5 $HClO_4$ extraction of tissue....40
2.5.6 ^{19}F MRS of cells and tissue extracts....40
2.5.7 IPGTT Test....40
2.5.8 Data post-processing....41

CHAPTER 3. TRI-MODAL *IN VIVO* IMAGING OF PANCREATIC ISLETS TRANSPLANTED SUBCUTANEOUSLY IN MICE....43
3.1 INTRODUCTION....43
3.2 RESULTS....44
3.2.1 In vitro characterization of labeled and transduced INS-1E cells....44
3.2.2 In vitro characterization of labeled and transduced pancreatic islets....46
3.2.3 Multimodal in vivo imaging of transplanted INS-1E cells....48
3.2.4 Multimodal in vivo imaging of transplanted pancreatic islets....50
3.3 DISCUSSION....52
3.4 CONCLUSIONS....54
3.5 MATERIALS AND METHODS....55
3.5.1 Fluorinated particles and lentiviral vector....55
3.5.2 Rodent pancreatic islets and cell lines....55
3.5.3 Lentiviral vector transduction experiments....55
3.5.4 Cell labeling using PFCE particles....56
3.5.5 ^{19}F NMR experiments....56
3.5.6 Confocal Microscopy....57
3.5.7 Islets viability and functionality tests assessment in vitro....57
3.5.8 In vitro BLI, FLI and ^{19}F MRI....57
3.5.9 Animal model....58
3.5.10 In vivo BLI, FLI and ^{19}F MRI....58
3.5.11 Histology....59
3.5.12 Image processing....59
3.5.13 Statistical Analysis....59
3.6 SUPPLEMENTARY DATA....60

CHAPTER 4. COMPARISON OF DIFFERENT COMPRESSED SENSING ALGORITHMS FOR LOW SNR ^{19}F MRI APPLICATION - IMAGING OF TRANSPLANTED PANCREATIC ISLETS AND CELLS LABELED WITH PERFLUOROCARBONS. 63
4.1 INTRODUCTION....63
4.2 RESULTS....65
4.2.1 CS Simulation: ^{19}F MRI phantom studies....65
4.2.2 CS Simulation: in vivo study....67
4.2.3 CS ^{19}F MRI acquisition of phantoms....68
4.2.4 CS acquisition for in vivo studies....69
4.3 DISCUSSION....71
4.4 EXPERIMENTAL....73
4.4.1 Perfluorocarbon particles....73
4.4.2 Rodent pancreatic islets/ beta cell isolation and labeling....74

4.4.3 Conventional data acquisition for assessment of simulations *74*
4.4.4 Compressed Sensing data acquisition *75*
4.4.5 CS Reconstruction and Signal Quantification *76*

CHAPTER 5. VISUALIZATION OF DELAYED RELEASE OF COMPOUNDS FROM PH-SENSITIVE CAPSULES IN VITRO AND IN VIVO IN A HAMSTER MODEL **79**
5.1 INTRODUCTION 79
5.2 RESULTS AND DISCUSSION 81
5.2.1 In vitro imaging *81*
5.2.2 In vivo imaging *83*
5.3 CONCLUSIONS 86
5.4 EXPERIMENTAL 87
5.4.1 Capsules and contrast agents *87*
5.4.2 Hamster model *87*
5.4.3 Magnetic Resonance Imaging *87*
5.4.4 Computed Tomography *88*

CHAPTER 6. GENERAL CONCLUSIONS & FUTURE PERSPECTIVES **89**
6.1 GENERAL CONCLUSIONS 89
6.2 FUTURE PERSPECTIVES 93

REFERENCES **97**

CURRICULUM VITAE **113**

Chapter 1. General Introduction

1.1. Diabetes Mellitus

Diabetes mellitus, also known as diabetes, is a chronic metabolic disease, characterized by hyperglycaemia over a prolonged period of time. Diabetes is a result of defects in insulin section mediated by pancreatic beta cells. The failure of beta cell function to produce insulin or loss of beta cell mass may explain the cause of the disease. Currently, over 422 million people are suffering from diabetes worldwide, making the disease one of most common non-communicable diseases[1].

Type I diabetes and type II diabetes are the two main types of diabetes. Type I diabetes usually develops in patients at young age. Due to T cell-mediated autoimmune attacks, type I diabetes is an auto-immune disease resulting in failure of sufficient insulin production and further leading to the loss of insulin-producing pancreatic beta cells. Although the exact mechanism and cause of type I diabetes is not yet fully understood, there is already some evidence that the onset of the disease is related to some environmental factors for genetically susceptible people[2]. On the other hand, type II diabetes, accounting for around 90% of all diabetes cases, is primarily associated with patients' life style. Factors like obesity, lack of physical activity and unhealthy diets contribute to the failure of pancreatic beta cells to respond to high blood glucose levels with sufficient insulin production, ultimately leading to insulin resistance[3].

The definite answer to the cause and mechanism of diabetes is still missing, so the prevention of the type I diabetes is not possible and the diagnosis of type II diabetes is often delayed[4,5]. Insulin therapy as current treatment for diabetes is effective while still has its constraints and challenges in terms of long-term cure to the disease and burden to the health system[6]. One potential strategy is pancreatic islet transplantation first introduced in 1970s with further successful clinical trials on type I diabetes patients[7-9]. Although this technique is not yet approved for routine clinical treatment, it directs the importance of beta cell and its resided in pancreatic islets for both clinical and preclinical diabetes research. Indeed, the key role played by beta cells in insulin secretion makes it essential to monitor its mass and function over the onset, progression and potential therapy of the disease.

Routine clinical tools, such as C-peptide, blood sugar and insulin measurements can only provide indirect information regarding beta cell mass. To visualize and quantify beta cells directly, invasive procedures like biopsies are possible[10-12]. However, they are possibly harmful to the patient and provide only snapshot information. To monitor beta cell mass and function longitudinally, non-invasive imaging techniques are recognized as a high-priority field in diabetes research by several international organizations, i.e. National Institute of Diabetes, European Commission etc[13]. However, the development of accurate, reproducible and clinically compatible non-invasive imaging techniques for beta cell imaging remains a big challenge due to the lack of intrinsic contrast that would distinguish beta cells and pancreatic islets from surrounding tissue[13].

The potential of molecular imaging is associated with several inherent traits of pancreatic beta cells. First of all, imaging endocrine pancreas is already difficult due to its anatomical location surround by the gastrointestinal system and liver. Second, the tissue where beta cells reside, known as islets of Langerhans, consists of small and dispersed entities all over the different regions of the pancreas.

Furthermore, pancreatic islets are present in a low density, which accounts for only 1% - 2% of the total mass of the pancreas. Finally, the high variability of the size of different islets makes the detection of beta cells even more difficult despite the fact that 65% -80% of islets cells are beta cells[14]. These challenges mainly concern the detection of the beta cells in pancreatic islets. Even more challenging is the *in vivo* assessment of functionality of beta cell, which requires beta cell specific markers (for example receptors or transporters) that can be visualized by targeted contrast agents or tracers. While some progress has been made (for example, glucagon-like peptide-1 (GLP-1) imaging)[15,16], there is currently no clinically used robust contrast agent/ tracer available for the non-invasive assessment of beta cell function.

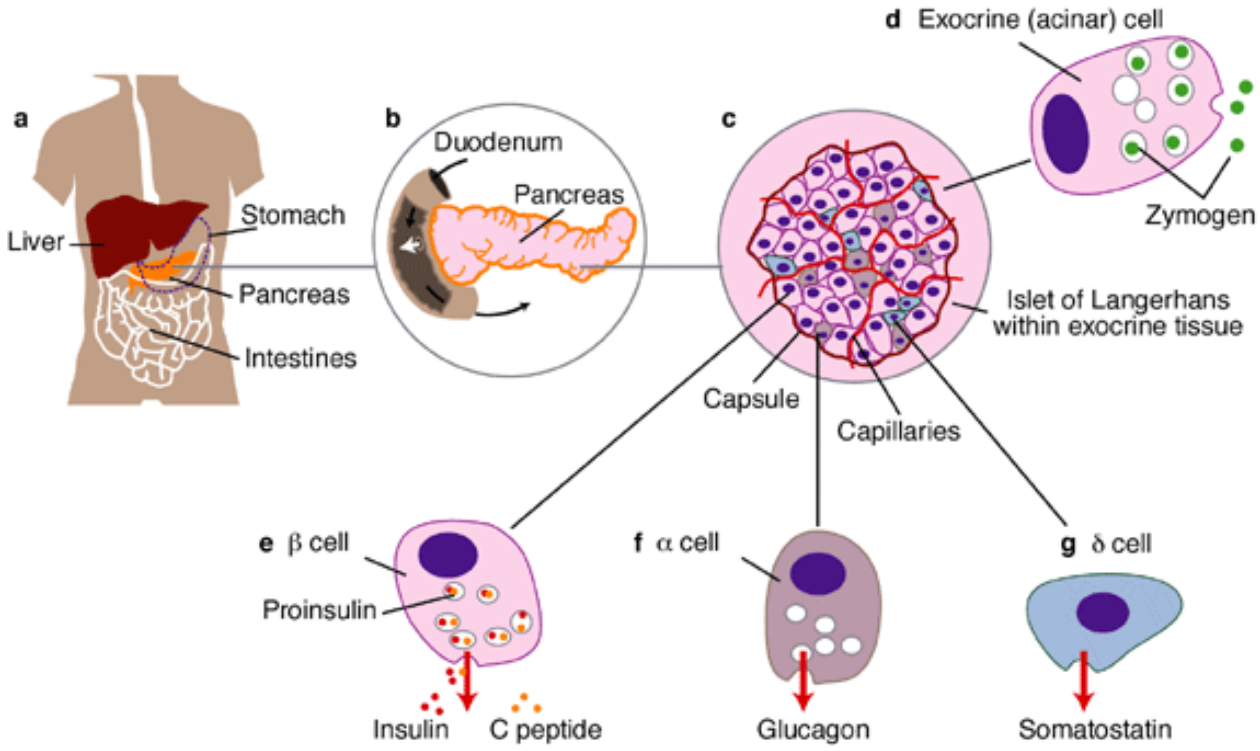

Fig. 1.1 Location of human beta cells in the islets of the pancreas (Adapt from Derek W.R. Gray et al. Expert Reviews in Molecular Medicine ISSN 1462-3994)

1.2. Non-invasive imaging techniques

Non-invasive imaging techniques facilitate clinical diagnosis and follow up of treatment of different types of diseases. Hereby, different imaging techniques are used, depending on the disease to be diagnosed and the organ to be examined. These techniques are also increasingly applied in pre-clinical research with the intention to (1) technical improvement and (2) use them for the assessment of animal models. In general, non-invasive imaging aims to generate visual representations of anatomical, molecular and functional information of an object inferred from physical interaction or biochemical reactions induced signals for various biomedical, bio-molecular and clinical applications. Different imaging modalities have been developed, applied and generalized in the field, which include optical imaging (OI), ultrasound (US), x-ray based computer tomography (CT), methods using radioactive tracers like positron emission tomography (PET) and single photon emission computed tomography (SPECT), magnetic resonance imaging (MRI) and other more research oriented methods. Among

these modalities, each has their own advantages and disadvantages concerning properties such as sensitivity, temporal resolution, spatial resolution, specificity, depth of penetration and safety issue. It is crucial to select the appropriate modalities for specific applications in order to maximize outcome and minimize costs. Utilizing multimodal imaging is sometimes also advisable as it is considered to be able to cross-validate results of different modalities and overcome limitations in terms of sensitivity, resolution and specificity of individual methods. Different imaging techniques are introduced below with a focus on *in vivo* pancreatic beta cell imaging. For more in depth information also see some selected review articles[16-19].

1.2.1. Optical Imaging (OI)

Optical imaging is one of the earliest and most fundamental techniques in biomedical research after the first microscope was introduced in 1674. Different types of optical techniques have been employed, making use of different properties of light (emission, absorption, fluorescence, luminescence, refraction etc.)[20]. Originally applied to mainly dead biological material (tissue sections), optical imaging is now also used for studying biological processes in life organisms *in vivo*. Here, we mainly focus on two macroscopic optical imaging modalities, namely fluorescence imaging (FLI) and bioluminescence imaging (BLI), which allow non-invasive *in vivo* imaging in small animals[21]. Although a charge-coupled device (CCD) is needed to capture the low energy photons for both imaging techniques, the underlying principle for generating images is quite different.

A fluorescence reporter gene, which can generate intrinsic fluorophores or contrast agents like quantum dots (QDs) or organic fluorescence dyes are needed for FLI. After light with a specific wavelength excites the relevant fluorescent reporters/ compound, photons will be emitted back with a longer wavelength, which are then detected by the CCD camera[22]. Attenuation will occur due to the scattering and absorption of the transmitted and emitted light by surrounding tissue. This limited depth penetration of light limits the applications of FLI. In addition, as the whole object is exposed to the excitation light, auto-fluorescence could happen, which will interfere with the signal of interested. Compared to its macroscopic application, FLI is more frequently used on a microscopic scale on tissue sections *ex vivo* (single cell level)[23,24]. The first report on using fluorescence optical imaging for beta cell and islets imaging was proposed by Bertera et al. [25]. They have used the Timer protein to monitor the insulin synthesis via the fluorescence frequency (colour) changes over time. More recently, utilizing the unique anterior chamber of the eye model as the platform for islet transplantation, Speier et al. establish a novel approach for non-invasive *in vivo* fluorescence imaging of pancreatic islets[26].

Bioluminescence is a natural process of light emitted by living organisms, such as firefly, sea pansy, beetles, different bacteria and other organisms using the expression of various luciferase genes[27]. For bioluminescence imaging, these luciferase genes are transfected to the targeted cells using different gene editing approaches[28]. In contrast to FLI, BLI does not require external light for excitement. Instead, a substrate is needed, which will be oxidized by the luciferase in order to emit light. Depending on the different types of luciferase, the interaction between luciferase and its substrate requires also energy resources, e.g. firefly luciferase (Fluc) requires ATP and magnesium as cofactors[29]. As such, bioluminescence signals are only retained in viable cells, which make this technique one of a few tools to assess cell viability *in vivo*. As tissue of the host is not endogenously

bioluminescent, the background signal in BLI is very low. This also contributes to the very high specificity of BLI signal. BLI exhibits very good sensitivity and specificity with detectability ranges around 10^{-15}-10^{-17} mole/L for limited depths (1-3 cm). Compared to other imaging modalities discussed in this thesis, BLI has highest signal-to-noise ratio for sites of low depth penetration. Transfection of different cell lines with different luciferase genes (emitting light with different frequencies) can be applied to distinguish these cells based on the applied substrate and frequency. Major limitations of BLI are the limited depth penetration of light, similar to most optical imaging modalities, and safety concerns related to the translation to clinical use, due to the genetical modification of cells and requirements of substrates.

BLI has been applied for tracking of pancreatic islets and beta cell mass. Hereby, either isolated islets were engineered to express Fluc[30] or transgenic mouse models were developed that constitutively express Fluc have been used for monitoring by BLI[31]. In these studies, linear corrections between pancreatic islets and/ or beta cell number and BLI signal intensity were found. Furthermore, both the transduction procedure and Fluc expression have no significant effect on the islets' function, which helps diabetic mice to restore euglycemia in models of islet engraftment[32]. In brief, sensitive BLI holds promise for pre-clinical imaging and monitoring of the fate of islets after transplantation[33].

1.2.2. Ultrasound (US)

Ultrasound imaging uses sound waves with 100 to 1000 times' higher frequency (1 to 20MHz) than the human ear can detect. Hereby, the sound waves are delivered by an US transducer and sent through the biological tissue[34]. The reflected waves, which are subsequently received, can be used to reveal in real time morphological information of the biological tissue that sound waves travel through and interact with. Contrast is generated based on different factors, such as imaging algorithms, tissue properties and sound speed. This technique has been applied for clinical practice over half a century thanks to its relative low cost, excellent temporal resolution and good safety profile. However, the major drawbacks of US, which limit its application for cellular tracking, is its relative low penetration depth, hampered by high frequency waves, its inability to image regions containing bone and air, whose attenuation coefficient of US wave is very high, and the lack of intrinsic contrast of the targeted cells. Hence contrast agents, e.g. micro-bubbles, gas-filled liposomes or biopolymer-coated bubbles are needed to enhance the specificity and sensitivity for visualization of targeted cells[35,36]. Although US has been utilized for imaging different types of nanoparticles including perfluorooctylbromide (PFOB)[37], gadolinium-gold[38] and super-paramagnetic iron oxide (SPIO)/ gold[39] labelled pancreatic islets and/ or beta cells, it serves as subsidiary modality for multi-modal studies and acts more for illustration purpose.

1.2.3. Computed Tomography (CT)

As a further developed version of conventional X-ray transmission, CT employs a tomographic approach and thus can generate three-dimensional images with high spatial resolution in a relatively short acquisition time. Major limitations of CT are its high exposure to radiation, which bears certain safety risks, and poor soft tissue contrast. Regarding cellular imaging, CT is not an ideal candidate due to this very low contrast in soft tissue, which requires the utilization of contrast agents like iodine or gold nanoparticles. However, these CT contrast agents have a relatively low sensitivity, which

further requires high local concentration of contrast agents[40,41]. Such high concentrations of contrast agents might cause additional safety concerns. However, some preliminary experiments had been carried out during the past decade, such as using iodinated NPs for imaging of macrophage infiltration[42] or targeted gold NPs for imaging cancer cells[43-45], which demonstrate potential future applications of CT for molecular imaging after additional research has been performed. Similar as US, CT has also been applied in multi-modal imaging approaches for research on pancreatic islets and/ or beta cells by providing supplemental information[37-39].

1.2.4. Nuclear Medicine: PET/SPECT

Positron emission tomography (PET) and single photon emission computer tomography (SPECT) are two radionuclide-imaging modalities, now frequently used for clinical diagnosis. PET and SPECT are traditionally used to follow metabolic/ molecular processes. Prior to imaging, synthesis of a tracer which includes a radioactive isotope (synonym: radionuclide) and targets a specific molecular target, cellular receptors or transporters is needed. Upon the injection to patients, radioisotopes emit gamma radiation, which can be detected by a gamma or a PET camera. Localization of the position of the corresponding radioisotope is achieved by different types of detectors[46]. The difference between SPECT and PET is the detection approaches, where SPECT measures the gamma radiation emitted by the radionuclide directly, PET measures two high energy photons with opposite directions generated by annihilation of a positron (emitted by the radionuclide) and a neighbouring electron.

In SPECT, single gamma rays will be emitted by radionuclides (such as ^{123}I and ^{111}In). A gamma camera rotates around the object to acquire different projections of the radiation source, which is used to reconstruct a tomographic image. Along with the gamma camera, a collimator is necessary to only include photons travelling at a right angles to the camera in order to make accurate estimations of the photons origin[47]. In PET, a positron is emitted by the radionuclides (e.g. ^{18}F, ^{11}C and ^{89}Zr). This positron will annihilate during its travelling in the surrounding tissue once it interacts with an electron. As a result of this annihilation, a pair of photons will be generated and emitted in opposite direction, each with an energy 511 keV. Simultaneous detection of the two photons traveling at a 180 ° angle will happen in opposite detectors of hundreds of detectors that are arranged in the form of a closed ring around the subject. Thus, the location of the origin is exactly on the crossing lines drawn between pairs of two detectors that have detected the event of the arrival of a photon within a given time span. The cross of multiple dual hits from same origin is used to determine the exact position of the PET tracer[48]. In principle, radionuclide-imaging techniques are extremely sensitive, which can be used for whole body imaging with high specificity and limitless depth of penetration. Between PET and SPECT, SPECT is less sensitive due to the use of a collimator[49]. The limitations of PET and SPECT are their low resolution and the lack of anatomic background information, which frequently requires combination with CT or MRI to provide an anatomic reference in the clinic[50]. Furthermore, radioactive isotopes used in nuclear medicine also require safety cautions, although, safety regulations are in place to make these methods clinically applicable[17]. The short half live of many radioactive isotopes can also limit their applications for some follow up studies, for example in cell tracking and cell imaging.

Different radioactive probes have been proposed for imaging pancreatic islets, beta cells and the function of the pancreas by targeting specific proteins[13,16]. For example, a monoamine-transporting integral membrane protein called vesicular monoamine transporter type 2 (VMAT2) can be targeted

as it is expressed in rodent and human pancreatic islets. Dihydrotetrabenazine (DTBZ) binds to VMAT2[51]. Hence, [^{11}C] DTBZ was synthesized and used to asses pancreatic function in diabetic rats[52,53]. Due to the high level of nonspecific binding of [^{11}C] DTBZ in the exocrine pancreas tissue, which may lead to potential overestimations of the beta cell mass, ^{18}F-FP-(+)-DTBZ was used next and applied in a clinical trial[54]. Using radioactive antibodies against selectively expressed proteins or lipids on the beta cell membrane is another interesting approach, where a monoclonal antibody against IC2 was labelled with ^{111}In. Linear correlation between beta cell mass and probe accumulation was found[55]. The GLP-1R was also targeted in some studies because it is highly expressed in beta cells and regulates glucose homeostasis. ^{111}In-DTPALys40-Exendin-3 and [^{125}I]BH-exendin (9-39) were developed and showed correlation between the radioactive signal and beta cell mass[56,57]. However, down-regulation of the receptor in rats and humans due to chronic hyperglycaemia can imply underestimation of beta-cell mass in diabetes. Although nuclear imaging techniques are probably most advanced in estimating beta cell mass and function, further optimization and development of alternative strategies for probe development have to be investigated[16].

1.3. Magnetic Resonance Imaging (MRI)

MRI, also known as NMRI or MRT was originated on the same concept as NMR spectroscopy, a physical phenomenon discovered independently by Felix Bloch and Edward Purcell back in the year 1946[58]. Since then, NMR has been used extensively for understanding molecular structure and diffusion using different NMR active nuclei such as ^{1}H, ^{13}C and ^{31}P. These nuclei must possess an odd number of protons or/and neutrons to generate an intrinsic nuclear spin angular momentum under an external magnetic field. By further incorporating with linear magnetic field gradients in the 1970s, first proton MR images were reported by Paul Lauterbur at Stony Brook University[59]. Thanks to the involvement of industry investment together with further academic research to improve the quality of MR images, this technique has eventually evolved into a clinical method in radiology departments that is used for routine diagnostic purposes[60]. Most imaging applications focus on the ^{1}H nucleus as it is the most sensitive and most abundant in the human body (mainly water and fat).

A major advantage of non-contrast enhanced MRI for clinical applications is the fact that only non-ionizing radiation is involved so that it is considered as a relatively safe technique. Potential hazards arise from the use of high magnetic field strength, body heating caused by the absorption of radiofrequency (RF) waves, acoustic noise during the scan and potential claustrophobia and discomfort experienced by some patients. Further safety issues such as nephrogenic system fibrosis and gadolinium deposition in brain may arise with the use of contrast agents, which has to be carefully regulated and monitored. From the imaging point of view, MRI can provide excellent contrast between different soft tissues with very high spatial resolution, making it a perfect method for cell tracking purposes where high resolution is prerequisite to visualize small details on a near cellular level. In addition to the high quality anatomic images provided by MRI, some physiological, metabolic and functional information can also be obtained by adjusting MR acquisition methods (pulse sequences) in so call advanced MR protocols[61-64].

Since the main focus of this thesis is on the development, optimization, validation and establishment of new MRI methods for pancreatic islets and beta cell imaging and quantification, a more detailed introduction to MRI technique will follow in the next section.

Imaging Modality	Anatomical Or Functional	Sensitivity	Temporal Resolution	Spatial Resolution	Safety Cellular Imaging
Optical Imaging	Functional	10^{-9} – 10^{-17} M	Seconds - Minutes	2 – 5 mm	Safe
Ultrasound Imaging	Both	With contrast agents 10^{-12} M	Seconds - Minutes	0.01 – 2 mm	Safe
Computed Tomography	Both	/	Minutes	50 – 200 um	Ionizing radiation
Nuclear Medicine	Functional	10^{-10} – 10^{-12} M	Seconds - Minutes	1 – 2 mm	Ionizing radiation
Magnetic Resonance Imaging	Both	10^{-3} – 10^{-5} M	Minutes - Hours	25 – 100 um	No ionizing radiation

Table. 1 Properties of most common non-invasive imaging modalities

1.3.1. MRI scanner

A modern MR Scanner mainly consists of three parts: a magnet, radio frequency (RF) system and magnetic field gradient system[65,66].

The magnet normally should exhibit a homogeneous, stable and high strength magnetic field (1.5 T to 3 T for clinical scanners and typically 1 T to 17 T for pre-clinical scanners). The so called B0 field will orient MR detectable spins parallel or anti-parallel in the direction of the applied field (also called z- or longitudinal direction) resulting in a net magnetization vector (M).

The RF system can act as both RF transmitter and RF detector by utilizing two separate coils or a sole coil for both tasks. Before acquiring an MR signal, RF transmitter is tuned and matched to the Larmor frequency of the targeted nucleus to generate a B1 field to disrupt the equilibrium state of the magnetization vector created by the B0 field. Depending on the B1 field strength and duration, the magnetization vector can be rotated to the xy or transverse plane by a pre-determined angle. The magnetization vector can be de-composited into a longitudinal component (M_z) and a transversal component (M_{xy}), depending on the applied flip angle. Once the transmitter is turned off, the magnetization vector will return to its equilibrium state. During this process, the RF detector will be

turned on, a current is induced and a free induction decay (FID) of the signal in the time domain will be acquired. This time domain signal will eventually be converted to an MR spectrum or image after Fourier transformation.

The magnetic field gradient system is an essential unit to generate MR images. Indeed, without the linear gradient field (G) generated by gradient coils, it is not possible to distinguish the signal from different spatial locations as the RF system is only responsible for excitation and detection of spins in the whole field of view. Thus, in addition to the main field B0, the linear gradient field G is applied to the excited spins. Depending on the spatial location of different spins, this G field exposes these different spins to different magnetic field strength, resulting in different Larmor frequencies of the spin and their location. Although the G field is small compared with the main B0 field, the spatial information is encoded which can be easily decoded during the Fourier transformation of the FID time domain signal during the image reconstruction.

1.3.2. MR endogenous contrast

The return of the magnetization vector to its thermal equilibrium but also the exchange of energy between individual spins results in modulations of the net-magnetization. These processes are known as relaxation. There are two different processes, referring to the two different physical phenomena, known as Spin-Lattice relaxation and Spin-Spin relaxation, respectively.

1.3.2.1. Spin-Lattice relaxation

Spin-Lattice relaxation is known as the process of restoring the longitude magnetization M_z back to its thermal equilibrium. This relaxation process mainly involves the interactions of the spins with the lattice (e.g., the molecules surrounding a spin), where the energy of spins is transferred to their external environment with the consequence of spins 'returning back' to their initial energy state, dispersing energy to the surroundings. This Spin-Lattice relaxation is also known as T1 relaxation with the relaxation time T1 to describe the time required for 63% recovery of the initial magnetization:

$M = M0 * (1-e^{-t/T1})$ (Eq.1)

1.3.2.2. Spin-Spin relaxation

Spin-Spin relaxation, on the other hand, is the process of decaying or dephasing of the net transverse magnetization M_{xy}. This relaxation process can involve several different mechanisms, which all result in a loss of the phase coherence (dephasing) between different spins, further leading to a decrease of the net transverse magnetization. The major mechanism causing this phenomenon is the slight difference of the local magnetic field that spins experience due to their different chemical environment. Besides, the T1 relaxation accompanied change of the spin's angular momentum can also contribute to the loss of phase coherence. In contrast to T1 relaxation, this Spin-Spin relaxation, also known as T2 relaxation with the relaxation time T2, describes the time required for the loss of 63% of its initial transverse magnetization:

$Mxy = M0 * e^{-t/T2}$ (Eq.2)

In reality, due to the imperfect B0 field homogeneity, T2* relaxation that also refer to spin-spin/transverse magnetization relaxation, is often considered as "effective T2" with faster relaxation rate and smaller value compared to T2.

In order to generate an MR signal and subsequently an MR image, a pulse sequence with different RF pulses is used to modulate the magnetization. This can then be used to modulate contrast, for example, in T1- or T2-weighted MRI protocols. Taken one of the most common sequences, the spin echo sequence, which consist of an 90 ° excitation pulse followed by an 180 ° refocusing pulse, the signal intensity of the image can be expressed as:

Signal ~ Dp * [1-exp(-TR/T1)] exp (-TE/T2) (Eq.3)

Where Dp is the proton (spin) density, TR is the repetition time between successional excitation pulses; TE is the echo time between the excitation and the reception. Modulating the parameters TR and TE generates different type of images as summarized in the table below:

TE value	TR value	Image type
Short	Long	Proton density
Short	Short	T1-weighted image
Long	Long	T2 weighted image

Table. 2 Different MR image type modulated by TR and TE

Since the intrinsic T1 and T2 between different tissues are different, by choosing the appropriated parameters of pulse sequences, the contrast of specific tissues can be generated and highlighted.

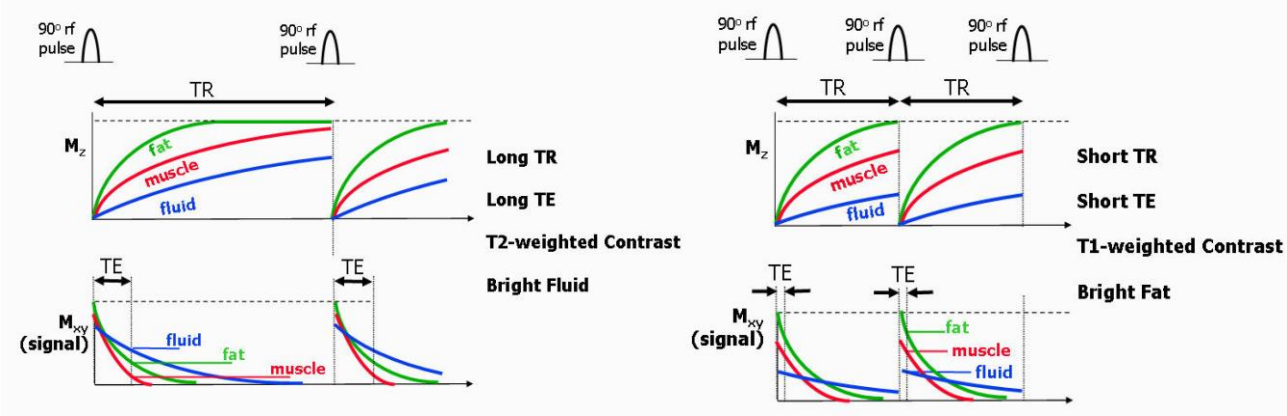

Fig. 1.2 Illustration of T2-weighted and T1-weighted spin echo for three different tissues (fat, muscle and fluid). T1-weighted images are characterized by bright fat and low signal intensity from static fluid and T2-weighted images are characterised by bright fluid and low signal intensity from muscle. (Adapt from John.P.Ridgway (2010) Journal of Cardiovascular Magnetic Resonance 12: 71.)

However, the sensitivity of endogenous MR contrast is still lower than for other imaging techniques without any or limited background signal such as BLI, PET or SPECT. In terms of cellular and/ or molecular imaging, it is more crucial to increase the sensitivity to better visualize the targeted cells or molecular processes at even a smaller scale. Hence, to achieve reasonable sensitivity of MRI for cell imaging, different exogenous MR contrast agents have been proposed, developed and used for labelling cells in order to generate extra cellular contrast against the background of the host's tissue.

1.3.3. MR exogenous contrast

MR contrast agents can be classified into two major categories: proton based contrast agent and hetero-nuclear (other than ^{1}H, MR detectable nuclei) contrast agents[67-70]. By changing the local magnetic properties (such as T1 relaxation, T2/ T2* relaxation and chemical shift), proton-based contrast agents enhance the contrast and hereby the sensitivity for targeting cells. On the other hand, hetero-nuclear based contrast agents, utilize other MR detectable nuclei (such as ^{13}C and ^{19}F) for imaging. In contrast to proton based contrast agents, these 'hot-spot' images enable direct and specific detection of these contrast agents due to the lack of background signal[68].

Proton based contrast agents can be further classified into two different groups based on the material used and their respective chemical properties.

Super-paramagnetic iron oxide particle (SPIO) based contrast agents are also known as T2/T2* contrast agents, since they exhibit low T2/ T1 or T2*/ T1 ratios, mainly due to a dramatic reduction of T2/T2* relaxation time. SPIOs cause a local disruption of the magnetic field homogeneity due to the large magnetic moment they process. This leads to magnetic susceptibility artefacts with a local signal quench, which causes hypo-intense (negative) contrast. The magnetic susceptibility effect range wider than the size of the nanoparticles, causing the so-called blooming effect[71]. Various factors can affect the sensitivity of SPIO, depending on the particle size, surface coating, cellular uptake efficacy and etc., which are discussed in more details in literature[72,73]. In principle, SPIOs are considered to have the highest sensitivity among different MR contrast agents, even single cell detection has been reported[74]. The feasibility of using SPIOs nanoparticles for longitudinal monitoring of pre-labelled pancreatic islets for up to 24 weeks has been shown in several studies including in first clinical trials[75-77]. In one of these studies, it is claimed that a single islet could be detected[76].

Paramagnetic lanthanide chelates or manganese (Mn^{2+}) based contrast agents are considered as T1 contrast agents as they increase the T2/T1 ratio due to a more pronounced reduction of the T1 relaxation time. This results in hyper-intense (bright) contrast on T1-weighted MR images. This is due to the interaction between unpaired electrons of paramagnetic ions with the surrounding water molecules, which decreases the T1 relaxation time of interacting protons. As free paramagnetic ions are considered toxic, chelating is needed to bind the free ions and make them biochemically inert. T1 contrast agents are less sensitive compared to T2 contrast agent, as their influence on T1 relaxation requires interaction with water molecules in close proximity of the ions, which reduces their spatial effect when compared with SPIOs. The estimated detection limit of Gd based contrast agents is in the order of 0.01mM - 0.1mM, which can translate to 100 to 1000 cells[78]. Certain factors, such as the number of ions per molecule, hydration numbers and the exchange rate between water molecules and the ions bound in the chelates are considered being key factors of further improving the sensitivity of

T1 contrast agents[79,80]. However, one big advantage of using T1 contrast agent when compared to T2/ T2* contrast agents is the positive (hyper-intense) contrast, which increases the possibility for quantitative analysis. Human islets have also been labelled with FDA approved paramagnetic gadolinium based T1 contrast agents, whose signal could still be retrieved 65 days after engraftment[81].

However, T1 contrast agents and T2 contrast agents are detected by proton MR imaging. As a consequence, they need to be detected against other sources of intrinsic T1 and T2 contrast in the anatomical background of the organism. This reduces the specificity of these contrast agents, makes it difficult to accurately localize and quantify the contrast agent and cells labelled with them. Making use of hetero-nuclei, which are either not present in biological tissues (e.g., ^{19}F) or with low natural abundance (e.g., ^{13}C) can overcome this issue. Using MR spectroscopy the chemical nature of these agents can be identified and quantification is direct, such as for hyperpolarized ^{13}C MRS[70] or for ^{31}P MRS of phosphorus-containing metabolites[67]. Thanks to its unique properties, ^{19}F MRI using fluorine-containing contrast agents became the focus of recent research also for cellular and molecular imaging during the past decade[82-87]. Since to a large extent ^{19}F MRI used as a key tool in this project for experimental design, validation and optimization, it will be more intensively reviewed and discussed in next sections, which will provide an overview of its history, applications and potential optimizations to overcome its limitations in terms of sensitivity.

1.4. Fluorine Magnetic Resonance Imaging and Spectroscopy

Fluorine-19 magnetic resonance spectroscopy is widely used in chemistry for the assessment of chemical syntheses and structures[88]. One of the big advantages of ^{19}F NMR is the relatively large chemical shift range, which makes it possible to detect even small differences in the chemical environment of a fluorine atom. More recently, fluorine is also used as contrast agent for *in vivo* MR imaging. Here, a brief overview will be provided about the technique of ^{19}F MRI and its application in preclinical research.

1.4.1. Introduction of ^{19}F MRI

In the year 1977, when the first magnetic resonance images (MRI) of the human body were acquired, the first ^{19}F MR images were also acquired by Holland et al. using phantoms made of fluorinated compounds: sodium fluoride (NaF) and perfluorotributylamine (PFTA)[89]. Hence, fluorinated compounds can be considered as one of the earliest contrast agents for MRI.

The ^{19}F nucleus has a spin quantum number of 1/2 with an 100% natural abundance. Its NMR sensitivity is 83% relative to proton. Taken its resonance frequency of 94% of that of proton into account, the MRI signal-to-noise ratio (SNR) of ^{19}F is approximately 88% of that of ^{1}H per nucleus with the assumption that the noise increases linearly with the resonance frequency[90]. Fluorine has the highest absolute NMR sensitivity among all other hetero-nuclei (non-proton NMR). Thanks to the close resonance frequency between ^{19}F and ^{1}H, double tuned RF coils are often made for performing both ^{1}H and ^{19}F MRI with proton image as an anatomical reference frame. More importantly for biomedical applications, unlike the ^{31}P or ^{13}C nuclei, which have significant endogenous MR signals within living tissue, endogenous ^{19}F signal is almost negligible in the body either due to the extremely low physiological concentration or the fast spin-spin (T2) relaxation of immobilized (solid) fluorine

in bone and teeth, which could not be detected by conventional MRI methods. This unique advantage of ^{19}F MRI makes the localization of signal easier with potential absolute quantification. With the administration of exogenous fluorinated compounds/ agents *in vivo*, ^{19}F MRI is often used for following the bio-distribution of the compounds while ^{19}F MRS as complementary technique can provide metabolic information of the compounds.

First applications in preclinical and biomedical research mainly focused on the study of biochemical reactions of fluorine containing sugars and amino acids[91,92], the transformation of therapeutic compounds like 5-fluorocytosine (5-FC) to 5-fluorouracil (5-FU) in cells and tissue[93,94] and the fate of fluorinated compounds used in biomedical research like anesthetics[95-97]. Over the years, ^{19}F NMR spectroscopy (MRS) and MRI found comprehensive applications not only in biochemistry and preclinical research but also in clinical studies[98-101]. In the following section, we will provide a brief overview of currently relevant research were ^{19}F MRS/ MRI is used, mainly in the field of 1. Drug delivery/ bio-distribution studies; 2. ^{19}F MR as a new pulmonary imaging platform; 3. Frequent applications in monitoring specific physiological parameters and 4. Cell tracking and molecular imaging.

1.4.2. Applications of ^{19}F MRI/ MRS

1.4.2.1. Assessment of pharmacological compounds

Hundreds of compounds that are of potential clinical use contain fluorine[102,103]. Their distribution and delivery to the target site could be studied non-invasively using ^{19}F MRI/ MRS if their pharmacological concentrations are high enough for monitoring by ^{19}F MRI/ MRS. Easy localization of the ^{19}F MR signal, potential quantification and broad chemical shift make this technique particularly interesting to address the effectiveness of drug targeting and its further metabolic by-products.

As a prototypical antineoplastic agent, 5-fluorouracil was the first drug studied using ^{19}F MRS between the late 1970s to the early 1980s[90,94,104,105]. The capacity to distinguish between prodrug, the drug and different metabolites of ^{19}F MRS helped researchers/developers to better understand the metabolic aspects and intrinsic toxicity of 5-FU. This further facilitated the design and development of 5-FU based drugs as anticancer agents, in particular for different neoplastic diseases (e.g. neoplasms of the head and neck, the colorectal system) with improved targeting the tumor sites and decreased systemic toxicity[106-108]. Other fluorinated drugs included fluoxuridine[109] and gefinitib[110] were also aimed for antineoplastic activity and studied by ^{19}F MRI/ MRS. Applications for other diseases included fluoexetine as antidepressant drug[111], flurazepam as an anti-anxiolytic compound[112] and FBAPTA as a calcium chelator[113], which have all been evaluated by using ^{19}F MRI/ MRS techniques.

Furthermore, common anaesthetic reagents/ gas mixtures also contain often fluorinated compounds like halothane, methoxyflurane and isoflurane. Several studies were carried out to study the wash in/ wash out kinetics of these anaesthetics. One of the first studies was conducted by Wyrwicz et al., to monitor the accumulation of different fluorinated anaesthetics in the rabbit brain[95]. Further investigations were also conducted in a clinical setting to study the isoflurane kinetics and function in humans[101,114,115].

Recently, ^{19}F MRI/ MRS was also proposed for targeting drugs that are not fluorinated compounds but that are incorporated into fluorinated shells[116] or encapsulated into fluorinated emulsion or with additional fluorinated compounds[117,118]. Under the assumption that fluorinated shells or liposomes and the targeted drugs are stably combined and follow the same route, the distribution and fate of the targeted drugs could be monitored and quantified by ^{19}F MRI/ MRS.

The broad applications of fluorinated compounds in medicinal chemistry and drug design has a huge potential for using ^{19}F MRI/ MRS to follow their distribution and metabolic fate and hereby to better understand mechanism of action of these drugs *in vivo*. However, this field is still quite challenging in particular due to the restricted sensitivity of ^{19}F MRI/ MRS where more technical improvements are needed to improve the feasibility of actual clinical use.

1.4.2.2. ^{19}F magnetic resonance as a novel pulmonary imaging platform

For lung imaging, ^{19}F MRI using inert fluorinated gases can act as a cost efficient alternative to MRI using hyperpolarized (HP) gases and offer similar information on lung morphology and function[119-121]. This has already been tested to assess the diagnostic potential and treatment prognosis in asthma and chronic obstructive pulmonary disease (COPD).

First gas phase ^{19}F MR imaging using tetrafluoromethane (CF_4) could be tracked back to the 1980s[122]. In addition to an economic advantage over HP MRI, utilization of fluorinated gases for pulmonary imaging also avoids the complex and extensive hyperpolarization steps prior to imaging, hereby improving the practicality and the patient safety with the presence of oxygen. This has only little effects on image quality. It further allows longer breath-holds and dynamic measurements.

Different types of studies were performed using this technique to acquire various parameters of pulmonary function. Most studies were performed under static breath-hold[120,121,123,124]. These studies have demonstrated the feasibility of performing ^{19}F MRI of inert fluorinated gases on both volunteers and patients with severe pulmonary diseases. Thanks to the substantial recent advance in MRI in terms of pulse sequence design, magnetic field strength, improved RF coils etc., the image quality has significantly improved to allow easier interpretation of the acquired data compared to initial ^{19}F MRI studies[119]. Other studies including dynamic ^{19}F MRI to investigate the kinetics of pulmonary ventilation by measuring the wash-in and/or washout of fluorinated gases[125-127]. Apparent diffusion coefficient (ADC) measurement of inert fluorinated gas were used to distinguish between healthy and emphysematous tissue[128,129]. Ventilation/ perfusion ratio (V/Q) mapping was estimated based on continuous breathing of a mixture of SF_6 and O_2[130,131].

In general, inert ^{19}F MRI can be considered as a potentially important clinical, diagnostic tool for pulmonary imaging and assessment of different respiratory diseases with the ability of dynamic assessment of the different respiratory phases and the detection of functional biomarkers.

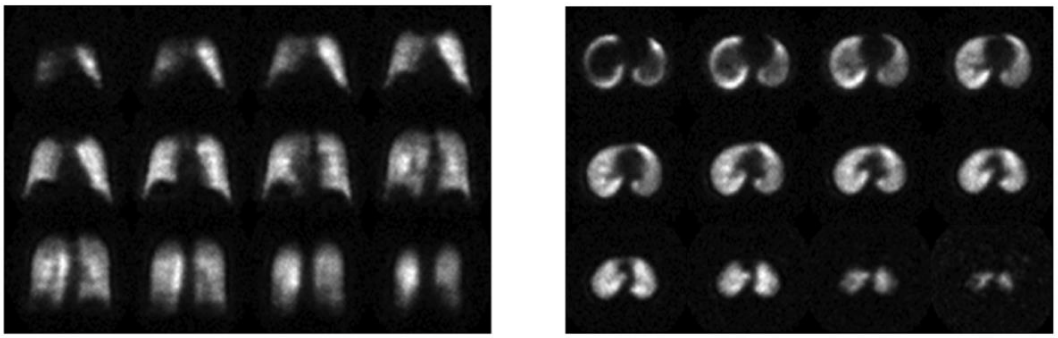

Fig. 1.3 ^{19}F 3D UTE MR images obtained from a healthy volunteer during a 15 s breath-hold after continuous breathing of a mixture of 79% PFP and 21% O2. Left: Coronal view; Right: Axial view. Due to the short T2* of inert fluorinated gases (as short as 2.2 ms for PFP in the lungs at 3 T), the SNR was expected to benefit from a short echo time. (Adapt from Couch et al. (2013) Radiology 269: 903-909.)

1.4.2.3. Assessment of physiological parameters using fluorine-containing probes

^{19}F MRI is also considered as a valuable tool for the evaluation and diagnosis of several physiological features, such as pH, tissue oxygenation and oxygen consumption etc., which are of importance for processes like inflammation, angiogenesis, amyloid beta imaging and others.

The development of stimuli-responsive nanoprobes becomes popular in the field of nanotechnology since various nanosystems respond to certain stimuli (e.g. enzymatic expression, temperature)[132,133]. The key role of the pH value plays in both the intracellular and extracellular milieu makes it as one of the most important physiological parameters to be considered[134]. Indeed, the dysregulated pH gradient across cell membrane of cancer cell compared to normal cell is recognized as an emergent hallmark for development of cancer-specific therapeutics[135]. Though different pH-responsive fluorinated nanoparticles have been proposed in literature, the principle is rather similar and straightforward [136,137]. The branched core of the probes often has two segments with one providing ^{19}F signal and the other offering pH-responsive properties. The ^{19}F T_2 relaxation time is highly dependent on the pH, while the T_1 relaxation time is constant. Based on the difference between pH value and pKa value of segment providing pH-responsive properties, the on/off status of ^{19}F signal could be created. Other similar on/off ^{19}F signal switch probe is also developed when it interacts with enzymes or targeting proteins[138,139].

It is well know that high oxygen consumption is associated with the presence of tumors leading to local hypoxia and decrease of radiotherapy and chemotherapy efficacy[140-142]. Thanks to the linear correlation between partial pressure of dissolved O_2 (pO_2) in hexafluorobenzene/ PFCs with the longitudinal relaxivity R1 (1/T1) of fluorine and the high sensitivity of the fluorine chemical shift to this pO_2, it is possible to map the tissue oxygenation based on the quantitative ^{19}F MRI signal[143,144]. First studies were already carried out in the 1990s[145,146]. Follow-up work mainly focused on different animal models in particular in oncology[143,147,148] and the comparison between ^{19}F MRI with other methods for oxygenation mapping, such as MR blood oxygenation level dependent (BOLD) signal[149], fluorescence quenching[144] and PET[150].

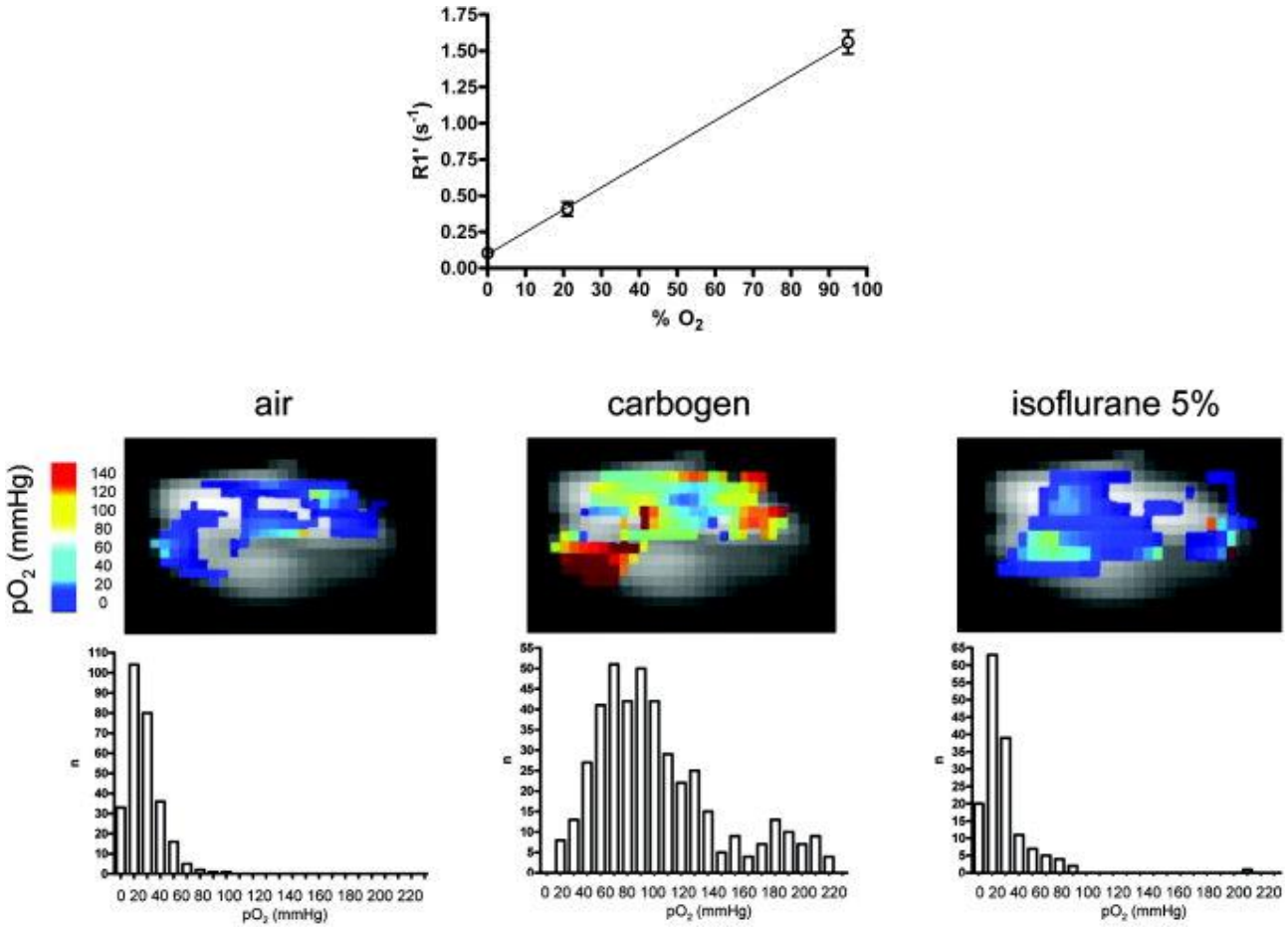

Fig. 1.4 ^{19}F as a tool for tissue oxygenation mapping. Upper: linear calibration (R1') of Hexafluorobenzene with respect to pO_2(mmHg); Below: typical oxygen maps of a typical tumor under air, carbogen, and isoflurane 5% (sacrifice) breathing conditions and their corresponding histograms. (Adapt Jordan et al. (2009) Magnetic Resonance in Medicine 61: 634-638.)

Angiogenesis plays a key role in cardiovascular diseases and cancer. Therefore, visualization and quantification of angiogenesis is also becoming more important in biomedical research and for diagnosis[151,152]. Thanks to the well-described neovascular proliferation biomarker αvβ3 integrin, it is possible to detect angiogenesis by functionalizing PFC emulsions with αvβ3-integrin antagonist. Anderson et al.[153] were the first to use this concept to reveal the presence of newly formed blood vessels in the rabbit cornea. The same strategy was also used to detect angiogenesis in other disease models, such as in tumor model[154,155], models of atherosclerosis[156,157] and overstretch injuries[158].

Amyloid-beta imaging is now considered a key step to better understand of Alzheimer's disease (AD) as the formation of amyloid plaques due to the deposition of amyloid-beta is the earliest pathological change in Alzheimer's disease[159,160]. First reports concerning the use of ^{19}F MRI for amyloid imaging were from Higuchi et al.[161]. Better ^{19}F probes were later on developed[162-164]. Hereby, the same group from Japan reported three different novel ^{19}F agents (FBS based on Congo red, ^{19}F-containing curcumin and styrylbenzoxazole derivatives), that after intravenous injection; can cross the blood-brain barrier (BBB) and bind to Aβ deposits in the brain of AD model mice. If these studies can be confirmed even in clinical trials, ^{19}F MRI would open up a new window in neuroimaging to diagnose and follow up Alzheimer's disease. However, compared to PET tracers targeting amyloid plaques, the reduced sensitivity of ^{19}F MRI still needs to be improved.

Inflammation is a part of the immune response to potentially harmful stimuli in an attempt of self-protection. Hence, it is involved in many different kinds of diseases, such as cancer, type I diabetes, multiple sclerosis, infectious diseases, neurodegeneration and others. For the visualization of an immune response, one often uses the fact that many immune cells, like macrophage populations, phagocytose foreign particles. For the MRI-based visualization of immune cells, one can use iron oxide containing nanoparticles (T2/ T2* contrast) or fluorine containing particles[72]. As the amount of PFC emulsions or nanoparticles taken up by monocytes and macrophages are supposed to correlate with the load of inflammation, this makes ^{19}F MRI potentially interesting to quantify the inflammation in certain organs or at sites of injury[165,166]. More than 30 years ago, first experiments were published on the use of ^{19}F MRI to assess the macrophage dysfunction *in vivo* after acute radiation damage[167]. Furthermore, different inflammation associated animal models have been used to study their pathology, for example: autoimmune encephalomyelity[168], myocardial infarction[169,170], brain inflammation[171], pulmonary inflammation[165], cardiac and cerebral ischemia[172], arthritic inflammation[173], acute deep venous thrombi and pulmonary thromboemboli[174]. Currently, imaging the success of immunotherapy is a hot topic[175-177]. Hereby, pre-labelled immune cells can be used to assess the successful administration of immune cells that are used in cancer therapy.

1.4.2.4. In vivo cell tracking

As already mentioned above, engrafted immune and other cells can be monitored after pre-labeling with contrast agents, which also includes fluorinated compounds and particles. Most of the ^{19}F MRI applications fall in this category of cell imaging and tracking. Ahrens et al.,[82] were the first using perfluropolyether (PFPE) based contrast agents to label and monitor dendritic cells (DCs) for immunotherapeutic purpose. Over the past decade, it has been shown that ^{19}F MRI/ MRS is a unique and powerful platform to visualize the location of engrafted, pre-labelled cells and potentially quantify their numbers in different scenario without any background signal[178]. In addition to pre-labeling, one can also use an approach of systematic *in situ* labeling[68,179].

In situ systemic labelling often works for phagocytic cells, such as macrophages, due to the relative ease of labelling and their biological behaviour of taking up foreign compounds. The tracking of macrophages is often used for studying inflammation as mentioned above[180]. Alternatively, antibodies could be attached to ^{19}F tracers for tracking specific cell types[181-183]. Malaisse et al., also proposed another systematic tracking method of GLUT2 expressing cells, e.g. hepatocytes and beta cells, by injection of fluorine containing mannoheptulose[184]. The uptake of this small molecule through specific transporters (GLUT2) could result in specific cell labelling. However, compared to phagocytic cells, reaching sufficient uptake of the contrast agent *in vivo* is still challenging[185].

Ex vivo pre-labelling of targeted cells and subsequent engraftment into a subject is a more widespread application as this strategy could be achieved in more precise and controlled way, using prior information on labelling efficiency and optimization of the labelling protocol. This has been utilized by many researches focusing on the engraftment of dendritic cells[83,186], stem cells[86,187,188] and T cells[85,175,189] and using ^{19}F MRI for *in vivo* tracking these cells. Some initial work has also been performed on the *in vivo* monitoring and characterization of other types of cells such as pancreatic islets/cells[190,191], red blood cells[139], neural cells[87,192].

Due to the more controlled uptake of contrast agents by pre-labelling of engrafted cells using fluorinated compounds and particles, cell imaging and tracking is one of the most promising applications of ^{19}F MRI/ MRS in biomedical research until now. More exciting, in a recent work published by Ahrens et al., this has already been applied in a clinical trial by intradermal transfer of perfluorocarbon labelled dendritic cells to colorectal adenocarcinoma patients[193].

1.4.3. Limitations of ^{19}F MRI/MRS

Despite the unique advantages of ^{19}F MRI/ MRS, the main obstacle to a broader use is the sensitivity/ local concentration issue. Although, ^{19}F MRI has almost a similar sensitivity as ^{1}H MRI, it requires the utilization of extraneous contrast agents. Local accumulation of fluorinated contrast agents can reach a millimolar range at its best while the concentration for ^{1}H MRI is in the molar range as tissue water and fat contributes to most of the signal. To compensate for the low concentrations, ^{19}F MRI/ MRS always requires acquisition of many averages, resulting in long scan time with relatively poor image quality in terms of resolution and SNR. Hence, improving the sensitivity of ^{19}F MRI is a key to broader applications especially for clinical studies. In the next sections, we would like to go through different aspects that are relevant to the sensitivity of ^{19}F MRI and address the published and potential future technical improvements that can further enhance the sensitivity with a focus on cell tracking and imaging.

Major points related to cellular and molecular imaging and the sensitivity of ^{19}F MRI that will be discussed are following: ^{19}F MRI probe design, cell labelling strategies, MRI hardware, MRI acquisition methods and MRI data processing including data quantification.

1.4.4. Improving the Sensitivity of ^{19}F MRI/ MRS

1.4.4.1. Probe/ contrast agent design

Currently fluorinated probes used for cellular and molecular imaging purposes can be divided into four different groups based on their chemical properties: emulsions, linear polymers, (hyper) branched derivatives and fluorinated small molecules[194].

Fluorinated small molecules have the advantage of being adapted to a specific cell functionality and are either identical to a substrate (for example fluorinated drugs) or they are only slightly chemically modified (for example FDG). This makes them highly specific for monitoring a targeted cell type or process. Published works including sugar based fluorinated molecules used for beta cell and hepatocyte imaging[185]; self-assembling nanoprobes acting like on/off switch for protein detection of live cells[139]; paramagnetic relaxation based ^{19}F probe to detect protease activity[195] and fluorinated drugs[94]. However, the main disadvantage of this type probes is that they only contain a limited number of chemically identical fluorine atoms, which limits their detectability.

On the other hand, (hyper)-branched derivatives can offer a very high fluorine density per molecule. Several hyper-branched polymers were synthesized with different end groups and some were applied for *in vivo* imaging in mice[103,196,197]. The main obstacle of using this type of tracers is the often difficult (or even impossible) and elaborate syntheses procedures, low reproducibility and the

complex cyto-compatibility and cell uptake mechanism, which is due to a more severe modification of the chemical structure of the original compound[194].

More than two third of the published ^{19}F MRI based cell or molecular imaging work used either fluorinated linear polymers or emulsions. Both types are mainly PFC-based as they provide high fluorine content per molecule. For fluorinated linear polymers, linear PFPEs are most frequently used. Hereby, hydrogen atoms of polyether are usually replaced with fluorine atoms. Different PFPE based polymers were proposed by using either single polymer or mixtures with different levels of poly-dispersity, such as PFPE oxide or fluorescent blended PFPE amides (FBPAs)[84,189,198]. These linear polymers have advantages in terms of increased fluorine content and good relaxation property (short T1 and sufficiently long T2). A minor concern is the fact that multiple ^{19}F peaks of PFPE are present in the spectrum, where some of them can cause chemical shift displacement effects or lead to signal loss if their chemical shift is not in a close range.

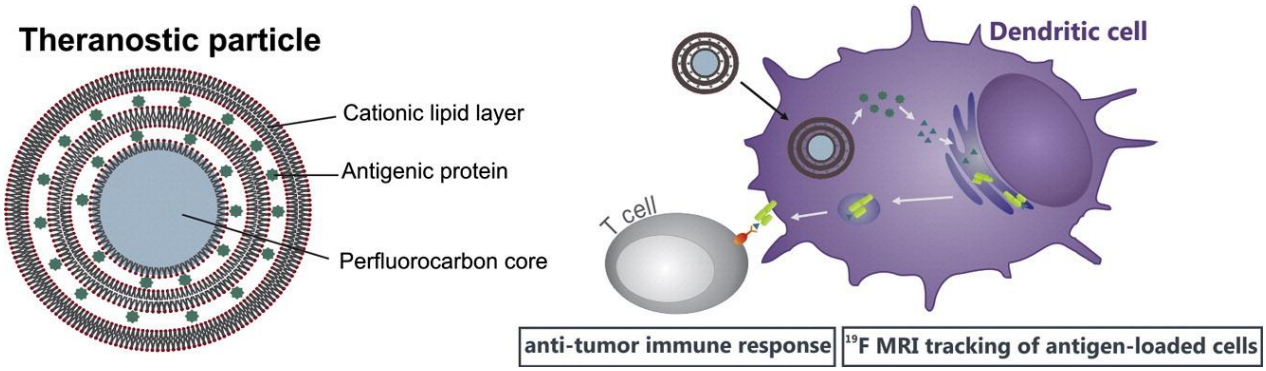

Fig. 1.5 Schematic of a typical ^{19}F theranostic particle for ^{19}F MRI tracking of dendric cell based vaccines. (Adapt Dewitte et al. (2013) Journal of Controlled Release 169: 141-9.)

The PFC molecules most frequently used are perfluorooctyl bromide (PFOB) and perfluoro-15-crown-5-ether (PFCE), formulated as emulsions. Both PFCE and PFOB are hydrophobic. In order to be used for biomedical research, a surfactant is needed to stabilize them and keep their dispersity in water. The most frequently used surfactants are phospholipids. They are the major component of cellular membranes and considered to be safe for *in vivo* use. Thanks to their high content of fluorine and their easy formulation, it makes these emulsions particular popular in the field of biomedical imaging. Furthermore, these emulsions could easily be conjugated with other agents to act as multimodal agent or to further improve their performance by linking them with targeting moieties. Potential shortcomings are the instability of the emulsions over time, causing fluorine signals to split and resulting in heterodisperse formulations. In addition, environmental effects (such as temperature) can have an effect on the relaxation time of emulsions[199]. PFOB and PFCE are more difficult to be chemically modified compared to PFPE.

In general, an 'ideal' ^{19}F probe should fulfil following the requirements:

- Biologically inert and chemically stable;
- Minimal or no cytotoxicity and effect on cell functions;
- Single resonant frequency on ^{19}F NMR spectrum;
- Sufficient uptake/ binding by/ to targeted cell;

- High fluorine content per molecule and favorable relaxation parameters[68].

The biological/chemical properties of ^{19}F probes and their effect on cell function have been extensively addressed in other reviews[83,90]. Here, we would only focus on discussing the categories that are directly or indirectly related to the sensitivity issue.

A first possibility is straightforward: how could more fluorine atoms be loaded to a molecular structure? As mentioned above, PFCs are well known for their high load of fluorine atoms. This is one major reason why PFC-based tracers are most popular at the moment. A further optimized and desired feature of these PFCs is that all fluorine atoms should be chemically identical, for example the three fluorine atoms in a CF_3-group, which can lead to a single peak in the ^{19}F NMR spectrum without potential loss of signal due to chemical shift effects. Among the above-mentioned PFCs, PFCE is in particular interesting as it exhibits 20 equivalent fluorine atoms per molecule, which maximizes the ^{19}F signal per molecule. More recently, Tirotta et al.,[200] presented a new super-fluorinated molecular probe, which is called PERFECTA. PERFECTA surpasses PFCE with 36 equivalent ^{19}F atoms. Furthermore, it possesses excellent cellular compatibility with high uptake during a short incubation time and it could be synthesized easily with good yield and large quantities via a simple one-step reaction.

Yu et al.,[201] have successfully presented a structure with up to 243 chemically identical fluorine atoms represented in one ^{19}F NMR signal in symmetric fluorocarbon dendrons. However, with increasing number of fluorine atoms, the molecular mobility will also be increasingly restricted, which affected the solubility of the probes and caused significant signal attenuation[202].

Efforts to design probes with more favourable relaxation parameters for MR imaging purposes are also numerous in the field. Favourable relaxation parameters for ^{19}F MRI are:

1. Independent of the environment in order to be able to predefine and optimize the scanning parameters except for special purpose, such as pH mapping[139].

2. Maximization of image SNR for a fixed scan time.

The second criterion is particularly important as often many repetitions are needed to reach the detection limits of a probe by using ^{19}F MRI. Thus, it is desired to reduce the repetition time (TR) to have as many repetitions as possible at a fixed time. Unfortunately, inherent low longitude relaxation rates (R1) of PFCE/ PFOB often result in relative low imaging efficiency[199]. This results in the open challenge to shorten T1 or increase the T2 (T2*)/ T1 ratio of fluorinated tracers.

In general, Mn^{2+}, Fe^{3+} and Gd^{3+}, are high-spin paramagnetic metal ions, which are capable to change relaxation parameters of MR contrast agents. Hence, several attempts have been made to use this paramagnetic enhancement method to increase the sensitivity by introducing these ions either intra- and/ or inter-molecularly. Neubauer et al.,[203] used an inter-molecular method by directly incorporating Gd into the lipid monolayer, which surrounds the PFCs core. The authors have claimed an 125% increase in signal with the freedom of fine-tuning the concentration of Gd to be quantitatively modulated to tailor the particle properties. More studies used intra-molecule method by introducing paramagnetic ions into the same molecular structure. Schimid et al.[181], used an ultrafast MRI sequence (zero echo time, ZTE) to detect fluorinated molecule that were combined with paramagnetic ions. They have gained an increase of sensitivity by a factor of 27. On the other hand, Chalmers et al.[204] proposed three CF_3-labelled lanthanide complexes, based on mono- and diamide cyclen ligands, which proved to result in an enhanced sensitivity for ^{19}F MRI. Several similar

approaches were also described in the literature[182,183,205,206]. Recently, Kislukhin et al.[207] introduced a new approach, which is a combination of both, an intra- and inter-molecular link to paramagnetic metal ions. They formulated an emulsion of PFPE-conjugated with metal-binding beta-diketones (FDK), and then metallated them with various transition element and lanthanide ions in the fluorous phase. The sensitivity for ^{19}F MR imaging could be enhanced by at least eight fold for routine clinical MRI scanners.

1.4.4.2. Cell labelling strategies

Parameters like the cell medium, length of incubation, optimal labelling concentration etc. will directly affect the cell labelling efficiency. For example, the size of ^{19}F tracers is especially crucial and debatable. A recent study[202] proposed a one-pot strategy for the fabrication of a small size multifunctional nanoprobe with high load of ^{19}F atoms. Thanks to its small size (around 20.8 nm), it exhibited good molecular mobility and was able to increase the cellular uptake. On the other hand, Waiczies et al.[208], claimed a different opinion that better uptake could be achieved by increasing size of emulsion. Hence optimization of these variables is always needed before real experiments since the optimal setups of different experiments can have huge variety.

For most cell labelling strategies, optimization is performed *ex vivo*. This is particularly true for nanoparticle based approaches, where contrast agents are relatively big (range from hundreds of nanometers to micrometers for fluorine containing liposomes). While labelling is straightforward for phagocytic cell types, cellular uptake enhancement is needed for non-phagocytic cells.

The most common method for fluorinated contrast agents is to add a positive charge to the lipid of the PFC emulsions, since the cellular membrane is anionic and the attractive force between them facilitates the uptake by the cells. In this way, different non-phagocytic cells have been labelled with reasonable amount of fluorine atoms for imaging[85,191,209]. Using transfection agents is another popular technique for improving the cellular uptake of fluorinated contrast agents. In the very first study of ^{19}F MRI based cell imaging, Ahrens et al. used a transfection agent for labelling dendritic cells[82]. Hereby, 26 fold-increased uptakes with only very little side effects on the DC's function was found. Other studies, using either T cell[84] or breast cancer cells[210] as targeted cells, also found that transfection agents improve cellular uptake of fluorinated contrast agents.

Peptide conjugated PFC emulsions for labelling various cell types were also considered valuable approaches for increasing uptake. Kok et al. used RGD-peptides to target the cell-internalizing α(v)β(3)-integrin expressed on endothelial cells[211]. Temme et al. proposed an α2-antiplasmin peptide (α2AP) for early venous thrombosis imaging[174]. Both reached excellent sensitivity compared to non-modified PFC emulsions. Furthermore, PFC binding with specific antibodies for targeting particular cell types has also proven to be helpful with a two folds gain in uptake[212]. Other potential techniques for improving cellular uptake include electroporation[213,214] and receptor-mediated uptake[215-217]. However, they were only used for proton based iron contrast agents and have not been applied for fluorinated contrast agents yet.

1.4.4.3. MRI hardware

As mentioned before, modern MRI scanner consists of three main parts: a static magnet, a magnetic field gradient system and a radio frequency (RF) system. Below, we will address the relation between the ^{19}F MRI sensitivity and each part of the MR hardware in more detail.

1.4.4.3.1. Static magnetic field

As shown in Eq.4, at a low static magnetic field B_0 (< 1T), the dominated thermal noise is from the resistance of the coils and for high B_0 (> 1T), and the resistance of the sample is the primary thermal noise. Hence, at low B_0, SNR~$B_0^{7/4}$; while at high B_0 (relevant for most of the clinical and pre-clinical MR scanners), SNR is proportion to B_0[218]. Independent of these considerations, the SNR is larger at a higher magnetic field strength, which could be translated to be able to detect either a lower number of fluorine labelled cells or detect the same number of cells during a shorter scan time or with a higher spatial resolution.

$$SNR \sim \frac{B0^2}{\sqrt{(Ns*B0^2+Nc*\sqrt{B0})}} \qquad \text{(Eq.4)}$$

B_0: static field; Ns: noise from sample; Nc: noise from coils

On the other hand, magnetic susceptibility effects will become significant at higher B_0, which will lead to faster T2* decay, causing extra signal loss. The T1 relaxation time will be increasing at higher B_0, which will require longer TR and prolong the scan to acquire an image that reaches the same initial magnetization or contrast. For fluorinated contrast agents with multiple peaks, a higher magnetic field strength increases the absolute chemical shift range. This may require higher receiver bandwidths to be able to pick up the signal from the whole spectrum for some cases (e.g. chemical shift imaging), which can cause indirect reductions of SNR since SNR is also reversely proportional to the square root of the receiver bandwidth.

Other aspects, not directly relevant to SNR are also potentially hindering a broader application of higher magnetic fields. Apart from the fact that homogeneous magnetic fields are more technical demanding to be generated at high field strength, higher field magnets are also more expensive and raise some safety issues since RF power deposition in the tissue is proportional to B_0^2.

1.4.4.3.2. Magnetic field gradient system

An ideal gradient coil should have high current efficiency (defined as the ratio of gradient generated to current drawn), short switching times (high slew rates), good linearity over a large volume, low power consumption and minimal eddy current[59,219]. The performance of gradient coils is especially critical for MR techniques, such as MR diffusion, perfusion and angiography imaging, as these techniques always need either high gradient strength and/ or rapid gradient switching.

In case of ^{19}F MRI, demands on the gradient system are of a lesser concern, as one has to deal with lower resolution images compared with other techniques. Therefore, routine setups of gradient systems provided by vendors are sufficient for most ^{19}F MRI applications. The gradient system may

play an important role only when specific fluorinated contrast agents with fast relaxation parameters are used for imaging. Then, fast imaging sequences are needed, leading to more eddy current introduced by gradient coils, which is prone to introduce artefacts for imaging, which can have substantial impact on ^{19}F MRI since its SNR is already quite low. Hence, post quantification and compensation of the eddy currents is needed[220,221].

1.4.4.3.3. Radio frequency (RF) system

For transmission and reception of an MR signal, RF coils are required. Ideal transmitter should generate a homogeneous B_1 field, which also applies to ^{19}F MRI. This is in particular true for quantitative applications, like the quantification of the numbers of cells. Receiver, on the other hand, is expected to be as sensitive as possible to maximize the signal while reducing the pickup of noise. Hence, optimization of transmitter homogeneity and receiver sensitivity is key for improving the quality of ^{19}F MR images.

In addition to general requirements for "ideal" RF transmitter/ receiver, a coil that is tuneable and matchable to the ^{19}F and ^{1}H frequency is needed for most applications of ^{19}F MRI since the ^{1}H MR image is required for providing anatomic information. The alternative of repositioning of different coils for the same imaging session would not be optimal as image registration would not be straightforward.

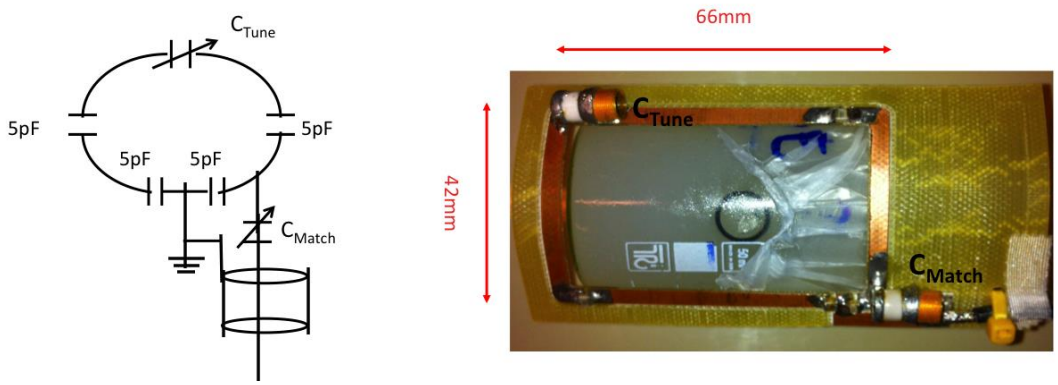

Fig. 1.6 Schematic of a typical double tunable and matchable (1H/ ^{19}F) surface coil, the resonant frequency could be altered by adjusting tuning/ matching capacitors. Left: schematic design of saddle shaped surface RF coil used in this thesis; Right: image of the surface RF coil with dimension and tuning/ matching capacitor indicated.

However, the commonly used shunting method and multiple poles method for designing dual-frequency coils only works well when the two MR detectable nuclei's resonance frequencies are well separated, such as for ^{1}H and ^{31}P (25.47 MHz/ T)[222]. Since the resonance frequencies of ^{1}H and ^{19}F are very close (2.6 MHz/ T), most ^{19}F MRI studies are using homemade surface coils with tuneable capacitors for tuning between the two frequencies[87,185]. Using this kind of surface coil has advantages in terms of ease to build them and a relative high sensitivity. Their disadvantages are potentially non-uniform B_1 fields, extra time for retuning and different sensitivity profiles for ^{1}H and ^{19}F.

To overcome the problems mentioned above, different strategies for building ^{1}H/ ^{19}F RF coils have been proposed. Hu et al. showed a generalized strategy for building ^{19}F/ ^{1}H dual frequency RF coils that permits multiple coil geometries. Based on a secondary coupled resonator, both birdcage and

saddle $^{19}F/\ ^{1}H$ volume coils were implemented and evaluated[223]. By changing the coupling between the sampling coil and the resonator, tuning and matching to both ^{19}F and ^{1}H channels were realized. This method could be beneficial in terms of identical and homogeneous B1 field distributions for both channels. However, this method may not be practical for larger inductance of a sample coil at higher magnetic field, because the capacitors in the coupled resonator circuit become impractically small (below one pF) and difficult to adjust. Similarly, Mazurkewitz et al. have also designed double tuned solenoid coils with practically identical sensitivity profile for ^{19}F and ^{1}H by including one well-designed parallel LC-circuit in series with coil conductors[224]. A double tuned RF coil has also been proposed that consists of three parallel-connected series inductor capacitor circuits[225]. Thanks to the reduced resistance component of its parallel connection, the sensitivity of such a double-tuned coil is relatively close to that of a single-tuned coil. Hockett et al. introduced an open RF coil design in conjunction with a coupled second auxiliary resonator to be able to image both ^{1}H and ^{19}F simultaneously at a clinical scanner[226]. With the current steering similar to a birdcage design, this design can provide a larger coil volume with enhanced B_1 field uniformity while maintaining adequate sensitivity.

There are also more other interesting designs for double tuned $^{1}H/^{19}F$ RF coils. Based on a balanced circuit with commercially available, variable capacitors, tuning between two different frequencies could be accurately performed within seconds using diodes controlled by a computer using digital potentiometers. In addition to ^{1}H and ^{19}F, ^{3}He imaging could also be acquired at 4.7T. This is especially beneficial for pulmonary MR imaging as both the fluorinated gas and the hyperpolarized gas are suitable MRI contrast agents for the lung[227]. Waiczies et al., showed a novel dual-tuneable $^{1}H/^{19}F$ birdcage probe with a shingled-leg design[171]. They eliminated solid chip capacitors by placing the birdcage's leg copper strips overlapping with strips extending from the end rings of the birdcage. Their coil exhibits boosted field homogeneity and good sensitivity for neuroimaging in mice, because of the small diameter with more legs. More recently, Ji et al. evaluated the feasibility of an eight-channel dual tuned transceiver surface RF coil array for combined $^{1}H/^{19}F$ MR of the human knee at 7.0 T following the application of fluorine containing drugs[228]. Array coils have advantages of enhancing the SNR, increasing the field of view and potentially being applied for parallel imaging with accelerating the acquisition by reducing the amount of k-space data[229]. Another promising strategy is the use of cryo-coils instead of coils operating at room temperature. Hereby, a considerable noise reduction could be achieved at extreme low temperature, which improves the SNR[230]. However, building this kind of coil often requires a complex design and may meet practical limitations. For ^{1}H MR, cryo-coils have already been used in a pre-clinical environment[231].

1.4.4.4. Software

In this section, we will discuss the relationship between sensitivity and 'software' settings in MRI. The term 'software' concerns here the choice of different pulse sequences, common and critical sequence parameters (e.g. TE, TR and flip angle) and post-processing methods for ^{19}F MRI signal processing and quantification.

1.4.4.4.1. Choice of the MR sequence

The choice of imaging sequences plays an important role in acquiring optimal images within a short timeframe. Conventional gradient echo (GE) or spin echo (SE) based sequences are most frequently used also for ^{19}F MRI studies. For these pulse sequences fast versions are preferred, such as GE based fast low angle shot (FLASH) and SE based rapid acquisition with relaxation enhancement (RARE)[84,232-235]. In general, RARE has a considerable predominance in published work due to an advantage of being less sensitive to susceptibility (T2*) artefacts. Nevertheless, the performance of different sequences also dependents strongly on the relaxation property of the fluorinated compound, which will ultimately lead to the selection of different imaging parameters. Optimization of acquisition parameters was already addressed in the very early ^{19}F MRI studies from the 1990s to optimize the SNR[236,237].

As ^{19}F MRI has attracted more attention during the past decade, some more recent work addressing optimization of imaging sequences is of interest. Mastropietro et al. calculated theoretical relative SNR changes at given relaxation times and mapped them in RARE parameter space (TR, number of echoes, flip angle) using a fixed acquisition tim[238]. Their simulations were then further validated with a potassium hexaflorophosphate (KPF6) phantom in different environments. They claimed that an increase of 30% SNR could be gained with their optimized settings even in the case of low T2/T1 ratios. In addition to optimization of parameters for common sequences, different research groups have also proposed novel/ different pulse sequences. Balanced steady-state free precession (bSSFP) was claimed to be one of the most SNR efficient pulse sequence in use[239]. It could be demonstrated that bSSFP is feasible for ^{19}F MRI applications, where accurate quantification can be provided and 3D images with short acquisition times can be acquired[240,241]. However, bSSFP has limitations due to banding artefacts especially at high magnetic fields, which can only be suppressed by shortening TR or by employing phase cycling. Making use of other fast imaging sequence, such as ultra-short TE (UTE) or zero-TE (ZTE) sequences, can also boost the SNR. However, this applies to the condition of fast relaxation times of the fluorinated compound in the range of 1-5ms and a high T2*/T1 ratio[181,204]. In contrast to cell and molecular imaging, these sequences are more often used for ^{19}F MRI of the lung, which deals with gas phase fluorinated compounds[120,242].

Although fluorinated compound exhibiting only one resonance peak can simplify the imaging task, many other compounds with multiple resonance peaks might be of interest in imaging studies. However, different resonance frequencies can introduce chemical shift artefacts to the image, which often results in ambiguous localization and quantification. Selective pulses can overcome this problem at the cost of reduced signal intensity. However, if the signal from all the peaks can be used, the sensitivity would also be improved. Hence, different techniques/ sequences have been proposed to address this problem. One possibility is to perform efficient k-space sampling strategy to further improve the SNR/t[243]. Goette et al., proposed a novel technique by using dual-frequency ^{19}F/^{1}H UTE sampled with a bSSFP pulse sequence and an 3D radial readout[244]. By validating the approach by using a PFOB phantom, their method manifests a two-fold better SNR when compared with traditional acquisition techniques, and alleviates problems caused by dephasing in complex spectra. By carefully choosing the bandwidth of the refocusing pulse in a spin echo sequence, J-coupling could be suppressed and allowed multi-echo accumulation as reported[245]. Four to six times better sensitivity than short TE/TR gradient echo and chemical shift imaging (CSI) acquisitions could be

achieved. Other methods including the use of back projections by taking advantage of short sampling times[246] and based on different resonance peaks, ^{19}F MR images of multi-resonance compounds can be obtained after carefully adjusting imaging parameters[247]. More recently, Meissner et al. proposed a de-convolution method, which is capable of correcting chemical shift artefacts to enhance the SNR and reveal signal that vanishes in the noise in the original image. With both, *in vitro* and *in vivo* ^{19}F MR images, they showed that the corrected image can increase the SNR by 20% to 50%[248].

1.4.4.4.2. Acquisition parameters

Not only the actual pulse sequence, but also the correct choice of acquisition parameters is critical. In general, the MR signal is proportional to the voxel volume and appropriately selected, sequence specific parameters for particular tissue types and contrast agents. The noise is related to the acquisition bandwidth and number of averages and encoding steps[65,249]. A generalized equation is shown in Eq.5. This equation is valid for 3D images, while for 2D MR images, the term Npe2 has to be left out as 2D sequences uses slice selection with Δz representing the slice thickness.

$$SNR \sim K * \Delta x * \Delta y * \Delta z * \sqrt{Nsa * Nre * Npe1 * Npe2}/\sqrt{rBW} \quad \text{(Eq.5)}$$

Δx, Δy and Δz: resolution along three different directions;

Nsa: number of signal averages;

Nre, Npe1 and Npe2: number of steps in read and two phases encoding directions;

rBW: receiver bandwidth.

Constant K: combines several factors such as hardware configurations, pulse sequence and relaxation behaviour of the tissue/ contrast agent.

According to Eq.5, an increased SNR is possible by increasing the number of averages, which will lead to a much longer scan time as SNR is proportional to the square root of Nsa. As MRI is a "compromised" technique, we need to trade-off between SNR and scan time, which makes the term SNR per scan time (SNR/ t) more reasonable in the case of ^{19}F MRI. For a 3D MR image, the scan time is expressed as:

$$Scan\ Time(t) = TR * Nsa * Npe1 * Npe2 \quad \text{(Eq.6)}$$

If we combined Eq.5 and Eq.6, we have our formula for SNR/ t:

$$\frac{SNR}{t} \sim K * \Delta x * \Delta y * \Delta z * \frac{\sqrt{Nre}}{TR*\sqrt{rBw*Nsa*Npe1*Npe2}} \quad \text{(Eq.7)}$$

Parameters: Δx, Δy, Δz, Nre, Npe1 and Np2 are coupled and related to the image resolution and field of view. Higher resolution images can resolve more details with a loss of SNR/t. By decreasing the image resolution or increasing the slice thickness, higher SNR could be achieved. Compared to proton MR images, ^{19}F MR images are often acquired with a much lower resolution, which is an easy way to boost the SNR in ^{19}F MRI. However, this approach could be restricted by hardware limitations (often certain MR systems, in particular clinical scanners, have restrictions for the lowest matrix size/maximum field of view) and partial volume effect, which underestimate the signal of small object

due to poor resolution[250]. To some extent, partial volume effect could be corrected during image post processing as described previously[84,85].

The receiver bandwidth (rBW) defines the frequency spectrum used for data collection. Higher SNR/t can benefit from a lower bandwidth. However, a broader bandwidth allows shorter minimal TE, which may help collecting more signal especially for fluorinated compounds with very rapid relaxation. As PFCs have a T1 in the order of a second at high field strength, broader rBW is not really necessary unless compounds with multiple resonance peaks are used with the intention of not losing signal from some of the peaks[199,245].

As immediately derived from the Eq.7, TR is inversely proportional to SNR/t. Unfortunately, this does not mean shorter TR always lead to better SNR/t, the optimal TR is highly dependent on the sequence and the relaxation behaviour of the fluorinated compound that has been used. For gradient echo sequences, the maximized signal could be achieved by setting the flip angle to the so-called Ernst angle for a specific TR value[240]. For spin echo sequences, the traditional excitation pulse is often a 90 °pulse and full recovery of the magnetization is desired to reduce the dephasing of spins thus leading to long TR. As the choice of TR depends on the T1 of the fluorinated compound, short T1 of contrast agents is always desired so that TR and the total acquisition time could also be reduced accordingly.

1.4.4.4.3. Post processing methods

In addition to the conventional acquisition methods, new MR acquisition approaches in combination with post-processing algorithms can also provide improvement on SNR/t. One of the most popular techniques are so-called compressed sensing (CS) techniques, making use of the sparsity of MR images[251]. Several studies have already used CS in association with ^{19}F MRI thanks to the sparsity in the imaging domain of ^{19}F MRI data[252-254]. Zhong et al. demonstrated that 3D CS could effectively increase SNR/t by a factor of 8 without degrading the image quality[253]. Liang et al. investigated the application of different CS reconstruction methods for low SNR applications of ^{19}F MRI[254]. The gain in terms of SNR/t was in the order of 3 to 4 fold.

Accurate quantification of the ^{19}F MRI signal is one of the important hallmarks of ^{19}F MRI based cell tracking experiments when compared to MRI that uses conventional T1 or T2 contrast agents. In most published work, *in vivo* quantification of labelled cell numbers requires prior information of labelling efficiency using NMR spectrometer, where the peak integral of labelled cells is compared with the number of pre-counted cells[82,85,87]. During *in vivo* MR imaging, a reference tube of a fluorinated compound of known concentration is placed adjacent to the subject and scanned simultaneously. The number of ^{19}F atoms could be derived under the assumption that the B_1 field of the RF coil is homogeneous and the SNR of ^{19}F MRI signal is linearly correlated with number of fluorine atoms. With this in mind and the assumption that the label is evenly distributed among the labelled cells, the number of labelled cell could be calculated based on the *in vitro* experiments.

However, for most of ^{19}F MRI applications, surface coils are used to increase the sensitivity at the cost of inherent inhomogeneous B_1 profile. Therefore, correction of the B1 field is often needed. Basse-Lusebrink et al. made use of the fact that most surface coils for ^{19}F MRI applications are double tuned[255]. They presented one possible solution by using fast ^{1}H Bloch-Siegert B1 mapping to assess the inhomogeneous ^{19}F MRI B_1 profile. They found that the spatial derived ^{1}H/^{19}F B_1 ratio was about

1.51 by cross-validation with two fast spectroscopic reference scans. Boehm-Sturm et al., on the other hand, used a scheme that maps the flip angle (FA) on the ^{1}H channel[256]. At the cost of an extra 10 minutes' scan time, the same B_1 profile for the ^{1}H and the ^{19}F channel could be generated Proof of concept experiments have been carried out, both *in vitro* and *in vivo*. More recently, Goette et al. used flip angle sweeping experiments on PFC nanoparticle point source phantoms with three custom-designed $^{19}F/^{1}H$ dual tuned coils[244]. An image-based correction technique using B_1 field mapping on ^{1}H to correct for correction in ^{19}F was developed. The optimized ^{19}F peak power differed significantly from that of the ^{1}H channel for each coil. By employing their correction method, an offset of about 66% for two identical ^{19}F PFC-nanoparticle samples placed in different locations was corrected. They further applied a similar method for molecular imaging of angiogenesis targeted by using fluorinated nanoparticles in an *in vivo* rabbit model. The correction method results in a more homogeneous ^{1}H MR image of the anatomy and it facilitates accurate measurement of the avb3-integrin targeting nanoparticles with ^{19}F MR imaging[257].

Other aspects of ^{19}F MRI quantification were also evaluated. Lee et al. showed a new method to perform quantitative ^{19}F MR imaging[258]. They described a synthetic signal injection method for quantification of metabolite content in real voxels of ^{19}F MR images. Vials containing different concentration of NaF were converted to units of moles by referencing to pre-calibrated synthetically injected voxels. By changing the coil loading, the robustness of their method was validated. Keupp et al. focused their research on the correction of physiological motion that might be introduced due to the long scan time of ^{19}F MRI[259]. They presented a simultaneous dual-nuclei MRI for motion corrected quantification of ^{19}F MR images. The simultaneous dual-nuclei MRI capability allowed the simultaneous acquisition of ^{1}H and ^{19}F MR images with different resolution, which offer efficient and precise anatomical localization of fluorine signals, which benefited ^{19}F MRI signal quantification.

1.5. Main objectives

Pancreatic islets and beta cells play an important role in diagnosis, follow-up and treatment of diabetes. Modern non-invasive imaging techniques are becoming valuable tools for monitoring pancreatic islets and beta cells. In addition to the excellent soft tissue contrast and high image resolution of magnetic resonance imaging (MRI), ^{19}F MRI can further provide more accurate quantitative estimation for cell tracking with high specificity due to the absence of interfering background signal. So far, ^{19}F MRI has been applied in numerous cellular imaging studies with a focus on phagocytic cells[68,82]. The feasibility of using ^{19}F MRI for pancreatic islets and beta cells has been shown before[190]. However, these initial studies require further validation and optimization in particular concerning different labelling strategies, choice of contrast agents, site of transplantation and protocols of image processing. This is necessary due to intrinsic properties of pancreatic islets and beta cells, the sensitivity limitations of the ^{19}F MRI technique, the lack of beta cell specific contrast agents etc.

Hence, by collaborating with academic partners from chemistry (University of Hamburg, Germany and University of Ghent, Belgium), the overall goal of the project was the development, evaluation, optimization and validation of the ^{19}F MRI methodology (including the development of purpose-build radiofrequency (RF) detectors, scan protocols and data post processing algorithms) for the detection of beta cells by using different fluorine containing contrast agents (^{19}FMH and PFC). Hereby, different labelling strategies (*in situ* systemic labelling and *ex vivo* pre-labelling) for tracking pancreatic islets and beta cells in animal model have been tested. Furthermore, the established ^{19}F

MR imaging platform was also tested for application on the controlled release of drugs from delivery capsules. To achieve these objectives, successful integration of several experimental procedures are necessary.

In this context, this PhD project encompassed the following main steps:

- **Develop novel RF coils for acquiring ^{1}H and ^{19}F MR images for different applications (organ systems).**
  Depending on the region of interest, we have designed, constructed and validated purpose-build RF coils for performing fluorine and proton MRI scans. Hereby, we have optimized the coil size, field homogeneity and detection sensitivity of the RF coils towards their specific applications.
- **Characterization and evaluation of fluorinated contrast agents *in vitro*.**
  Fluorinated compounds provided by our collaborators were tested for their suitability as MRI contrast agents. Hereby, we have used a NMR spectrometer to characterize and evaluate their MR properties, such as fluorine concentration, chemical shift and T1, T2 and T2* relaxation parameters. Furthermore, *in vitro* labeling with isolated pancreatic islets and the INS-1E cell line was also performed to determine the labeling efficiency and optimize the labeling protocol. Using the results from the *in vitro* testing, we were able to provide feedback to the chemists for optimization of the fluorinated compounds and to establish optimized protocols for *in vivo* imaging.
- **Assessment of the specificity of fluoro-deoxy-mannoheptuloses (^{19}FMH) for *in vivo* and *ex vivo* quantification of GLUT-2 expressed cells.**
  We have tested the suitability of ^{19}FMH for systematic tracking of GLUT-2 expressing cells (beta cells, hepatocytes) *in vivo*. Potential side effects of ^{19}FMH, *ex vivo* confirmation of cellular uptake using IPGTT and NMR spectrometer were performed for validation purposes. Hereby, we obtained critical information on the specificity of ^{19}FMH for GLUT-2 expressing cells, efficiency of labeling, potential adverse effects on cell biology and detectability limitations.
- **Multi-modal *in vivo* monitoring of transplanted (subcutaneous) cells and islets labeled with PFC based contrast agents.**
  By incorporating a fluorescent dye in PFC based emulsions, we aimed to monitor labeled pancreatic islets and INS-1E cells by using both ^{19}F MRI and fluorescent imaging. The chosen subcutaneous transplantation site was suitable for cross-validating the transplantation and imaging procedures. Furthermore, transfection of the islets and INS-1E cells by using a lentiviral vector for the expression of luciferases makes tri-modality imaging possible. This multi-modal platform would provide complementary information for follow-up studies and validation by histology.
- **Optimization of novel imaging and processing protocols for rapid and sensitive imaging using the compressed sensing technique.**
  It is known that the ^{19}F MRI technique is limited by its sensitivity for broader applications. As such, we have tried to implement different compressed sensing reconstruction algorithms, both, on offline simulations and online acquisitions with a focus on low signal-to-noise ratio (SNR) datasets. This would improve ^{19}F MRI in terms of speeding up the data acquisition or detecting signals that are otherwise missed by traditional ^{19}F MRI scans.
- **Utilizing the developed ^{19}F MRI platform for other potential preclinical research applications (controlled release).**
  The application of ^{19}F MRI is not only limited to cell imaging. Here, we have developed a novel imaging approach by combining ^{19}F MRI and CT using ^{19}FDG and $BaSO_4$ as contrast agents to

monitor the fate of pH-sensitive polymer coated capsules in the gastrointestinal tract of a hamster model. This approach will enable the *in vitro* and *in vivo* evaluation of the drug delivery vehicles and their further technical improvement to be applied in controlled drug delivery and release strategies.

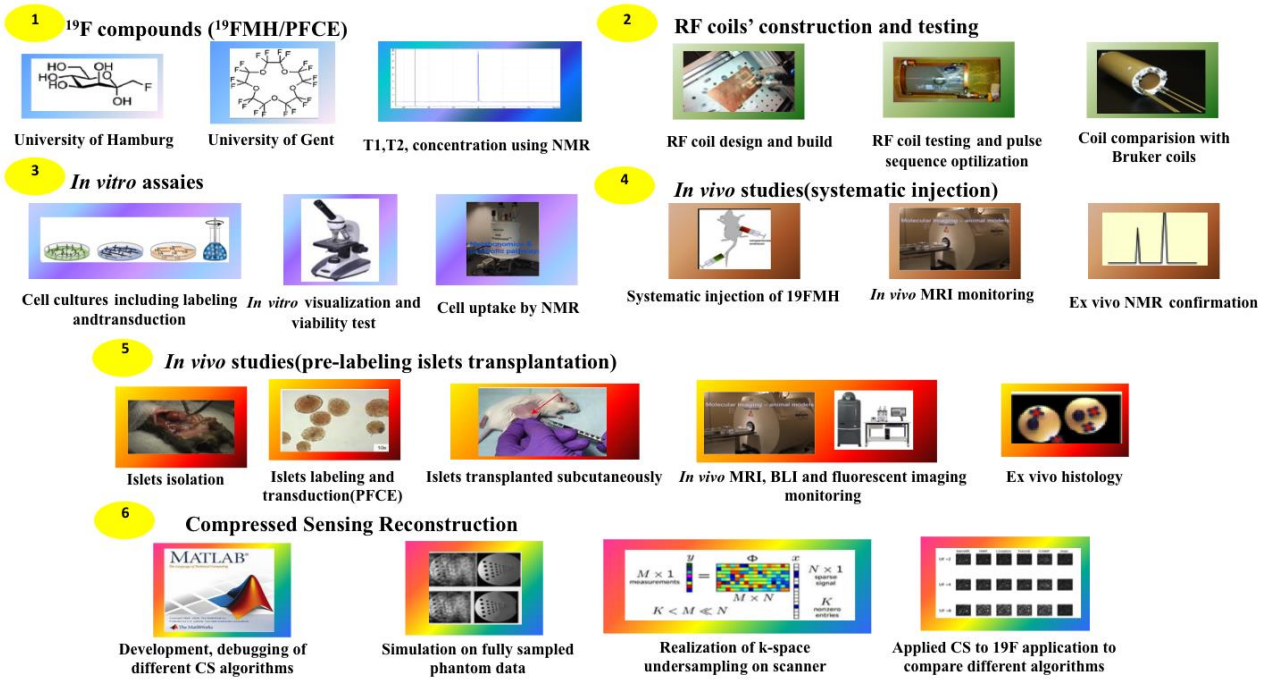

Fig. 1.7 Roadmap of this PhD thesis with experimental procedures including characterization of ^{19}F particle, RF coil construction, optimization of MRI protocol, *in vitro* verification, *in vivo* applications and *ex vivo* validation.

1.6. Outline of research

In **Chapter 1**, a general introduction to the different research areas of this PhD is provided. The urgency of tackling diabetes using *in vivo* visualization strategies for pancreatic islets and beta cells is addressed. An overview of different non-invasive imaging modalities with their advantages and disadvantages for cell imaging is provided. In addition, the current state of pancreatic islet and beta cell imaging by using different imaging modalities is reviewed. MRI methods are explained in more detail together with hardware considerations and contrast generation approaches. The history of ^{19}F MRI, current applications and potential techniques for improving its sensitivity are presented.

The use of GLUT-2 specific ^{19}FMH for tracking beta cells and pancreatic islets *in vivo* after systemic administration is explored in **Chapter 2**. *In vitro* uptake of ^{19}FMH by isolated pancreatic islets, *in vivo* bio-distribution and IPGTT tests of ^{19}FMH in healthy animals as well as *ex vivo* NMR spectroscopy of $HClO_4$ tissue extracts were performed to validate the potential feasibility of ^{19}FMH as contrast agent to assess GLUT-2 expressing cells.

In **Chapter 3**, a tri-modal imaging platform of subcutaneously transplanted pancreatic islets and INS-1E cells is presented. The *in vitro* PFCE labelling and LV transduction of pancreatic islets and INS-1E cells were optimized and established. Furthermore, *in vivo* tracking of transplanted pancreatic islets and INS-1E cells were demonstrated with ^{19}F MRI, FLI and BLI.

Comparison of different compressed sensing (CS) algorithms for low SNR ^{19}F MRI applications (imaging of transplanted pancreatic islets and cells labelled with PFCE) is described in **Chapter 4**. Offline simulations of fully sampled *in vitro* and *in vivo* datasets were performed. Furthermore, *in vitro* and *in vivo* CS acquisitions were also demonstrated as proof of principle to confirm our findings in real-life applications.

Combining our ^{19}F MRI protocols with micro-CT, we show the feasibility of visualizing different temporal and spatial events during the release of compounds in **Chapter 5**. Capsules containing ^{19}FDG and $BaSO_4$ as contrast agents were assessed in terms of compound release from the pH-sensitive polymer coated capsules, both *in vitro* and *in vivo* with a focus on the gastrointestinal tract of a hamster model.

A general conclusion of the presented work is provided in **Chapter 6** with future perspectives for the field of ^{19}F MRI and cell tracking.

Chapter 2. *In vivo* and *ex vivo* 19-fluorine magnetic resonance imaging and spectroscopy of beta-cells and pancreatic islets using GLUT-2 specific contrast agents

This Chapter has been compiled based on the following publication

Liang S., Louchami K., Kolster H., Jacobsen A., Zhang Y., Thimm J., Sener A., Thiem J., Malaisse W., Dresselaers T., Himmelreich U. (2016). ***"In vivo and ex vivo 19-fluorine magnetic resonance imaging and spectroscopy of beta-cells and pancreatic islets using GLUT-2 specific contrast agents."*** *Contrast Media & Molecular Imaging, 11, 506-513.*

2.1 Introduction

Diabetes mellitus is considered a highly prevalent disease with a rapid increase in incidence[260]. Insulin deficiency or reduced insulin secretion is a main characteristic of the disease. As pancreatic β cells are responsible for producing and storing insulin, it is crucial to monitor the β cell mass (BCM) and functionality for both diagnosis and therapy staging of diabetes. Techniques such as the C-peptide level test, oral or intravenous glucose tolerance tests have been used in daily clinical practice[12,261,262]. However, these techniques can only give indirect information regarding BCM.

Non-invasive imaging of β cells remains challenging due to the small size and high dispersity of its resided site, the pancreatic islets throughout the pancreas. Among different imaging modalities, magnetic resonance imaging (MRI) is considered as a suitable candidate for cell tracking thanks to its high resolution and deep tissue penetration without using any ionizing radiation[263]. Despite the advantages that MRI offers, the main shortcoming of MRI is its relative low sensitivity compared with other imaging modalities such as positron emission tomography (PET). In order to distinguish between specific cell types and background tissue, contrast agents are needed, such as super-paramagnetic iron-oxide (SPIO) particles or gadolinium (Gd)-based agents, which have been used intensively in the field of cellular imaging[72,264]. However, proton-based MRI together with the use of contrast agents that modulate relaxation of protons is still prone to misleading intrinsic sources of similar contrast, which makes it difficult to correlate and quantify contrast changes in MRI with specific cell types, especially when follow-up of disease progression or treatment is needed[68]. During the past decade, 19-fluorine MRI has drawn increased attention in the field of cell tracking after the initial work by Ahrens et al[82] using perfluoropolyethers (PFPE) for monitoring dendritic cells *in vivo* (for review see also[84,178]).

Suitable analogs of D-mannoheptulose (DMH) were reported to be able to target GLUT-2-expressing cells, such as β-cells or hepatocytes, via the GLUT-2 transporter and further stay inside the cells after their phosphorylation[265]. This feature makes DMH a potential tool for labeling and imaging these cells. Hence, these compounds are potential agents for β-cell imaging after synthesizing ^{19}F containing deoxy-DMH, which can be detected by ^{19}F MRI and further used for cell imaging after their entrapment in those cells[266,267]. Initial *in vitro* studies on the uptake of different ^{19}F-

deoxyfluoromannoheptuloses (^{19}FMH) by rat hepatocytes and their effects upon glucose-induced insulin release from isolated rat pancreatic islets have already been successful in a proof-of-concept study[184]. The current study will mainly focus on the *in vivo* application of ^{19}FMHs and ^{19}F deoxyfluoroglucose (see Fig. 2.1) and its validation following systematic injection and the assessment of its feasibility to quantify GLUT-2 expressing cells. Quantification of ^{19}FMH uptake by different tissue was performed using *ex vivo* ^{19}F magnetic resonance spectroscopy (MRS).

2.2 Results

2.2.1 Hardware considerations

The in-house build ^{1}H/ ^{19}F RF coil showed high sensitivity in a relatively large field-of-view (~30mm) in the longitude direction due to its compact size and saddle shape. The RF coil also showed good field homogeneity. Within the same transverse plane, this coil exhibits good linear relationships (Y=0.67X+2) between the SNR and the concentration of ^{19}F spins as shown in Fig. 2.2 B, which is essential for the quantification of the fluorinated compounds and ultimately for the quantification of the number of cells. The detection limit for ^{19}F MRI is approximately 5*10^{15} F spins/pixel using a gradient echo 3D sequence with 120 averages and repetition time of 1s, which is in a similar range (10^{15}-10^{16}) as described in the literature[87,268].

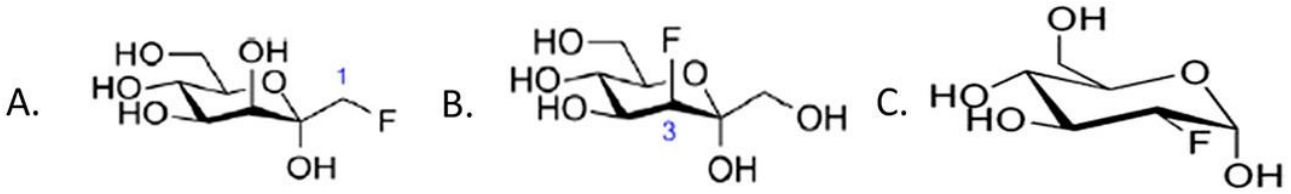

Fig. 2.1 Chemical structure of ^{19}F contained compounds: (A) 1-deoxy-1-fluoro-D-manno-hept-2-ulose; (B) 3-deoxy-3-fluoro-D-manno-hept-2-ulose; (C) 2-fluoro-2-deoxy-D-glucose.

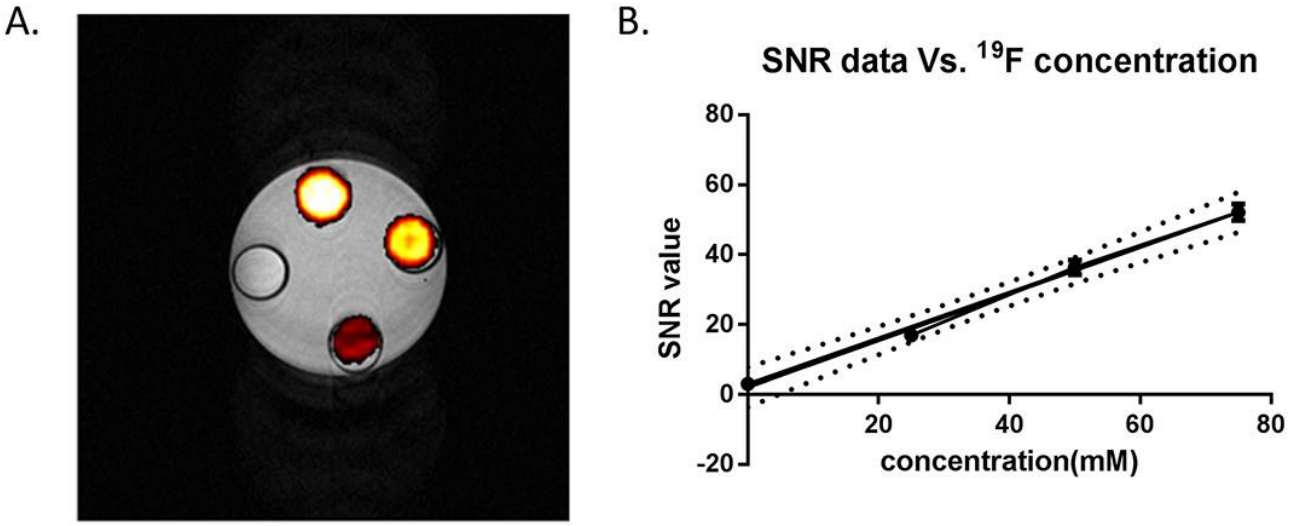

Fig. 2.2 *In vitro* phantom test of the RF coil profile. A phantom filled with 2% agarose was prepared with four Eppendorf tubes containing different concentration of NaF solutions. (A) Representative ^{19}F signal (red-hot scaled, scan time ~ 30 min) overlaid on proton image (gray scaled); left tube: negative

control (0 mM); upper tube: 75 mM; right tube: 50 mM; bottom tube: 25 mM; (B) Relationship between signal-to-noise ratio of a region of interest (respective tubes from A) and its ^{19}F spin concentration.

2.2.2 Uptake of ^{19}F-deoxymannoheptulose by isolated pancreatic islets

^{19}F MRS illustrated good uptake of ^{19}FMH by isolated islets. Considering an islet volume of 200 to 400 nm[269,270], the intra-islet concentration averages 0.5 to 4 M after overnight incubation of islets at 37 ℃ in the presence of 15 mM of 3-^{19}FMH (see also Fig. 2.3). This was based on a measured average 18 nmol ^{19}F spins per islet. Considering that each islet consists of 1000 to 2000 cells, this was also in agreement with previous measurements on isolated cell lines were cellular amounts of 2 pmol/ cell were found[184]. It was also noticed that the islets labeling did not introduce any significant change in the chemical shift or J-coupling of ^{19}FMH, indicating its chemical integrity.

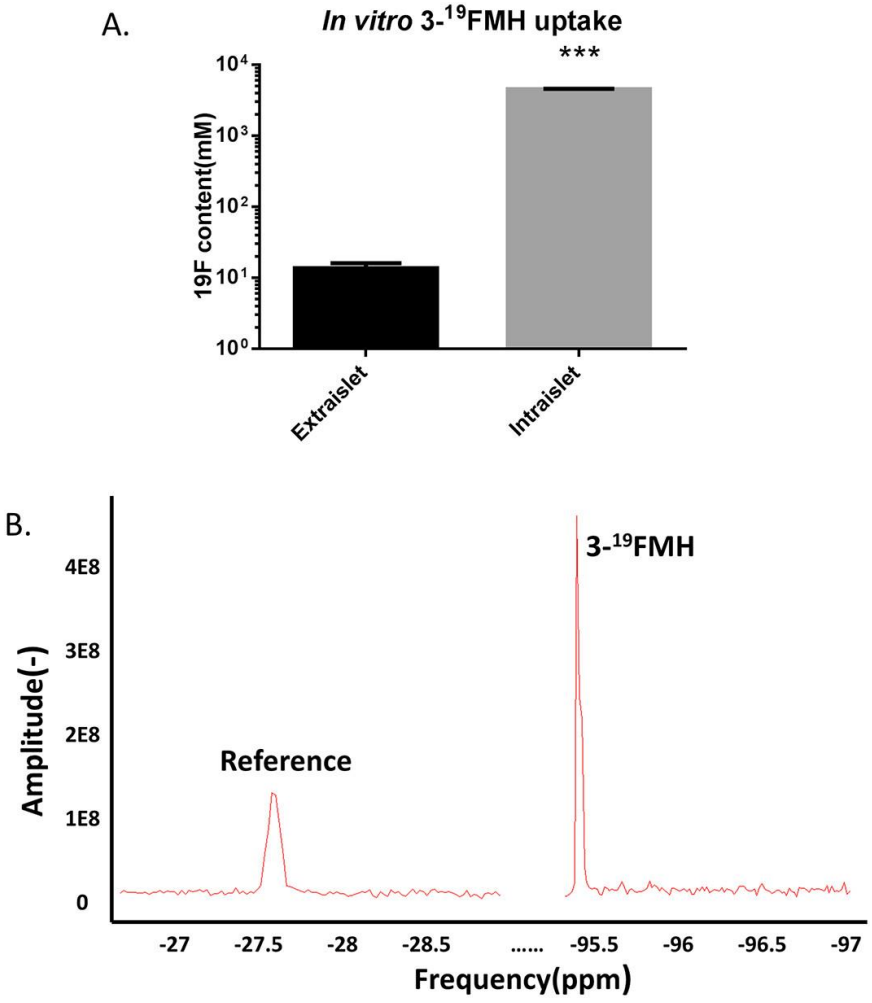

Fig. 2.3 *In vitro* 3-^{19}FMH uptake by isolated islets: (A) Extra-islet and intra-islet concentration of ^{19}F spins after 24 hours incubation with 15 mM 3-^{19}FMH. Concentrations were calculated based on an average islet diameter of 200 µm, resulting in a volume of 4 nl. Note that rat islet diameter can vary between 100 to 400 µm[269,270]; (B) Representative ^{19}F MR spectrum of 3-^{19}FMH labeled islets.

2.2.3 In vivo results

Co-registration of the *in vivo* ^{19}F MRI signal with the ^{1}H MR images shows that the ^{19}F MR signal originates from the bladder within twenty minutes after the injection, which indicates rapid clearance of ^{19}FMH from the circulation (kidney, bladder). According to the acquired *in vivo* MR images, there is no significant difference between different ^{19}FMHs two hours after injection of FMH (1-FMH: n=3 and 3-FMH: n=4, data not shown). For some mice, relative good ^{19}F MR signal was also seen in the kidneys, liver and potentially from the pancreas (see Fig. 2.4). However, we also noted considerable variability between different mice. For two mice, only weak or no detectable ^{19}F MR signal was seen in the liver and pancreas due to low accumulation of ^{19}FMH. Continued acquisition of sequential ^{19}F MR images for two hours after injection confirmed that the major fraction of ^{19}FMH was removed from circulation within this time frame. Only low retention in the liver and pancreas was found. Follow-up scans acquired 24 hours after the injection did not result in the detection of any remaining ^{19}F signal neither by ^{19}F MRI nor by *in vivo* ^{19}F MR spectroscopy, which indicates complete clearance of the ^{19}FMH. For the animals receiving ^{19}FDG, similar as for animals receiving ^{19}FMH, high signal intensity was detected from the bladder immediately after the injection and low signal intensity was noticed from the kidneys, liver and potentially from the pancreas. Multiple injections of 1-FMH or 3-FMH did not significantly improve the *in vivo* detectability (data not shown).

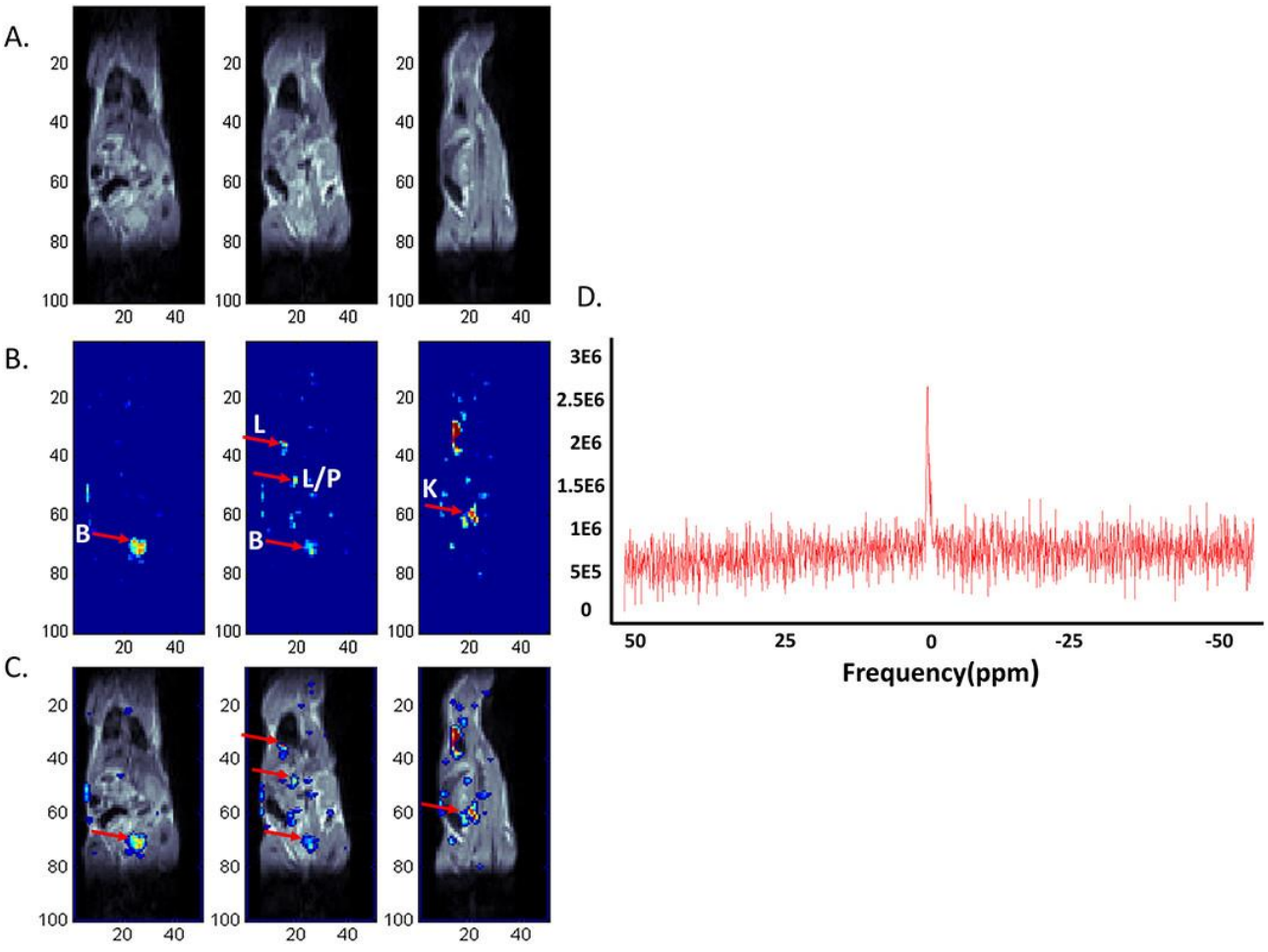

Fig. 2.4 Representative *in vivo* ^{1}H MRI and ^{19}F MR images upon injection of 3-^{19}FMH. Three consecutive slices are shown. The shown images were acquired from the animal that showed the highest SNR in the liver region of the ^{19}F MRI. (A) ^{1}H MR images (gray scaled); (B) Corresponding ^{19}F MRI signals (RGB scaled, scan time ~ 1h) after post processing. Arrows point at the following organs: B - bladder; L - liver; L/P - liver or pancreas; K - kidney; (C) Overlay of ^{1}H MR image from (A) with ^{19}F MR image from (B);

(D) Representative, whole-body *in vivo* ^{19}F MR spectrum of 3-FMH. The spectrum shows only the 3-FMH but no isoflurane signal, due to the chosen bandwidth of 75 ppm, which is substantially smaller than the chemical shift difference between 3-FMH and isoflurane (~110 ppm, see also Fig. 2.5). Note, no localization of the MR spectrum was performed.

2.2.4 Ex vivo ^{19}F MRS measurements

Animals were sacrificed either two hours (n = 6) or the 24 hours (n =2) after ^{19}F agents' injection for collecting tissue and to perform *ex vivo* ^{19}F MRS. The purpose of the *ex vivo* study was to validate and quantify the *in vivo* MRI experiments with higher sensitivity. For tissue collected two hours after ^{19}FMH administration, we could detect clear ^{19}F MRS signal from both the bladder (urine) and the kidneys, which confirmed rapid clearing of FMH via the urinary track (see Fig. 2.5). Low but detectable ^{19}F MRS signal (~2*10^{17} F spins/ tissue) was observed from the pancreas and liver (see Fig. 2.5), which also explains the difficulties for in vivo detection. Taken the example of the liver shown in Fig. 2.4, the calculated ^{19}F spin concentration was approximately 10^{15}/pixel assuming a total volume of the mouse liver of 0.3 cm^{3271}, which covers approximately 180 pixels in our ^{19}F MRI protocol. This is lower than the coil's detection limit of 5*10^{15} F spins/ pixel with our scan protocol. No uptake/negligible ^{19}FMH in muscle tissue was detected. Our bio-distribution study of ^{19}FMH confirms a preferential uptake in tissue with high expression of the GLUT-2 transporter. Such transporters are mainly found in the liver, endocrine pancreas and kidney, while it is absent from tissue such as muscle. No differences in bio-distribution were found between 1-FMH and 3-FMH (see Fig. 2.5B). Complete clearance was observed after 24 hours. Again, this is in agreement with our *in vivo* observations.

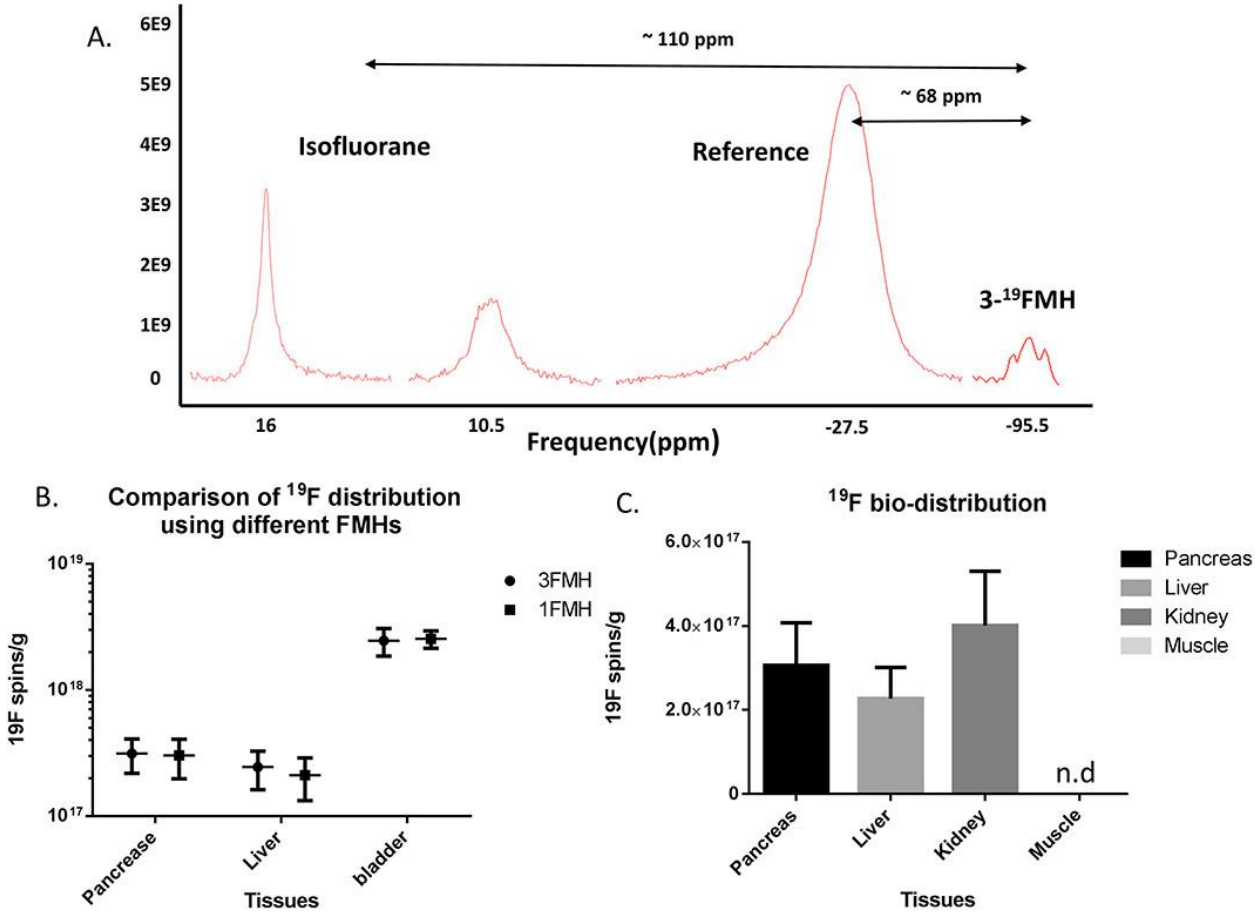

Fig. 2.5 Quantification of the FMH retained in different tissues using *ex vivo* ^{19}F MR spectroscopy. Tissue was excised and prepared for *ex vivo* NMR immediately after the last *in vivo* MRI experiment, which commenced 2 hours after injection of the respective FMHs. (A) Representative ^{19}F MR spectrum of homogenized liver tissue obtained from an animal injected with 3-FMH; (B) Comparison of the distribution of 1-FMH (n = 3), 3-FMH (n = 3) and 19FDG (n = 2) in the pancreas, liver and bladder. (C) Combined quantification of 1-FMH and 3-FMH in different tissues two hours after the injection of the respective FMHs. Note, no signals of 1-FMH (n = 1) and 3-FMH (n = 1) were detectable by ^{19}F MRS in the same organs 24 hours after injection. FMH concentrations in panel B and C are mean values. Error bars indicate standard deviations.

2.2.5 IPGTT results

Compared to the effect of ^{19}FDG, the effect of ^{19}FMH on the IPGTT was similar to that of unlabeled DMH. Thirty minutes after injection of high concentrations of D-glucose (1mg/g body weight of mice) and co-injection of these mannoheptuloses to reach 10 mM as extracellular concentration, glycaemia remained significantly higher than in the control experiments (see Fig. 2.6A). These findings were also supported by the blood insulin measurements (see Fig. 2.6B). The insulin release seemed inhibited by the DMH and its ^{19}F-derivatives. This temporal increase of glycaemia and decrease of insulin levels lasted for approximately two hours until the physiological conditions of the animals returned to a normal state. This phenomenon also indirectly confirms the findings from *in vivo* ^{19}F MRI that the clearance of ^{19}FMH occurred within two hours after injection.

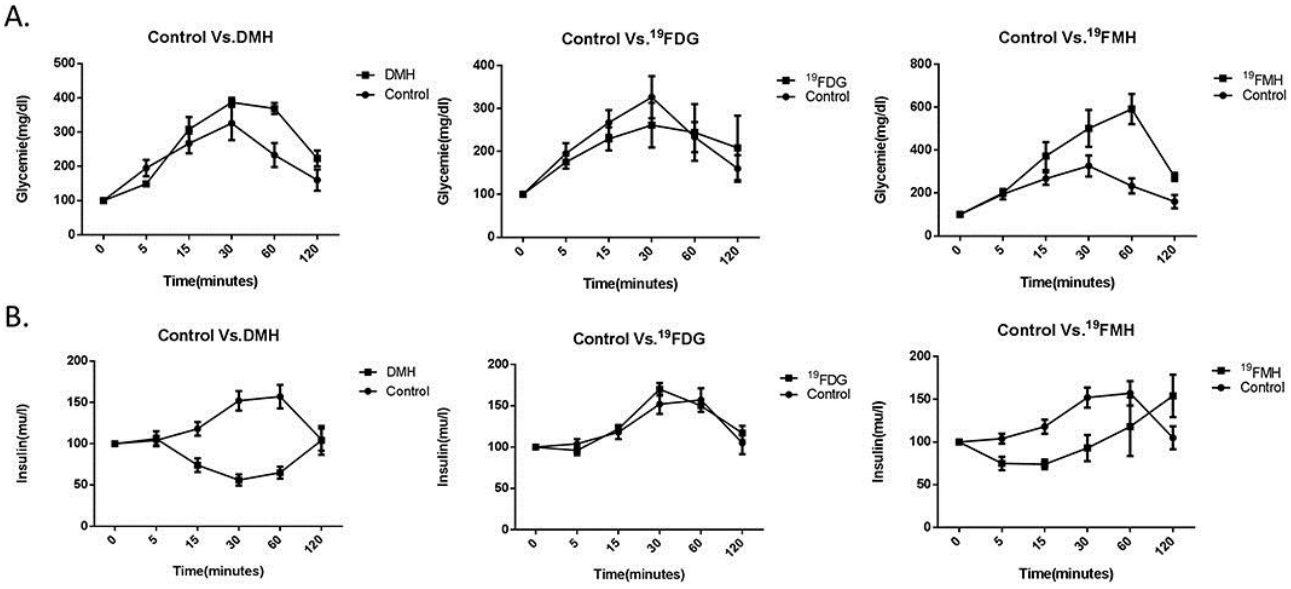

Fig. 2.6 Intraperitoneal glucose tolerance test using DMH, ^{19}FMH and ^{19}FDG co-injected with D-glucose for 2 hours monitoring of blood glycaemia and insulin level: (A) Blood glycaemia level upon the injection of specific compound compared with control group; (B) Blood insulin level upon the injection of specific compound compared with control group.

2.3 Discussion

Since ^{19}F MRI was introduced almost at the same time as the first human ^{1}H MRI applications[89], it has been used for many different applications in the field. Important to note is that for over two thirds of published work related to using ^{19}F MRI for molecular imaging purposes, perfluorocarbons (PFC) emulsions were used as a contrast agent[82]. PFC emulsions have certain advantages over most other

^{19}F-labelled compounds. Many of them are formulated as emulsions or nanoparticles, which makes it relatively easy to synthesis them[178]. In addition, nanoparticles could also be combined with optical dyes for multimodal imaging and subsequent confirmation by microscopic methods. More importantly, PFCs can contain several equivalent fluorine atoms, hereby increasing the concentration of the contrast-generating nucleus. In particularly perfluoro-15-crown-5 ether (PFCE) with 20 identical ^{19}F atoms could provide 20-fold ^{19}F signal per molecule compared with the single fluorine atom of ^{19}FMH. However, as PFC emulsions are considered large molecules for non-specific contrast generation, they are mainly used for phagocytic cells such as dendritic cells and macrophages[272]. Thus, using ^{19}FMH has a disadvantage of limited sensitivity but the benefit of being cell specific. As ^{19}FMHs are small molecules, they are able to potentially reach all targeted cells and being taken up by cell specific transporters. As they are similar to naturally occurring sugars that are also present in vegetables, they are less problematic than foreign compounds[273]. However, one has to consider that FMHs temporarily increase blood glucose levels and inhibit insulin secretion, which lasted only 1-2 hours in our experimental setting. Apart from natural clearing from the blood stream, ^{19}FMHs were only taken up by GLUT-2 expressing cells such as hepatocytes or ßcells as confirmed by *ex vivo* ^{19}F MRS.

For potential clinical applications, the sensitivity of ^{19}F MRI still remains a major concern due to the relative low concentration of ^{19}F atoms in our application. In general, for reliable detection a threshold of approximately 10^{16} fluorine spins/voxel is considered (one hour acquisition time at 9.4T)[268]. For this study, the *in vivo* detection limit of our home built surface coil was approximately $5*10^{15}$ ^{19}F spins/ voxel, which is comparable to previous work for performing ^{19}F MRI. Due to its saddle shape and relative small size, it also shows reasonable B1 field homogeneity for further quantification. However, the difficulties of visualizing the ^{19}FMH taken up by hepatocytes or ßcells *in vivo* not only results from the low fluorine content of ^{19}FMH itself, but also comes from the small portion of ^{19}FMH taken up by these cells and its subsequent rapid clearance of the compound from the circulation system. In previous *in vitro* experiments, it was shown that isolated islets incubated with FMHs for 24 hours show good uptake of FMH by ßcells[184], which is further evidence that the short circulation time of FMH hinders its application for *in vivo* ^{19}F MRI. We were able to confirm these previous cell experiments by *ex vivo* ^{19}F MRS of excised liver and pancreas tissue. However, these concentrations were far too low for robust detection by *in vivo* ^{19}F MRI, indicating that our current approach is insufficient for non-invasive detection. Technical improvements like higher field strength, better RF coils (for example cryogen cooled ^{19}F coils) and pulse sequences could potentially improve ^{19}F MRI sensitivity. Recent advanced techniques such as parallel imaging[274] or compressed sensing[253] may be applied for speeding up ^{19}F MRI. However, extra validations and efforts are needed before they can be implemented in normal routings. A more promising approach could be the synthesis of ^{18}F-DMH derivatives for *in vivo* imaging by positron emission tomography (PET), which only requires pico- or nanomolar local concentrations.

High concentrations of ^{19}F-DMH derivatives showed a temporal effect on insulin secretion, which would potentially affect blood glucose levels in patients. At higher D-glucose concentration, D-mannoheptulose inhibits glucokinase/ hexokinases and can reduce D-glucose phosphorylation, which provokes a transient inhibition of insulin release[275,276]. Although this effect is temporal and does not influence ß-cell survival, it has to be addressed by careful administration of exogenous insulin if high amounts of ^{19}F-DMH derivatives are administered to patients.

2.4 Conclusions

We have validated the suitability of ^{19}FMH for specific uptake by the GLUT-2 transporter for targeted *in vivo* imaging. It was previously found that mannoheptuloses show high specificity towards GLUT-2 transporters. Fluorine labeled DMHs were found to show a similar specificity towards GLUT-2 expressing cells when compared to DMH studied *in vitro* using beta and liver cells[184]. Our study also confirmed *in vitro* studies that ^{19}FMHs inhibit insulin secretion and increase the blood glucose level in mice temporarily. Hereby, no difference was found between different fluorinated DMH derivatives. By using a home-built RF surface coil for whole body imaging, we were able to assess the distribution of FMHs *in vivo* with a temporal resolution of approximately 20 minutes. Our MRI results showed a quick removal of bulk ^{19}FMH from circulation within two hours. While *ex vivo* ^{19}F NMR confirms accumulation of ^{19}FMHs in the pancreas, the local ^{19}FMH concentrations were insufficient for *in vivo* detection by ^{19}F MRI. No indication of further metabolism of FMHs was found. However, phosphorylation cannot be excluded as this has only a very small effect on the chemical shift of fluorinated carbohydrates, which is beyond the detection limit of our setup.

In summary, FMHs are potentially suitable for visualizing and tracking GLUT-2 expressing cells. However, current bottlenecks of this approach related to the quick clearance of the compound and relative low sensitivity of ^{19}F MRI need to be overcome before it can be applied for *in vivo* cell imaging.

2.5 Experiments

2.5.1 ^{19}FMH and ^{19}FDG

Fig. 2.1 shows the chemical structures of the two ^{19}FMH (1-deoxy-1-fluoro-D-manno-hept-2-ulose [1-^{19}FMH], 3-deoxy-3-fluoro-D-manno-hept-2-ulose [3-^{19}FMH]) and 2-fluoro-2-deoxy-D-glucose [^{19}FDG] used in this study. The ^{19}FMH were synthesized according to[266,267] and ^{19}FDG was purchased from Behring Diagnostics (La Jolla, CA).

2.5.2 In vitro uptake of ^{19}FMH and ^{19}FDG by isolated pancreatic islets

Pancreatic isles were obtained by the collagenase digestion method[277] from Wistar rats (female, 8-10 weeks). RPMI-1640 medium (Life Technologies, Gent, Belgium) supplemented with 10% FBS (Life Technologies, Gent, Belgium) and 1% penicillin/streptomycin (Life Technologies, Gent, Belgium) was prepared to culture isolated islets. ^{19}FMH was added to the culture medium (final ^{19}F concentration ~ 15 mM) and co-incubated with the islets for 24 hours for labeling. Labeled islets were picked manually and washed three times with PBS before being used for MRI or lysed for quantification by ^{19}F MRS experiments.

2.5.3 Study design of the in vivo experiments

Solutions of the three different fluorinated compounds were prepared by mixing the respective compound with 1 ml 0.9% saline to reach relative high fluorine concentrations (~ 200 mM). Eight C57bl6 mice (age 9-12 weeks, 25-30 g) received intravenous injections (tail vein) of 200 µl solution

of 1-^{19}FMH [n = 3], 3-^{19}FMH [n = 4] or ^{19}FDG [n = 2] using a 27 gauge needle immediately after anatomical ^{1}H MR Images were acquired. Then, the distribution of the fluorinated compounds was monitored by ^{19}F MRI for approximately two hours using repeated ^{19}F MRI. For one mouse that has received 3-^{19}FMH, a second injection of 200 µL 3-^{19}FMH was performed 30 minutes after the first injection. After the last imaging session, mice were sacrificed and tissue of interest (liver, kidney, pancreas, muscle and bladder) was removed together with blood and urine. Samples were stored at a temperature of -20 ℃ until further use for *ex vivo* ^{19}F MRS. Two mice were kept for follow-up monitoring of the clearance of FMH for up to 24 hours. All experiments were performed in accordance with national and European regulations on animal welfare and were approved by the local ethical committee and animal care commission of KU Leuven (approval number 060/2008).

2.5.4 Magnetic resonance imaging

MRI was carried out using a 9.4 Tesla Bruker Biospec small animal MR scanner (Bruker Biospin, Ettlingen, Germany) with a 20 cm horizontal bore magnet. A home-built, inductively coupled, saddle shaped, symmetric single-loop surface coil with a dimension of 66 x 42 mm, covering the whole mouse torso, was used for both, radiofrequency (RF) transmission and reception. This coil could be tuned and matched for both ^{1}H (400 MHz) and ^{19}F (376 MHz) resonance frequencies at 9.4 Tesla.

Mice were scanned *in vivo* under 1-2% isoflurane using oxygen as a carrier gas. A monitoring and gating device from SA Instruments Inc. (type 1030, Stony Brook, NY, USA) was used to observe and regulate physiological parameters in real time. Hereby, the body temperature and respiration rate of animals were monitored using a rectal probe and a pressure sensitive pad underneath the thorax, respectively. Both body temperature and respiration rate were maintained at reasonable physiological ranges: around 37 ℃ and 60-90 breathes min^{-1}, respectively. Animals were fixed using the manufacturer's animal holder (Bruker BioSpin). The tails of animals were left outside of the coil to facilitate the systematic injection of fluorinated agents using a pre-fixed infusion line with a 27-gauge butterfly needle.

Anatomical ^{1}H MR images were acquired using a rapid spin echo (RARE) sequence (repetition time = 6 s; effective echo time = 15.9 ms; eight echoes/ excitation; number of averages = 2; number of slices = 50; slice thickness = 0.5 mm; field of view = 8 x 4 cm; matrix size = 400 x 200; total acquisition time = 7 min 30 s). After acquisition of a non-localized pulse-acquisition ^{19}F MR spectrum (repetition time = 100 ms, number of average = 1000, flip angle = 20 °) to determine the exact ^{19}F frequency of ^{19}F FMH or ^{19}F FDG upon the injection of a fluorinated compound, ^{19}F MRI was performed using similar parameters as for the ^{1}H MRI with following modifications (repetition time = 1 s; effective echo time = 15.9 ms; number of averages = 250; number of slices = 10; slice thickness = 2.5 mm; matrix size = 100 x 50; acquisition time = 20 mins; center frequency set to the ^{19}F signal of FMH or FDG). The bandwidth was 75 ppm to avoid detection of isoflurane, which has a resonance frequency of at least 110 ppm downfield of FMH's (see also Figures 2.4 and 2.5). Orientation and dimension of the slice packages were identical for ^{1}H and ^{19}F MRI to improve co-registration. Multiple ^{19}F MR images were continuously acquired using the same scan protocol to obtain dynamic information on the distribution of the injected fluorinated compounds. The total scan time, including the injection, was not more than 2.5 hours. All MRI measurements were respiration gated.

2.5.5 $HClO_4$ extraction of tissue

Collected organs from euthanized mice were homogenized for about 15 minutes in 60% $HClO_4$ (sample to solution ratio 1:9) using a tissue homogenizer (Tissue Master 125, OMNI International, NW Kennesaw, GA, USA). Supernatants were extracted after centrifugation for two minutes at a speed of 25 rpm. Neutralization of the supernatant with precipitation of the surplus acid was done by adding KOH and titrating with $KHCO_3$ to a final pH of 7 to 7.5 (yellow to blue/green conversion) using a Bromothymol blue indicator. An additional centrifugation step (2 mins, 25 rpm) was required to remove the precipitate. Then, the remaining supernatant was kept in a freezer (-20 ℃) overnight. A final centrifugation was performed (2 mins, 25 rpm) before the sample underwent lyophilization using a Speedvac plus SC210A freeze-dryer (Fisher Scientific, Aalst, Belgium) at low drying speed until small white pellets formed (usually overnight). These pellets were then suspended in 0.4 ml deuterated water (99.9 atom % D water, Sigma-Aldrich BVBA, Diegem, Belgium) for locking and shimming during NMR spectroscopy. All procedures mentioned above were carried out at a sample temperature of 4 ℃.

2.5.6 ^{19}F MRS of cells and tissue extracts

A 400 MHz Bruker Avance II NMR spectrometer (Bruker Biospin, Rheinstetten, Germany) was used to perform ^{19}F NMR with a 5 mm broadband probe, which can operate at 376.5 MHz for both *in vitro* and *ex vivo* experiments. The prepared sample (0.4 ml, mixed with D_2O) was transferred to a 5mm NMR tube (Wilmad, Vineland, NJ, USA). As a reference compound, 5-fluorocytosine or sodium fluoride (0.1 ml, 5 mM ^{19}F concentration) was added to determine the chemical shift and ^{19}F concentration for each sample. The pH value of the sample was confirmed to be around 7 when preparing the sample using Bromothymol blue indicator and the temperature was maintained at 37 ℃ during the experiment. The acquisition parameters were as follows: frequency = 376.5 MHz, spectral width = 350 ppm, relaxation delay = 5 s, data points = 64 k. The number of acquisitions was adjusted for the different experiments (128 for *in vitro*, 4096 for *ex vivo* samples). After phase and baseline correction of the acquired ^{19}F NMR spectra using the Topspin software (Bruker Biospin, Rheinstetten, Germany), the ^{19}F NMR signals were quantified relative to the 5-fluorocytosine or sodium fluoride signals by peak integration.

2.5.7 IPGTT Test

To detect disturbances in glucose metabolism by ^{19}FMH, the intraperitoneal (IP) glucose tolerance test (IPGTT) was performed. Hereby, the clearance of the injected ^{19}FMH, DMH and ^{19}FDG, co-injected with D-glucose (^{19}F concentration ~ 200 mM)), from the body was measured. The effect of the different compounds was compared with a control group that only received D-glucose. Animals were fasted for approximately 16 hours and the fasted blood glucose levels were determined before a solution of the respective compound was administered by IP injection. Subsequently, the blood glucose/insulin level was measured at different time points during the following two hours. Hereby, the blood glucose and insulin levels were measured at 5, 15, 30, 60 and 120 minutes' time points after the injection. Indeed by placing a small drop of blood on the test strip of the Bayer Contour

Glucometer (Bayer Diabetes Care, Whippany, NJ, USA) the plasmatic glucose concentration was measured and the insulin was determined by using the radioimmunoassay method[278].

2.5.8 Data post-processing

MR images reconstructed using the Paravison 5 software (Bruker Biospin, Ettlingen, Germany) were further processed using the Matlab R2010b software (MathWorks, Inc. MA, USA). Masks of different animals were generated by setting threshold value (three times background noise) on their proton image (^{1}H MRI) to remove background noise. This mask was then applied to all ^{19}F MR images after they were rescaled to the same matrix size of the corresponding ^{1}H MR image. All ^{19}F MRI scans from the same scanning session were reweighted depending on their scanning time and combined to virtually increase the scan averages and further signal-to-noise ratio (SNR). By applying a Gaussian kernel filter, the final ^{19}F MR image was smoothed. The pixel-wise ^{19}F signal intensity was considered significant if larger than twice the standard deviation of the background noise ($p < 0.025$). These pixels were outlined and superimposed onto the ^{1}H MR image. Both IPGTT and MRS data were analyzed using the Prism6 (GraphPad Software, CA, USA). A Student's t-test was used to determine statistical differences between different experimental groups when needed. P-values less than 0.05 were regarded significant.

Sayuan Liang was responsible for development and validation of RF coils, performing *in vitro* islets labeling, *in vivo* MRI and *ex vivo* MRS experiments, data analysis and image post-processing. Together with his supervisor, he has designed the study. Sayuan Liang also made original draft of the paper with further reviewing and editing.

Chapter 3. Tri-modal *in vivo* imaging of pancreatic islets transplanted subcutaneously in mice

This Chapter has been compiled based on the following publication

Liang S., Louchami K., Holvoet B., Verbeke R., Deroose C., Manshian B., Lentacker I., Himmelreich U. ***"Tri-modal in vivo imaging of pancreatic islets transplanted subcutaneously in mice."*** *Molecular Imaging and Biology (Manuscript in Submission)*

3.1 Introduction

Patients with type 1 diabetes (T1D) suffer from hyper-glycaemia due to the loss of insulin-producing beta cells in the pancreatic islets (PIs), which is caused by an autoimmune attack mediated by T cells[279]. Current clinical therapies, such as insulin injections or insulin pumps, can control blood glucose levels to some extent. However, insulin administration is often not sufficient for T1D patients. Most of those patients will still have abnormally high levels of blood glucose and are at risk for long-term complications like blindness, neuropathy, kidney disease and others[280]. One alternative therapeutic approach is the engraftment of pancreatic islets.

After the first introduction of PI and beta cell transplantation in rats[7,8] and further successful clinical trials on T1D patients by Paul Lacy et al.[9], important improvements in terms of process of PI isolation from donors, strategies for immunosuppression, management of immunomodulation of recipients and anti-inflammatory drugs after surgery were made both in pre-clinical and clinical settings[281,282]. Some of these initial results have already been tested in clinical trials or are in the process of becoming real treatment options for patients[283-285].

One of the main remaining obstacles for PI transplantation is the variable outcome of islet engraftment a strong influence of the site of transplantation. Currently, the liver serves as the most practical clinical transplantation site for PIs or beta cells thanks to the relatively simple transplantation technique resulting in minimal surgical intervention[286]. This is also reflected by the number of completed clinical trials where patients underwent intra-portal transplantation via the portal vein of the liver to receive donor islets[287-289]. However, the efficiency of this technique is still not optimal due to potential long-term complications and relapse of diabetes. Therefore, other potential sites for PI or beta cell transplantation have also been proposed, such as subcutaneous tissue, renal (sub-capsule), the omentum, the muscle and the anterior chamber of the eye[26,290]. All of these transplantation sites have their own strength and limitations in terms of surgery, impact on cell metabolism, tissue perfusion or immunological aspects[14]. Therefore, the best transplantation site for PIs into patients is still under debate, requiring more comprehensive assessment methods. One of the key steps to validate islet engraftment could be the longitudinal, *in vivo* monitoring of the exact location and fate of the transplanted PIs, with the possibility of quantification without invasive intervention.

Non-invasive imaging techniques are increasingly available for longitudinal *in vivo* cell tracking including in the field of islet transplantation and diabetes research[13]. Different imaging modalities have been proposed for the visualization of both, endogenous and exogenous pancreatic islets/ beta

cells. Bioluminescence imaging (BLI) requires prior engineering of islets to express a luciferase gene. After transduction and engraftment, BLI provides quantitative measures of the number of viable islets, which can be monitored for periods of up to one year[30,291,292]. Fluorescent imaging (FLI) requires either cells that express fluorescent reporter genes or cells preloaded with fluorescent dyes. In a study by Speier et al.[26], FLI was successfully used for continuous monitoring of the survival of PIs isolated from transgenic mice expressing GFP under the control of the rat insulin-1 promoter (RIP-GFP). Radionuclide imaging, including positron emission tomography (PET) and single photon emission computed tomography (SPECT), has also been used for PI and beta cell imaging after pre-labeling with radiotracers[293,294] or by using transfected/ transduced cells for reporter gene based approaches[295,296]. However, PET and SPECT have a relatively low resolution and require radioactive tracers. Magnetic resonance imaging (MRI) is another widely used tool for exogenous islet imaging. Different contrast agents have been used for pre-labeling and further enhancement of MR contrast for *in vivo* islets and beta cell tracking. Contrast agents for proton MRI, such as super-paramagnetic iron oxide (SPIOs) nanoparticles and paramagnetic gadolinium chelates have been used in several studies for longitudinal monitoring purposes, including clinical trials with a retrievable signal for up to 24 weeks[75-77,297] and 65 days, respectively[81]. Recently, cell tracking using fluorine containing contrast agents and ^{19}F MR imaging has opened new perspectives for quantitative *in vivo* islet imaging[298,299]. However, each of the different techniques has advantages and disadvantages, which are in some cases linked to the transplantation site[17]. For example, optical imaging (BLI or FLI) is surface-weighted and often limited to superficial tissues by its limited signal depth penetration and light scattering. But, it can provide important information such as *in vivo* cell viability (BLI). ^{19}F MRI is superior in terms of specificity and potential quantification of transplanted islets or cells due to the lack of MR detectable ^{19}F signal in biological tissues. Its downside is its relatively low sensitivity so that several thousand cells are required for sufficient MR signal intensity, also resulting in relatively long scan times[68].

To overcome the limitations in sensitivity, resolution and specificity of individual imaging techniques, multi-modal imaging serves as a potential solution for cross validation, better visualization and follow-up of the fate of transplanted islets and beta cells *in vivo*. In this study, we aimed to combine BLI, FLI and ^{19}F MRI techniques in a multi-modal approach for *in vivo* monitoring of transplanted rodent islets and beta cell like cell lines. Hereby, we have either used transduced cell lines or cells pre-labeled with ^{19}F contrast agents.

3.2 Results

3.2.1 In vitro characterization of labeled and transduced INS-1E cells

Initial experiments were performed with the INS-1E cell line because of their beta cell like properties and easy handling in particular for longitudinal labeling and time consuming transduction experiments. First, we generated a stable firefly luciferase expressed INS-1E cell line using a multicistronic LV carrying the hEF1α promoter to drive 3flagFluc and PuroR for selection of transduced cells after adding puromycin. This resulted in a transduction rate of over 90%.

By varying the nanoparticle concentration (final fluorine concentration: 10-50mM) and labeling duration (4h and 24h), PFCE labeling conditions were optimized to achieve sufficient PFCE uptake while retaining cell viability and function. A relatively long labeling time was necessary to improve

the intracellular uptake as shown in Fig. 3.1a. Using the same PFCE concentration, 24h-labeling resulted in significant higher fluorine concentration per cell when compared with a 4h labeling. Unexpectedly, no significant differences in uptake were seen for concentrations between 10mM and 30mM, while a significantly higher uptake of PFCEs was seen for a concentration of 50mM. Cell viability, relative to unlabeled cells, was assessed for the different concentrations after labeling for 24h by counting viable cells (Fig. 3.1b). Although no significant difference was found between the control group and PFCE labeled INS-1E cells, high concentrations (e.g. 50mM) showed a marginally lower number of viable cells. This might be an implicit reflection of adverse effects on the cellular doubling time, considering the relatively long doubling times of INS-1E cells. Based on previous work on the required intracellular fluorine concentrations for detection by ^{19}F MRI and to avoid any adverse effects on cell biology, we established a concentration of 20mM fluorine and a labeling time of 24h for pre-labeling INS-1E cells with PFCE in subsequent experiments[185]. This results in an average of 3.7*10^{12} fluorine atoms per cell.

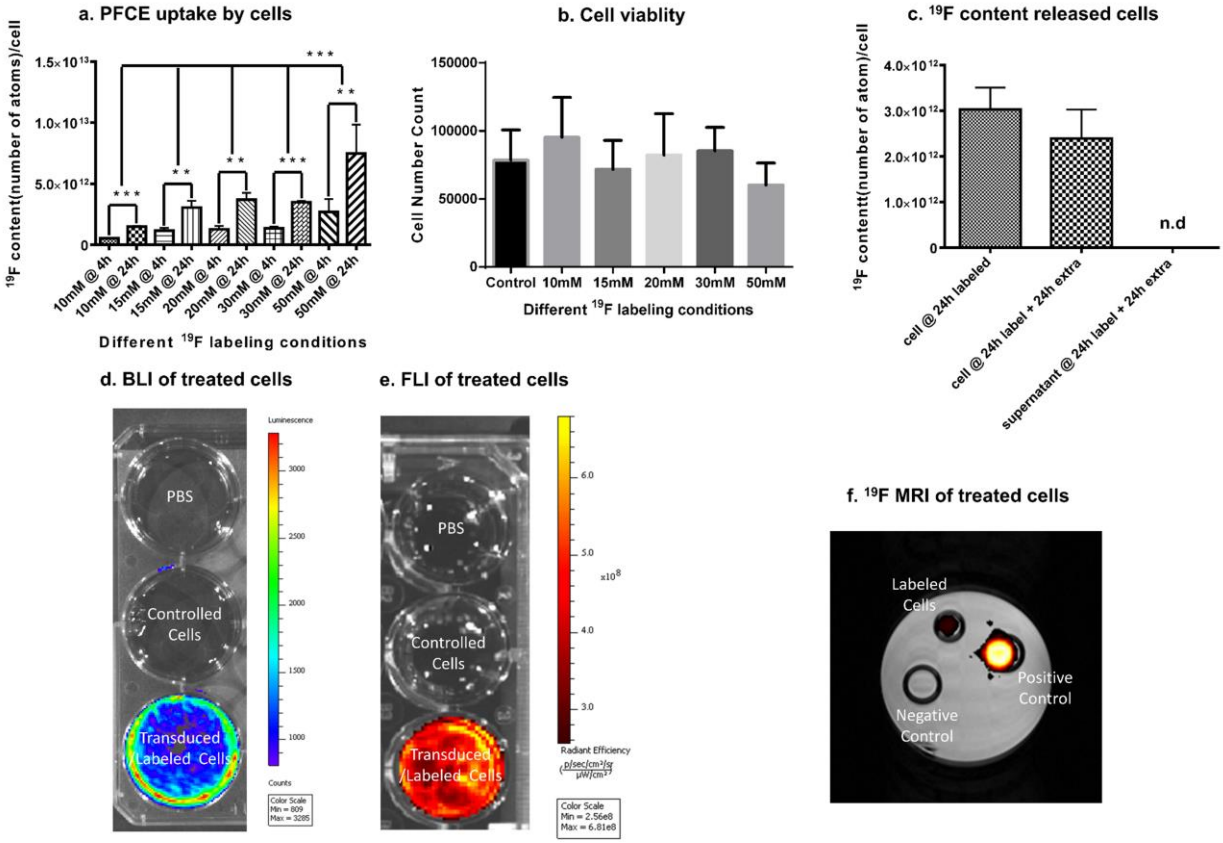

Fig. 3.1 *In vitro* characterization of labeled and transduced INS-1E cells (error bar indicates standard deviation). (a) Determination of PFCE nanoparticle uptake by INS-1E cells based on ^{19}F NMR spectroscopy and expressed as fluorine content (number of atoms) per cell. Fluorine uptake was determined for the different labeling conditions (concentration: 10mM, 15mM, 20mM, 30mM and 50mM; labeling time: 4h and 24h). Significant difference found between 4h and 24h at different concentrations ($p < 0.001$ @10mM, $p = 0.0055$ @15mM, $p = 0.0025$ @20mM, $p < 0.001$ @30mM, $p = 0.0036$ @50mM), significant difference found between 50mM with other concentrations at both 4h and 24h ($p<0.001$). (b) Cell viability determined after exposing INS-1E cells for 24hours to different concentrations of PFCE particles (final fluorine concentration: 10mM, 15mM, 20mM, 30mM and 50mM) for 24 hours (no significant difference found). (c) Assessment of PFCE released by labeled INS-1E cells. The fluorine content of PFCE labeled cells (24h labeled with 20mM final fluorine concentration) was assessed after labeling and after extra 24h incubation in PFCE (fluorine) free medium. In addition, the

supernatant from the latter cells were also collected for ^{19}F NMR spectroscopy (no significant difference found). (d) Representative BLI (rainbow scaled) of treated INS-1E cells overlaid with background photo (Top: PBS; Middle: untransduced control cells; Bottom: 3*10^5 PFCE labelled cells that were transduced with a LV carrying the hEFlα promoter). (e) Representative FLI (hot scaled, excitation wavelength: 648 nm and emission wavelength: 670 nm) of treated INS-1E cells overlaid with background photo (Top: PBS; Middle: unlabeled control cells; Bottom: 3*10^5 PFCE labeled (24h labeling with 20 mM fluorine concentration) and transduced cells). (f) Representative ^{19}F MR image (hot scaled, scan time ~ 30 min) of a phantom consisting of Eppendorf tubes in agar. The ^{19}F MR image is overlaid with its proton MR image (grey scaled). The respective Eppendorf tubes contain 5*10^5 unlabeled INS-1E cells (negative control), 5*10^5 labeled INS-1E cells and PFCE particles (25 mM fluorine, positive control).

In addition, the stability of the fluorine label inside the cells was tested by prolonging the cell culture time of pre-labeled cells for another 24h in the medium in the absence of any PFCE contrast agent. As shown in Fig. 3.1c, no significant change of intracellular fluorine content was found. Furthermore, we were not able to detect ^{19}F NMR signal from the supernatant of the culture medium with our routine ^{19}F NMR spectroscopy protocol. Despite potential signal loss due to cell death or proliferation, the PFCE label was considered stable inside the pre-labeled cells.

For illustration purposes, in vitro BLI, FLI and ^{19}F MR images of labeled, transduced INS-1E cells are shown in Fig. 3.1d-f. In contrast to the negative controls (untreated cells and PBS), PFCE-labeled and transduced INS-1E cells (3*10^5 cells seeded in a 6 well plate resulting in a few hundred cell/ mm^3) were detectable by both BLI and FLI (Fig. 3.1d and e). Furthermore, within an acquisition time of approximately 30 minutes, 5*10^5 INS-1E cells (~ four to five thousand cells/ pixel) could be detected by ^{19}F MRI with a signal-noise ratio (SNR) of about 8 (Fig. 3.1f), which indicates a detection limit (SNR threshold at 5) of a few thousands cells/ pixel with our imaging parameters.

3.2.2 In vitro characterization of labeled and transduced pancreatic islets

Considering the more complex composition of PIs, which consist of 1000 to 2000 endocrine cells when compared to the INS-1E cell line and the fact that isolated PIs cannot be maintained for a long time in culture, a modified strategy was needed for labeling and transducing PIs. Using the same protocol as for the INS-1E cell transduction, luciferase expression by PIs failed almost completely as also shown in the *in vitro* BLI experiments (Fig. 3.2a). Doubling the LV concentration was also not successful. However, prolonging the incubation time from 24h to 48h resulted in successful PI transduction and successful detection by BLI.

In contrast, the same PFCE labeling procedure as used for the INS-1E cells could be used to label PIs with PFCE. Maximum uptake was achieved after 20 to 24 hours of exposure to PFCE resulting in a total fluorine content of 20mM. On average, each islet contained approximately 1.44*10^{15} fluorine atoms (Fig. 3.2b). The release study again confirmed that there was no significant leakage of PFCE label from the PIs even after 48h in fluorine free medium (Fig. 3.2c). Since the cells of isolated PI do not proliferate as the INS-1E cells, it can be expected that the sustainability of the fluorine label in PIs would be longer than for the cell line. Hence, the ultimate procedure for PI labeling consisted of an initial 24h exposure of PIs to LV (5µl per well) and a subsequent addition of PFCE particles (final fluorine concentration: 20mM) to the LV containing medium with an exposure for another 24h. Hereby, we were able to simultaneously label and transduce PIs.

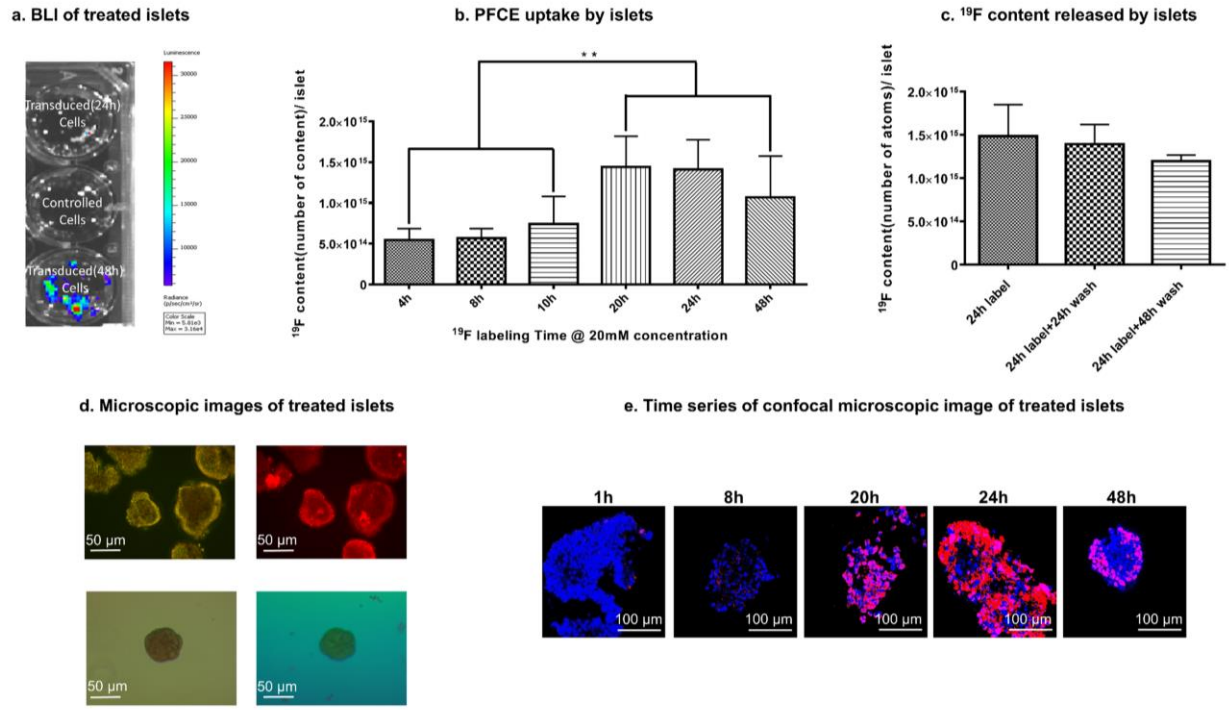

Fig. 3.2 *In vitro* characterization of PFCE-labelled and transduced pancreatic islets (error bar indicates standard deviation). (a) Representative BLI image (rainbow scaled) of a LV carrying the hEFlα promoter to drive 3flagFluc and a PuroR gene transduced PIs overlaid with background photo (Top: 50 PIs with 24h transduction; Middle: 50 controlled PIs; Bottom: 50 PIs with 48h transduction). (b) Determination of PFCE particle uptake (final fluorine concentration: 20mM) by PIs after increasing incubation times (4h, 8h, 10h, 20h, 24h and 48h) using ^{19}F NMR spectroscopy (significant difference between short incubation times (4, 8, 10h) with long incubation times (20, 24, 48h), p = 0.0071). (c) Assessment of PFCE released by pancreatic islets. The ^{19}F content of labelled PIs (24 h labelling with 20mM final ^{19}F concentration) were compared with islets underwent same labelling procedure with extra wash and 24h/ 48h incubation in PFCE/ ^{19}F free medium (no significant difference found). (d) Representative microscopy images of both labelled and transduced pancreatic islets (Top/ Bottom left: light microscopy images of PIs; Top right: fluorescence microscopy image of PIs; Bottom right: fluorescent microscopy of PIs after trypan blue staining). Scale bar, 50 µm. (e) Time series of confocal microscopy of labelled pancreatic islets (Blue: nuclei counterstained with Hoechst dye; Red: PFCE particles containing DiD dye; Pink: co-localization of nuclei and PFCE particles). From left to right: representative islets at different time points of incubation with PFCE particles (1h, 8h, 20h, 24h and 48h). Scale bar, 100 µm.

By the incorporation of the lipophilic fluorescent dye DiD in the lipid shell of the PFCE containing particles, uptake and internalization of the PFCE particles by PIs could be confirmed by fluorescence microscopy (Fig. 3.2d). Trypan blue staining of treated PIs confirmed the viability of the intact PIs (Fig. 3.2d). The insulin content of control PIs (898 ± 50 µU/islet) and treated PIs (972 ± 38 µU/islet) was similar. This suggests that the labeling and transduction procedure dose not impair the capacity of PIs to produce insulin. Furthermore, the results obtained from the GSIS test shows that the secretory responsiveness to the hexose is preserved in both control and transduced PIs. The insulin secretion increased from 56 ± 1 µU/ islet (glucose 2,8 mM) to 353 ± 66 µU/ islet (glucose 16,7mM) in the control group. While, in the transduced PIs the insulin secretion increment was from 50 ± 3 µU/ islet (glucose 2,8 mM) to 169 ± 15 µU/ islet (glucose 16,7mM). These tests indicate, that the pre-labeling and transduction procedure does not affect the PIs' viability and functionality *in vitro*.

To further confirm localization of PFCE nanoparticles within the islets, a series of confocal microscopy images of labeled PIs were acquired after exposure to PFCE nanoparticles for 1 to 48h (Fig. 3.2e). Particles were found both inside the cells and in the interstitial spaces of PIs. Furthermore, the different fluorescence signal intensities for the different PFCE labeling experiments further confirmed our findings that the optimal labeling time should be between 20 to 24h. Z-stack slicing of individual cells (S1, supplementary data) further indicated a notable uptake of PFCE nanoparticles in the cells of PIs after a 24-hour incubation time.

For bioluminescence imaging, several sub-regions of the well plate showed detectable BLI signal if at least 50 islets were plated, which indicates a detection limit of a few islets by *in vitro* BLI (Fig. 3.2a). The islets in phantoms for fluorescence imaging were more clustered. However, the high signal intensity against background showed a similar detection limit as for BLI (S2, supplementary data). Using ^{19}F MRI, ten islets per pixel were detectable using hundreds of averages, resulting in an acquisition time of 30 minutes and a SNR ~ 12 (S3, supplementary data).

3.2.3 Multimodal in vivo imaging of transplanted INS-1E cells

Multimodal *in vivo* imaging of subcutaneously transplanted INS-1E cells was performed by grafting one million unlabeled and untransduced INS-1E cells as well as PFCE-labeled and transduced (Fluc) INS-1E cells subcutaneously at the left and right thigh of the same animal, respectively. As expected, neither ^{19}F MRI signal nor FLI signal could be detected from the unlabeled and untransduced cells residing at the left thigh of the animal (Fig. 3.3a and c). Both, FLI and ^{19}F MRI sustained detectable signal for PFCE-labeled cells over a period of 21 days. A significant drop in signal intensity was observed over time (Fig. 3.3b and d). The FLI signal of labeled cells was gradually reduced to 53 ± 4.6% of its original intensity after the implantation. A similar decrease to 68 ±4.1% of its initial value was also observed for the ^{19}F MR measurements. A linear correlation between the intensity of ^{19}F MRI and FLI signal intensity was noticed (FLI signal = 1.621*[^{19}F] signal - 0.6345, R = 0.9671, see Fig. 3.3e), which is an indirect indication of a stable incorporation of the PFCE emulsions and the attached fluorescent dye, which follow both a similar clearance path from the injection site.

In contrast to external contrast agents, BLI provides direct information on the viability of transplanted cells, which results in a considerably larger variability between different animals (Fig. 3.3f). As shown in Fig. 3.3g, due to the harsh environment (limited oxygen and nutrition supply) at the transplantation site and a potential immune response mediated by the engrafted cells, a rapid loss in BLI signal intensity (reduction by 70% within one day after transplantation) and hereby of viable cells were observed. Until three days after engraftment, only about 14 ± 15.5% of cells remained viable. From this time point on, the BLI signal intensity and number of cells started to grow again (81% increase from day 3 to day 5 and from day 5 to day 7), most likely due to cell proliferation. However, the time period between day 7 and day 10 seemed to be critical, as only one animal out of three showed remaining detectable BLI signal present on day 10 with a further 62.4% increase in cell numbers (signal intensity) until day 21.

a. Representative *in vivo* FLI of transplanted cells

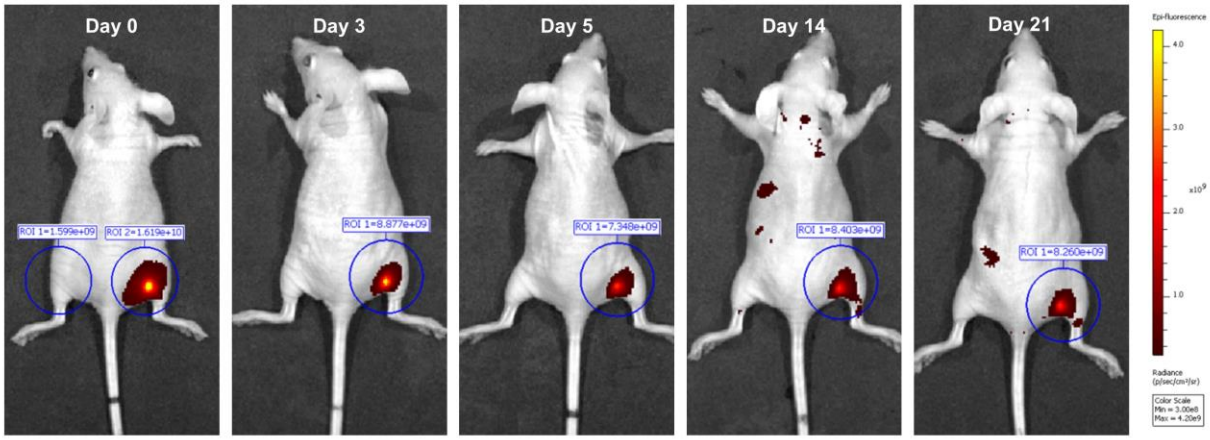

b. Representative *in vivo* ^{19}F MRI of transplanted cells

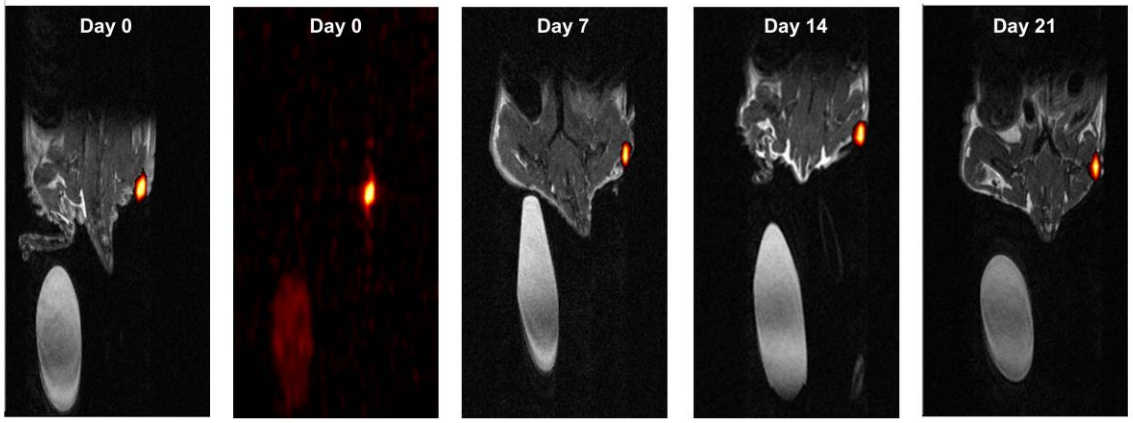

c. Representative *in vivo* FLI of transplanted cells

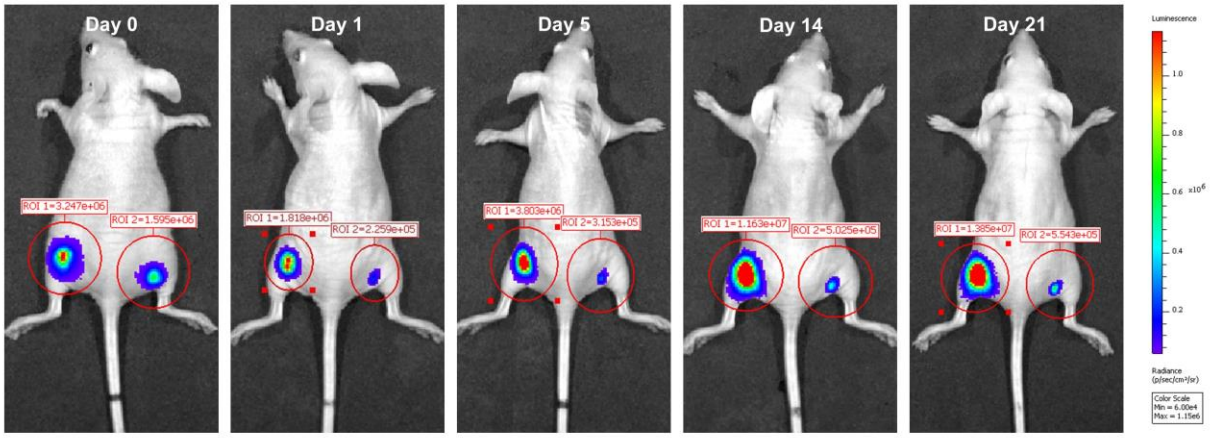

d. Quantitative FLI signal

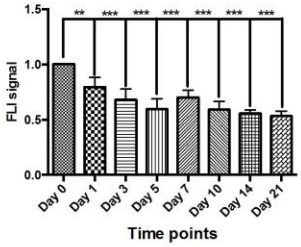

e. Quantitative ^{19}F MRI signal

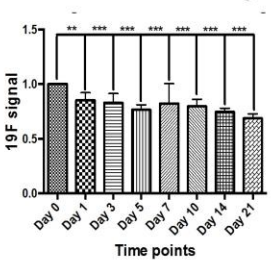

f. Correlation between FLI signal and ^{19}F MRI signal

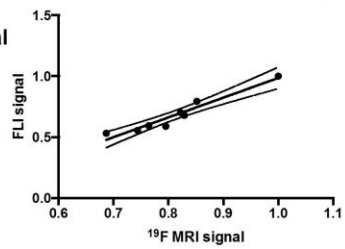

g. Quantitative BLI signal

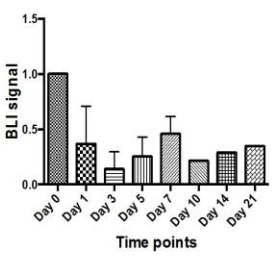

Fig. 3.3 Multimodal *in vivo* imaging of transplanted INS-1E cells (10^6 cells suspended in 100-200 µl medium were injected at both the right (labeled and transduced) and left (only transduced) thigh, n = 6, Swiss Nude mice, female, 7-9 weeks old) (error bar indicates standard deviation). (a) Representative *in vivo* FLI images (hot scaled) of transplanted INS-1E cells overlaid with background photographic images at different time points after engraftment (from left to right: day 0, day 3, day 5, day 14 and day 21). (b) Quantification of *in vivo* FLI signal intensity of transplanted INS-1E cells over 21 days (significant difference found between all time points to day 0, p = 0.007 for day 1 and p < 0.001 for all other time points). (c) Representative *in vivo* ^{19}F MR images (hot scaled, scan time ~ 30 min) of INS-1E cells overlaid with anatomical ^{1}H MR image (gray scaled) at different time points (from left to right: day 0, day 0 (only ^{19}F MRI without anatomical background), day 7, day 14 and day 21). R represents a reference containing 15 mM (fluorine) of PFCE particles. (d) Quantification of *in vivo* ^{19}F MRI signal intensity of engrafted INS-1E cells over 21 days. For quantification purposes, regions-of-interest from the site of engraftment were compared with respective regions in the Eppendorf tube containing 15 mM (fluorine) of PFCE particles as a reference (significant difference found between all time points to day 0, p = 0.0014 for day 1 and p < 0.001 for all other time points). (e) Correlation between *in vivo* FLI and ^{19}F MRI signal intensity of transplanted INS-1E cells over a time period of 21 days (Y (FLI signal) = 1.621* X (^{19}F signal) -0.6345, R = 0.9671). (f) Representative *in vivo* BLI (rainbow scaled) of transplanted INS-1E cells overlaid with background photo at different time points (Left -> Right: day 0, day 1, day 5, day 14 and day 21). (g) Quantification of *in vivo* BLI signal intensity of the region containing transplanted INS-1E cells over a time period of 21 days (significant difference found between day 1, 3, 5 and 7 to day 0, p = 0.0032 for day 1 and p < 0.001 for other time points).

3.2.4 Multimodal in vivo imaging of transplanted pancreatic islets

Longitudinal *in vivo* tracking of transplanted PIs was carried out after transplanting approximately 200 transduced and PFCE-labeled PIs to the right thigh of animals. PBS injections served as a negative control on the left thigh. Compared to INS-1E cell engraftment, PIs were monitored for a longer period (up to 70 days after engraftment). Similar to the temporal profile of transplanted INS-1E cells, both FLI and ^{19}F MRI signal intensity decreased over time. A similar linear correlation between the two methods was observed (Fig. 3.4a-e). More interestingly, after the last time point at day 70, there was still 47 % of ^{19}F MRI signal and 9% FLI signal intensity remaining. This provides evidence that labeling with PFCE particles is suitable for longitudinal cell tracking for up to several months. The larger drop in FLI signal intensity when compared to the ^{19}F MRI signal intensity is most likely due to the degradation of the fluorescent dye.

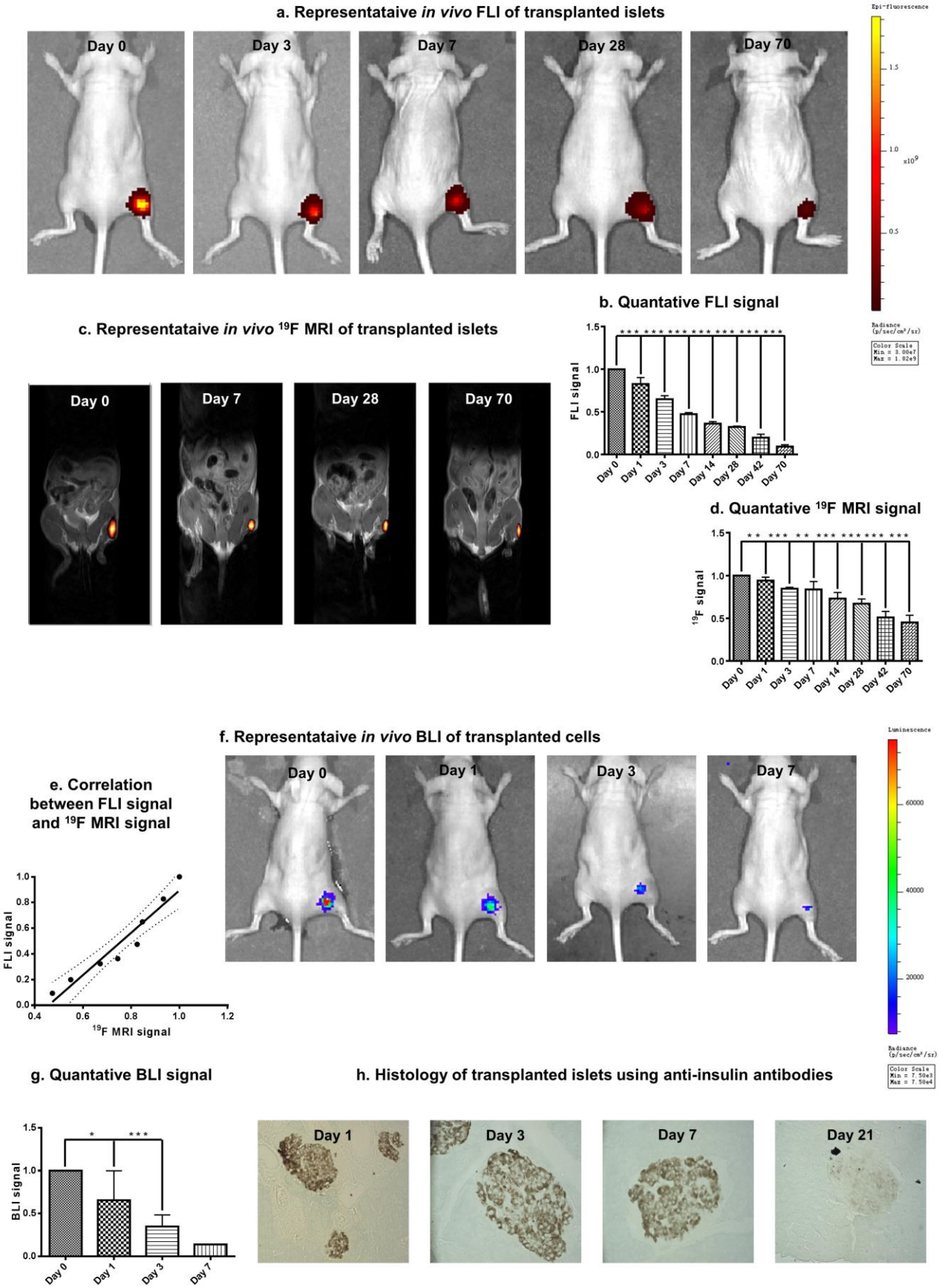

Fig. 3.4 Multimodal *in vivo* imaging of transplanted pancreatic islets (200 PIs (labeled and transduced) mixed with 100-200 µl medium at right thigh and 200 µl PBS at left thigh, n = 6, Swiss Nude mice (female, 7-9 weeks old)). (a). Representative *in vivo* FLI images (hot scaled) of transplanted pancreatic islets overlaid with background photo at different time points (Left -> Right: day 0, day 3, day 7, day 28 and

day 70). (b). Quantitative FLI signal of *in vivo* tracking transplanted pancreatic islets over 70 days (significant difference found between all time points to day 0, $p < 0.001$). (c). Representative *in vivo* ^{19}F signal (hot scaled, scan time ~ 30 min) of transplanted pancreatic islets overlaid with overlaid with proton image (gray scaled) at different time points (Left -> Right: day 0, day 7, day 28 and day 70). (d). Quantitative ^{19}F signal of *in vivo* tracking transplanted pancreatic islets over 70 days (significant difference found between all time points to day 0, $p = 0.0054$ for day 1 and $p < 0.001$ for all other time points). (e). Correlation between FLI signals with ^{19}F signal of *in vivo* tracking transplanted pancreatic islets over 70 days (Y (FLI signal) = 1.647* X (^{19}F signal) -0.7528, R = 0.9628). (f). Representative *in vivo* BLI images (rainbow scaled) of transplanted pancreatic islets overlaid with background photo at different time points (Left -> Right: day 0, day 1, day 3, and day 7). (g). Quantitative BLI signal of *in vivo* tracking transplanted pancreatic islets over 70 days (significant difference found between day 1 to day 0, $p = 0.0347$ and day 3 to day 0, $p < 0.001$). (h). Light microscopy of pancreatic islets using Guinea Pig anti-insulin antibodies (Left -> Right: day 1, day 3, day 7, day 21). Arrow points to labeled PIs.

For BLI, the signal intensity showed a dramatic drop on the first day (Fig. 3.4f and g). Starting from day 14, there was no signal detectable by BLI for all animals. This indicates that the number of remaining viable islets was below the detection limit of BLI. We were able to confirm by immunohistochemistry (anti-insulin labeling using avidin-biotin-peroxidase complex with diaminobenzidine see Fig. 3.4h) that viable, insulin producing PIs were still present after day 7 and even after day 21 (in the latter case with considerably degraded PI morphology). This indicates that most likely the transduced cells of PIs at the outer sphere of the islets started to die first, while some untransduced cells remained functional.

3.3 Discussion

Thanks to its unique advantage of negligible background signal, ^{19}F MRI has found its way in cellular imaging over the last decade[82]. Together with high resolution ^{1}H MRI, which provides an anatomical reference, ^{19}F MRI can offer accurate information regarding the location of transplanted cells *in vivo* and the possibility of direct quantification. Among different fluorinated contrast agents described in the literature[178,300], about two third are perfluocarbon (PFC) based. A remarkable strength of PFC is its often-high payload of fluorine atoms per molecule, which is essential for improving the sensitivity of ^{19}F MRI. As such, the PFCE used in this study is often considered a good candidate since it contains 20 equivalent fluorine atoms, which exhibits one single resonance peak in its ^{19}F NMR spectrum. By using positively charged PFCE particles, we showed in this study that for the INS-1E cells and cells of PIs can be labeled with fluorinated particles without using transfection agents or targeting moieties. With our optimized labeling protocol, the average fluorine uptake per INS-1E cell or islet cell was about 1.5 to $4*10^{12}$. This level of cell labeling is comparable with the typical range of cellular fluorine label required for ^{19}F MRI based cell tracking (10^{11}~10^{13}) reported in the literature[68,189]. Taken into account the theoretical detection limit for experimental MRI systems (^{19}F MRI) and an acquisition time below one hour, approximately 10^{16} fluorine spins per voxels are required to result in sufficient SNR, which results in a detection limit of several thousand cells or close to ten PIs. In addition to the suitable contrast properties of PFCE particles, they have also shown to be biologically inert, resulting in no or only limited impact on cellular phenotypes and cell function[13,209,301]. This has been confirmed in our study for beta cell like cell lines and pancreatic islets where no adverse effects of the fluorine label on cell viability and functionality was observed. However, the side effects on cells are known to be strongly dose-dependent[302]. With the highest fluorine concentration in culture medium (50mM), the reduction of cellular viability based on cell density could be expected. This is not surprising according to a previous study[86], where an effect of fluorine particle labeling on the migratory and

proliferation capacity on neural stem cells was found. Hence, detailed characterization and optimization of cell labeling with fluorinated agents is needed before further utilization of contrast media.

Incorporation of a fluorescent dye into PFC emulsions has been described before, which allows confirmation of cell labelling by fluorescence microscopy and flow cytometry but also by *in vivo* optical imaging[13,303]. We have used a lipophilic membrane-bound red fluorescent DiD dye in our PFCEs, which can be integrated rapidly and in a stable manner with long retention and limited toxicity[304-306]. The internalization of PFCE particles into cells was hereby confirmed even several months after PI engraftment. The red-shift of the DiD dye also allowed relatively reliable *in vivo* detection of PFCE labeled cells by fluorescence imaging. This has resulted in a linear correlation between *in vivo* ^{19}F MRI and FLI signal intensities of transplanted INS-1E cells and PIs, which also indicates a strong conjugation of DiD to PFCE, which is in agreement with other similar reagents[189]. As the PFC emulsions were determined to be stable inside the INS-1E cells/ PIs, it is suggested that both ^{19}F MRI and FLI allow quantification of cell/ PI numbers *in vivo* after *in vitro* pre-calibration and under the assumption that the cell labeling is uniform so that the number of cells/ PIs is proportional to the signal strength. However, the translation to the *in vivo* situation is not straightforward, where cell division, phagocytosis of dead cells or released labels could lead to misinterpretation of data and hereby to inaccuracy of the determination of cell numbers.

One limitation of MRI and FLI is the fact that directs quantification of the cell viability is not possible. In contrast, *in vivo* BLI of genetically modified INS-1E cells and PIs to express Fluc can provide semi-quantitative information on cell viability. As shown before, genetically engineered cells and PIs did show survival rates and cell functionality comparable to wild type cells or PIs[30,32], indicating that genetic engineering of cells/ PIs has no apparent deleterious effect on islet function. With the direct visualization of viable INS-1E cell/ PI numbers using BLI, the process and outcome of cell/ PIs engraftment associated with the surrounding environment can closely be monitored. *In vivo* monitoring of INS-1E cells and PIs by using BLI identified early onset of some substantial graft rejection (almost immediately after the transplantation), while both ^{19}F MRI and FLI showed delayed response as residual signal remained for a much longer time period, resulting in an overestimation of remaining cells or PIs. This underlies the importance of multimodal imaging approaches for cross-validation and proper image interpretation.

A subcutaneous transplantation site is an attractive location for cell/ PI tracking since the related transplantation procedure is considered simple and safe and is minimally invasive. From an imaging point of view, the superficial location of the subcutaneous space is a perfectly suited for performing optical imaging techniques with improved sensitivity compared to traditional transplantations sites like intraportal liver injection. Possible problems for the acquisition of MR images (too close to the surface) were not noticed. As shown in our data, the downside of this transplantation site is the poor survival rate of transplanted cells/ PIs due to a potentially evoked immune response together with hypoxia and a hypo-vascular environment[307]. Numerous studies have already shown that the primary cause of early loss of transplanted cells is hypoxia and insufficient vascular support despite the site of transplantation and type of cells[308-310]. Considering the hypoxic space of the subcutaneous site, the loss of transplanted cells/ PIs due to hypoxia and hypo-vascularization is even more severe. As such, the minimum number of islets required for recovering diabetic animal models are reported to be 800 for mice and 5000 for rats[311,312]. Hence, prevention of hypoxia is a major challenge to promote subcutaneous transplantation sites as a primary choice for PI transplantation. Different strategies have

been developed to improve the outcome of PI transplantation with focus on tackling hypoxia and hypo-vascularization. Pre-vascularization is a popular method by implantation of biodegradable foreign material such as biodegradable PGA polymers[313] and stainless steel mesh[314] or scaffolds made of extracellular matrices[315]. Induction of angiogenesis before transplantation leads to better results for subcutaneous transplantation. Other novel methods, such as co-transplanted PIs with adipose and bone marrow stem cells for vascularization [316] are also potentially of benefit. Immunological aspects are also important to be considered in PI transplantation. For portal vein transplantation, immunosuppressive drugs are often needed though certain drugs like sirolimus and tacrolimus could introduce side effect to islets[317]. In general, as subcutaneous space is not an immune-privileged site, the reaction of the immune system is considered less active. Our preliminary *in vivo* BLI data with both fluorine labeled and unlabeled cells grafted at different sides of the animals suggests a more active effect of the immune system on the labeled cells. However, this speculation still needs further in-depth investigation which is beyond the scope of this thesis. Nevertheless, newly proposed methods of encapsulation of PIs for transplantation may serve as a promising tool for immune isolation[37] without the need for immunosuppressive drugs.

In summary, we optimized the transduction and labeling protocols for both PIs and INS-1E cells, which confirmed internalization of PFCE particles and expression of firefly luciferase. No significant side effects on cell viability and function were noticed for the conditions used in this study, making this a safe approach. The feasibility of using the proposed imaging methods was demonstrated both *in vitro* and *in vivo*. Our data suggested ^{19}F MRI is suitable for high-resolution localization of transplanted cells and PIs; FLI is essential for confirmation of contrast agent localization by histology; and BLI is a reliable method to assess cell viability and survival after transplantation. With the complementary information acquired by the different imaging modalities, this tri-modal imaging strategy has the potential to overcome limitations concerning sensitivity, resolution, specificity and functional assessment by the individual methods. This imaging platform is not only limited to subcutaneous transplantation, but can also be applied to other PI transplantation sites, such as the muscle, the kidney renal, the omentum, the anterior chamber of the eye and others[286]. Although not all imaging methods are translatable for clinical applications (namely BLI), this non-invasive approach to assess islet transplantation is valuable for future preclinical studies to compare different sites for PI transplantation.

3.4 Conclusions

We propose a tri-modal imaging platform by combining BLI, FLI and ^{19}F MRI for tracking subcutaneously transplanted PIs or beta cell-like cells (INS-1E cells) for the *in vivo* characterization of experimental models for islet transplantation. With this imaging approach, novel strategies for improving outcome of PI transplantation could be better evaluated and compared in longitudinal studies, reducing the number of animals needed and reducing statistical variability when compared with studies entirely relying on histology at particular time points.

3.5 Materials and Methods

3.5.1 Fluorinated particles and lentiviral vector

For pre-labeling purpose, cationic perfluoro-15-crown-5 ether (PFCE) particles (particle concentration: $4.5*10^9$ particles/ ml, particle mean size: 0.9 ± 0.4 μm) were prepared as previously reported[318]. PFCE particles consist of a PFCE liquid core stabilized by a phospholipid monolayer containing DOTAP (1,2-dioleoyl-3-trimethylammonium-propane), DOPE (1,2-dioleoyl-sn-glycero-3-phosphoethanolamine), DSPE-PEG(2000) (1,2-distearoyl-sn-glycero-3-phosphoethanolamine-N-[amino(polyethylene glycol)-2000]) and cholesterol (see also supplementary material). To allow the cross-validation of ^{19}F MRI with *in vivo* fluorescence imaging and confocal microscopy, 3.5 mol% of the total lipid coating was replaced by the lipophilic DiD fluorescent dye (Thermo Scientific).

Fluorine concentrations of each batch of PFCE particles were determined by ^{19}F NMR spectroscopy and adjusted in case of minor batch variations. Lentiviral vector (LV) carrying the hEFlα promoter to drive triple flag tagged firefly luciferase (3flagFluc) and a puromycin resistance gene (PuroR) was used for islets/ cells transduction as described in[319].

3.5.2 Rodent pancreatic islets and cell lines

The PIs used in this study were isolated from Wistar rats (female, 8-10 weeks, 200-250 g) using the collagenase digestion method[277]. Animals were euthanized by an overdose of Nembutal (CEVA, Brussels, Belgium). After digestion using 0.54mg/ml collagenase (Roche, Belgium), pancreatic tissue was washed three times (3x) with cold Hanks' Balanced Salt Solution (HBSS, Gibco, Brussels, Belgium). Islets were cultured in RPMI-1640 medium (+L-Glutamine, Gibco, Ghent, Belgium) supplemented with 10% fetal bovine serum (FBS, Hyclone, Aalst, Belgium) and 1% penicillin/streptomycin (Cellgro, Manassas, USA) after handpicking and counting.

The pancreatic beta cell like INS-1E cell line, used at passage 52, was a kind gift from C.B. Wollheim (Department of Cell Physiology and Metabolism, University Medical Center, Geneva, Switzerland). Those cells were cultured in RPMI-1640 medium supplemented with 10% FBS, 10 mM HEPES (Sigma, Bornem, Belgium), 1 mM sodium-pyruvate (Gibco), 0.05 mM 2-mercaptoethanol (Gibco) and 1% penicillin/ streptomycin (Cellgro, Manassas, USA). A humidified incubator (CB series, Binder GmbH, Tuttlingen, Germany) using normoxic conditions with 5% CO_2 and a temperature of 37 ℃ was used for incubation of both PIs and INS-1E cells.

3.5.3 Lentiviral vector transduction experiments

In order to generate firefly luciferase expressing INS-1E cells, untreated cells (~$4*10^5$ cells/well) were seeded into 6-well plates (Sigma) containing medium and LV (concentration: 5μl /well) and were incubated for 24 hours. 2mg /mL puromycin (Merck Millipore, Darmstadt, Germany) was also added to the growth medium to be able to select the transduced cells. After washing (3x) with phosphate buffered saline (PBS without Mg^{2+} and Ca^{2+}, Gibco), selected cells were further cultured for later use.

By placing 100-200 PIs/ well into 6-well plates, the transduction of PIs was firstly optimized by modifying the concentrations of LV (5µl, 10µl /well) and incubation times (24 and 48 hours) in preliminary experiments. Optimized conditions (10µl/ well with 48 hours' incubation) were determined and used for further experiments.

3.5.4 Cell labeling using PFCE particles

INS-1E cell labeling experiments were performed using different final fluorine concentrations (10, 15, 20, 30 and 50mM) with different incubation times (4 and 24 hours). After co-incubation with PFCE particles, cells were washed with PBS (3x), trypsinized with 0.05% trypsin (Gibco) and further divided for fluorescence microscopy (Olympus CKX 41, Olympus, Antwerpen, Belgium), total cell counts using an automatic cell counter (Chemometec, Lillerod, Denmark) and ^{19}F nuclear magnetic resonance (^{19}F NMR) spectroscopy to assess PFCE particle uptake and cell viability.

For optimization of PI labeling, different incubation times (4, 8, 10, 20, 24 and 48 hours) were used in the presence of PFCE particles, resulting in a 20mM fluorine concentration. Similar to the INS-1E cells, PIs were handpicked and divided for different *in vitro* assays such as fluorescence microscopy, confocal microscopy and NMR spectrometer after incubation and washing. Unlabeled PIs/ cells were always included as negative controls in all the experiments.

After optimization of PFCE labeling protocols, studies on the release of the fluorine labels from pre-labeled PIs and INS-1 cells were also conducted. After the washing step, labeled PIs/ cells were harvested and cultured for another 24 or 48 hours in fluorine free medium. At the end of the incubation, both the supernatant and PIs/ cells were collected for ^{19}F NMR spectroscopy experiments to quantify their fluorine content and possible chemical modification of the fluorinated compounds.

3.5.5 ^{19}F NMR experiments

All ^{19}F NMR experiments were performed using an 400 MHz Bruker Avance II NMR spectrometer (Bruker Biospin, Rheinstetten, Germany) equipped with an 5 mm broadband probe, which was also tunable to 376.5 MHz for ^{19}F NMR spectroscopy. Pre-labeled PIs (number of islets = 25) / cell samples (cell number = $2.5*10^4$) were lysed and prepared in a PBS solution (made up with 0.4 ml D_2O) and were then transferred to a 5 mm NMR tube (Wilmad, Vineland, NJ, USA). As a reference compound, 5-fluorocytosine (0.1 ml, 5 mM, δ = -77.5 ppm) was added for calibration of the chemical shift and for determining the fluorine concentration in each sample. The pH value of the sample was adjusted to a value of approximately 7. The temperature was maintained at 37 ℃ during the NMR experiment. The acquisition parameters were as following: frequency = 376.5 MHz, spectral width = 350 ppm, relaxation delay = 5 s, data points = 64 k and number of averages = 128. After phase and baseline correction of the acquired ^{19}F NMR spectra using the Topspin software (Bruker Biospin, Rheinstetten, Germany), the ^{19}F signals were quantified relative to the 5-fluorocytosine signals by peak integration.

3.5.6 Confocal Microscopy

Confocal microscopy images (including z-stacked images) were acquired using a Nikon A1R Eclipse confocal microscope (Nikon, Brussels, Belgium) to verify the internalization of PFCE by cells of the PIs. The samples were prepared as following: after pre-labeling, PIs were fixed with 4% PFA for 15 minutes at room temperature and washed (3x) with PBS. PIs were then seeded in Nunc 4-well glass bottom trays (Nunc) at 5 islets/ well. The nuclei were counterstained with Hoechst dye (ThermoFisher Scientific) solution (1:2000 in PBS), which was protected from light for 5-10 minutes according to the manufacturer's instructions. Following this, PIs were again washed with PBS (3x), after which 500 µl fresh PBS was added to each well.

3.5.7 Islets viability and functionality tests assessment in vitro

To confirm the viability and function of PIs after labeling and transduction, Trypan blue staining, insulin content measurement and glucose stimulated insulin secretion tests were performed. Trypan blue staining was performed by adding 20 µl of a 0.4% solution of Trypan blue (ThermoFisher Scientific) to 1 ml medium containing PIs (n ~ 50) in a 12 well plate with subsequent fluorescence microscopy (Olympus CKX 41). The insulin secretion function of PIs was performed after labeling and/ or transduction by comparing the insulin content with unlabeled/ non-transduced control PIs. After handpicking and counting, 50 PIs were sonicated on ice, and frozen at -20 ℃ until insulin content measurements were performed.

To further investigate the insulin section function of labeled/ transduced PIs to glycaemia modification, glucose stimulated insulin secretion (GSIS) of unlabeled, labeled/ transduced PIs was assessed as described previously[320] with PIs (n = 8) placed in 1 ml assay tubes. In brief, after a 30-minute pre-incubation in HEPES-buffered NaCl solution without bicarbonate, PIs were incubated with basal Krebs-Ringer buffer (KRB) for 90 minutes at 37 ℃ in the presence of D-glucose (concentration: 2.8 or 16.7 mM) under constant and gentle shaking. At the end of the incubation, 0.2 ml or 0.5 ml of incubation supernatant was taken out and stored at -20 ℃ until determining the insulin content by enzyme-linked immunosorbent assay (ELISA, #10-1250-10 Insulin, rat ELISA, Mercodia, Uppsala, Sweden).

3.5.8 In vitro BLI, FLI and ^{19}F MRI

In vitro BLI, FLI and ^{19}F MRI was carried out to determine the feasibility of imaging pre-labeled and transduced PIs/ cells with multi-modal imaging and to determine the advantages and disadvantages of each technique. For BLI and FLI, phantoms were prepared by placing PIs (n ~ 50) or INS-1E cells (n ~ $3*10^5$) in 6-well plates containing PBS. All BLI and FLI experiments were acquired using an IVIS Spectrum optical imaging system (PerkinElmer, Massachusetts, USA). For BLI, D-luciferin, dissolved in PBS (15 mg/ ml), was also added prior to the imaging sessions. Consecutive frames were acquired (one per minute) until the maximum signal intensity was reached. For FLI acquisition, the EPI mode was used with an excitation wavelength of 648 nm and an emission wavelength of 670 nm for the DiD fluorescence dye according to the default setting of the system's software (Living Imaging, Perkin Elmer).

For ^{19}F MRI, phantoms were prepared using 2% agarose (Sigma) suspensions in 0.5 ml Eppendorf tubes (Eppendorf, Rotselaar, Belgium). Hereby, Eppendorf tubes were either filled with PFCE labeled PIs (n ~ 100), PFCE labeled INS-1E cells (n ~ $5*10^5$), pure PFCE particles (final ^{19}F concentration: 25mM, positive control) or PBS (negative control). The Eppendorf tubes were then placed parallel in a 25 ml plastic cylinder with a 2.8 cm diameter, which also contained 2% agarose.

All MR experiments were performed using an 9.4 T Bruker Biospec small animal MR scanner (Bruker Biospin, Ettingen, Germany) equipped with a home-built saddle shaped surface coil, which was tuneable and matchable to both the ^{19}F and ^{1}H resonances[185]. Both ^{1}H and ^{19}F MR images were acquired using a 2D RARE sequence with the following acquisition parameters: TE = 15.9 ms, TR= 3 s (^{1}H) / 1 s (^{19}F), RARE factor = 8, FOV = 6.4 x 6.4 cm, matrix size = 256 x 256 (^{1}H) / 64 x 64 (^{19}F), NA = 2 (^{1}H) / 256 (^{19}F), slice thickness = 0.5 mm (^{1}H)/ 2.5 mm (^{19}F), total acquisition time ~ 40 mins.

3.5.9 Animal model

All animal experiments were performed in accordance with national and European regulations and approved by the local Animal Ethics Committee of KU Leuven. In total, eleven Swiss Nude mice (female, 7-9 weeks old, Charles River, Chatillon-sur-Chalaronne, France) were included in the longitudinal study. Animals were further divided into two groups according to the engrafted cells: PI group (n = 6) and INS-1E cell group (n = 5). After collected in an insulin syringe (mixed with 100-200 µl medium), either pre-labeled and transduced PIs (n = 200) or INS-1E cells (n = 10^6) were subcutaneously engrafted at the right thigh of the animals. Control injections were performed on the left side for all animals (200 µl PBS for animals receiving PIs and 10^6 unlabeled, transduced INS-1E cells for animals receiving INS-1E cells). During the transplantation procedure and the subsequent imaging sessions, animals were anesthetized with a ketamine 1000 (100 mg/ ml, CEVA, Brussels, Belgium)/ domitor (1 mg/ ml, Janssen Pharmaceutica, Beerse, Belgium)/ saline cocktail via intra-peritoneal injection (0.06ml/ kg). The following time points were used for imaging the animals of the two groups: PI group: day 0, 1, 3, 7, 14, 28, 42 and 70); INS-1E cell group: day 0, 1, 3, 5, 7, 10, 14 and 21). For PI group animals, single animals were sacrificed for confirmation by histology at day 1, 3, 7, 21 and 70.

3.5.10 In vivo BLI, FLI and ^{19}F MRI

For *in vivo* imaging, the same instruments (IVIS Spectrum and 9.4 Bruker MRI) were used for multi-modal imaging as for the *in vitro* experiments. Prior to *in vivo* BLI sessions, D-luciferin, dissolved in PBS (15 mg/ ml), was injected intravenously (126 mg/ kg body weight). All *in vivo* optical images were acquired using the same protocols and settings as for the *in vitro* experiments.

For all *in vivo* MRI sessions, the body temperature and respiration rates of the animals were monitored using a rectal probe and a pressure sensitive pad placed underneath the thorax. A monitoring and gating model (type 1030) from SA Instruments (Stony Brook, NY, USA) was used to regulate and maintained the body temperature and respiration rate of the animal at reasonable physiological ranges of approximately 37 ℃ and 80-120 breaths min^{-1}, respectively.

For both ^{1}H and ^{19}F MRI, animals were fixed using the manufacturer's animal holder (Bruker BioSpin). The tails of animals were left outside of the coil to facilitate the injection of anesthetics using a pre-fixed infusion line with a 27-gauge butterfly needle. Anatomical ^{1}H MR images were acquired using a rapid spin echo (RARE) sequence (TR = 3 s; TE = 15.9 ms; eight echoes/ excitation; number of averages = 2; number of slices = 50; slice thickness = 0.5 mm; field of view = 8 x 4 cm; matrix size = 400 x200; total acquisition time ~ 8 mins). After acquisition of a non-localized pulse-acquisition ^{19}F MR spectrum (TR = 100 ms, number of average = 1000) to determine and set the center frequency to the ^{19}F frequency of PFCE, ^{19}F MRI was performed using similar parameters as for the ^{1}H MRI with the following modifications (TR = 1 s; TE = 15.9 ms; number of averages = 250; number of slices = 10; slice thickness = 2.5 mm; matrix size = 100 x 50; acquisition time ~ 30 mins). Orientation and dimension of the slice packages was kept identical for ^{1}H and ^{19}F MRI to facilitate co-registration. All MRI measurements were respiration gated.

3.5.11 Histology

Animals that underwent PI transplantation were sacrificed at different time points (day 1, 3, 7, 21 and 70) and perfused with 4% paraformaldehyde for fixation. Right femoral tissue from the PI transplantation was collected for performing insulin staining. The standard ABC-DAB technique using the avidin-biotin kit (Vector Laboratories, Burlingame, USA) were followed for immunohistochemical detection of insulin[321]. Tissue slides were incubated overnight at 4 ℃ with the first antibody: anti-insulin (Santa Cruz Biotechnology, CA, USA).

3.5.12 Image processing

All reported BLI and FLI images were superimposed by a grey-scale photographic image with anatomical information and a pseudo-color image with functional/ optical information. The BLI/ FLI signals were expressed as total photon flux (p/s/sr) from a circular region of interests (ROI) using the Living Imaging software (Perkin Elmer). MRI data was processed using the ImageJ software (NIH, USA). All presented ^{19}F MRI signals (hot scale) were overlaid with corresponding 1H images (gray scale) as anatomical reference. The quantification of ^{19}F MR signal and comparison at the different time points was performed by calculating the SNR (mean value of signal to standard deviation of background) of selected ROIs (one region with signal and one background region) with receiver gain calibrated. For the longitudinal study, each animal's quantified BLI, FLI and ^{19}F MR signals from the different time points were normalized to the data from the corresponding first time point.

3.5.13 Statistical Analysis

All statistical analyses and linear regressions were performed using the Prism 6 software (GraphPad Software, CA, USA). Either an ANOVA test with a Bonferroni post-test for multiple groups' comparisons or a Student's t-test for two group comparisons was used to determine statistical differences between different experimental groups. P-values less than 0.05 were regarded significant.

3.6 Supplementary Data

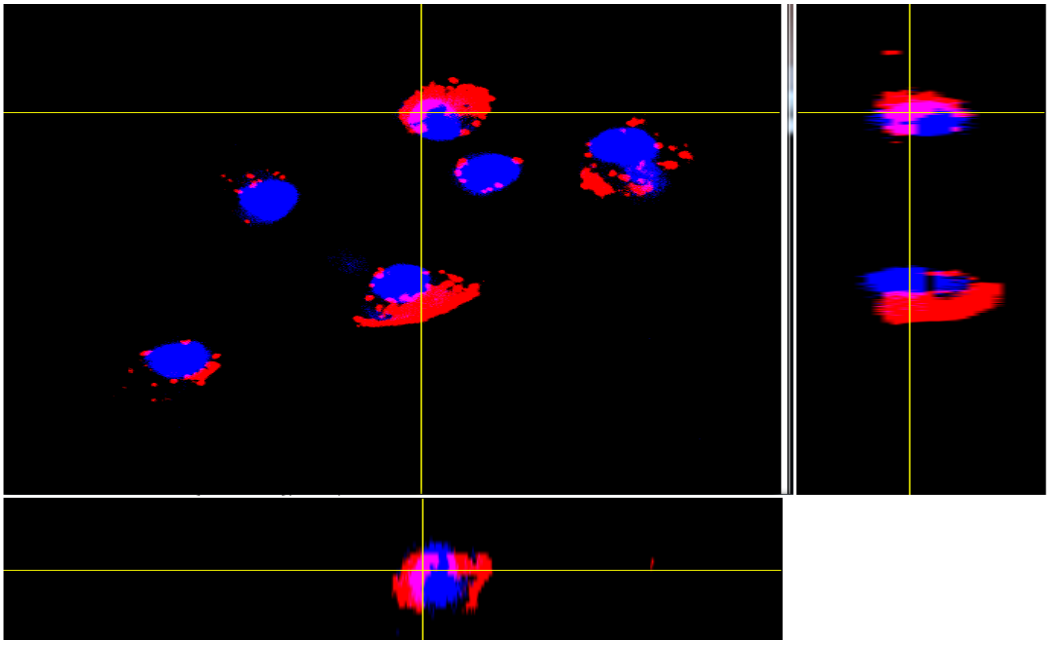

S1. Representative confocal microscopy orthogonal z-stack slicing of individual cells of labeled pancreatic islet islets (Blue: nuclei counterstained with Hoechst dye; Red: PFCE particles containing DiD dye; Pink: co-localization of nuclei and PFCE particles). The pink signal of the marked cells indicated a notable uptake of PFCE nanoparticles in the cells of PIs after a 24-hour incubation time.

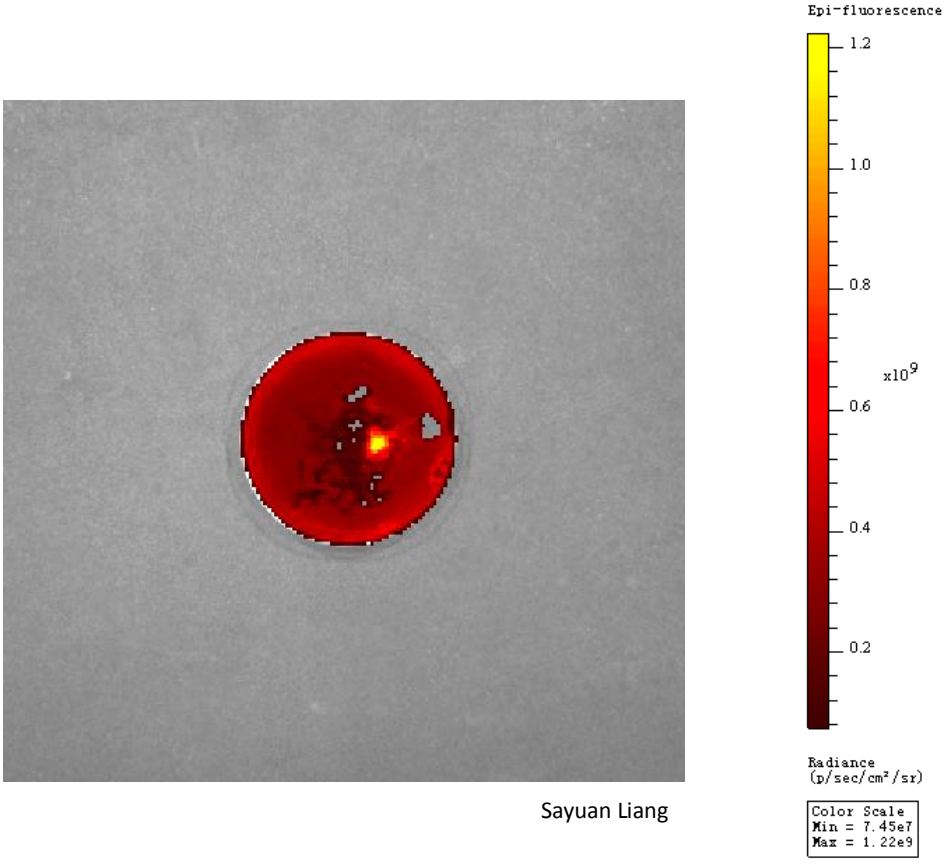

S2. Representative FLI (hot scaled, excitation wavelength: 648 nm and emission wavelength: 670 nm) of treated pancreatic islets (n ~ 50) overlaid with background photo. The high optical signal intensity against background showed a detection limit of a few islets by *in vitro* FLI.

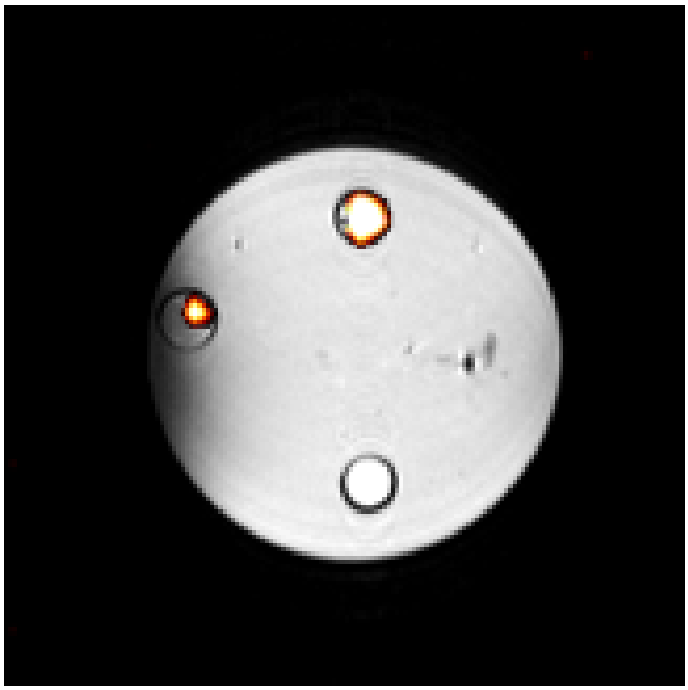

S3. Representative ^{19}F MR image (hot scaled) of treated pancreatic islets phantom consisting of Eppendorf tubes in agar. The ^{19}F MR image is overlaid with its proton MR image (gray scaled). The respective Eppendorf tubes contain (from top to bottom): PFCE particles (25mM fluorine, positive control), one hundred labeled PIs and one hundred unlabeled PIs (negative control). About ten islets per pixel were detectable using hundreds of averages, resulting in an acquisition time of 30 minutes and a SNR ~ 12.

Sayuan Liang was involved in experimental design, performing *in vitro* labeling and transduction optimization, *in vivo* imaging experiments, image post-processing and statistics. He has designed the concept of the study. Sayuan Liang also wrote the original draft of the paper with further reviewing and editing.

Chapter 4. Comparison of different compressed sensing algorithms for low SNR ^{19}F MRI application - imaging of transplanted pancreatic islets and cells labeled with perfluorocarbons.

This Chapter has been compiled based on the following publication

Liang S., Dresselaers T., Louchami K., Zhu C., Liu Y., Himmelreich U. (2017). ***"Comparison of different compressed sensing algorithms for low SNR ^{19}F MRI application - imaging of transplanted pancreatic islets and cells labeled with perfluorocarbons."*** *NMR in Biomedicine, 11, 24-31.*

4.1 Introduction

Diabetes is one of the most common metabolic diseases with impaired insulin regulation/production and sustained hyperglycaemia[322]. For the most severe forms of type I diabetes, caused by the loss of pancreatic beta cell mass or function, standard treatment using regular insulin administration is inadequate to achieve optimal regulation of the blood glucose levels. Transplantation of donor pancreatic islets becomes a potential treatment option for patients suffering from severe forms of type I diabetes[323]. However, clinical data shows that the outcome of islets transplantation is still insufficient and variable, despite multiple donor supplies and an improved immunosuppression regimen[324]. Reliable non-invasive imaging for localization and quantification of pancreatic islets becomes necessary to monitor the fate of engrafted islets, to better understand mechanisms of islet degradation and further improve transplantation techniques[13].

Different imaging modalities have been proposed for visualizing exogenous pancreatic islets including bioluminescence imaging (BLI), radionuclide imaging (Positron Emission Tomography and Single Proton Emission Computed Tomography) and Magnetic Resonance Imaging (MRI)[14]. BLI requires prior engineering of islets for the expression of a luciferase gene. It could potentially provide a quantitative measure for the number of viable islets, which could sustain for more than one year in some cases[30,291,292]. For radionuclide imaging, islets could be either pre-labeled with radioactive compounds[293,294] or tracers can accumulate in islet cells after cell transfection, resembling a reporter gene method[295,296]. MRI is another potential candidate thanks to its high resolution and good contrast between different soft tissues. Contrast agents are necessary for pre-labeling and enhancement of MR contrast between the labeled pancreatic islets and host tissue[14]. The feasibility of using super-paramagnetic iron oxide (SPIOs) nanoparticles for longitude monitoring of pre-labeled pancreatic islets for up to 24 weeks has been demonstrated in several studies including clinical trials[75-77,297]. In one of these studies, it was claimed that single islets are detectable[76]. Human islets have also been labeled with FDA approved paramagnetic gadolinium based T_1 contrast agents. Although they are less sensitive than SPIOs, signal could still be retrieved 65 days after engraftment[81]. However, all mentioned techniques have their own disadvantages in terms of clinical translation (BLI, radionuclide imaging), difficulties for longitudinal follow up (radionuclide imaging) and non-specific contrast in the generated image (MRI with conventional contrast agents).

Cell tracking using fluorine containing contrast agents and ^{19}F MRI may open new perspective for islet imaging due to the lack of MR detectable ^{19}F signal in biological tissues, which results in high specificity and quantitative ^{19}F MRI[84,325]. The major limitation of this technique is its relative low sensitivity, as high local fluorine concentrations are required. As only limited amounts of ^{19}F-based contrast agents can be administrated without risking adverse effects on cell biology, ^{19}F MRI suffers often from low signal to noise ratios (SNR). This has become apparent in the application of carbohydrates that are sensitive to the GLUT-2 transporter of beta cells but failed to achieve robust *in vivo* detection[184,299]. To overcome this sensitivity limitation, many efforts have been made to synthesize new ^{19}F MRI contrast agents, namely particles either loaded with higher concentration of ^{19}F spins or coated with certain vehicles to facilitate high uptake by certain cell types[170,178,300,318]. So far, perfluorocarbon (PFC) based particles are most frequently used due to their clinical applicability and most importantly due to the fact that they often contain several chemically identical ^{19}F atoms per molecule. For example, perfluorooctylbromide (PFOB) labeled human islets can be imaged by ^{19}F MRI after sub-capsular transplantation to the kidney of mice, as shown by Barnett et al[190]. However, several thousand islets were needed to achieve sufficient SNR for imaging purposes. So far, perfluoro-15-crown-5-ether (PFCE) with 20 identical fluorine atoms was one of the most sensitive agents for cell detection *in vivo*[326].

A highly anticipated strategy for improving the sensitivity of MRI is the utilization of novel image reconstruction techniques to speed up scanning. One of the recent advancements is the introduction of compressed sensing (CS). Lustig et al. have demonstrated that CS can be used as a generalizable tool to significantly reduce the MR scan time in a variety of applications, such as angiography, chemical shift imaging and dynamic imaging[251]. In order to implement the CS approach, the target dataset has to meet three pre-requisites: sparse representation in a known transform domain, incoherent (noise-like) aliasing artifacts caused by pseudo-randomized k-space under-sampling and non-linear reconstruction to enforce both sparsity of image representation and consistency with the acquired data. The intrinsic, background-free feature of ^{19}F MRI, leading to highly sparse ^{19}F signal in the image domain, makes it a particularly suitable candidate for CS. Previous studies related to ^{19}F MRI and CS have been reported in the context of chemical shift imaging and catheter imaging[252,327]. Furthermore, Zhong *et al*. investigated three-dimensional (3D) CS methods for accelerated ^{19}F MRI toward cell tracking applications[253]. They have shown that CS with an acceleration factor of up to 8-fold, can dramatically enhance SNR per acquisition time without seriously affecting ^{19}F MRI quantification. However, in all of these studies, mainly high SNR datasets (SNR ~ 20 or even higher) together with a single CS reconstruction algorithm were used. Important issues, such as performance of CS on low SNR datasets, comparison of different existing CS algorithms and whether gain in scan time results in lower detection limits still need to be further studied.

In this study, we have investigated and compared different CS methods for low SNR ^{19}F MRI datasets. This was then tested on applications of ^{19}F-labeled pancreatic islets/ beta cells, both *in vitro* and *in vivo* after subcutaneous transplantation. Using Cartesian under-sampling of k-space with central emphasis, both numerical simulation of fully sampled datasets and hardware CS acquisition of under-sampled datasets were used for CS reconstruction. Five different existing CS algorithms were modified and adjusted for this study, including SPARSEMRI: a traditional convex method for MRI applications, which served here as golden standard in this study[251]; orthogonal multi-matching pursuit (OMMP): a recently proposed greedy algorithm[328]; compressive sampling matching pursuit (CoSaMP): a balanced algorithm between the faster greedy algorithm and more accurate convex algorithm[329]; iterative reweighted L1 minimization (IRWL1): a slower non-convex algorithm with

better accurancy[330]; two-level L1 minimization (Two-level): which approximates the reweighted L1 minimization piecewise-linearly to generate similar results with faster speed[331].

4.2 Results

4.2.1 CS Simulation: ^{19}F MRI phantom studies

By using a ^{19}F MRI dataset of a phantom containing vials with PFCE and labeled islets and Cartesian k-space down sampling pattern, CS acquisition was simulated to evaluate the impact of different CS algorithms on low SNR ^{19}F MR images and their quantification. For fully sampled images (Fig. 4.1A, G, and M), two SOIs were detected. Both have relativly low SNRs within a small region (positive control (25 mM ^{19}F): SNR ~ 13 within 9 pixels, red arrow; labeled pancreatic islets: SNR ~ 8 with 3 pixels, blue arrow). The detection threshold is set at an uncorrected SNR of 5[179].

CS reconstruction with fully sampled data (UF = 1) is in good agreement with the original image. With an UF of up to 4-fold, both SOIs could still be detected, while for UF = 8, distortion and blurring appears on the high SNR spot, while the low SNR spot is so underestimated that the signal could not be visually recognized any more (Fig. 4.1N-R). Different algorithms result in similar performance except CoSaMP whose reconstructed images are more prone to noise.

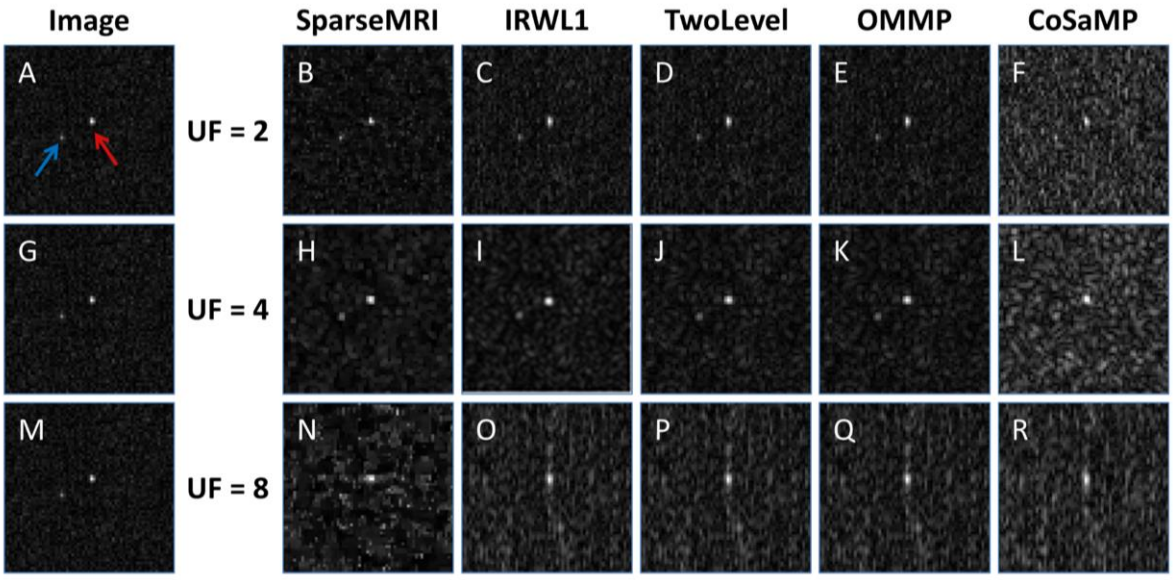

Fig. 4.1 2D CS simulation and reconstruction of ^{19}F MRI *in vitro* dataset using different UFs and CS algorithms. Red arrow, positive control (pure PFCE 25mM ^{19}F concentration, SNR level is about 13 covering six pixels, scan time ~ 30 min); blue arrow, labeled pancreatic islets (SNR is about 8 covering three pixels). All images are displayed with the same intensity scale.

These visual comparisons were confirmed by quantification of the two SOIs by using the different under-sample patterns (Fig. 4.2A-B). By normalizing the SNR of CS reconstructed ^{19}F MRI signals to the SNR of their fully sampled images, a 3- to 4-fold increase in terms of normalized SNR per scan time (SNR/t) could be achieved for both SOIs. Base on the normalized SNR per scan time parameter, different algorithms were also compared with the gold standard SPARSE MRI algorithm. A nonparametric Mann-Whitney U test indicated no significant differences between the algorithms and

SPARSEMRI except for the CoSaMP algorithm, which had degraded performance compared with SPARSEMRI at different UFs (Fig. 4.2).

The relative difference of reconstructed SOIs to the fully sampled image is also calculated (Fig. 4.2C-D). As expected, increased UF parameter led to more differences/ errors of reconstructed signal in SOIs compared with the fully sampled image. There is only marginal difference between the two different SOIs. For the relative high SNR SOI, the SPARSEMRI algorithm gives the most accurate result with an average of 2-2.5% difference from the true value. Other algorithms tend to overestimate the signal and result in an increased difference. Possible reasons for such overestimations could be the normalization of all voxels with maximal intensity to linear rescale the intensities to a range of [0,1]; the chosen sampling pattern with only a limited number of randomly chosen patterns; or the fact that CS de-noises the reconstructed image[251], which leads to an overestimation of SNR of regions with originally high SNR. However, the mean difference was limited to 5% except for the CoSaMP algorithm. For lower SNR SOI, the mean difference was also within the 5% range. No significant difference was found between the SPARSEMRI, Two-level, OMMP and IRWL1 algorithms.

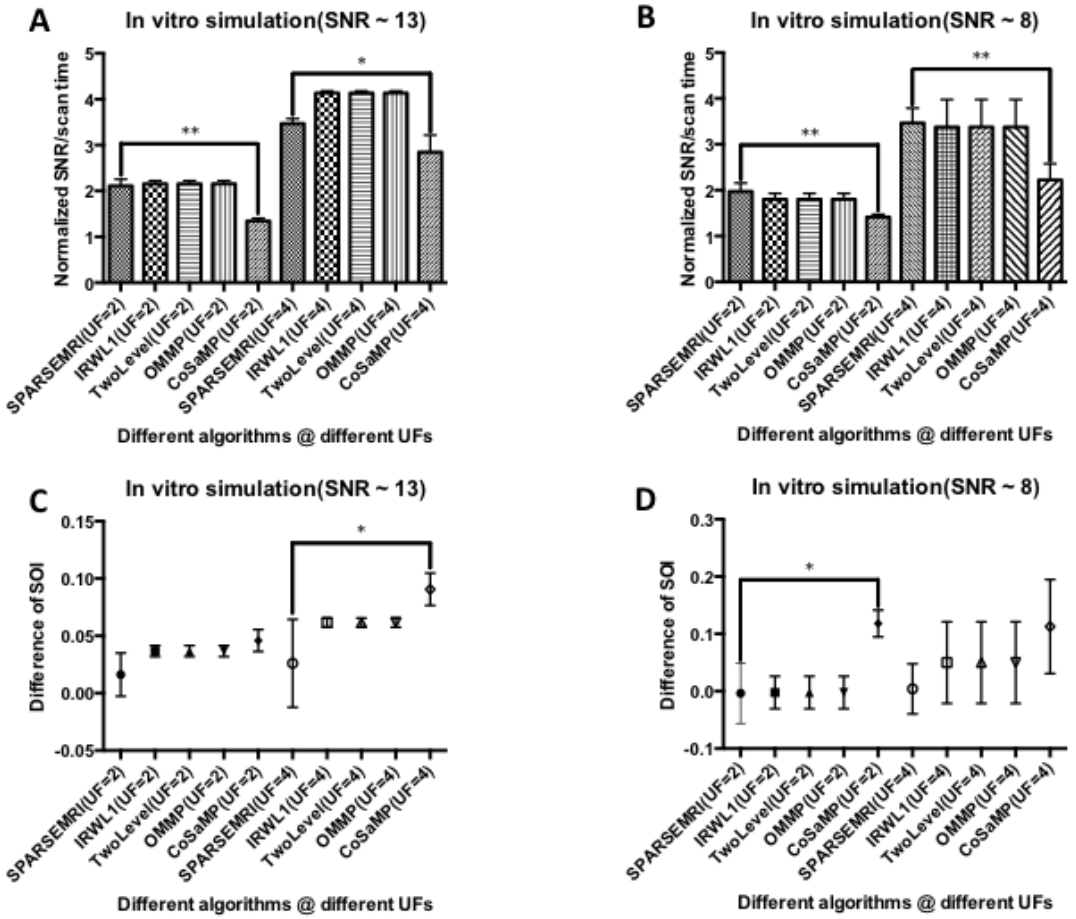

Fig. 4.2 Quantification of 2D CS simulation and reconstruction of ^{19}F MRI *in vitro* dataset using different UFs and CS algorithms. A, B, the normalized SNR per scan time is calculated by normalizing SNR values of a certain SOI in CS reconstructed images to its original SNR value in fully sampled images and then further multiplied by the applied UFs. C, D, the relative difference of the SOI between CS reconstructed images and fully sampled images by calculating the difference between the mean value of SOI in the CS reconstructed image and fully sampled image, then further dividing by the mean value of SOI of the fully sampled image. The error bars are the standard deviation among different undersample patterns for reconstruction.

4.2.2 CS Simulation: in vivo study

For *in vivo* datasets, 200 labeled islets were used for subcutaneous transplantation near the right thigh of the animal similar to the *in vitro* phantom study. This resulted in one signal of interest covering a 9-pixel area with an SNR of approximately 7. The SNR level is similar for the same amount of islets compared to the *in vitro* phantom study. The fact that the covered area is larger *in vivo* than in the phantom study is due to a more dispersed islet distribution after transplantation. Again, different Cartesian k-space sampling patterns were applied for simulation purposes.

As shown in Fig. 4.3, the results obtained from the *in vivo* simulation study are similar to the *in vitro* simulation, in particular regarding the low SNR SOI. This was expected, as the images have similar SNRs. Again, a SNR/t increase by a factor of at least 3-4 was obtained with similar reconstructed image quality and less sharp contrast. Statistical analysis (Fig. 4.4A) confirmed that there is no significant difference between different algorithms by applying different under-sampling patterns with similar levels of central k-space emphasis at UF = 2 and 4. The relative difference between the reconstructed SOI and fully sampled data (Fig. 4.4B) was only 1-2% for all algorithms.

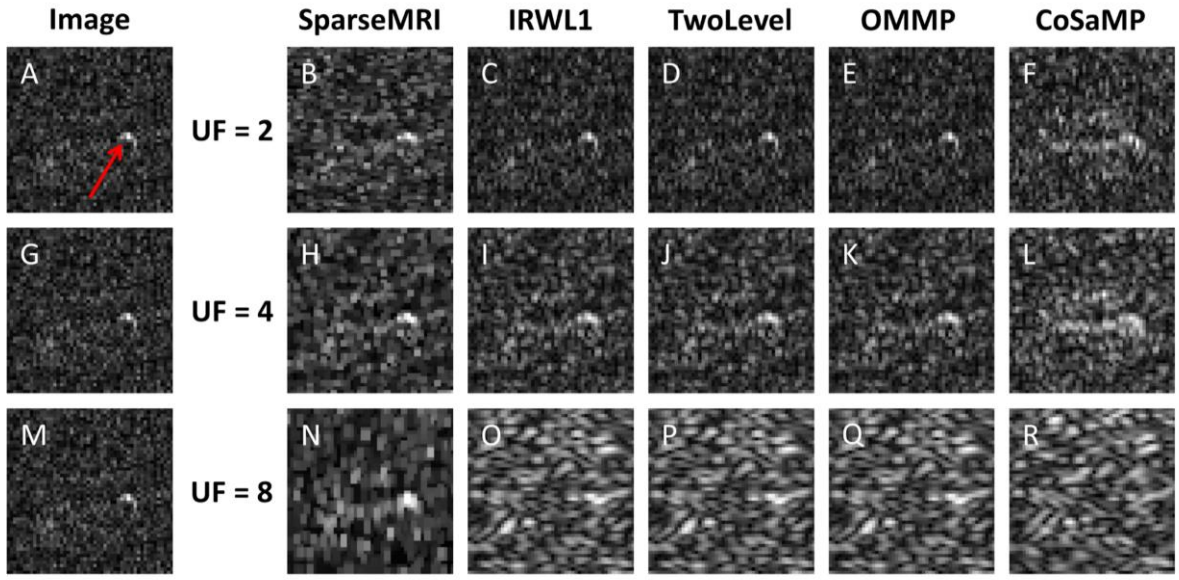

Fig. 4.3 2D CS simulation and reconstruction of ^{19}F MRI *in vivo* dataset with different UFs and CS algorithms. Red arrow, labeled pancreatic islets transplanted subcutaneously near the right thigh (SNR is about 7, covering nine pixels, scan time ~ 30 min). All images are displayed on the same intensity scale.

Computation time was also taken into account (Fig. 4.4C). Algorithms like SPARSEMRI, IRWL and Two-level algorithms result in similar computation time regardless of the UFs, while for the greedy pursuit algorithms, such as OMMP and CoSaMP, computational time decreased dramatically when UF increased. This could be explained by the fact that with an increase of UF, fewer indexes are available to be pursuit for greedy pursuit methods, hence the computational time decreased. Among the different algorithms, the newly developed Two-level algorithm is preferred as it has the most efficient performance.

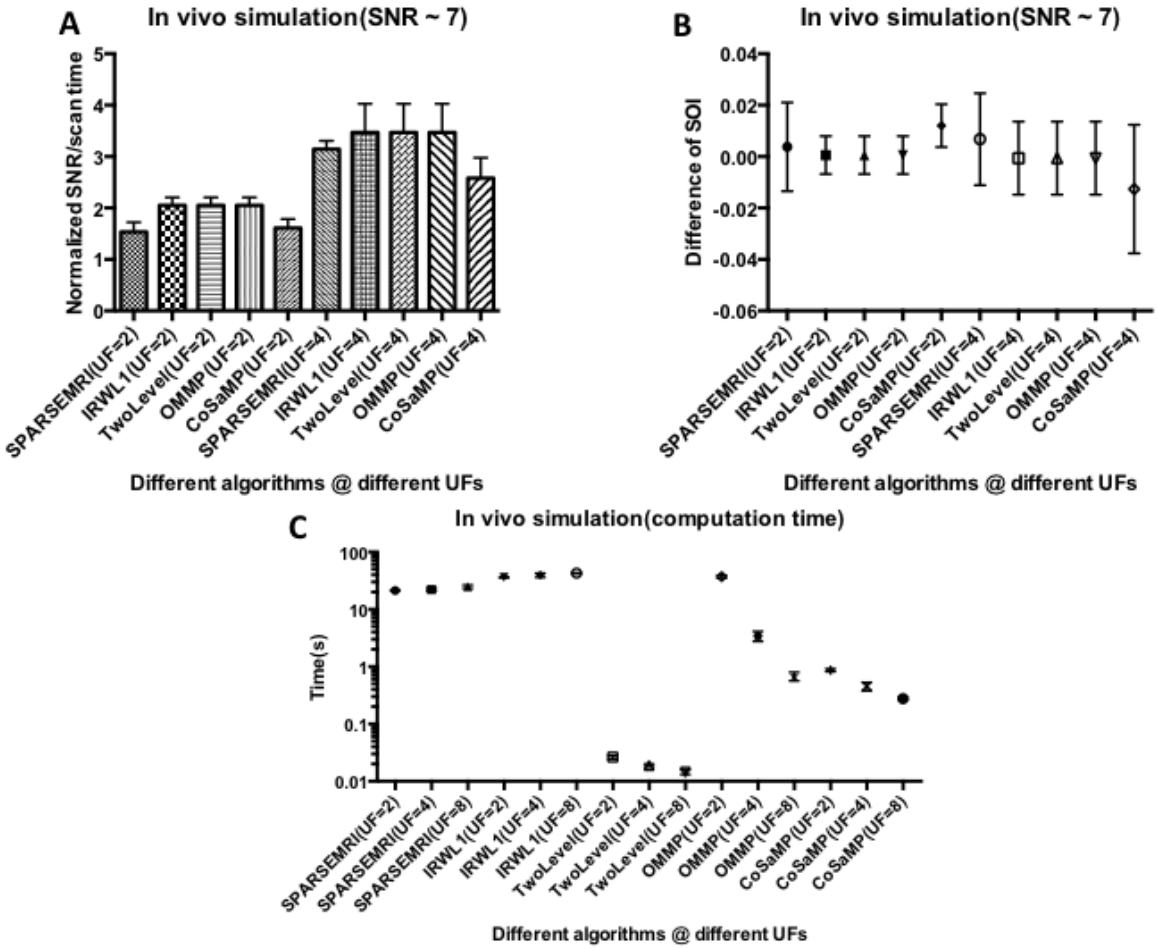

Fig. 4.4 Quantification results from 2D CS simulation and reconstruction of ^{19}F MRI *in vivo* dataset at different UFs and CS algorithms. A, the normalized SNR per scan time is calculated by normalizing the SNR value of the SOI in CS reconstructed images to its original SNR value in the fully sampled image and then further multiplying it by the applied UFs. B, the relative difference of SOI between CS reconstructed images and fully sampled images obtained by calculating the difference between the mean value of the SOI in the CS reconstructed image and fully sampled image, then further dividing by the mean value of the SOI of the fully sampled image. C, the recorded computation time of different algorithms using different UFs.

4.2.3 CS ^{19}F MRI acquisition of phantoms

The ^{19}F MRI phantoms for CS acquisition were designed with individual Eppendorf tubes filled with different concentration of cells. Based on our previous experience with PFCE labeling of INS-1E cells (~10^{12} ^{19}F/cell)[191], we could roughly estimate the expected ^{19}F spin concentration for each Eppendorf tube. Combined with known detection limits for our acquisition hardware and scan protocols (sequence parameters, RF coil), theoretical SNR values could be derived. For the phantom used in this study by using a fully sampled 3D FLASH sequence with 1mm isotropic resolution, only signal from the two Eppendorf tubes with the highest cell concentration could be detected (SNR ~ 14 and 8, respectively).

Based on the previous CS simulation result, an under-sampling factor of 4 was applied for CS acquisition, which results in reduction of the scan time by a factor of 4. To verify our CS acquisition method, a fully sampled image was also under-sampled using the same under-sampling pattern offline (Fig. 4.5A, G, and M). The ^{19}F MRI signal differences between the CS acquisitions based

reconstructed image and the CS simulation based reconstructed image using different algorithms were minimal (Fig. 4.5N-R).

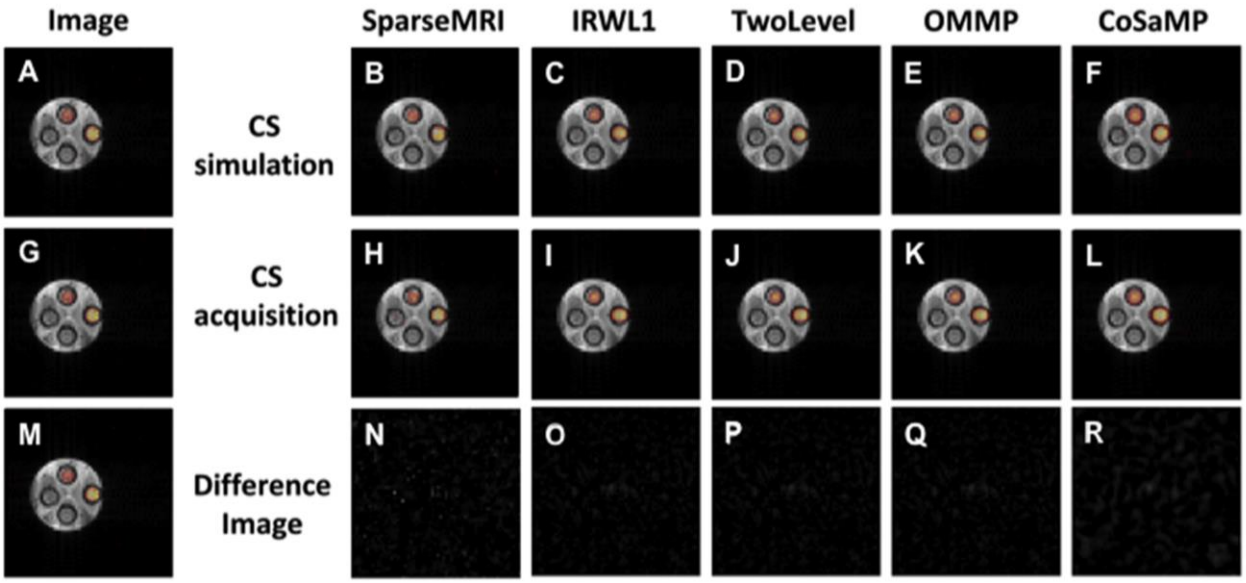

Fig. 4.5 3D CS acquisition and reconstruction of ^{19}F MRI *in vitro* dataset using different CS algorithms and UF = 4 (grey scale, proton MR image; hot scale, ^{19}F MRI signal; the four small circles in the proton MR image represent different concentrations of cells (from right counterclockwise, 10^4, 5×10^3, 2.5×10^3 and 10^3 cells mm^{-3}). Top row, CS image reconstruction by offline undersampling of the fully sampled dataset, scan time ~ 80 min; middle row, CS acquisition and image reconstruction by online undersampling, scan time ~ 20 min; bottom row, difference between top row and middle row images.

Furthermore, when the number of averages for the CS acquisition was four-fold higher (NA = 64), thereby resulting in the same scan time as for the conventional acquisition (fully sampled, NA = 16), the SNR of ^{19}F MRI signal approximately doubled, consistent with theory (Fig. 4.6M). As a result, the signal from the Eppendorf tube containing the second lowest level of cellular concentration reached the detection threshold (SNR level = 5) after reconstruction using the different CS algorithms, except for the CoSaMP algorithm. This demonstrates that by using the CS technique, extra SOI could be detected which might be otherwise missed by using conventional ^{19}F MRI acquisition schemes.

4.2.4 CS acquisition for in vivo studies

For *in vivo* CS acquisition experiments, the number of islets for transplantation were increased by a factor of 2.5 compared with simulation experiments (200 islets used *in vivo*) due to the higher resolution needed for CS acquisition with UF = 4. A proton MR image (Fig. 4.7A) together with two fluorine images with different averages (NA = 64 for Fig. 7B and NA = 256 for Fig. 7C, respectively) were fully sampled and acquired. As shown in Fig. 7C, signal from labeled islets (SNR ~ 9 with 22 pixels) could be visualized at the right thigh of the animal after a 70-minute acquisition. However, for scans with a quarter of the number of averages (Fig. 4.7B), no clear ^{19}F MRI signal was detected. With the information of the location of ^{19}F MRI signal in Fig. 4.7C, the SNR of the same region of interest in Fig. 4.7B was determined to be 4.2, which is lower than the SNR detection limit of 5 (Fig. 4.7D shows an overlay of Fig. 4.7A with Fig. 4.7C).

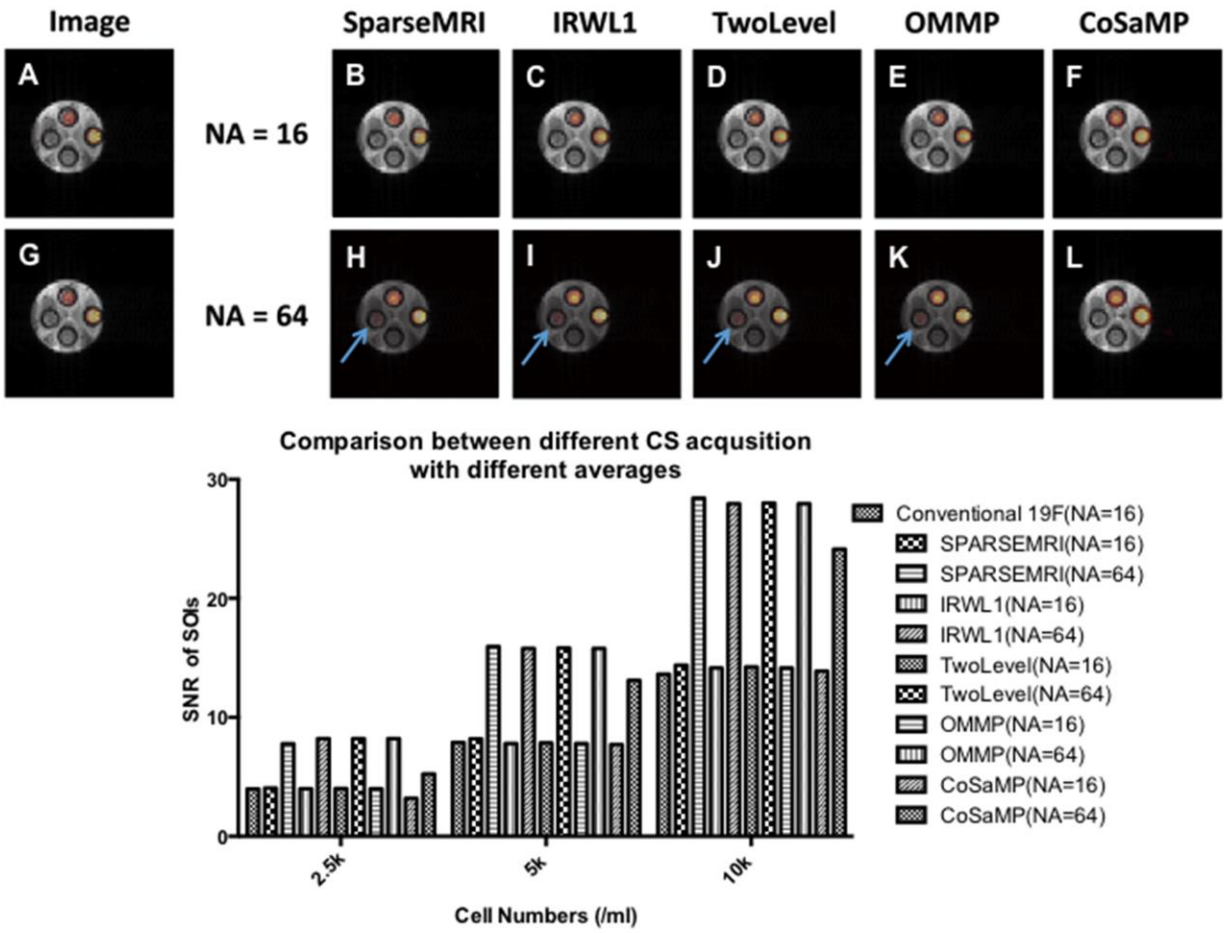

Fig. 4.6 3D CS acquisition, reconstruction and quantification of ^{19}F MRI in vitro dataset with different CS algorithms and different averages using UF = 4 (grey scale, proton image; hot scale, ^{19}F MRI signal; the four small circles in the proton image represent different concentrations of cells (from right counterclockwise, 10^4, 5×10^3, 2.5×10^3 and 10^3 cells mm^{-3}). A- F, CS image reconstruction by online undersampling (NA = 16, scan time ~ 20 min); GL, CS acquisition and image reconstruction by online undersampling (NA = 64, scan time ~ 80 min); M, quantitative data on SNR value between NA = 64 and NA = 16 CS acquisition images at different cell densities.

CS acquisition was performed with NA = 256 and UF = 4, which results in the same scanning time as for fully sampled acquisition with NA = 64. Reconstructed ^{19}F MRI signals using different CS algorithms overlaid with the respective proton MR image are displayed in Fig. 4.7 (E for SPARSEMRI, F for OMMP, G for IRWL1, H for Two-level and I for CoSaMP). Again, except for the CoSaMP algorithm, the other algorithms could successfully retrieve most SOI with similar a SNR level. Although, there were some false positive findings in these CS reconstructed signals (indicated in Fig. 4.7 with red arrows), which may be due to the non-perfect under-sampling scheme used in this case. Instead of two phase encoding directions, only one phase encoding direction was under-sampled as this was a 2D MRI scan.

Nevertheless, this prove-of-principle *in vivo* study demonstrates again CS techniques together with appropriate reconstruction algorithms are useful to reduce the scan time of ^{19}F MRI applications even at a low SNR regime up to undersampling factors of 4.

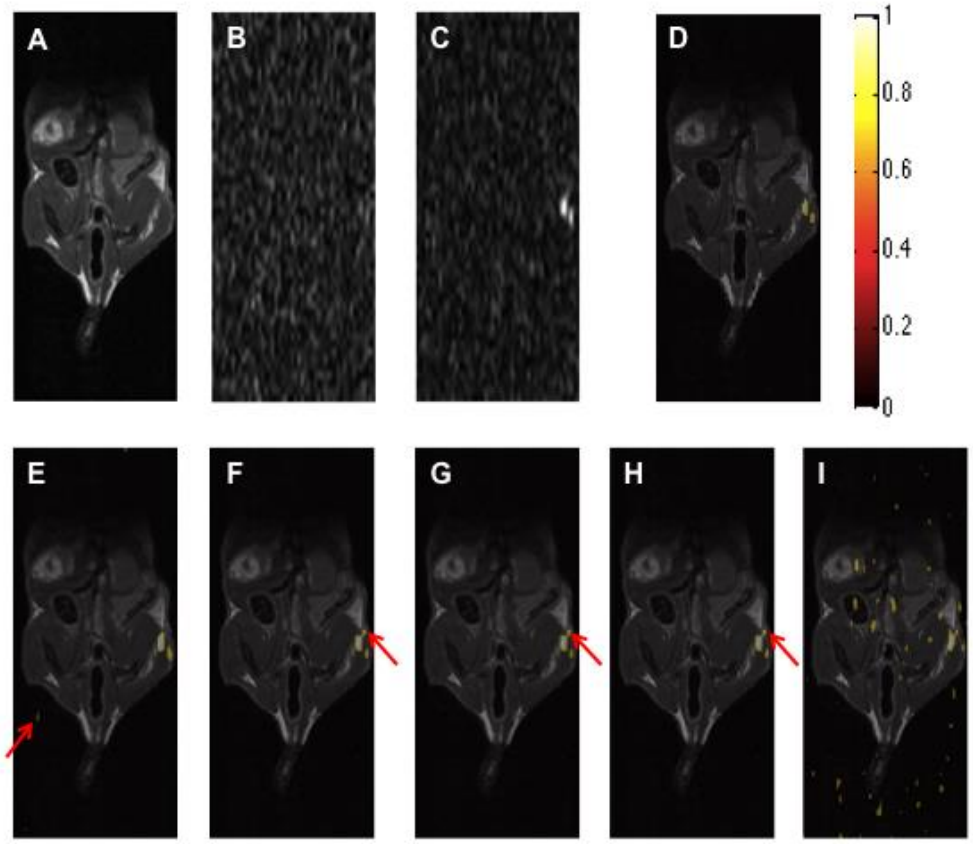

Fig. 4.7 2D CS acquisition, reconstruction and quantification of ^{19}F MRI *in vivo* dataset with different CS algorithms and different averages using UF = 4. A, single slice proton image; B, ^{19}F image with UF = 1 and NA = 64, scan time ~ 5 min, without clear signal detected; C, ^{19}F MR image with UF = 1 and NA = 256, scan time ~ 20 min; D, ^{1}H (gray scale) and ^{19}F (hot scale) fused MR image of A + C; E, ^{1}H (gray scale) and ^{19}F (hot scale) fused image of A + SPARSEMRI reconstructed ^{19}F MRI signal with UF = 4 and NA = 256, scan time ~ 5 min; F, ^{1}H (gray scale) and ^{19}F (hot scale) fused MR image of A + OMMP reconstructed ^{19}FMR signal with UF = 4 and NA = 256, scan time ~ 5 min; G, ^{1}H (gray scale) and ^{19}F (hot scale) fused image of A + IRWL1 reconstructed ^{19}F MR signal with UF = 4 and NA = 256, scan time ~ 5 min; H, ^{1}H (gray scale) and ^{19}F (hot scale) fused MR image of A + Two - level reconstructed ^{19}FMR signal with UF = 4 and NA = 256, scan time ~ 5 min; I, ^{1}H (gray scale) and ^{19}F (hot scale) fused MR image of A + CoSaMP reconstructed ^{19}F signal with UF = 4 and NA = 256, scan time ~ 5 min.

4.3 Discussion

^{19}F MRI is emerging as a useful tool for cell imaging thanks to its unique features: lack of background signal leading to high specificity and the possibility for quantification[82,174,299]. On the other hand, this also results in long scan times with low SNR images as relatively low amounts of external 19-fluorine compound/particle are injected/ transplanted for different applications where relatively small numbers of ^{19}F labeled cells are often desired. By exploiting data sparsity and under-sampling k-space beyond the Nyquist criteria, the CS technique was presented as a novel method to significantly increase SNR of MR images per scan time as long as data sparsity presented in a certain domain[251]. Thanks to its sparsity in the image domain, ^{19}F MRI has also been demonstrated as a rational application for CS[253]. In this study, we adjusted and applied different existing CS reconstruction algorithms for ^{19}F MR images by both offline simulation and online acquisition for the first time. More importantly from a practical point of view, as for most ^{19}F MRI applications, only low SNR

images are dealt with. We focus on low SNR datasets, which is considered to be a challenge for applying CS. For both, phantom and *in vivo* fully sampled dataset simulation, we found that CS is efficient in reducing the image acquisition time by a factor of 3-4 without seriously affecting SNR regardless of algorithms used in this study (except for the less performing CoSaMP algorithm). Furthermore, in CS acquisition experiments, we show that the four-fold gain in scan time by using CS could be used to increase scan averages by four times and hereby detect signal that might be otherwise missed by conventional MR acquisition. Overall, different types of CS algorithms have been evaluated and demonstrated to be applicable for ^{19}F MRI applications with similar reconstructed image quality. Among different algorithms, the two-level L1 method has best performance if the computational time is also taken into account. CS could be either used to dramatically reduce scan time of low SNR ^{19}F MRI signal or detect more potential signals within the same scan time, thus broaden the application of ^{19}F MRI in terms of less cell/compound injection or lower field strength, which is in particular of interest for clinical applications. We have shown CS simulation (3D) and CS acquisition experiments (2D), which also demonstrate the beneficial effect for low SNR ^{19}F MRI applications for both, 2D and 3D images.

The CS reconstructed ^{19}F MR image is affected by different factors. A previous study showed that the under sampling factor is the most important one, which can reach eight-fold[253]. As we only dealt with low SNR images, only 3- to 4-fold is feasible without signal degradation. Nevertheless, this is still the most crucial factor to be considered as it is directly linked to the effectiveness of the CS technique. It should also be noted that the RARE sequence used for the PFCE particles in our study (T1/ T2 = 1000ms/ 350ms) is suitable but was not further optimized. According to Schmid et al., a bSSFP sequence should further increase the SNR/ t for this T1/ T2 combination of PFCE particles[181].

The feature size of SOI was also considered important. However, in this study, similar results were obtained for most algorithms by comparing similar SNR level (SNR ~ 7/8) of both *in vitro* and *in vivo* simulation datasets (Fig. 4.1 and Fig. 4.3) with different image features. Despite the similar SNR level, the image pattern between two datasets used in the simulation study is quite different in terms of signal distribution. Although, the accuracy of *in vivo* reconstructed signal was a marginally better than the *in vitro* dataset in our case, the very similar results obtained from both studies confirms the robustness of different algorithms for performing CS construction on different low SNR images. Further confirmation is also needed by applying this approach to more datasets from different applications. On the other hand, a different under-sampling pattern plays an important role as a relatively high standard deviation is obtained by using a random selected under-sampling pattern (Fig. 4.2 and Fig. 4.4). This suggests that prior knowledge about the signal distribution in k-space may further improve the CS reconstruction results. Other parameters, such as physiological motion and presence of residual respiratory motion may also contribute to CS reconstruction. However, proof-of-principle *in vivo* CS acquisition experiments show that this will not necessarily result in significant differences.

Different algorithms have been applied in this study. By comparison with the gold standard (SPARSEMRI), we conclude that most algorithms have similar performance in terms of normalized SNR/ scan time. However, SPARSEMRI does give better results for conserving the feature of SOI as shown by calculating the difference between reconstructed and fully sampled images, in particular for the high SNR SOIs. This may be explained by the additional use of TV constraints in SPARSEMRI, which constrains reconstruction under the assumption that the ^{19}F MR image has only few numbers of intensity variations between neighboring pixels. Nevertheless, the mean error is

limited within 5%, which will not severely affect the interpretation of SOI. The other algorithms can enhance their performance if the TV constrains are properly incorporated. If taking computation time into account, the newly developed two-level L1 method is considered the fastest one, which can finalize a 2D dataset reconstruction within 0.1 seconds. This is of benefit if large amount of data need to be processed.

Although different algorithms were compared in this study, only basic regularization terms were included, such as L0-norm and L1-norm minimization term. To further improve CS reconstruction quality of these algorithms, additional regularization terms can be introduced, such as phase constraints[332], geometry constraints[333] and more generic forms of constraints[334]. As already mentioned, the under sampling pattern also plays an important role in CS. As in this study, only Cartesian k-space sampling in two phase encoding directions was applied, which indicates that there is still room for improvement. As shown by others before, non-Cartesian k-space sampling patterns (radial[335,336] and spiral sampling[337]) and Bayesian selection[338,339], which intrinsically sample densely near the k-space center, may optimize the random k-space trajectories and improve the CS results.

Attention needs to be paid in future studies to some limitations that have not been addressed in our study. As discussed by Zhong et al., the noise distribution of the CS reconstructed image remains undefined, indicating that this need to be addressed further[253]. Although, we assume in this work that the noise is spatially of homogeneous Gaussian distribution, we realized between different algorithms that the noise pattern seems to be altered to a small extent, which may have an effect on the accuracy of CS quantification. Furthermore, as we worked with low SNR datasets, further corrections for the bias created by the Rician distributed noise may further improve our results[340].

Overall, we have shown in this study that different existing CS algorithms could be effectively used for low SNR ^{19}F MRI applications. The gain in reducing scan time is about four-fold for our applications. This gain could be used of for two aspects, either for the reduction of scan time or the increase of averages to potentially detect otherwise undetected signal when compared with conventional ^{19}F MRI acquisitions. Reducing scan time would be beneficial especially for clinical applications, while increasing SNR would be particularly useful for experimental longitudinal *in vivo* studies with the perspective of better quantification and for *ex vivo* applications with low retention of ^{19}F MRI signal. Hereby, the tracking and quantification of engrafted pancreatic islets is a feasible application. As pancreatic islets consist of more than one thousand cells, it would be feasible to even visualize a single islet *in vivo*, considering detectability threshold for ^{19}F MRI based cell tracking reported in the literature[190,341]. It remains to be proven to what extent quantitative ^{19}F MRI is representative for the number of engrafted cells[68,342]. Using CS in ^{19}F MRI, scan time limitations should become less of a problem than with conventional acquisition schemes.

4.4 Experimental

4.4.1 Perfluorocarbon particles

For pre-labeling purposes of beta cells and pancreatic islets, PFCE containing cationic liposomes were prepared according as reported previously[318].

4.4.2 Rodent pancreatic islets/ beta cell isolation and labeling

The pancreatic islets used in this study were isolated from Wistar rats (female, 8-10 weeks, 200-250g) using the collagenase digestion method[343]. After isolated islets were handpicked and counted, they were cultured in RPMI-1640 medium (+ L-Glutamine, Gibco, Ghent, Belgium) supplemented with 10% fetal bovine serum (FBS, Hyclone, Aalst, Belgium) and 1% penicillin/streptomycin (Cellgro, Manassas, USA). PFCE particles were also added for labeling purpose (final ^{19}F concentration: 10 mM). Islets were incubated with PFCE particle for 24 hours and then washed three times with phosphate buffered saline (PBS). Labeled islets were then used for preparing phantom for in vitro ^{19}F MRI and for subcutaneous transplantation in vivo. The pancreatic beta cell like INS-1E cell line was a kind gift from C.B. Wollheim (Department of Cell Physiology and Metabolism, University Medical Center, Geneva, Switzerland). Those cells were cultured in RPMI-1640 medium (+ L-Glutamine, Gibco, Ghent, Belgium) supplemented with 10% fetal bovine serum (FBS, Hyclone, Aalst, Belgium), 10 mM Hepes (Sigma, Bornem; Belgium), 1 mM sodium-pyruvate (Gibco), 0.05 mM 2-mercaptoethanol (Gibco) and 1% penicillin/ streptomycin (Cellgro, Manassas, USA). INS-1E cells underwent a similar labeling and incubation procedure as for islets, and were used for parts of CS in vitro acquisition experiments.

4.4.3 Conventional data acquisition for assessment of simulations

In vitro ^{19}F MRI phantom

A phantom was prepared by filling PFCE labeled islets (n = 200) suspended in 2% agar, pure PFCE particles (25 mM, positive control) and PBS (negative control), respectively into three Eppendorf tubes. All three Eppendorf tubes were then placed parallel in a 25 ml plastic cylinder with a 2.8 cm diameter containing 2% agarose. As only a limited amount of labeled islets (n = 200) was used, a low SNR was expected for the ^{19}F MR image of the Eppendorf tube containing labeled pancreatic islets.

In vivo subcutaneous transplantation model

For *in vivo* studies, subcutaneous engraftment at the right thigh was used for islet transplantation. All animal experiments were executed in accordance with national and European regulations and approved by the Animal Ethics Committee of the KU Leuven. Male C57BL/6J mice were anesthetized with a ketamine 1000 (CEVA, Brussels, Belgium)/ domitor (Janssen Pharmaceutica, Beerse, Belgium)/ saline cocktail via intraperitoneal injection. Similar to our *in vitro* phantom experiments, the same amount of PFCE labeled islets (n = 200) was collected in an insulin syringe (in 50-100 µl medium) and subcutaneously transplanted at the area of the right hind leg. After the engraftment, animals were scanned immediately by MRI.

MR acquisition

All MR experiments were performed using an 9.4 T Bruker Biospec small animal MR scanner (Bruker Biospin, Ettingen, Germany) equipped with a home built saddle shaped surface coil, which was tuneable and matchable to both the ^{19}F and ^{1}H MR resonances.

For all *in vivo* imaging sessions, the body temperature and respiration rates of the animals were monitored using a rectal probe and a pressure sensitive pad placed underneath the thorax. A monitoring and gating model (type 1030) from SA Instruments (Stony Brook, NY, USA) was used to regulate and maintained the body temperature and respiration rate of the animal at reasonable physiological ranges of approximately 37 ℃ and 80-120 breaths min^{-1}, respectively.

For simulation purpose, fully sampled *in vitro* phantom and *in vivo* ^{19}F MR images were acquired using an 2D RARE sequence with the following parameters: TE/ TR = 15.9 ms / 1 s, RARE factor = 8, FOV = 6.4 x 6.4 cm (phantom) / 8 x 4 cm (in vivo), matrix size = 64 x 64 (phantom) / 50 x 50 (in vivo), NA = 256, slice thickness = 2.5 mm, total acquisition time ~ 30 mins. Different under sampling factors (UF = 2, 4, 8) were used. The sampling pattern was generated by the SPARSEMRI[251] built in function with a polynomial power (p) that increased monotonically with UF (p = 5 for UF =2 to p = 7 for UF = 8).

4.4.4 Compressed Sensing data acquisition

In vitro ^{19}F MRI using a phantom

Similar to the phantom made for simulation experiments, four Eppendorf tubes were placed parallel in a 25 ml plastic cylinder containing 2% agarose. In this case, instead of pancreatic islets, different concentrations of PFCE labeled INS-1E cells ($1*10^4$ cells/ mm^3, $5*10^3$ cells/ mm^3, $2.5*10^3$ cells/ mm^3, $1*10^3$ cells/ mm^3) were used. According to previous experience, low SNR was expected for the ^{19}F MRI signal even for the cases with the highest cell concentrations due to the relative low uptake of PFCE by INS-1E cells (~10^{12} ^{19}F spins per cell)[341].

In vivo MRI studies

Again, subcutaneous engraftment at the right thigh of male C57BL/6J mice was used for islet transplantation with 500 PFCE labeled islets in an insulin syringe (in 50-100 µl medium).

CS MRI acquisition

For CS *in vitro* data acquisition, MR images were acquired using CS k-space sampling with an 3D gradient echo (FLASH) pulse sequence, which was developed to incorporate a predetermined phase encoding gradient table yielding a pseudorandom, non-uniform sampling pattern that emphasized the k-space center. Imaging parameters were: TE/ TR = 5/ 100 ms, NA = 16, FOV = 6.4 x 6.4 x 6.4 cm^3 and matrix size = 64 x 64 x 64 with UF = 4 and a total scan time of ~ 20 mins. In addition, both a fully sampled dataset using the same parameters and a CS sampled dataset with quadruple number of averages were also acquired, which resulted in a four-fold increase in scan time for both cases.

For CS *in vivo* data acquisition, the animal was scanned using a ^{19}F 2D RARE sequence by pseudo-random, non-uniform under-sampling the phase direction using the following parameters: TE/ TR = 15.9 ms / 1 s, RARE factor = 8, FOV = 6.4 x 3.2 cm, matrix size = 128 x 64, NA = 256, slice thickness = 2.5 mm with UF = 4, resulting in a total scan time of ~ 20 mins. In addition, fully sampled datasets

(UF = 1) were acquired using the same NA (resulting in a four-fold increase in scan time) or a quarter of the NA (NA= 64; resulting in the same scan time).

For both *in vitro* and *in vivo* CS acquisition, half of the acquired k space lines were selected from the center of k space, while the other half were randomly picked outside k space center.

4.4.5 CS Reconstruction and Signal Quantification

At least five major classes of image reconstruction using CS were previously described, including greedy pursuit, convex relaxation, Bayesian framework, non-convex Lq optimization ($0 \leq q < 1$) and Brute force[344]. As the Bayesian method does not offer theoretical guarantees and the Brute force method only remains plausible for small-scale problems[344], we have applied only algorithms belonging to greedy pursuit, convex L1 optimization and non-convex Lq optimization for comparison purposes in this study.

SPARSEMRI is a traditional convex method using a non-linear conjugate gradient descent algorithm with backtracking line search. It was the first CS algorithm for MRI applications introduced by Lustig et al[251]. It also serves as gold standard algorithm in this study. Briefly, the objective function of this algorithm is used to minimize the combination of L1-norm and total-variation (TV) with the constraint to enforce data consistency. Minimization of L1 norm results in promoting sparsity while minimization of TV norm results in finite-differences sparsity. The parameter α is also included to trade these two norms.

Iterative reweighted L1 minimization (IRWL1) is a non-convex method proposed by Candes et al[330]. IRWL1 iteratively updates the weights of the weighted L1 norm until convergence or the number of iterations meets a predefined parameter l_{max}. Although this algorithm solves a convex optimization problem on each iteration, globally it attempts to find a local minimum of a concave penalty function, which resembles the L0 norm.

Two-level L1 minimization is a newly developed algorithm, which approximates the reweighted L1 method[331]. The major difference between two-level L1 minimization and reweighted L1 minimization is to set weights according to the order not the value, hence the sparsity is enhanced and penalties become piecewise linear. By focusing on the order instead of magnitude, the computational time will be reduced. Similar as for IRWL1, the stopping criteria, maximum iteration number or level of 'convergence' are pre-defined.

Greedy pursuit belongs to another promising class of algorithms for sparse approximation by iteratively refining one or more components that yield the greatest improvement in quality. In this study, one of them called OMMP has been chosen[328]. OMMP is an extended version of one of the earliest greedy pursuit methods, Orthogonal Matching Pursuit (OMP). Like for all typical implementations of OMP, the identification step of OMMP to find the correct index is the most expensive step for computation time. However, OMMP has proven to be able to find at least one correct index at each iteration while OMP could only find one. Several stopping criteria are possible: fixed number of iterations, threshold residual or if no more correct index could be found.

Compressive Sampling Matching Pursuit (CoSaMP) is another greedy pursuit method[329]. Compared with traditional OMP methods, some enhancements are included, such as multiple selections at each iteration, iteratively solving the least squares problems and pruning active selections. Restricted

Isometry Property (RIP) could also be applied for a theoretical analysis with more control, which may elongate the computation time. The stopping criteria of CoSaMP are similar to OMMP.

All algorithms were implemented and used to reconstruct images from compressive measurements in MATLAB (MATLAB R2013a, MathWorks, Eindhoven, Netherlands). As ^{19}F MR images are considered sparse in the image domain, no sparse transformation is needed here. The stop criteria were set the same at 10^{-6} for different algorithms in order to compare the time efficiency.

The signal intensity of reconstructed ^{19}F MR images were linearly rescaled from an arbitrarily large scale to the range of [0, 1] by normalizing every voxel to the maximum intensity voxel in the FOV. For ^{19}F MRI signal quantification, the same signals of interest (SOIs) were delineated for images of the same experiment reconstructed by different algorithms. The SNR was calculated by dividing the average signal intensity in the delineated SOI by the standard deviation of background noise intensity distant from the SOI. The SNR estimated from CS reconstructed images were then further normalized to the SNR obtained from fully sampled data. Although, noise will not necessarily follow a bivariate Gaussian distribution in CS images as CS methods use non-linear reconstructions with regularization terms, we have still used conventional methods for SNR calculation as the influence on the actual comparison might be minimal.

The relative difference of reconstructed SOI to the fully sampled image in simulation studies were calculated by dividing the mean value of fully sampled SOI by the difference between the mean values of CS reconstructed and fully sampled SOI. A non-parametric Mann-Whitney U test (Prism 5, GraphPad Software, La Jolla, CA, USA) was used for statistical analysis by comparing different algorithms with our gold standard (SPARSEMRI) SNR values and relative difference to the fully sampled image.

Sayuan Liang designed the experiments, acquired original image data, tested different CS algorithms for comparison and validation. He also performed pulse sequence, did data post-processing and prepared the original draft of the paper with further reviewing and editing.

Chapter 5. Visualization of delayed release of compounds from pH-sensitive capsules in vitro and in vivo in a hamster model

This Chapter has been compiled based on the following publication

Staelens D., Liang S.*, Appeltans B., Van de Wouwer M., Van den Mooter G., Van Assche G., Himmelreich U., Vande Velde G. (2016).* ***"Visualization of delayed release of compounds from pH-sensitive capsules in vitro and in vivo in a hamster model."*** *Contrast Media & Molecular Imaging, 11, 24-31. (* Authors contributed equally)*

5.1 Introduction

Controlled release of therapeutic compounds at the disease location is a strategy that aims for a local effect and more precise targeting of pathological processes. It is anticipated that oral administration and delivery of therapeutic compounds directly inside the intestine (also called luminal delivery) can have considerable advantages over systemic administration. These include lower concentrations of drug needed, which reduces costs and lowers systemic side effects[345]. One example where targeted delivery to the gastrointestinal tract could improve outcome is the controlled and localized release of antibodies targeting virulence factors against Clostridium difficile associated disease, which accounts for 71% of gastrointestinal nosocomial infections, but has currently a cure rate of only 70% with standard systemic administration of antibiotics[346-349].

This situation and other clinical settings may benefit from an approach where therapeutic compounds are enclosed within a capsule for oral administration, designed to release its content only when it reaches its target location, in this case the small intestine. The pH in the human gastrointestinal tract increases progressively from the stomach (pH 2-3), the small intestine (pH 6.5-7) to the colon (pH 7-7.8)[350], with intra- and inter-individual differences. This makes it possible to coat a capsule with a polymer that is resistant to low pH and thus passes the stomach and dissolves at increased pH in a specific part of the gastrointestinal tract. Targeted drug release by capsules coated with pH-sensitive materials has been described for a wide variety of cases[351]. A rise in pH induces dissolution or swelling of the polymers, thereby leading to a disruption of the capsule coating, resulting in the release of its content[352].

Delivery of a drug inside the gastrointestinal tract can be analyzed with a variety of techniques including enzyme-linked immunosorbent assay and mass spectrometry on luminal content[353,354]. Nevertheless, these techniques have the disadvantage that animals need to be sacrificed for sample collection. Moreover, these approaches only provide snapshot data on the location and physical integrity of the capsule at the moment of sacrifice, and lack information on compound release. The existing non-invasive option, i.e. measuring drug levels in fecal samples, lacks information on the exact site of release. To validate and optimize controlled release strategies and enable translational studies evaluating these novel therapeutic approaches, there is the need for a sensitive, non-invasive method to longitudinally evaluate capsule integrity, the anatomical location and the (early) release of compounds.

Different medical imaging modalities have been applied frequently in both clinical and pre-clinical research providing new perspectives for biomedical research[17]. Despite differences in resolution, sensitivity, penetration and safety, the main advantage of imaging techniques is that they provide non-invasive, non-destructive and direct information both *in vitro* and *in vivo*. As such, gamma scintillation is frequently used as an imaging technique in clinical research for controlled release studies[355,356]. It offers good sensitivity and a relatively simple procedure for acquiring images to follow capsule movement by means of a radioactive tracer that is included in the capsule just before administration. A potential concern with this technique is the need of gamma emitting radionuclides, which may hinder longitudinal monitoring due to their restricted half-lives and involve possible safety issues. Furthermore, the low resolution and the lack of anatomical background information make it difficult to interpret the images. Alternatively, endoscopy has also been applied for direct visualization of intraluminal drug delivery studies in humans[357]. Although this technique could provide direct information regarding time and place of capsule rupture, dispersion characteristics and the surrounding physiological environment, the investigation with the large encapsulated camera is intrusive and offers only a limited field of view.

In a preclinical research context, there is even more need for a sensitive, non-invasive approach to evaluate controlled release in the 3D-context of the animal's anatomy. MRI and CT are valuable imaging modalities, employed in a wide range of studies thanks to their ability to provide 3D anatomical images with excellent resolution and without the need for radioactive tracers[17]. Especially MRI has been employed in pharmaceutical studies as it is devoid of any ionizing radiation[358,359]. Due to its relatively low sensitivity, conventional contrast agents such as superparamagnetic iron oxide and paramagnetic gadolinium/manganese are frequently used to enhance the contrast against the background[72,360,361]. However, the contrast generated by those agents is not directly quantifiable and not always unambiguous due to similar intrinsic contrast changes, in particular in the abdomen. This can be overcome by the use of ^{19}F-containing contrast agents. These have shown to be complementary to the acquisition of traditional proton-based, anatomical images (^{1}H-MRI)[342]. Due to the lack of MR-detectable ^{19}F signal inside biological tissues, all signal from ^{19}F-MRI origins from the (dissolved) contrast agent, which makes the technique very specific and quantifiable[68]. In this study, 2-fluoro-2-deoxy-D-glucose (^{19}F-FDG) is used as contrast agent for ^{19}F-MRI as it is only MR-detectable when dissolved in water and, as a glucose analog, is considered to be safe[362]. On the other hand, barium sulphate ($BaSO_4$), based on the high atom-number and hence high x-ray absorption of barium, is used as a CT contrast agent for gastrointestinal tract imaging to increase the contrast between the gastrointestinal contents compared to the surrounding soft tissues[363,364]. Moreover, $BaSO_4$ can be safely used for oral administration because of the absence of toxicity[41].

By loading the pH-sensitive capsules with both contrast agents and by combining CT and ^{19}F MRI, we hypothesized that the ^{19}F-MRI FDG signal would provide information on early permeability of the capsule material to water and its location, while the $BaSO_4$ contrast and the CT images can be used to monitor capsule integrity and the exact anatomical location of the site of release.

In this study, we evaluated the ability of this dual imaging approach as a tool to evaluate the resistance of coated capsules at different pHs *in vitro* and *in vivo* after oral administration to hamsters. The objective is to combine different imaging modalities to non-destructively and longitudinally visualize and explore the kinetics of controlled release under different conditions.

5.2 Results and Discussion

5.2.1 In vitro imaging

In a first set of experiments, we conducted *in vitro* studies to investigate the resistance of coated capsules at different levels of acidity (pH = 1, 3, 5 and 7) with both MRI and CT (figure 5.1 and 5.2, respectively). For MR imaging, the ^{19}F signal was overlaid with the anatomical ^{1}H image. At the first time point, one hour after the capsule was added to the solutions, the capsules at pH 5 and 7 showed quantifiable ^{19}F-FDG signal (figure 5.1A). This indicates that the surrounding solution enters into the capsule and dissolves some of the otherwise not visible, encapsulated ^{19}F-FDG, which was then picked up by ^{19}F-MRI. This is in contrast to the capsules at low pH (pH 1 and 3), where the ^{19}F-MRI signal could only be seen after one hour and a half (figure 5.1D), which indicates that the coating has more resistance at lower pH than at higher pHs. In the timeframe of 2-4 hours, for the capsules at all pHs, maximal signal intensity was reached, albeit at different time points (figure 5.1B and 5.1D). The time point, at which the maximal signal intensity was reached, depended on the extra-capsular pH. The lower the pH, the longer the time needed to fully dissolve the ^{19}F-FDG (figure 5.1D). In general, the ^{19}F-MRI signal was first limited to the area of the actual capsule, indicating that although the ^{19}F-FDG inside the capsule was dissolved, the exchange with the extra-capsular space was slow. After the ^{19}F-FDG peak intensity reached a maximum, the signal gradually decreased (figure 5.1D). This process could be explained by the gradual diffusion of the ^{19}F-FDG outside the capsule, which was confirmed by a rise in signal intensity observed in a MRI slice outside the capsule but inside the micro-centrifuge tube (figure 5.1E). Later, this process is further accelerated by the degradation of the capsule. The signal intensity ratio between the intra- and extra-capsular spaces reached equilibrium after 8-10 hours (depending on the pH). A macroscopic examination of the phantom after the MRI session confirmed that the capsules were degraded and their content dissolved.

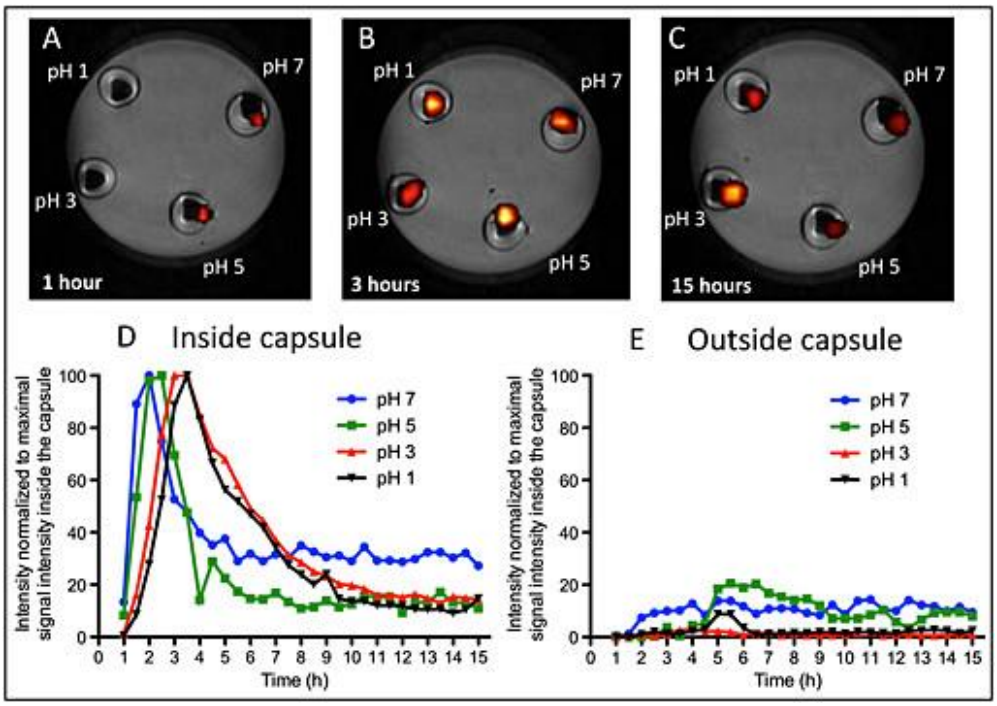

Fig. 5.1 *In vitro* ^{19}F-MRI monitoring. Coated capsules containing ^{19}F-FDG in microcentrifuge tubes containing solutions of different pH were monitored for 15 h by ^{19}F-MRI. The time to reach the maximum signal intensity depended on the pH in which the capsule was incubated. The ^{19}F NMR signal

was first detectable in the capsules incubated at the highest pH. After three h, a signal was observed for all capsules incubated within the pH range 1–7. (A)–(C) Representative ^{1}H-MRI slices (gray scale) are overlaid with the corresponding ^{19}F signal (red-hot scale, scan time ~ 30 min) after 1 (A), 3 (B) and 15 h (C) in the solution. The same ^{19}F-MRI signal intensity threshold was set manually for all images. (D), (E) Quantitative ^{19}F-MRI signal inside (D) and outside (E) the capsule of a representative slice based on the ^{1}H-MRI image. Time resolution is 30 min for the different pH values. The signal intensities are normalized to the maximum signal intensity (=100%) of the slice inside the capsule. Signal intensities were retrieved from locations corresponding to the intra-capsular space (D) or from a slice outside the capsule (E).

More information about the structure of the capsule with higher spatial and temporal resolution was acquired by performing CT of capsules containing $BaSO_4$ (figure 5.2). The time span of the longitudinal scans that were acquired from the same material as for the MRI experiments was limited to 8 hours. The results of the CT imaging clearly showed the degradation of the capsule after 230 minutes in pH 5 and 7. The red arrowheads in figure 5.2 indicate the site of the capsule where degradation was first observed. This confirms the observation that the coated capsules are resistant to low pH. The physical degradation could be clearly visualized leading to the loss of contrast from the capsule material (see arrows in figure 5.2). The degradation of the capsule coincided with the accumulation of $BaSO_4$ on the bottom of the micro-centrifuge tube. Based on these results, CT imaging provides additional information about the later event of physical capsule degradation after the early increased permeability that was observed by MRI. The fact that there is no clear difference between the timing of degradation at pHs 5 and 7 does not conflict with the strategy to achieve a controlled release upon transit through the stomach, which normally has a lower pH. A complete degradation of all capsules at pH 1 was only observed after 400 minutes.

Based on the data acquired from the *in vitro* assessment of the low pH resistance of the coated capsules, we showed that MRI and CT result in complementary data regarding both permeability of the capsule to water and degradation of the capsule. Moreover, we demonstrated the resistance against low pH for up to 2 hours by MRI and CT, which overcomes the normal transit time of the stomach[365].

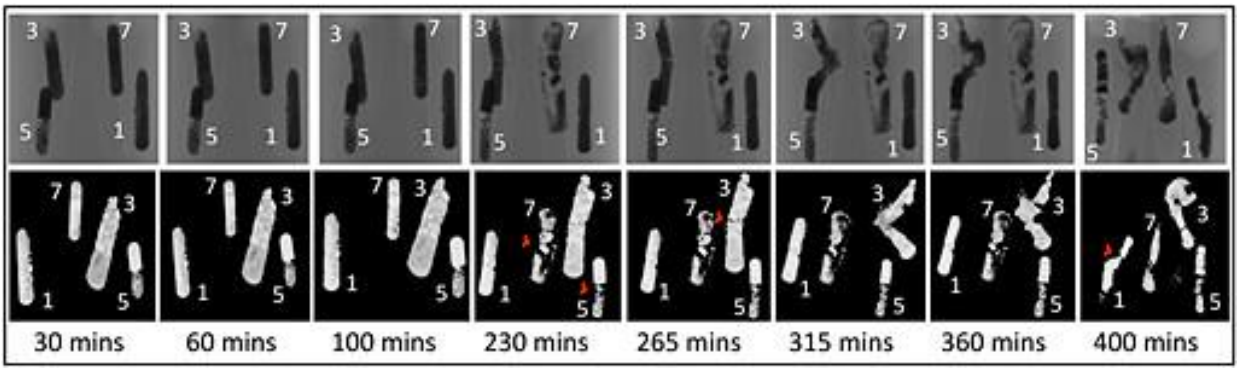

Fig. 5.2 *In vitro* CT monitoring. Coated capsules containing BaSO4 in microcentrifuge tubes containing solutions at different pH values (indicated in the figure by 1, 3, 5 and 7) were monitored for 8 h by CT. Upper row, longitudinal 2D projection images; bottom row, corresponding 3D volume-rendered reconstructed images. Capsule disintegration occurred after 230 min at pH 5 and 7, whereas at pH 1 the capsule only disintegrated after 400 min. Note that all capsules have the same size; the apparent different size between different capsules is due to the 3D rendering viewing angle. The red arrows indicate the site in the capsule where the first clear indication of degradation is observed.

5.2.2 In vivo imaging

In a next set of experiments, we longitudinally monitored capsules containing both ^{19}F-FDG and $BaSO_4$ using *in vivo* MRI and CT after oral administration to hamsters. In all animals, a clear ^{19}F-MRI signal was observed in the stomach 2 hours after administration (figure 5.3A-C). The extent of the detected ^{19}F-MRI signal was within the range of the physical size of the capsule based on the ^{1}H-MR images. This indicates that fluid from the stomach entered into the capsule and dissolved the ^{19}F-FDG. However, the capsule was not disintegrated. This is in line with the *in vitro* results. Figure 5.3D shows that after 5 hours, there was no detectable ^{19}F-MRI signal due to the degradation of the capsule leading to the release of ^{19}F-FDG from the capsule and further dilution of the ^{19}F-MRI signal below the detectability threshold. Non-localized *in vivo* ^{19}F NMR spectra of the abdominal cavity show similar signal amplitudes at these two time points, which confirmed that the total amount of ^{19}F -FDG inside the animal remains at a similar level but is no longer entirely localized in the capsule after 5 hours (figure 5.3E). The ^{19}F NMR spectra in figure 5.3E were generated by using a non-localized single pulse sequence instead of the localized PRESS sequence to cover the whole field of view. Quantification of the ^{19}F-signal normalized to the signal at the 2 hour time point confirms almost constant signal intensity (100 % vs. 97 %, insert in figure 5.3E).

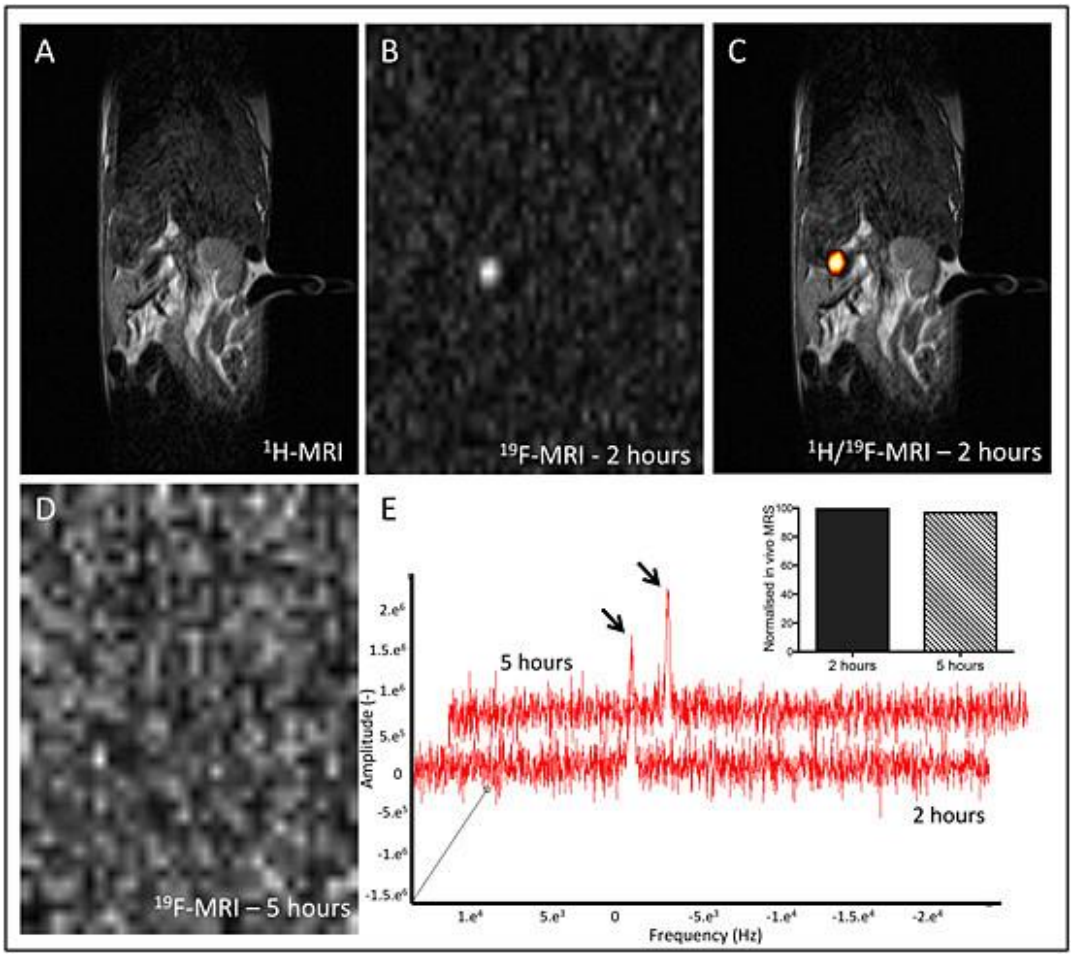

Fig. 5.3 *In vivo* MRI monitoring of the ^{19}F-MR signal in the digestive tract of hamsters. Coated capsules containing ^{19}F-FDG and $BaSO_4$ were administered to hamsters and subsequently visualized by ^{19}F-MRI. (A) Representative 1H-MR image slice visualizing the stomach; (B) corresponding ^{19}F MR image (grey scale, scan time ~ 30 min) 2 h after oral administration of the capsule (grey scale); (C) composite of (A) and (B) (with the ^{19}F MR image red-hot scaled with a manually set threshold), illustrating that after 2 h

a ^{19}F signal clearly localizes in the stomach. (D) Corresponding ^{19}F-MR image 5 h after capsule administration (grey scale) that shows the absence of detectable localized signal, indicating the complete disintegration of the capsule and uptake of ^{19}F-FDG. (E) Non-localized ^{19}F-NMR spectra acquired by a pulse–acquisition sequence from the abdominal region at the same 2 (lower spectrum) and 5 h (upper spectrum) time points. The inset shows the quantification of the MR spectrum normalized to the signal at the 2 h time point. These data illustrate that the total signal intensity of ^{19}F-FDG inside the body has not changed. However, it is more dispersed, resulting in the absence of a localized ^{19}F-MRI signal after 5 h. The two ^{19}F MR spectra were purposely shifted to enable better visualization and discrimination between the two spectra.

CT of the same capsule and animal was also used for the localization of the capsule and the assessment of the integrity of the capsule (figure 5.4). The $BaSO_4$-containing capsule was clearly visible in the stomach right after administration, even from a 2D, non-reconstructed projection image (figure 5.4A). The early events of increased permeability of the capsule, as was seen by ^{19}F-MRI, could not be visualized by CT. On the other hand, a clear degradation of the capsule and the release of the mainly non-dissolved $BaSO_4$-content into the stomach were observed after 6 hours (figure 5.4B-D). CT using $BaSO_4$ gives anatomical information with good sensitivity and high resolution both spatially and temporally. It provides positive contrast from the beginning until the degradation of the capsule and enables imaging of release of the solid capsule content into the gastrointestinal tract. The insolubility of barium salts has particularly the advantage that the contrast agent is trapped in the gastrointestinal tract resulting in reduced toxicity.

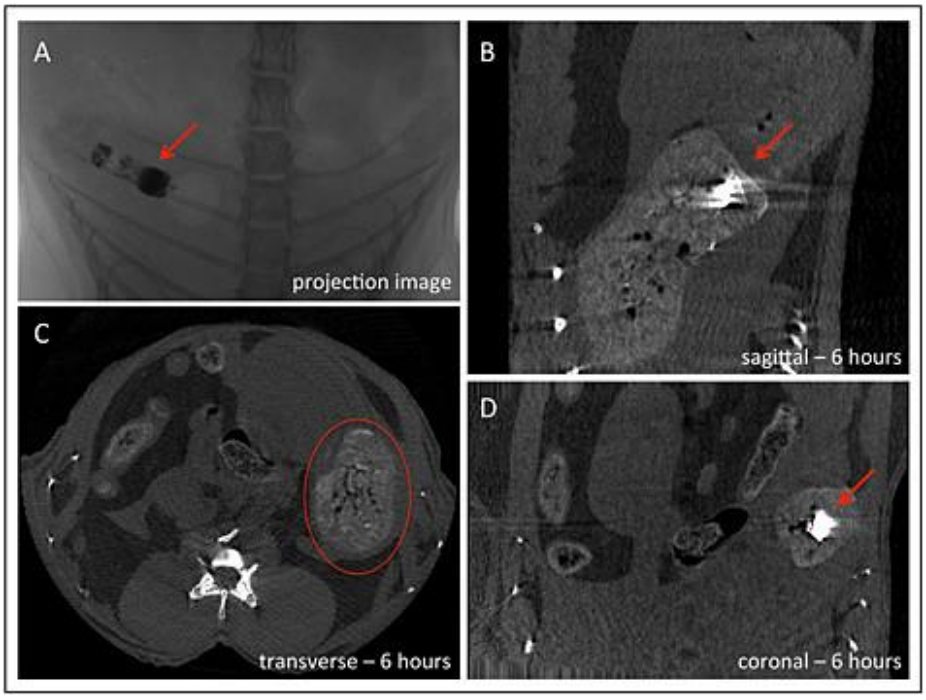

Fig. 5.4 CT of the capsule localized in the stomach. Coated capsules containing ^{19}F-FDG and $BaSO_4$ were administered to hamsters and subsequently visualized by CT. The stomach is filled with contrast agent 6 h after administering the capsule. (A) 2D projection image of a capsule (red arrow) directly after administration, showing the intact capsule at the level of the stomach. (B)–(D) Reconstructed image 6 h after administration of sagittal view (B), transverse view (C) and coronal view (D), illustrating the disintegration of the capsule inside the stomach. The red arrows indicate the location of the capsule inside the stomach, encircled in red in (C). The stomach content is hyper intense due to $BaSO_4$ released from the capsule.

The *in vivo* findings verify our *in vitro* results that the coated capsule could resist the low pH environment of the stomach without degradation for at least two hours. During this time, the location and integrity of the capsule can be monitored with CT, for both cases where the capsule remains trapped in the stomach for 6 hours (3 out of 4 hamsters tested), or passes the stomach and reached the small intestine (1 observation), 3 hours after administration (figure 5.5), consistent with previous studies in rats regarding capsule size and gastric retention[364,366]. When ^{19}F-FDG is dissolved, diffused out of the capsule and taken up by cells/ in the blood stream, it leads to the loss of a clearly localized ^{19}F-MRI signal (figure 5.5A). The feeding status of animals is a known factor that influences the transit of capsules[364]. In our study, all animals were in a fed state. Another important aspect is the time during the day (activity vs. resting phase) when the capsule was administered. In this study, hamsters were dosed with the capsules during the light cycle. However, we did not observe any difference in transit time when the capsules were administered during the dark cycle (n=2, data not shown).

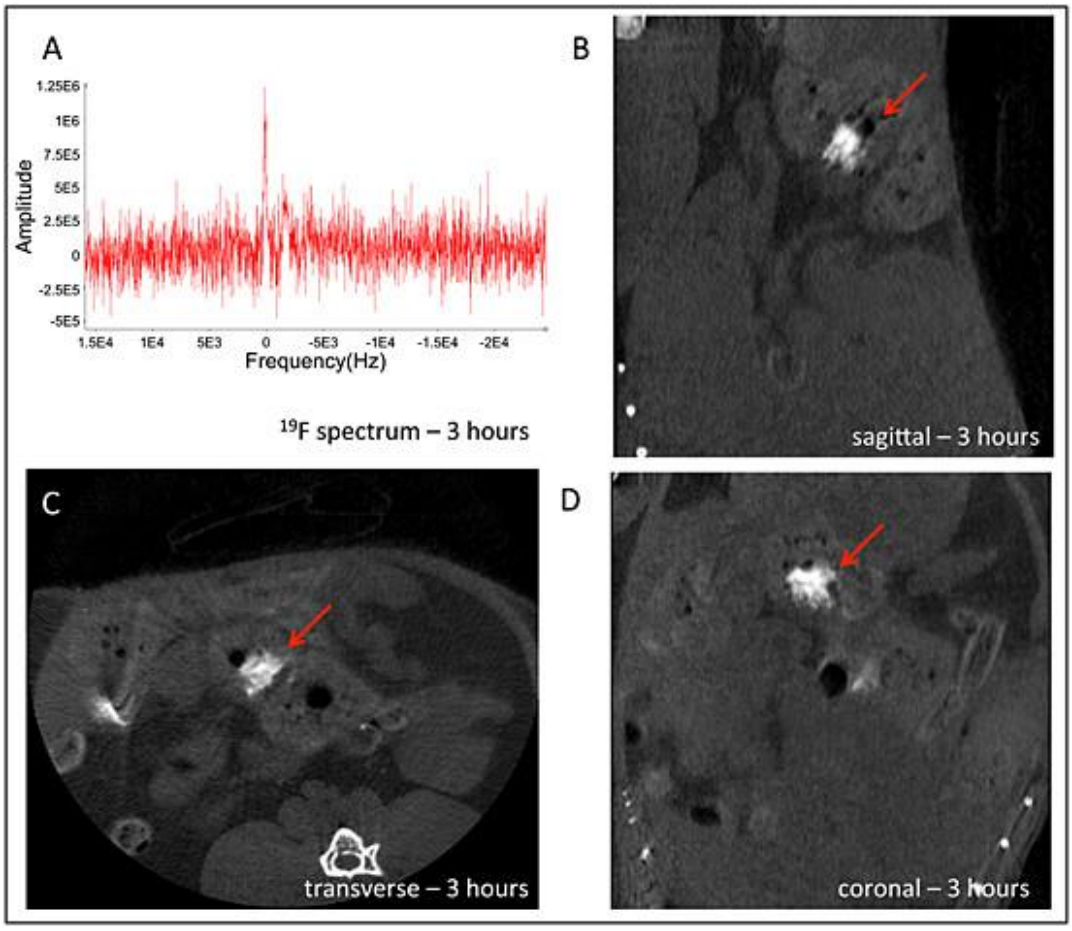

Fig. 5.5 CT and MRI of the capsule localized in the small intestine. A coated capsule containing ^{19}F-FDG and $BaSO_4$ was localized (red arrow) in the small intestine 3 h after administration. (A) The ^{19}F-NMR spectrum shows the presence of ^{19}F-FDG inside the body (the arrow indicates the ^{19}F peak). (B)–(D) Reconstructed CT image of sagittal (B), transverse (C) and coronal views (D), demonstrating the presence of capsule remains and released $BaSO_4$ in the small bowel of the hamster.

The dual-modal imaging approach proposed in this study could in principle be applied to any other studies of controlled release from capsule material, as both CT and MRI are readily available in modern clinical and pre-clinical environments for routine diagnosis and research purpose. Barium sulfate enhanced CT has already been used for gastrointestinal tract imaging to increase the contrast between the gastrointestinal contents compared to the surrounding soft tissues[364] due to the high atom-

number and hence high x-ray absorption of barium. Furthermore, barium sulfate can also be safely used for oral administration because of the absence of toxicity[41].

On the other hand, to the best of our knowledge, this is the first time that ^{19}F-MRI was applied for controlled release studies from capsule material in an animal model. Thanks to its high specificity and quantitative feature, ^{19}F-MRI used in this study provides detailed information to better understand the early events of capsule degradation, starting with an increase in permeability leading to an influx of liquids. Due to the relatively low sensitivity of MRI and the relatively low concentrations of ^{19}F-FDG, ^{19}F-MRI as applied in our study has only a temporal resolution in the order of 30 minutes and does not provide information on the capsule itself once the ^{19}F-FDG has been released. Optimization of the magnetic resonance pulse sequence could be a key to reduce the scan time. This was shown to result in similar signal-to-noise ratio but reduced scan time, which should be further explored by analyzing the characteristics of ^{19}FDG[342]. Recently, compressed sensing is also considered a reliable reconstruction technique to speed up the MRI scanning. According to Zhong et al., by under-sampling the k-space factor of 8, compressed sensing could still retrieve the image with a similar signal-to-noise-ratio[253]. Other methods including different coil set-ups and higher field strength could also be considered as potential ways to improve the sensitivity of the technique, reducing scan time and thus improving temporal resolution. The ^{19}F-MRI technique could potentially be applied for clinical use as clinical trials have already been carried out by using perfluorocarbons[348]. The safety of fluorodeoxyflucose at physiological concentrations has been demonstrated by its frequent use as a tracer for positron emission tomography in the clinic[367]. Higher FDG concentrations used for ^{19}F MRI have not yet been assessed from a toxicological point of view. However, some pre-clinical studies did not indicate any adverse effects[362].

Based on our proof-of-principle data, a future step will be to evaluate a pH-controlled delivery in the gastrointestinal tract of antibodies against C. difficile by a pH-sensitive polymer coated capsule. Our dual-modality imaging approach enabled us to evaluate *in vivo* both the location and integrity of the capsule. As antibodies are generally well soluble, we would anticipate that they would distribute similar to the FDG used in our study. In order to test antibody release in the hamster model, parameters like different capsule sizes or capsule coating have to be further optimized for their ability to pass the stomach. By reducing the size of the capsule or modifying capsule coating to withstand low pH for longer, we expect the success rate to increase.

5.3 Conclusions

We were able to show that combined application of ^{19}F-MRI and CT provides information on the location, integrity and graduate release of material from oral administered capsules into the gastrointestinal tract of small animal models. This will form the basis for further studies on the delivery of therapeutic compounds, e.g. antibodies against Clostridium difficile infection.

Both imaging modalities provide complementary information about the position and release of contrast agents (or drugs) inside the gastrointestinal tract. CT was shown to be useful for monitoring the localization of the capsule as well as the integrity of it. On the other hand, ^{19}F-MRI enabled the visualization of the rise in permeability of the capsule. A ^{19}F-MRI signal could only be detected when ^{19}F-FDG was dissolved and this happened when there was influx of water into the capsule. Furthermore, it should be noted that the degree of compound release is influenced by the solubility

of the compound itself. For example, lyophilized antibodies can be stable and are well solubilized. As an intermediate step in the development of the oral administration of encapsulated antibodies, we envisage capsules to be filled with both, ^{19}F-FDG and $BaSO_4$ as well as the antibody. In that way the controlled release can be monitored non-invasively.

Overall, we have proposed and demonstrated an imaging platform to monitor the mechanism of controlled release *in vitro* and *in vivo*. This multimodal platform could overcome the limitations in terms of sensitivity, resolution, specificity and quantitation of one individual method. We believe that this imaging approach could also be applied to other models where controlled release mechanisms need to be understood and evaluated.

5.4 Experimental

5.4.1 Capsules and contrast agents

Gelatin size 9 capsules (8.4 mm in length, 2.7 mm external diameter and 25 µl maximal volume, Torpac, Fairfield, USA) were filled with FDG and/or $BaSO_4$ (average amounts were 3.63 mg (equal to 20 µmol) and 14.49 mg (equal to 62 µmol), respectively). Afterwards, the capsules were dip-coated with a solution of 12.5% Eudragit L100 (Evonik Industries, Essen, Germany) in isopropanol. Triethylcitrate (10% w/w) was added as plasticizer.

5.4.2 Hamster model

All animal experiments were executed in accordance with national and European regulations and approved by the Animal Ethics Committee of the KU Leuven (approval numbers P009/2010 and P083/2011). Four male Syrian Golden hamsters (120-150 g, Janvier Laboratories) were given capsules via oral gavage using a dosing syringe (Torpac, Fairfield, USA). All animals were dosed and imaged during the light cycle while being in a fed ad libitum. Additional experiments were performed whereby two animals were dosed and imaged during the dark cycle but this did not impact the results discussed here (data not shown).

5.4.3 Magnetic Resonance Imaging

MRI was carried out on a 9.4 Tesla Bruker Biospec small animal MR scanner (Bruker Biospin, Ettlingen, Germany; horizontal bore, 20cm) equipped with actively shielded gradients (600 mT m^{-1}) and running under the operating system ParaVision 5.1. For radiofrequency transmission and reception, a home-built, inductively coupled, saddle shaped surface coil, tunable from 376 MHz for ^{19}F to 400 MHz for ^{1}H was used for all experiments.

For *in vitro* MRI, a phantom was prepared by filling 2% agarose in a plastic container containing 4 micro-centrifuge tubes (Eppendorf, Hamburg, Germany). Each tube contained 400 µl PBS with different pH (pH = 1, 3, 5 and 7) adjusted by adding HCl (1M). In each tube, one intact capsule loaded with ^{19}F-FDG was added. A positioning and anatomic ^{1}H-MRI scan was performed using a 2D turbo spin echo sequence (RARE sequence, 8 echoes/excitation, 7.6 s/15.9 ms repetition time/effective echo time, 6.4 cm*6.4 cm field of view, 256*256 matrix, 100 consecutive, coronal,

0.25 mm slice thickness, number of average is 2, 6 min scanning time). The settings for non-localized ^{19}F-NMR spectroscopy were: 100 ms repetition time, 1000 numbers of average, flip angle of 20 °and total scan time of 100 s. ^{19}F-MRI 2D images were obtained using the same sequence as for ^{1}H-MRI imaging with some parameters modified (1.142 s repetition time, 64*64 matrix, 15 consecutive 1 mm thick slices in coronal orientation, 250 number of average, 28:30 min scan time). Repeated in vitro images were acquired over a period of 15 hours, until the capsules were considered to be totally disintegrated.

For *in vivo* MRI, hamsters were scanned under inhalation anesthesia (1-2% isoflurane mixed with carrier gas oxygen). A monitoring and gating model (type 1030) from SA Instruments Inc. (Stony Brook, NY, USA) was used to regulate the physiological parameters and respiratory gating in real time. The body temperature and respiration rate of animals were monitored using a rectal probe and a pressure sensitive pad placed underneath the thorax, respectively. Both body temperature and respiration rate were maintained at reasonable physiological range of approximately 37 ℃ and 30-50 breaths/min, respectively. Both anatomical images (^{1}H-MRI) and ^{19}F-MR images were acquired using RARE sequences with modified parameters: 15.9 ms effective echo time; 6 s (^{1}H)/1 s (^{19}F) repetition time, 8 echoes/excitation; 6 cm * 8 cm field of view; 300*400 (^{1}H)/50*50 (^{19}F) matrix; 50 (^{1}H)/10 (^{19}F) consecutive, coronal slices of 0.5 mm (for ^{1}H) and 2.5 mm (for ^{19}F) thickness; number of averages was 2 for ^{1}H and 500 for ^{19}F; scan time was 7:24 min for ^{1}H and 33:20 min for ^{19}F. Multiple ^{19}F MR images were obtained using the same scan protocol. The total scan time was maximum 2.5 hours. The ^{19}F NMR spectra were analyzed using the jMRUI software, version 4.0[368].

5.4.4 Computed Tomography

CT images were acquired on a dedicated small animal microCT scanner (SkyScan 1076, Bruker microCT, Kontich, Belgium), reconstructed and visualized using software provided by the manufacturer (NRecon, DataViewer, CTvox).

In vitro microCT phantom scans were acquired using the following scan parameters: 100 kVp X-ray source voltage combined with a 1.0 mm aluminum filter, 100 µA source current, 220 ms exposure time per projection, resulting in a total scan time of less than 7 minutes.

For the acquisition of *in vivo* CT scans, hamsters were anesthetized with 1 – 1.5% isoflurane in 100% oxygen. Scan parameters were: 50 kVp X-ray source voltage combined with a 0.5 mm aluminum filter, 180 µA source current, 450 ms exposure time per projection, acquiring 2 projections (for averaging) per position with 0.7 °increments over a total angle of 180 °and a field-of-view covering the stomach and bowels, resulting in a scanning time of 12 minutes. This yielded a reconstructed 3D datasets with 35 µm ^{3}isotropic voxel size.

Sayuan Liang participated in planning experiments, performing *in vitro* and *in vivo* MRI acquisition, post-processing of imaging data. Sayuan Liang and Dominiek Staelens have drafted the paper and coordinated further reviewing and editing.

Chapter 6. General Conclusions & Future Perspectives

6.1 General Conclusions

Diabetes remains one of the relevant threats to human health with over 422 million people suffering the disease all over the world[1,260]. Over time, this disease leads to serious secondary damage to different organs of patients, such as the eyes (blindness), kidneys (kidney failure), extremities (poor vascularization of legs) etc[279]. This chronic metabolic disease harms the quality of life and increases the burden on the healthcare system. Therefore, diagnosis and early prevention with effective monitoring of pre- and post- therapy of the disease is urgently needed. Although the mechanism of type 1 and type 2 diabetes is different, the impairment and loss of insulin production by the pancreas is currently considered a common trait of both diseases[2,4,5]. This indicates the importance of pancreatic islets (PIs) and in particular their beta cells, as they are responsible for producing insulin to balance the blood glucose level. Different techniques have been applied in daily clinical routine to determine beta cell mass (BCM), such as C-peptide level tests, oral and/ or intravenous glucose tolerance tests and others[12,261,262]. However, these tests only provide an indirect estimation of the BCM. The fast development of various non-invasive imaging techniques over the last decades opens a new window for both intrinsic and extrinsic cell tracking and cell quantification. Indeed, the unique advantages of imaging techniques, such as the direct visualization and quantification of cells non-invasively and repeated imaging in one subject over time, make *in vivo* cell imaging a high-priority field of research for various international organizations and funding agencies, such as European Commission, National Institute of Diabetes, Juvenile Diabetes Research Foundation and etc[13,14,31,263]. Because of its multidisciplinary nature, non-invasive imaging modalities like MRI, CT, PET/ SPECT and ultrasound imaging have been widely used in different research fields, ranging from physics to material science, from a preclinical to a clinical environment. Irrespective of the advantages and disadvantages of different imaging modalities for conducting *in vivo* cell and molecular imaging, external probes and contrast agents are often needed to target the cells of interest at high sensitivity against the host background. For example, ultrasound often uses microbubbles, PET/ SPECT requires radio-ligands, CT needs iodine- or gold-based contrast and MRI makes use of different types of MR based contrast agents like SPIOs, Gd-chelates and others[17,369].

We have focused our research on MRI due to its excellent contrast between different soft tissues without any ionizing radiation. The application of MRI towards cell and molecular imaging is still in its infancy because of its relative low sensitivity. Conventional proton MR based T1 or T2 weighted contrast agents could further suffer from the ambiguous localization and quantification of the signal of interest[72,264]. Thanks to its advantageous feature of being background free, newly proposed fluorine based contrast agents using the ^{19}F MRI technique became the main tool in this study for answering our biomedical questions on tracking PIs and beta cells[68,178,179,300].

In **chapter 1,** a **General Introduction**, an overview of the working principle of different non-invasive imaging modalities was presented together with a more in depth explanation of MRI and, in particular, a detailed discussion of ^{19}F MRI from historical, technical and application perspectives. The development of ^{19}F MRI techniques involves multidisciplinary efforts, from chemistry (contrast agent synthesis) to engineering (RF coil construction), from MR physics (MR sequence optimization) to

biomedical applications (cell labelling, characterization and imaging). The synthesis of a suitable fluorine containing contrast agent with favourable MR properties, such as a single resonance peak in the fluorine MR spectrum with a high ratio of T2/T1 relaxation parameter, and biomedical compatibility is considered as a preliminary, key step for cell imaging using ^{19}F MRI.

In this thesis, mainly two different contrast agents, obtained from our collaborators, were assessed in more detail: ^{19}F-deoxyfluoromannoheptuloses (^{19}FMH) (**chapter 2**) and perfluoro-5-crown-5 (PFCE) (**chapter 3**). They have been characterized, tested and validated for tracking PIs and beta cells both *in vitro* and *in vivo* combined with hardware development (RF coil building, MR sequence optimization). Based on the different labelling approaches for these two contrast agents, different strategies have been applied for *in vivo* imaging:

*(1) In situ labeling GLUT-2 expressed cells after systemic injection of FMH (**chapter 2**)*
*(2) Ex vivo pre-labeling of isolated PIs and beta cell lines with subsequent transplantation and in vivo imaging (**chapter 3**).*

The inherent sensitivity issue of ^{19}F MRI was addressed in **chapter 4** from a data reconstruction perspective using compressed sensing methods for the detection of PFCE labelled PIs and beta cells. Furthermore, combining our ^{19}F MRI setup with the CT technique, we extended our interest to the field of drug delivery by proposing a new dual imaging system for monitoring controlled drug release in **chapter 5**.

In an ideal scenario, only targeted cells would internalize abundant targeting contrast agents after their systemic administration. This is also known as targeted labelling based on particular receptor, enzyme or transporter expression of the cell type of interest. GLUT-2 transporters are highly expressed by beta cells and hepatocytes. As previously reported, D-mannoheptuloses (DMHs) show high specificity towards GLUT-2 transporters. Therefore, fluorine labelled DMHs (^{19}FMH) have the potential to target these cells *in vivo.* As DMHs would also stay inside the cells after phosphorylation, they would be suitable for monitoring these cells longitudinally using ^{19}F MRI. Indeed, our preliminary *in vitro* studies have also confirmed that fluorinated ^{19}FMH had a similar specificity towards GLUT-2 expressing cells as DMHs[184]. The main focus of **chapter 2** is the *in vivo* application of ^{19}FMH and its validation following systemic injection and the assessment of its feasibility to quantify GLUT-2 expressing cells. *Ex vivo* ^{19}F MRS was also used for confirmation and quantification of ^{19}FMH uptake by different tissues. First, we established an in-house built ^{1}H/^{19}F double tuneable and matchable RF coil for sensitive *in vivo* mouse body imaging with a relative large field-of-view (~30mm). This coil showed similar good sensitivity as reported in the literature with detection limit of $5*10^{15}$ ^{19}F spins/pixel using an 3D gradient echo sequence with 120 averages[86,342]. Thanks to its unique saddle shape, this coil also exhibited good field homogeneity with linear correlation between SNR and ^{19}F spin concentration, which is essential for quantification of cell numbers. We were then able to assess the distribution of FMHs *in vivo* with a temporal resolution of approximately 20 minutes. The clearance of ^{19}FMH from the circulation was rapid as the ^{19}F MRI signal was already detected in the bladder and kidneys from the first time point (approximately 20 minutes after injection), and the bulk clearance of ^{19}FMH from circulation occurred within two hours. This phenomenon was also indirectly confirmed by intraperitoneal glucose tolerance test (IPGTT) experiments, where the temporal increase of glycaemia and decrease of insulin levels after ^{19}FMH administration was similar as for DMH and lasted for approximately two hours until the physiological conditions of the animals returned to a norm-glycaemic state. Complete clearance of the ^{19}FMH was observed 24 hours after the injection. *In vivo* ^{19}F MRI detected some signal in the liver and potentially

from the pancreas with low retention for some animals, although, we have noticed considerable variability between different mice. Furthermore, *ex vivo* ^{19}F NMR spectroscopy confirmed preferential uptake of ^{19}FMH in tissue with high expression of the GLUT-2 transporter. These transporters are mainly found in the liver and pancreas, while it is absent from tissue such as muscle. However, the local ^{19}FMH accumulation in the liver and the pancreas were relative low (~$2*10^{17}$ F spins/ tissue) and therefore, based on the low detection limit of the technique, explains the difficulties for *in vivo* detection by ^{19}F MRI. Hence, current bottlenecks of this approach, namely the quick clearance of the compound and the relative low sensitivity of ^{19}F MRI, need to be overcome before ^{19}FMH becomes suitable for visualizing and tracking GLUT-2 expressing cells after systemic ^{19}FMH administration. Although not straightforward from a chemistry point of few, synthesis of ^{18}F-labeled FMH and detection by the highly sensitive PET could be a potential solution for the future.

In order to increase the sensitivity of ^{19}F MRI, using contrast agents with more fluorine atoms is another potential option. Due to their high payload with fluorine atoms per molecule, about two third of ^{19}F MRI related publications in literature are based on prefluorocarbons (PFCs)[90,178,300,325]. As PFCs are both hydrophobic and lipophobic, they are often phospholipid coated to facilitate cellular uptake. Except for the detection of inflammation by targeting phagocytic immune cells by *in situ* labelling, *ex vivo* pre-labelling of targeted cell types with PFCs followed by transplantation and *in vivo* tracking is a frequently used strategy. **In chapter 3**, isolated PIs/ INS-1E cells were labelled *ex vivo* with PFCE and followed up by ^{19}F MRI after subcutaneous transplantation. In addition, lipophilic DiD fluorescent dyes were included in the lipid coating of PFCE for detection by FLI. BLI was also performed after transduction of PIs and INS-1E cells using a lentiviral vector (LV) carrying the hEFlα promoter to drive 3flagFluc expression. Using these labelling strategies, a tri-modal imaging method has been proposed and validated for tracking PIs and INS-1E cells after transplantation. The aim of this approach was to follow beta cells in treatment models of type I diabetes using islet transplantation. The PFCE labelling and LV transduction protocols were optimized for both PIs and INS-1E cells *in vitro* to achieve sufficient PFCE uptake and a high transduction rate while retaining the viability and functionality of PIs and INS-1E cells. Optimized PFCE labelling conditions were the same for PIs and INS-1E cells (20mM fluorine concentration and 24h incubation time), which resulted in $1.44*10^{15}$/ $3.7*10^{12}$ fluorine atoms per PI and cell, respectively. These results are in agreement with previously reported labelling efficacies of similar particles, resulting in uptake in the range of 10^{11} to 10^{13} fluorine atoms/ cell[178]. Confocal microscopy images confirmed the internalization of PFCE by PIs and cells. The transduction of PIs by LV had to be extended to 48h instead of 24h to achieve sufficient transduction rates of the cells due to the more complicated structure of PIs. Nevertheless, transduction rates over 90% were reached. The stability of the fluorine label inside the cells was tested and no significant leakage was found despite potential signal loss due to cell death or cell proliferation. Furthermore, the *in vitro* detection limit of the three modalities were compared, resulting in a few PIs or hundreds of INS-1E cells for FLI and BLI, and ten PIs and a few thousands INS-1E cells/ pixel for ^{19}F MRI. Longitudinal multimodal *in vivo* imaging of transplanted PIs and INS-1E cells at subcutaneous sites demonstrated the feasibility of longitudinal cell tracking for up to several months with our PFCE labels. Irrespective of the degradation of the fluorescent dye, a linear correlation between the ^{19}F MRI signal and the FLI signal indicated indirectly a stable incorporation of the PFCE emulsions with its attached fluorescent dye as they had a similar clearance rate from the transplantation site. In contrast to ^{19}F MRI and FLI, BLI data showed different results with considerable larger variability between different animals. Only one animal that received INS-1E cells could still sustain BLI signal after 14 days post transplantation, most likely due to cell

proliferation. As BLI provided direct information on the viability of transplanted PIs and cells with almost immediately identification of potential graft rejection, the delayed disappearance seen by ^{19}F MRI and FLI was due to delayed clearance of the PFCEs after islets and cells have already been rejected. This disagreement between *in vivo* ^{19}F MRI/ FLI and BLI underlines the importance of a multimodal imaging approach. Our data suggests that ^{19}F MRI is suitable for high-resolution localization of transplanted cells and PIs; FLI is essential for confirmation of the contrast agent localization by histology; and BLI is a reliable method to assess cell viability and survival after transplantation. With the imaging approach presented in this chapter, novel strategies for improving the outcomes of PI transplantation could be better evaluated and compared in longitudinal studies. Furthermore, it reduces the number of animals needed and the statistical variability of the results when compared with studies entirely relying on histology at particular time points.

In **chapter 4**, the sensitivity limitation of ^{19}F MRI has been tackled from a novel image reconstruction perspective by implementing and comparing different compressed sensing (CS) techniques[251]. The promising application of CS for ^{19}F MRI has already been demonstrated previously[252,253]. However, a remaining challenge was dealing with low SNR images as often encountered by ^{19}F MRI. By making use of the established experimental design from **Chapter 3**, we investigated and compared different existing CS methods for PFCE labelled PIs and INS-1E cells, both *in vitro* and *in vivo* after subcutaneous transplantation. Fully sampled low SNR datasets (both *in vitro* and *in vivo*) were firstly Cartesian under-sampled with central emphasis and different undersampling factors. Offline CS reconstruction showed a similar result, namely a three- to fourfold increase of SNR per time, achieved by different algorithms (except the CoSaMP algorithm) used in the study. The quantitative difference of signal of interests (SOIs) between reconstructed images and original images were marginal (within 5%) and confirmed the validity of CS techniques for low SNR ^{19}F MRI data. To go one step further, 3D and 2D CS acquisitions were implemented and verified on the MRI scanner and tested for *in vitro* and *in vivo* data, respectively. These results not only demonstrated again that the CS technique together with appropriate reconstruction algorithms is useful to reduce the scan time for ^{19}F MRI applications with low SNR, but also gave evidence that by using the CS technique, extra SOI could be detected, which might be missed otherwise by using conventional ^{19}F MRI acquisition schemes within the same scan time. Although further understanding and optimization in terms of fundamental noise distribution of low SNR ^{19}F MR images, undersampling patterns, reconstruction algorithms is still needed, the CS method already opened a new window for broader applications of ^{19}F MRI.

We did not limit our interest to ^{19}F MRI based cell imaging but applied ^{19}F MRI also to other field of preclinical research, such as controlled release of a therapeutic compound, as described in **chapter 5**. The initiative started from the need to monitor the accurate release of antibodies targeting virulence factors via oral administration, which is considered a better treatment for *Clostridium difficile* associated diseases[347,348]. The concept of enclosing therapeutic compounds in a pH-sensitive coated capsule could be helpful in releasing these compounds at the desired location[350,352]. In order to verify the technique noninvasively, we proposed a novel dual imaging approach by combining ^{19}F MRI and CT. Loading fluoro-deoxyglucose (FDG) and $BaSO_4$ inside the pH-sensitive capsules as contrast agents for ^{19}F MRI and CT, respectively, we evaluated our imaging method both *in vitro* and *in vivo* in a hamster model. The *in vitro* ^{19}F MRI data provided information on the early permeability of the capsule material, as the ^{19}F MRI signal only appeared when the water entered the leaky capsule to dissolve the FDG. As expected, the coating of the capsule was more resistance at lower pH than at higher pH, with delayed ^{19}F MRI signal detection in the latter case. On the other hand, higher spatial and temporal resolution of CT could not only confirm the observation that the coated capsules are

resistant to low pH, but also clearly showed the integrity of the capsule with its exact anatomical location at the site of release. The resistance of the capsule against low pH for up to two hours as demonstrated by both MRI and CT showed the feasibility of bypassing the stomach and allowing the capsule to reach its desired location (in this case, the small intestine). Our *in vivo* data also confirmed a similar timeframe of resistance of the capsule at low pH (stomach), which was in line with the *in vitro* data. From a biological point of view, a relative negative outcome was that only in one of the four animals the capsule successfully passed the stomach and reached the small intestine. This might be explained by different factors, such as the capsule size, gastric retention or feeding status of the animals. Nevertheless, taking into account the absence of toxic effects of FDG and $BaSO_4$ at low concentration, this imaging approach could serve as a basis for any subsequent studies of controlled release from optimized capsule material using imaging equipment available in modern clinical and pre-clinical environments for routine diagnosis and research purpose.

Overall, the work summarized in this thesis contributes to the further development, evaluation, and validation of ^{19}F MRI as a preclinical imaging tool for cell tracking with a strong emphasis on PIs and beta cell imaging and on controlled release of fluorinated compounds. We have utilized different fluorinated contrast agents and proposed different strategies for tracking PIs and beta cells *in vivo*. It was shown that it is feasible to use ^{19}F MRI for longitudinal imaging of PIs and beta cells in a quantitative way without interfering background signal. The necessity of tackling the low sensitivity issue of ^{19}F MRI was also emphasized from different perspectives (both the contrast agent and the data reconstruction aspect). Moreover, multi-modality imaging provides complementary information for cross-validation of different experimental approaches. Finally, the future of ^{19}F MRI remains bright due to its versatile applications in preclinical research. The translation of the technique to clinical routine still needs additional efforts, for example for the implementation of hardware and data processing components. In this thesis, we have established and validated different ^{19}F MRI relevant methodologies that could potentially contribute to future improvements of the technique.

6.2 Future Perspectives

This year is the 40th anniversary of the first publication on ^{19}F MRI[89]. However, this technique only found sporadic applications in the field of pharmaceutical research, anaesthesiology and oncology for the development, testing and validation of relevant fluorinated compounds. With the promising results of Ahrens et al., showing the feasibility of tracking immunotherapeutic cells (DC cells) using PFPE particles, this technique quickly attracted attention from the cell imaging community[82]. Indeed, with the rapid development and high prospective of cellular therapy by transferring specific cells for treatment (such as islets graft, dendritic cell vaccination, stem cell therapy etc.), a reliable, sensitive and quantitative non-invasive imaging technique was urgently needed for monitoring and assessment of transplanted cells longitudinally *in vivo*. Thanks to its MR nature, accompanied with routine ^{19}F MRI, ^{1}H MRI is often acquired, which could provide detailed anatomical information with excellent inherent soft tissue contrast and high resolution while avoiding ionizing radiation. Furthermore, the unique advantage of being virtually background free in biological tissues makes ^{19}F MRI very appealing to conduct cell imaging in terms of easy localization and the feasibility of quantification of fluorine labelled cells.

Over the last decade, numerous studies have been carried out by testing different cell types for ^{19}F labelling and imaging to explore the potential for clinical applications[84-87,169]. Nevertheless, before

moving forward with ^{19}F MRI technique to *in vivo* studies in humans, systematic and detailed *in vitro* validations are necessary. These *in vitro* assays will involve extensive cell culture work with different techniques (e.g. flow cytometer, confocal microscopy, trypan blue staining, toxicological studies and etc.). As such, certain aspects, for example, the labelling efficiency under optimized labelling conditions, the effect of the ^{19}F labels on cell viability and functionality, and the stability of the ^{19}F label inside the labelled cells, should be carefully explored and will serve as a key step towards successful *in vivo* imaging.

In general, *in vivo* tracking of targeted cells could be done by either *in situ* or *ex vivo* labelling strategies. Most of the current ^{19}F MRI related studies use the latter method with high efficiency and good reproducibility. Although successful *in situ* labelling has mainly involved tracking and detection of phagocytic cells in inflammation for the moment, it would be of huge benefit if comprehensive information for diagnosis and therapy follow up could be provided using targeted contrast agents that bind to a specific receptor or being taken up by a specific transporter with high affinity (e.g. in the case of diabetes, for following up the mass of beta cells).

The research scope for cellular ^{19}F MRI is focusing on preclinical studies at the moment. Although already part of some clinical trials, the translation of ^{19}F MRI from preclinical to clinical research and applications is not straightforward from different perspectives. First of all, the difference of magnetic field strengths often being used for preclinical and clinical research (7T to 11.7T versus 1.5T to 3T in the clinic) can results in different sequence parameters, image SNR and SAR consideration. Hence, several prior work including *in vitro* characterization of PFC relaxation parameters[370,371] and *in vivo* study of arthritic rabbit model[226] using ^{19}F MRI on clinical scanners have been carried out. Although these studies demonstrated the feasibility of performing ^{19}F MRI on clinical settings, tremendous work is still needed to fine tune to optimal parameters and cross the technical barriers. Another important issue that has to be taken into account is the fate of fluorinated contrast agents in the biological system. Both ^{19}FMH and PFCE tested in this thesis are considered safe within the context of short term preclinical research. As a derivative of DMH, ^{19}FMH is a heptose, a monosaccharide with seven carbon atoms. Shown in chapter 2, ^{19}FMH exhibited similar effect as DMH with temporary hexokinase inhibition and relative quick clearance via the urine (signal accumulation in the bladder). Although the safety issues of DMH usage especially in patients with diabetes have been debated for decades, DMH has been used to treat leucine-sensitive hypoglycaemia. Considering the facts that DMH is found in avocado (0.66g /100g) and no significant effect for daily consumption of avocado have been reported, as long as the amount of administrated of ^{19}FMH is well controlled, the side effects of using this sugar based contrast agent should be minimal. Thanks to its long history with various clinical applications, the toxicity profile and clearance pathway of PFCs have been well addressed in the literature. In general, higher molecular weight PFCs with long C-F chains are dealt with by the reticuloendothelial system while smaller PFCs often used as contrast agents are taken up by macrophages, first in liver and spleen and eventually cleared through exhalation from the lungs. Again the length of chain could affect the timing of the clearing process with heavier PFCs lingering for a longer period of time[372]. Furthermore, due to the extremely strong bond of C-F, PFCs are not likely to be broken down *in vivo* by enzymatic interference since no metabolites of these products have been found until now. Nevertheless, it is notable that all side effects of PFCs are concentration dependent[302]. Compared to its traditional clinical applications as artificial blood substitutes or oxygen carriers for traumatic surgery, the amount of PFCs delivered for cellular imaging is often several orders of magnitude lower. Overall, it is suggested that PFCs as contrast agents of cellular imaging are applicable for human use with low expected toxicity. Last but not least, the inherent low sensitivity

remains the key hurdle to promote the ^{19}F MRI technique for broader applications. The necessary long scan time with still relatively low SNR images almost prohibits the transition of the technique from research to clinical routine. Different aspects could be considered to tackle the problem, such as synthesizing new ^{19}F contrast agents with high payload of fluorine and more favourable MRI properties, developing new RF probes with better sensitivity (for example cryogen cooled coils), implementing new MR sequences and reconstruction methods for faster imaging etc[194,207,253,342]. Furthermore, multimodal imaging could be another potential option for overcoming limits of single modality imaging. By combining different imaging modalities together with ^{19}F MRI, more and deeper insights could be provided especially for follow-up studies where often the loss of fluorine labels due to cell division, cell death or nonspecific uptake of resident macrophages is a leading cause for false interpretation of imaging data. Nevertheless, the very first cellular imaging related clinical trial using ^{19}F MRI has been presented recently[193]. By transferring PFC labelled dendritic cells to colorectal adenocarcinoma patients, Ahrens et al. demonstrated the possibility of using ^{19}F MRI for clinical applications to validate the delivery and to track a broad range of cell types, thereby highlighting the future of ^{19}F MRI for clinical applications. Beyond molecular and cell imaging, this translation towards the clinic could also apply/ has already applied to other fields (for example, drug delivery[98,106], functional lung imaging[373] etc.), where ^{19}F MRI proved to be an effective tool.

Finally, it is clear that ^{19}F MRI has the potential to become a valuable tool for cell imaging. The advancement of this technique involves multidisciplinary inputs, hence close collaborations between chemists, biologist, physicians, clinicians and biomedical researchers are necessary to address the existing problems and limitations and to further promote this technique for broader applications with better outcomes. Continuous efforts would surely elevate the importance of the technique in the field. With the hope that this technique could eventually reach clinical routine and impact the personalized assessment of patient diagnosis, treatment and therapy with the final goal of achieving better patient care and less healthcare burden.

References

1. Fact sheet: http://www.who.int/mediacentre/factsheets/fs312/en/. (2016).
2. Pociot, F. & Lernmark, A. Genetic risk factors for type 1 diabetes. *Lancet* **387**, 2331-2339 (2016).
3. http://apps.who.int/iris/bitstream/10665/66040/1/WHO_NCD_NCS_99.2.pdf?ua=1. (2016).
4. Smyth, S. & Heron, A. Diabetes and obesity: the twin epidemics. *Nat Med* **12**, 75-80 (2006).
5. Daneman, D. Type 1 diabetes. *Lancet* **367**, 847-858 (2006).
6. Beran, D., Ewen, M. & Laing, R. Constraints and challenges in access to insulin: a global perspective. *Lancet Diabetes Endocrinol* **4**, 275-285 (2016).
7. Ballinger, W.F. & Lacy, P.E. Transplantation of intact pancreatic islets in rats. *Surgery* **72**, 175-186 (1972).
8. Ballinger, W.F., Lacy, P.E., Scharp, D.W., Kemp, C.B. & Knight, M. Isografts and allografts of pancreatic islets in rats. *Br J Surg* **60**, 313 (1973).
9. Scharp, D.W.*, et al.* Insulin independence after islet transplantation into type I diabetic patient. *Diabetes* **39**, 515-518 (1990).
10. Klinke, D.J., 2nd. Extent of beta cell destruction is important but insufficient to predict the onset of type 1 diabetes mellitus. *PLoS One* **3**, e1374 (2008).
11. Cersosimo, E., Solis-Herrera, C., Trautmann, M.E., Malloy, J. & Triplitt, C.L. Assessment of pancreatic beta-cell function: review of methods and clinical applications. *Curr Diabetes Rev* **10**, 2-42 (2014).
12. Jones, A.G. & Hattersley, A.T. The clinical utility of C-peptide measurement in the care of patients with diabetes. *Diabet Med* **30**, 803-817 (2013).
13. Malaisse, W.J., Louchami, K. & Sener, A. Noninvasive imaging of pancreatic beta cells. *Nature reviews. Endocrinology* **5**, 394-400 (2009).
14. Arifin, D.R. & Bulte, J.W. Imaging of pancreatic islet cells. *Diabetes Metab Res Rev* **27**, 761-766 (2011).
15. van der Kroon, I.*, et al.* Noninvasive Imaging of Islet Transplants with 111In-Exendin-3 SPECT/CT. *J Nucl Med* **57**, 799-804 (2016).
16. Ahlgren, U. & Gotthardt, M. Approaches for imaging islets: recent advances and future prospects. *Adv Exp Med Biol* **654**, 39-57 (2010).
17. James, M.L. & Gambhir, S.S. A molecular imaging primer: modalities, imaging agents, and applications. *Physiological reviews* **92**, 897-965 (2012).
18. Holmberg, D. & Ahlgren, U. Imaging the pancreas: from ex vivo to non-invasive technology. *Diabetologia* **51**, 2148-2154 (2008).
19. Jodal, A., Schibli, R. & Behe, M. Targets and probes for non-invasive imaging of beta-cells. *European journal of nuclear medicine and molecular imaging* **44**, 712-727 (2017).
20. Schmolze, D.B., Standley, C., Fogarty, K.E. & Fischer, A.H. Advances in microscopy techniques. *Arch Pathol Lab Med* **135**, 255-263 (2011).
21. Debbage, P. & Jaschke, W. Molecular imaging with nanoparticles: giant roles for dwarf actors. *Histochem Cell Biol* **130**, 845-875 (2008).
22. Massoud, T.F. & Gambhir, S.S. Molecular imaging in living subjects: seeing fundamental biological processes in a new light. *Genes Dev* **17**, 545-580 (2003).
23. Chudakov, D.M., Matz, M.V., Lukyanov, S. & Lukyanov, K.A. Fluorescent proteins and their applications in imaging living cells and tissues. *Physiological reviews* **90**, 1103-1163 (2010).
24. Stephens, D.J. & Allan, V.J. Light microscopy techniques for live cell imaging. *Science* **300**, 82-86 (2003).
25. Bertera, S.*, et al.* Body window-enabled in vivo multicolor imaging of transplanted mouse islets expressing an insulin-Timer fusion protein. *Biotechniques* **35**, 718-722 (2003).
26. Speier, S.*, et al.* Noninvasive in vivo imaging of pancreatic islet cell biology. *Nat Med* **14**, 574-578 (2008).
27. Mezzanotte, L., van 't Root, M., Karatas, H., Goun, E.A. & Lowik, C. In Vivo Molecular Bioluminescence Imaging: New Tools and Applications. *Trends in biotechnology* **35**, 640-652 (2017).
28. Sadikot, R.T. & Blackwell, T.S. Bioluminescence imaging. *Proc Am Thorac Soc* **2**, 537-540, 511-532 (2005).

29. Seliger, H.H. & McElroy, W.D. The Colors of Firefly Bioluminescence: Enzyme Configuration and Species Specificity. *Proc Natl Acad Sci U S A* **52**, 75-81 (1964).
30. Lu, Y.*, et al.* Bioluminescent monitoring of islet graft survival after transplantation. *Mol Ther* **9**, 428-435 (2004).
31. Yong, J.*, et al.* Multimodality imaging of beta-cells in mouse models of type 1 and 2 diabetes. *Diabetes* **60**, 1383-1392 (2011).
32. Fowler, M.*, et al.* Assessment of pancreatic islet mass after islet transplantation using in vivo bioluminescence imaging. *Transplantation* **79**, 768-776 (2005).
33. Medarova, Z. & Moore, A. Non-invasive detection of transplanted pancreatic islets. *Diabetes Obes Metab* **10 Suppl 4**, 88-97 (2008).
34. Liang, H.D. & Blomley, M.J. The role of ultrasound in molecular imaging. *Br J Radiol* **76 Spec No 2**, S140-150 (2003).
35. Stride, E. & Saffari, N. Microbubble ultrasound contrast agents: a review. *Proc Inst Mech Eng H* **217**, 429-447 (2003).
36. Goldberg, B.B., Liu, J.B. & Forsberg, F. Ultrasound contrast agents: a review. *Ultrasound Med Biol* **20**, 319-333 (1994).
37. Barnett, B.P.*, et al.* Fluorocapsules for improved function, immunoprotection, and visualization of cellular therapeutics with MR, US, and CT imaging. *Radiology* **258**, 182-191 (2011).
38. Arifin, D.R.*, et al.* Trimodal gadolinium-gold microcapsules containing pancreatic islet cells restore normoglycemia in diabetic mice and can be tracked by using US, CT, and positive-contrast MR imaging. *Radiology* **260**, 790-798 (2011).
39. Kim, J.*, et al.* Multifunctional capsule-in-capsules for immunoprotection and trimodal imaging. *Angew Chem Int Ed Engl* **50**, 2317-2321 (2011).
40. Hainfeld, J.F., Slatkin, D.N., Focella, T.M. & Smilowitz, H.M. Gold nanoparticles: a new X-ray contrast agent. *Br J Radiol* **79**, 248-253 (2006).
41. Krause, W. Delivery of diagnostic agents in computed tomography. *Adv Drug Deliv Rev* **37**, 159-173 (1999).
42. Hyafil, F.*, et al.* Noninvasive detection of macrophages using a nanoparticulate contrast agent for computed tomography. *Nat Med* **13**, 636-641 (2007).
43. Kim, D., Jeong, Y.Y. & Jon, S. A drug-loaded aptamer-gold nanoparticle bioconjugate for combined CT imaging and therapy of prostate cancer. *ACS Nano* **4**, 3689-3696 (2010).
44. Popovtzer, R.*, et al.* Targeted gold nanoparticles enable molecular CT imaging of cancer. *Nano letters* **8**, 4593-4596 (2008).
45. D'Hollander, A.*, et al.* Development of nanostars as a biocompatible tumor contrast agent: toward in vivo SERS imaging. *International journal of nanomedicine* **11**, 3703-3714 (2016).
46. Bailey, D.L.T., D.W; Valk, P.E; Maisey, M.N. *Positron Emission Tomography: Basic Sciences*, (Springer-Verlag, 2005).
47. Beekman, F.J.*, et al.* U-SPECT-I: a novel system for submillimeter-resolution tomography with radiolabeled molecules in mice. *J Nucl Med* **46**, 1194-1200 (2005).
48. Phelps, M.E. Positron emission tomography provides molecular imaging of biological processes. *Proc Natl Acad Sci U S A* **97**, 9226-9233 (2000).
49. Blake, P., Johnson, B. & VanMeter, J.W. Positron Emission Tomography (PET) and Single Photon Emission Computed Tomography (SPECT): Clinical Applications. *J Neuroophthalmol* **23**, 34-41 (2003).
50. Pichler, B.J., Judenhofer, M.S. & Pfannenberg, C. Multimodal imaging approaches: PET/CT and PET/MRI. *Handb Exp Pharmacol*, 109-132 (2008).
51. Maffei, A.*, et al.* Identification of tissue-restricted transcripts in human islets. *Endocrinology* **145**, 4513-4521 (2004).
52. Simpson, N.R.*, et al.* Visualizing pancreatic beta-cell mass with [11C]DTBZ. *Nucl Med Biol* **33**, 855-864 (2006).
53. Souza, F.*, et al.* Longitudinal noninvasive PET-based beta cell mass estimates in a spontaneous diabetes rat model. *The Journal of clinical investigation* **116**, 1506-1513 (2006).
54. Kung, M.P.*, et al.* In vivo imaging of beta-cell mass in rats using 18F-FP-(+)-DTBZ: a potential PET ligand for studying diabetes mellitus. *J Nucl Med* **49**, 1171-1176 (2008).

55. Moore, A., Bonner-Weir, S. & Weissleder, R. Noninvasive in vivo measurement of beta-cell mass in mouse model of diabetes. *Diabetes* **50**, 2231-2236 (2001).
56. Mukai, E.*, et al.* GLP-1 receptor antagonist as a potential probe for pancreatic beta-cell imaging. *Biochem Biophys Res Commun* **389**, 523-526 (2009).
57. Wild, D.*, et al.* [Lys40(Ahx-DTPA-111In)NH2]exendin-4, a very promising ligand for glucagon-like peptide-1 (GLP-1) receptor targeting. *J Nucl Med* **47**, 2025-2033 (2006).
58. AB, N.M. The Nobel Prize in Physics 1952. (2014).
59. Lauterbur, P.C. Image formation by induced local interactions. Examples employing nuclear magnetic resonance. 1973. *Clin Orthop Relat Res*, 3-6 (1989).
60. Ai, T.*, et al.* A historical overview of magnetic resonance imaging, focusing on technological innovations. *Investigative radiology* **47**, 725-741 (2012).
61. Chhabra, A., Madhuranthakam, A.J. & Andreisek, G. Magnetic resonance neurography: current perspectives and literature review. *European radiology* (2017).
62. Huber, L., Uludag, K. & Moller, H.E. Non-BOLD contrast for laminar fMRI in humans: CBF, CBV, and CMR02. *NeuroImage* (2017).
63. Sujlana, P., Skrok, J. & Fayad, L.M. Review of dynamic contrast-enhanced MRI: Technical aspects and applications in the musculoskeletal system. *Journal of magnetic resonance imaging : JMRI* (2017).
64. Warbrick, T., Rosenberg, J. & Shah, N.J. The relationship between BOLD fMRI response and the underlying white matter as measured by fractional anisotropy (FA): A systematic review. *NeuroImage* **153**, 369-381 (2017).
65. McRobbie, D.W., Moore, E.A., Graves, M.J. & Prince, M.R. *MRI from picture to proton*, (2006).
66. Hornak, J.P. *The Basic of MRI*, (2014).
67. Kemp, G.J., Meyerspeer, M. & Moser, E. Absolute quantification of phosphorus metabolite concentrations in human muscle in vivo by 31P MRS: a quantitative review. *NMR Biomed* **20**, 555-565 (2007).
68. Srinivas, M., Heerschap, A., Ahrens, E.T., Figdor, C.G. & de Vries, I.J. (19)F MRI for quantitative in vivo cell tracking. *Trends Biotechnol* **28**, 363-370 (2010).
69. Keshari, K.R. & Wilson, D.M. Chemistry and biochemistry of 13C hyperpolarized magnetic resonance using dynamic nuclear polarization. *Chemical Society reviews* **43**, 1627-1659 (2014).
70. Wilson, D.M. & Kurhanewicz, J. Hyperpolarized 13C MR for molecular imaging of prostate cancer. *J Nucl Med* **55**, 1567-1572 (2014).
71. Ojeda-Fournier, H., Choe, K.A. & Mahoney, M.C. Recognizing and interpreting artifacts and pitfalls in MR imaging of the breast. *Radiographics : a review publication of the Radiological Society of North America, Inc* **27 Suppl 1**, S147-164 (2007).
72. Himmelreich, U. & Dresselaers, T. Cell labeling and tracking for experimental models using magnetic resonance imaging. *Methods* **48**, 112-124 (2009).
73. Bulte, J.W. & Kraitchman, D.L. Iron oxide MR contrast agents for molecular and cellular imaging. *NMR Biomed* **17**, 484-499 (2004).
74. Shapiro, E.M.*, et al.* MRI detection of single particles for cellular imaging. *Proc Natl Acad Sci U S A* **101**, 10901-10906 (2004).
75. Evgenov, N.V., Medarova, Z., Dai, G., Bonner-Weir, S. & Moore, A. In vivo imaging of islet transplantation. *Nat Med* **12**, 144-148 (2006).
76. Jirak, D.*, et al.* MRI of transplanted pancreatic islets. *Magn Reson Med* **52**, 1228-1233 (2004).
77. Tai, J.H.*, et al.* Imaging islets labeled with magnetic nanoparticles at 1.5 Tesla. *Diabetes* **55**, 2931-2938 (2006).
78. Caravan, P. Strategies for increasing the sensitivity of gadolinium based MRI contrast agents. *Chemical Society reviews* **35**, 512-523 (2006).
79. Langereis, S., Geelen, T., Grull, H., Strijkers, G.J. & Nicolay, K. Paramagnetic liposomes for molecular MRI and MRI-guided drug delivery. *NMR Biomed* **26**, 728-744 (2013).
80. Aime, S., Barge, A., Cabella, C., Crich, S.G. & Gianolio, E. Targeting cells with MR imaging probes based on paramagnetic Gd(III) chelates. *Curr Pharm Biotechnol* **5**, 509-518 (2004).
81. Biancone, L.*, et al.* Magnetic resonance imaging of gadolinium-labeled pancreatic islets for experimental transplantation. *NMR Biomed* **20**, 40-48 (2007).

82. Ahrens, E.T., Flores, R., Xu, H. & Morel, P.A. In vivo imaging platform for tracking immunotherapeutic cells. *Nature biotechnology* **23**, 983-987 (2005).
83. Srinivas, M.*, et al.* Customizable, multi-functional fluorocarbon nanoparticles for quantitative in vivo imaging using 19F MRI and optical imaging. *Biomaterials* **31**, 7070-7077 (2010).
84. Srinivas, M., Morel, P.A., Ernst, L.A., Laidlaw, D.H. & Ahrens, E.T. Fluorine-19 MRI for visualization and quantification of cell migration in a diabetes model. *Magn Reson Med* **58**, 725-734 (2007).
85. Srinivas, M.*, et al.* In vivo cytometry of antigen-specific t cells using 19F MRI. *Magn Reson Med* **62**, 747-753 (2009).
86. Boehm-Sturm, P.*, et al.* A multi-modality platform to image stem cell graft survival in the naive and stroke-damaged mouse brain. *Biomaterials* **35**, 2218-2226 (2014).
87. Boehm-Sturm, P., Mengler, L., Wecker, S., Hoehn, M. & Kallur, T. In vivo tracking of human neural stem cells with 19F magnetic resonance imaging. *PLoS One* **6**, e29040 (2011).
88. Pretsch, E., Bühlmann, P. & Badertscher, M. Heteronuclear NMR Spectroscopy. in *Structure Determination of Organic Compounds: Tables of Spectral Data* 1-26 (Springer Berlin Heidelberg, Berlin, Heidelberg, 2009).
89. Holland, G.N., Bottomley, P.A. & Hinshaw, W.S. 19F magnetic resonance imaging. *J Magn Reson* **28**, 133-136 (1977).
90. Ruiz-Cabello, J., Barnett, B.P., Bottomley, P.A. & Bulte, J.W. Fluorine (19F) MRS and MRI in biomedicine. *NMR Biomed* **24**, 114-129 (2011).
91. Brey, W.S.B., M.L. Fluorine-19 NMR. in *Encyclopedia of NMR* (ed. Grant, D.M.H., P.K.) 2063-2071 (Wiley, New York 1996).
92. Ulrich, A.S. High resolution 1H and 19F solid state NMR. in *Encyclopedia of Spectroscopy and Spectrometry* (ed. Lindon, J.T., G.;Holmes,J.) 813-825 (Academic Press, London, 2000).
93. Aboagye, E.O., Artemov, D., Senter, P.D. & Bhujwalla, Z.M. Intratumoral conversion of 5-fluorocytosine to 5-fluorouracil by monoclonal antibody-cytosine deaminase conjugates: noninvasive detection of prodrug activation by magnetic resonance spectroscopy and spectroscopic imaging. *Cancer Res* **58**, 4075-4078 (1998).
94. Dresselaers, T.*, et al.* Non-invasive 19F MR spectroscopy of 5-fluorocytosine to 5-fluorouracil conversion by recombinant Salmonella in tumours. *Br J Cancer* **89**, 1796-1801 (2003).
95. Wyrwicz, A.M.*, et al.* Noninvasive observations of fluorinated anesthetics in rabbit brain by fluorine-19 nuclear magnetic resonance. *Science* **222**, 428-430 (1983).
96. Wyrwicz, A.M., Conboy, C.B., Ryback, K.R., Nichols, B.G. & Eisele, P. In vivo 19F-NMR study of isoflurane elimination from brain. *Biochim Biophys Acta* **927**, 86-91 (1987).
97. Chen, M.*, et al.* An in vivo 19F NMR study of isoflurane elimination as a function of age in rat brain. *NMR Biomed* **5**, 121-126 (1992).
98. Wolf, W.*, et al.* Fluorine-19 NMR spectroscopic studies of the metabolism of 5-fluorouracil in the liver of patients undergoing chemotherapy. *Magn Reson Imaging* **5**, 165-169 (1987).
99. Gewiese, B.K.*, et al.* Human eye: visualization of perfluorodecalin with F-19 MR imaging. *Radiology* **185**, 131-133 (1992).
100. Komoroski, R.A.*, et al.* In vivo 19F spin relaxation and localized spectroscopy of fluoxetine in human brain. *Magn Reson Med* **31**, 204-211 (1994).
101. Lockwood, G.G.*, et al.* Magnetic resonance spectroscopy of isoflurane kinetics in humans. Part I: Elimination from the head. *Br J Anaesth* **79**, 581-585 (1997).
102. Wolf, W., Presant, C.A. & Waluch, V. 19F-MRS studies of fluorinated drugs in humans. *Adv Drug Deliv Rev* **41**, 55-74 (2000).
103. Wang, J.*, et al.* Fluorine in pharmaceutical industry: fluorine-containing drugs introduced to the market in the last decade (2001-2011). *Chem Rev* **114**, 2432-2506 (2014).
104. Shani, J. & Wolf, W. A model for prediction of chemotherapy response to 5-fluorouracil based on the differential distribution of 5-[18F]fluorouracil in sensitive versus resistant lymphocytic leukemia in mice. *Cancer Res* **37**, 2306-2308 (1977).
105. Stevens, A.N., Morris, P.G., Iles, R.A., Sheldon, P.W. & Griffiths, J.R. 5-fluorouracil metabolism monitored in vivo by 19F NMR. *Br J Cancer* **50**, 113-117 (1984).
106. Wolf, W., Waluch, V. & Presant, C.A. Non-invasive 19F-NMRS of 5-fluorouracil in pharmacokinetics and pharmacodynamic studies. *NMR Biomed* **11**, 380-387 (1998).

107. O'Connell, M.J*., et al.* Improving adjuvant therapy for rectal cancer by combining protracted-infusion fluorouracil with radiation therapy after curative surgery. *N Engl J Med* **331**, 502-507 (1994).
108. McSheehy, P.M.J., Lemaire, L.P. & Griffiths, J.R. Fluorine-19 MRS: application in oncology. in *In Encyclopedia of Nuclear Magnetic Resonance*, Vol. 2 (eds. Grant, D.M. & Harris, R.K.) 2048-2052 (1996).
109. van Laarhoven, H.W., Klomp, D.W., Kamm, Y.J., Punt, C.J. & Heerschap, A. In vivo monitoring of capecitabine metabolism in human liver by 19fluorine magnetic resonance spectroscopy at 1.5 and 3 Tesla field strength. *Cancer Res* **63**, 7609-7612 (2003).
110. Solomon, B*., et al.* Modulation of intratumoral hypoxia by the epidermal growth factor receptor inhibitor gefitinib detected using small animal PET imaging. *Mol Cancer Ther* **4**, 1417-1422 (2005).
111. Henry, M.E*., et al.* A comparison of brain and serum pharmacokinetics of R-fluoxetine and racemic fluoxetine: A 19-F MRS study. *Neuropsychopharmacology* **30**, 1576-1583 (2005).
112. Keston, M. & Brocklehurst, J.C. Flurazepam and meprobamate: a clinical trial. *Age Ageing* **3**, 54-58 (1974).
113. Metcalfe, J.C., Hesketh, T.R. & Smith, G.A. Free cytosolic Ca2+ measurements with fluorine labelled indicators using 19FNMR. *Cell Calcium* **6**, 183-195 (1985).
114. Lockwood, G.G*., et al.* Magnetic resonance spectroscopy of isoflurane kinetics in humans. Part II: Functional localization. *Br J Anaesth* **79**, 586-589 (1997).
115. Menon, D.K. *Fluorine-19 MRS: General Overview and Anaesthesia*, (2007).
116. (!!! INVALID CITATION !!! []).
117. Patel, S.K., Zhang, Y., Pollock, J.A. & Janjic, J.M. Cyclooxgenase-2 inhibiting perfluoropoly (ethylene glycol) ether theranostic nanoemulsions-in vitro study. *PLoS One* **8**, e55802 (2013).
118. Staelens, D*., et al.* Visualization of delayed release of compounds from pH-sensitive capsules in vitro and in vivo in a hamster model. *Contrast Media Mol Imaging* **11**, 24-31 (2016).
119. Couch, M.J*., et al.* Inert fluorinated gas MRI: a new pulmonary imaging modality. *NMR Biomed* **27**, 1525-1534 (2014).
120. Couch, M.J*., et al.* Pulmonary ultrashort echo time 19F MR imaging with inhaled fluorinated gas mixtures in healthy volunteers: feasibility. *Radiology* **269**, 903-909 (2013).
121. Halaweish, A.F*., et al.* Perfluoropropane gas as a magnetic resonance lung imaging contrast agent in humans. *Chest* **144**, 1300-1310 (2013).
122. Heidelberger, E. & Lauterbur, P.C. Gas phase 19F-NMR zeugmatography: a new approach to lung ventilation imaging. in *Proceedings of the Annual Meeting ISMRM*, Vol. 1 70-71 (1982).
123. Kuethe, D.O., Caprihan, A., Fukushima, E. & Waggoner, R.A. Imaging lungs using inert fluorinated gases. *Magn Reson Med* **39**, 85-88 (1998).
124. Wolf, U*., et al.* Fluorine-19 MRI of the lung: first human experiment. in *Proceedings of the 16th Annual Meeting of ISMRM*, Vol. 16 3207 (2008).
125. Wolf, U., Scholz, A., Heussel, C.P., Markstaller, K. & Schreiber, W.G. Subsecond fluorine-19 MRI of the lung. *Magn Reson Med* **55**, 948-951 (2006).
126. Wolf, U*., et al.* Visualization of inert gas wash-out during high-frequency oscillatory ventilation using fluorine-19 MRI. *Magn Reson Med* **64**, 1478-1483 (2010).
127. Scholz, A.W*., et al.* Comparison of magnetic resonance imaging of inhaled SF6 with respiratory gas analysis. *Magn Reson Imaging* **27**, 549-556 (2009).
128. Perez-Sanchez, J.M*., et al.* In vivo diffusion weighted 19F MRI using SF6. *Magn Reson Med* **54**, 460-463 (2005).
129. Jacob, R.E*., et al.* 19F MR imaging of ventilation and diffusion in excised lungs. *Magn Reson Med* **54**, 577-585 (2005).
130. Kuethe, D.O., Caprihan, A., Gach, H.M., Lowe, I.J. & Fukushima, E. Imaging obstructed ventilation with NMR using inert fluorinated gases. *J Appl Physiol (1985)* **88**, 2279-2286 (2000).
131. Adolphi, N.L. & Kuethe, D.O. Quantitative mapping of ventilation-perfusion ratios in lungs by 19F MR imaging of T1 of inert fluorinated gases. *Magn Reson Med* **59**, 739-746 (2008).
132. Lehner, R., Wang, X., Wolf, M. & Hunziker, P. Designing switchable nanosystems for medical application. *J Control Release* **161**, 307-316 (2012).
133. Shao, K*., et al.* Nanoparticle-based immunotherapy for cancer. *ACS Nano* **9**, 16-30 (2015).

134. Kanamala, M., Wilson, W.R., Yang, M., Palmer, B.D. & Wu, Z. Mechanisms and biomaterials in pH-responsive tumour targeted drug delivery: A review. *Biomaterials* **85**, 152-167 (2016).
135. Webb, B.A., Chimenti, M., Jacobson, M.P. & Barber, D.L. Dysregulated pH: a perfect storm for cancer progression. *Nat Rev Cancer* **11**, 671-677 (2011).
136. Wang, K.W., Peng, H., Thurecht, K.J., Puttick, S. & Whittaker, A.K. pH-responsive star polymer nanoparticles: potential F-19 MRI contrast agents for tumour-selective imaging. *Polym Chem-Uk* **4**, 4480-4489 (2013).
137. Huang, X*., et al.* Multi-chromatic pH-activatable 19F-MRI nanoprobes with binary ON/OFF pH transitions and chemical-shift barcodes. *Angew Chem Int Ed Engl* **52**, 8074-8078 (2013).
138. Tanabe, K*., et al.* Monitoring of biological one-electron reduction by (19)F NMR using hypoxia selective activation of an (19)F-labeled indolequinone derivative. *J Am Chem Soc* **131**, 15982-15983 (2009).
139. Takaoka, Y*., et al.* Self-assembling nanoprobes that display off/on 19F nuclear magnetic resonance signals for protein detection and imaging. *Nat Chem* **1**, 557-561 (2009).
140. Moding, E.J., Kastan, M.B. & Kirsch, D.G. Strategies for optimizing the response of cancer and normal tissues to radiation. *Nat Rev Drug Discov* **12**, 526-542 (2013).
141. Rockwell, S., Dobrucki, I.T., Kim, E.Y., Marrison, S.T. & Vu, V.T. Hypoxia and radiation therapy: past history, ongoing research, and future promise. *Curr Mol Med* **9**, 442-458 (2009).
142. Harrison, L. & Blackwell, K. Hypoxia and anemia: factors in decreased sensitivity to radiation therapy and chemotherapy? *Oncologist* **9 Suppl 5**, 31-40 (2004).
143. Mignion, L*., et al.* Hexafluorobenzene in comparison with perfluoro-15-crown-5-ether for repeated monitoring of oxygenation using 19F MRI in a mouse model. *Magn Reson Med* **69**, 248-254 (2013).
144. Jordan, B.F., Cron, G.O. & Gallez, B. Rapid monitoring of oxygenation by 19F magnetic resonance imaging: Simultaneous comparison with fluorescence quenching. *Magn Reson Med* **61**, 634-638 (2009).
145. Mason, R.P., Rodbumrung, W. & Antich, P.P. Hexafluorobenzene: a sensitive 19F NMR indicator of tumor oxygenation. *NMR Biomed* **9**, 125-134 (1996).
146. Eidelberg, D*., et al.* 19F imaging of cerebral blood oxygenation in experimental middle cerebral artery occlusion: preliminary results. *J Cereb Blood Flow Metab* **8**, 276-281 (1988).
147. Liu, S*., et al.* Quantitative tissue oxygen measurement in multiple organs using 19F MRI in a rat model. *Magn Reson Med* **66**, 1722-1730 (2011).
148. Kadayakkara, D.K., Janjic, J.M., Pusateri, L.K., Young, W.B. & Ahrens, E.T. In vivo observation of intracellular oximetry in perfluorocarbon-labeled glioma cells and chemotherapeutic response in the CNS using fluorine-19 MRI. *Magn Reson Med* **64**, 1252-1259 (2010).
149. Zhao, D., Jiang, L., Hahn, E.W. & Mason, R.P. Comparison of 1H blood oxygen level-dependent (BOLD) and 19F MRI to investigate tumor oxygenation. *Magn Reson Med* **62**, 357-364 (2009).
150. Tran, L.B*., et al.* Hypoxia imaging with the nitroimidazole 18F-FAZA PET tracer: a comparison with OxyLite, EPR oximetry and 19F-MRI relaxometry. *Radiother Oncol* **105**, 29-35 (2012).
151. Folkman, J. Tumor angiogenesis: therapeutic implications. *N Engl J Med* **285**, 1182-1186 (1971).
152. Otto, C.M., Lind, B.K., Kitzman, D.W., Gersh, B.J. & Siscovick, D.S. Association of aortic-valve sclerosis with cardiovascular mortality and morbidity in the elderly. *N Engl J Med* **341**, 142-147 (1999).
153. Anderson, S.A*., et al.* Magnetic resonance contrast enhancement of neovasculature with alpha(v)beta(3)-targeted nanoparticles. *Magn Reson Med* **44**, 433-439 (2000).
154. Giraudeau, C*., et al.* 19F molecular MR imaging for detection of brain tumor angiogenesis: in vivo validation using targeted PFOB nanoparticles. *Angiogenesis* **16**, 171-179 (2013).
155. Schmieder, A.H*., et al.* Molecular MR imaging of melanoma angiogenesis with alphanubeta3-targeted paramagnetic nanoparticles. *Magn Reson Med* **53**, 621-627 (2005).
156. Waters, E.A*., et al.* Detection and quantification of angiogenesis in experimental valve disease with integrin-targeted nanoparticles and 19-fluorine MRI/MRS. *J Cardiovasc Magn Reson* **10**, 43 (2008).
157. Winter, P.M*., et al.* Molecular imaging of angiogenesis in early-stage atherosclerosis with alpha(v)beta3-integrin-targeted nanoparticles. *Circulation* **108**, 2270-2274 (2003).
158. Cyrus, T*., et al.* MR three-dimensional molecular imaging of intramural biomarkers with targeted nanoparticles. *J Cardiovasc Magn Reson* **8**, 535-541 (2006).

159. Braak, H., de Vos, R.A., Jansen, E.N., Bratzke, H. & Braak, E. Neuropathological hallmarks of Alzheimer's and Parkinson's diseases. *Prog Brain Res* **117**, 267-285 (1998).
160. Hardy, J.A. & Higgins, G.A. Alzheimer's disease: the amyloid cascade hypothesis. *Science* **256**, 184-185 (1992).
161. Higuchi, M.*, et al.* 19F and 1H MRI detection of amyloid beta plaques in vivo. *Nat Neurosci* **8**, 527-533 (2005).
162. Yanagisawa, D.*, et al.* In vivo detection of amyloid beta deposition using (1)(9)F magnetic resonance imaging with a (1)(9)F-containing curcumin derivative in a mouse model of Alzheimer's disease. *Neuroscience* **184**, 120-127 (2011).
163. Yanagisawa, D.*, et al.* Preferred features of a fluorine-19 MRI probe for amyloid detection in the brain. *J Alzheimers Dis* **39**, 617-631 (2014).
164. Tooyama, I.*, et al.* Amyloid imaging using fluorine-19 magnetic resonance imaging (19F-MRI). *Ageing Res Rev* (2016).
165. Ebner, B.*, et al.* Early assessment of pulmonary inflammation by 19F MRI in vivo. *Circ Cardiovasc Imaging* **3**, 202-210 (2010).
166. Temme, S.*, et al.* Technical advance: monitoring the trafficking of neutrophil granulocytes and monocytes during the course of tissue inflammation by noninvasive 19F MRI. *J Leukoc Biol* **95**, 689-697 (2014).
167. Ratner, A.V.*, et al.* Detection of acute radiation damage to the spleen in mice by using fluorine-19 MR imaging. *AJR Am J Roentgenol* **151**, 477-480 (1988).
168. Zhong, J., Narsinh, K., Morel, P.A., Xu, H. & Ahrens, E.T. In Vivo Quantification of Inflammation in Experimental Autoimmune Encephalomyelitis Rats Using Fluorine-19 Magnetic Resonance Imaging Reveals Immune Cell Recruitment outside the Nervous System. *PLoS One* **10**, e0140238 (2015).
169. Bonner, F.*, et al.* Monocyte imaging after myocardial infarction with 19F MRI at 3 T: a pilot study in explanted porcine hearts. *Eur Heart J Cardiovasc Imaging* **16**, 612-620 (2015).
170. Jacoby, C.*, et al.* Probing different perfluorocarbons for in vivo inflammation imaging by 19F MRI: image reconstruction, biological half-lives and sensitivity. *NMR Biomed* **27**, 261-271 (2014).
171. Waiczies, H.*, et al.* Visualizing brain inflammation with a shingled-leg radio-frequency head probe for 19F/1H MRI. *Scientific reports* **3**, 1280 (2013).
172. Flogel, U.*, et al.* In vivo monitoring of inflammation after cardiac and cerebral ischemia by fluorine magnetic resonance imaging. *Circulation* **118**, 140-148 (2008).
173. Balducci, A., Helfer, B.M., Ahrens, E.T., O'Hanlon, C.F., 3rd & Wesa, A.K. Visualizing arthritic inflammation and therapeutic response by fluorine-19 magnetic resonance imaging (19F MRI). *J Inflamm (Lond)* **9**, 24 (2012).
174. Temme, S.*, et al.* Noninvasive Imaging of Early Venous Thrombosis by 19F Magnetic Resonance Imaging With Targeted Perfluorocarbon Nanoemulsions. *Circulation* **131**, 1405-1414 (2015).
175. Zhong, J., Sakaki, M., Okada, H. & Ahrens, E.T. In vivo intracellular oxygen dynamics in murine brain glioma and immunotherapeutic response of cytotoxic T cells observed by fluorine-19 magnetic resonance imaging. *PLoS One* **8**, e59479 (2013).
176. Srinivas, M.*, et al.* Imaging of cellular therapies. *Adv Drug Deliv Rev* **62**, 1080-1093 (2010).
177. Bonetto, F.*, et al.* A large-scale (19)F MRI-based cell migration assay to optimize cell therapy. *NMR Biomed* **25**, 1095-1103 (2012).
178. Srinivas, M., Boehm-Sturm, P., Figdor, C.G., de Vries, I.J. & Hoehn, M. Labeling cells for in vivo tracking using (19)F MRI. *Biomaterials* **33**, 8830-8840 (2012).
179. Srinivas, M.*, et al.* In vivo 19F MRI for cell tracking. *J Vis Exp*, e50802 (2013).
180. Stoll, G., Basse-Lusebrink, T., Weise, G. & Jakob, P. Visualization of inflammation using (19) F-magnetic resonance imaging and perfluorocarbons. *Wiley Interdiscip Rev Nanomed Nanobiotechnol* **4**, 438-447 (2012).
181. Schmid, F., Holtke, C., Parker, D. & Faber, C. Boosting (19) F MRI-SNR efficient detection of paramagnetic contrast agents using ultrafast sequences. *Magn Reson Med* **69**, 1056-1062 (2013).
182. Hu, L., Zhang, L., Chen, J., Lanza, G.M. & Wickline, S.A. Diffusional mechanisms augment the fluorine MR relaxation in paramagnetic perfluorocarbon nanoparticles that provides a "relaxation switch" for detecting cellular endosomal activation. *Journal of magnetic resonance imaging : JMRI* **34**, 653-661 (2011).

183. de Vries, A.*, et al.* Relaxometric studies of gadolinium-functionalized perfluorocarbon nanoparticles for MR imaging. *Contrast Media Mol Imaging* **9**, 83-91 (2014).
184. Malaisse, W.J.*, et al.* (19)F-heptuloses as tools for the non-invasive imaging of GLUT2-expressing cells. *Archives of biochemistry and biophysics* **517**, 138-143 (2012).
185. Liang, S.*, et al.* In vivo and ex vivo 19-fluorine magnetic resonance imaging and spectroscopy of beta-cells and pancreatic islets using GLUT-2 specific contrast agents. *Contrast Media Mol Imaging* (2016).
186. Waiczies, S.*, et al.* Anchoring dipalmitoyl phosphoethanolamine to nanoparticles boosts cellular uptake and fluorine-19 magnetic resonance signal. *Scientific reports* **5**, 8427 (2015).
187. Tennstaedt, A., Mastropietro, A., Nelles, M., Beyrau, A. & Hoehn, M. In Vivo Fate Imaging of Intracerebral Stem Cell Grafts in Mouse Brain. *PLoS One* **10**, e0144262 (2015).
188. Gaudet, J.M., Ribot, E.J., Chen, Y., Gilbert, K.M. & Foster, P.J. Tracking the fate of stem cell implants with fluorine-19 MRI. *PLoS One* **10**, e0118544 (2015).
189. Janjic, J.M., Srinivas, M., Kadayakkara, D.K. & Ahrens, E.T. Self-delivering nanoemulsions for dual fluorine-19 MRI and fluorescence detection. *J Am Chem Soc* **130**, 2832-2841 (2008).
190. Barnett, B.P.*, et al.* Use of perfluorocarbon nanoparticles for non-invasive multimodal cell tracking of human pancreatic islets. *Contrast Media Mol Imaging* **6**, 251-259 (2011).
191. Liang, S.*, et al.* Tri-modal in vivo imaging of the rodent pancreatic islets transplanted in the subcutaneous site. in *Proceedings of the 23rd Annual Meeting ISMRM*, Vol. 23 4681 (2015).
192. Bible, E.*, et al.* Non-invasive imaging of transplanted human neural stem cells and ECM scaffold remodeling in the stroke-damaged rat brain by (19)F- and diffusion-MRI. *Biomaterials* **33**, 2858-2871 (2012).
193. Ahrens, E.T., Helfer, B.M., O'Hanlon, C.F. & Schirda, C. Clinical cell therapy imaging using a perfluorocarbon tracer and fluorine-19 MRI. *Magn Reson Med* **72**, 1696-1701 (2014).
194. Tirotta, I.*, et al.* (19)F magnetic resonance imaging (MRI): from design of materials to clinical applications. *Chem Rev* **115**, 1106-1129 (2015).
195. Mizukami, S.*, et al.* Paramagnetic relaxation-based 19f MRI probe to detect protease activity. *J Am Chem Soc* **130**, 794-795 (2008).
196. Thurecht, K.J.*, et al.* Functional hyperbranched polymers: toward targeted in vivo 19F magnetic resonance imaging using designed macromolecules. *J Am Chem Soc* **132**, 5336-5337 (2010).
197. Ogawa, M.*, et al.* Synthesis and Evaluation of Water-Soluble Fluorinated Dendritic Block-Copolymer Nanoparticles as a F-19-MRI Contrast Agent. *Macromolecular Chemistry and Physics* **211**, 1602-1609 (2010).
198. Celsense. http://www.celsense.com. (2014).
199. Kadayakkara, D.K., Damodaran, K., Hitchens, T.K., Bulte, J.W. & Ahrens, E.T. (19)F spin-lattice relaxation of perfluoropolyethers: Dependence on temperature and magnetic field strength (7.0-14.1T). *Journal of magnetic resonance* **242**, 18-22 (2014).
200. Tirotta, I.*, et al.* A superfluorinated molecular probe for highly sensitive in vivo(19)F-MRI. *J Am Chem Soc* **136**, 8524-8527 (2014).
201. Yu, Y. & Jiang, Z.X. Highly Fluorinated Surfactants and Methods of Making and Using Same. (2012).
202. Chen, H.*, et al.* Ultrahigh (19)F Loaded Cu1.75S Nanoprobes for Simultaneous (19)F Magnetic Resonance Imaging and Photothermal Therapy. *ACS Nano* **10**, 1355-1362 (2016).
203. Neubauer, A.M.*, et al.* Gadolinium-modulated 19F signals from perfluorocarbon nanoparticles as a new strategy for molecular imaging. *Magn Reson Med* **60**, 1066-1072 (2008).
204. Chalmers, K.H., Botta, M. & Parker, D. Strategies to enhance signal intensity with paramagnetic fluorine-labelled lanthanide complexes as probes for 19F magnetic resonance. *Dalton Trans* **40**, 904-913 (2011).
205. De Luca, E.*, et al.* Characterisation and evaluation of paramagnetic fluorine labelled glycol chitosan conjugates for (19)F and (1)H magnetic resonance imaging. *J Biol Inorg Chem* **19**, 215-227 (2014).
206. Funk, A.M., Fries, P.H., Harvey, P., Kenwright, A.M. & Parker, D. Experimental measurement and theoretical assessment of fast lanthanide electronic relaxation in solution with four series of isostructural complexes. *J Phys Chem A* **117**, 905-917 (2013).
207. Kislukhin, A.A.*, et al.* Paramagnetic fluorinated nanoemulsions for sensitive cellular fluorine-19 magnetic resonance imaging. *Nat Mater* **15**, 662-668 (2016).

208. Waiczies, H.*, et al.* Perfluorocarbon particle size influences magnetic resonance signal and immunological properties of dendritic cells. *PLoS One* **6**, e21981 (2011).
209. Ruiz-Cabello, J.*, et al.* In vivo "hot spot" MR imaging of neural stem cells using fluorinated nanoparticles. *Magn Reson Med* **60**, 1506-1511 (2008).
210. Bartusik, D. & Tomanek, B. Application of 19F magnetic resonance to study the efficacy of fluorine labeled drugs in the three-dimensional cultured breast cancer cells. *Archives of biochemistry and biophysics* **493**, 234-241 (2010).
211. Kok, M.B.*, et al.* Quantitative (1)H MRI, (19)F MRI, and (19)F MRS of cell-internalized perfluorocarbon paramagnetic nanoparticles. *Contrast Media Mol Imaging* **6**, 19-27 (2011).
212. Lanza, G.M.*, et al.* Targeted antiproliferative drug delivery to vascular smooth muscle cells with a magnetic resonance imaging nanoparticle contrast agent: implications for rational therapy of restenosis. *Circulation* **106**, 2842-2847 (2002).
213. Walczak, P., Kedziorek, D.A., Gilad, A.A., Lin, S. & Bulte, J.W. Instant MR labeling of stem cells using magnetoelectroporation. *Magn Reson Med* **54**, 769-774 (2005).
214. Xiong, R.*, et al.* Cytosolic Delivery of Nanolabels Prevents Their Asymmetric Inheritance and Enables Extended Quantitative in Vivo Cell Imaging. *Nano letters* (2016).
215. Ahrens, E.T., Feili-Hariri, M., Xu, H., Genove, G. & Morel, P.A. Receptor-mediated endocytosis of iron-oxide particles provides efficient labeling of dendritic cells for in vivo MR imaging. *Magn Reson Med* **49**, 1006-1013 (2003).
216. Bulte, J.W.*, et al.* Magnetodendrimers allow endosomal magnetic labeling and in vivo tracking of stem cells. *Nature biotechnology* **19**, 1141-1147 (2001).
217. Cromer Berman, S.M., Walczak, P. & Bulte, J.W. Tracking stem cells using magnetic nanoparticles. *Wiley Interdiscip Rev Nanomed Nanobiotechnol* **3**, 343-355 (2011).
218. Kuperman, V. Magnetic Resonance Imaging: Physical Principles and Applications. 182 (2010).
219. Turner, R. Gradient coil design: a review of methods. *Magn Reson Imaging* **11**, 903-920 (1993).
220. Spees, W.M.*, et al.* Quantification and compensation of eddy-current-induced magnetic-field gradients. *Journal of magnetic resonance* **212**, 116-123 (2011).
221. Trakic, A., Liu, F., Lopez, H.S., Wang, H. & Crozier, S. Longitudinal gradient coil optimization in the presence of transient eddy currents. *Magn Reson Med* **57**, 1119-1130 (2007).
222. Mispelter, J., Lupu, M. & Briguet, A. *NMR Probeheads for Biophysical and Biomedical Experiments: Theoretical Principles and Practical Guidelines*, (2006).
223. Hu, L.*, et al.* A generalized strategy for designing (19)F/(1)H dual-frequency MRI coil for small animal imaging at 4.7 Tesla. *Journal of magnetic resonance imaging : JMRI* **34**, 245-252 (2011).
224. Mazurkewitz, P.Z., Leussler, C., Keupp, J. & Schaeffter, T. A double-resonant 19F/1H transmit/receive solenoid coil for MRI. in *Proc. Int. Soc. Mag. Reson.*, Vol. 14 (2006).
225. Otake, Y., Soutome, Y., Hirata, K., Ochi, H. & Bito, Y. Double-tuned radiofrequency coil for (19)F and (1)H imaging. *Magn Reson Med Sci* **13**, 199-205 (2014).
226. Hockett, F.D.*, et al.* Simultaneous dual frequency 1H and 19F open coil imaging of arthritic rabbit knee at 3T. *IEEE Trans Med Imaging* **30**, 22-27 (2011).
227. de Alejo, R.P.*, et al.* Automatic tuning and matching of a small multifrequency saddle coil at 4.7 T. *Magn Reson Med* **51**, 869-873 (2004).
228. Ji, Y.*, et al.* Eight-channel transceiver RF coil array tailored for (1)H/(1)(9)F MR of the human knee and fluorinated drugs at 7.0 T. *NMR Biomed* **28**, 726-737 (2015).
229. Deshmane, A., Gulani, V., Griswold, M.A. & Seiberlich, N. Parallel MR imaging. *Journal of magnetic resonance imaging : JMRI* **36**, 55-72 (2012).
230. Junge, S. Cryogenic and Superconducting Coils for MRI. in *eMagRes*, Vol. 1 (2012).
231. Baltes, C., Radzwill, N., Bosshard, S., Marek, D. & Rudin, M. Micro MRI of the mouse brain using a novel 400 MHz cryogenic quadrature RF probe. *NMR Biomed* **22**, 834-842 (2009).
232. Bornert, P.*, et al.* Fast Perfluorocarbon Imaging Using F-19 U-Flare. *Magnetic Resonance in Medicine* **29**, 226-234 (1993).
233. Noth, U., Jager, L.J.E., Lutz, J. & Haase, A. Fast F-19-Nmr Imaging in-Vivo Using Flash-Mri. *Magnetic Resonance Imaging* **12**, 149-153 (1994).
234. Jager, L.J., Noth, U., Haase, A. & Lutz, J. Half-life of perfluorooctylbromide in inner organs determined by fast 19F-NMR imaging. *Adv Exp Med Biol* **361**, 129-134 (1994).

235. Noth, U*., et al.* In-Vivo Measurement of Partial Oxygen-Pressure in Large Vessels and in the Reticuloendothelial System Using Fast 19f-Mri. *Magnetic Resonance in Medicine* **34**, 738-745 (1995).
236. Nelson, T.R., Newman, F.D., Schiffer, L.M., Reith, J.D. & Cameron, S.L. Fluorine nuclear magnetic resonance: calibration and system optimization. *Magn Reson Imaging* **3**, 267-273 (1985).
237. Gong, B.Z*., et al.* Parameter optimization and calibration of 19F magnetic resonance imaging at 1.5 Tesla. *Magn Reson Imaging* **9**, 101-106 (1991).
238. Mastropietro, A*., et al.* Optimization of rapid acquisition with relaxation enhancement (RARE) pulse sequence parameters for (1)(9)F-MRI studies. *Journal of magnetic resonance imaging : JMRI* **40**, 162-170 (2014).
239. Scheffler, K. & Lehnhardt, S. Principles and applications of balanced SSFP techniques. *European radiology* **13**, 2409-2418 (2003).
240. Ribot, E.J., Gaudet, J.M., Chen, Y., Gilbert, K.M. & Foster, P.J. In vivo MR detection of fluorine-labeled human MSC using the bSSFP sequence. *International journal of nanomedicine* **9**, 1731-1739 (2014).
241. Partlow, K.C*., et al.* 19F magnetic resonance imaging for stem/progenitor cell tracking with multiple unique perfluorocarbon nanobeacons. *FASEB J* **21**, 1647-1654 (2007).
242. Bommerich, U*., et al.* Hyperpolarized 19F-MRI: parahydrogen-induced polarization and field variation enable 19F-MRI at low spin density. *Phys Chem Chem Phys* **12**, 10309-10312 (2010).
243. Hennig, J. K-space sampling strategies. *European radiology* **9**, 1020-1031 (1999).
244. Goette, M.J., Lanza, G.M., Caruthers, S.D. & Wickline, S.A. Improved quantitative (19) F MR molecular imaging with flip angle calibration and B1 -mapping compensation. *Journal of magnetic resonance imaging : JMRI* **42**, 488-494 (2015).
245. Giraudeau, C*., et al.* A new paradigm for high-sensitivity 19F magnetic resonance imaging of perfluorooctylbromide. *Magn Reson Med* **63**, 1119-1124 (2010).
246. Yildirim, M., Diaz-Lopez, R., Nicolay, K. & Rolf, L. In vivo 3D spectroscopic imaging of 19F compounds using backprojection. in *Proc Int Soc Magn Reson Med*, Vol. 21 4009 (2013).
247. Srinivas, M., Bonetto, F., Tel, J. & al., e. Simultaneous and quantitative tracking of distinct cell populations using 19F MRI. in *Intl Soc Mag Reson Med*, Vol. 20 4370 (2012).
248. Meissner, M*., et al.* Revealing signal from noisy (19) F MR images by chemical shift artifact correction. *Magn Reson Med* **73**, 2225-2233 (2015).
249. Elster, A.D. & Burdette, J.H. *Questions and Answers in Magnetic Resonance Imaging, 2e 2nd Edition*, (2001).
250. Gonzalez Ballester, M.A., Zisserman, A.P. & Brady, M. Estimation of the partial volume effect in MRI. *Med Image Anal* **6**, 389-405 (2002).
251. Lustig, M., Donoho, D. & Pauly, J.M. Sparse MRI: The application of compressed sensing for rapid MR imaging. *Magn Reson Med* **58**, 1182-1195 (2007).
252. Kampf, T*., et al.* Application of compressed sensing to in vivo 3D (1)(9)F CSI. *Journal of magnetic resonance* **207**, 262-273 (2010).
253. Zhong, J., Mills, P.H., Hitchens, T.K. & Ahrens, E.T. Accelerated fluorine-19 MRI cell tracking using compressed sensing. *Magn Reson Med* **69**, 1683-1690 (2013).
254. Liang, S*., et al.* Comparison of different compressed sensing algorithms for low SNR 19F application --- imaging of transplanted pancreatic islets with PFCE labeled. in *ISMRM*, Vol. 23 0693 (2015).
255. Basse-Lüsebrink, T.C*., et al.* Fast, indirect assessment of the 19F B1 profile by 1H Bloch-Siegert B1 mapping using double-resonant 1H/19F coils in *Proc. Intl. Soc. Mag. Reson. Med*, Vol. 20 3367 (2012).
256. Boehm-Sturm, P., Pracht, E.D., Aswendt, M., Henn, N. & Hoehn, M. B1 Correction for Quantitative in vivo 19F Magnetic Resonance Imaging with Surface Coils. in *ISMRM*, Vol. 20 (2012).
257. Goette, M.J*., et al.* Quantitative molecular imaging of angiogenesis-targeted fluorinated nanoparticles: new approaches for B1-mapping compensation for 19F-MRI. *J Cardiovasc Magn Reson* **15**(2013).
258. Lee, D., Marro, K., Shankland, E. & Mathis, M. Quantitative 19F imaging using inductively coupled reference signal injection. *Magn Reson Med* **63**, 570-573 (2010).
259. Keupp, J*., et al.* Simultaneous dual-nuclei imaging for motion corrected detection and quantification of 19F imaging agents. *Magn Reson Med* **66**, 1116-1122 (2011).
260. Wild, S., Roglic, G., Green, A., Sicree, R. & King, H. Global prevalence of diabetes: estimates for the year 2000 and projections for 2030. *Diabetes care* **27**, 1047-1053 (2004).

261. Palmer, J.P.*, et al.* C-peptide is the appropriate outcome measure for type 1 diabetes clinical trials to preserve beta-cell function: report of an ADA workshop, 21-22 October 2001. *Diabetes* **53**, 250-264 (2004).
262. Roden, M. *Clinical diabetes research : methods and techniques*, (John Wiley & Sons, Chichester, West Sussex, England ; Hoboken, NJ, 2007).
263. Ahlgren, U. & Kostromina, E. Imaging the Pancreatic Beta Cell. in *Type 1 Diabetes - Pathogenesis, Genetics and Immunotherapy* (ed. Wagner, D.) (InTech, 2011).
264. Himmelreich, U. & Hoehn, M. Stem cell labeling for magnetic resonance imaging. *Minim Invasive Ther Allied Technol* **17**, 132-142 (2008).
265. Malaisse, W.J. On the track to the beta-cell. *Diabetologia* **44**, 393-406 (2001).
266. Waschke, D., Leshch, Y., Thimm, J., Himmelreich, U. & Thiem, J. Synthesis of Fluorinated Ketoheptoses as Specific Diagnostic Agents. *Eur J Org Chem*, 948-959 (2012).
267. Waschke, D., Thimm, J. & Thiem, J. Highly efficient synthesis of ketoheptoses. *Organic letters* **13**, 3628-3631 (2011).
268. Amiri, H.*, et al.* Cell tracking using F-19 magnetic resonance imaging: Technical aspects and challenges towards clinical applications. *European radiology* **25**, 726-735 (2015).
269. von Mach, M.A.*, et al.* Size of pancreatic islets of Langerhans: a key parameter for viability after cryopreservation. *Acta Diabetol* **40**, 123-129 (2003).
270. Elayat, A.A., el-Naggar, M.M. & Tahir, M. An immunocytochemical and morphometric study of the rat pancreatic islets. *J Anat* **186 (Pt 3)**, 629-637 (1995).
271. Wareham, K.A. & Williams, E.D. Estimation of the primordial pool size of the mouse liver using a histochemically demonstrable X-linked enzyme in the adult female mouse. *Journal of embryology and experimental morphology* **95**, 239-246 (1986).
272. van Heeswijk, R.B.*, et al.* Fluorine MR Imaging of Inflammation in Atherosclerotic Plaque in Vivo. *Radiology* **275**, 421-429 (2015).
273. Dai, N.*, et al.* Overexpression of Arabidopsis hexokinase in tomato plants inhibits growth, reduces photosynthesis, and induces rapid senescence. *The Plant cell* **11**, 1253-1266 (1999).
274. Keil, B. & Wald, L.L. Massively parallel MRI detector arrays. *Journal of magnetic resonance* **229**, 75-89 (2013).
275. Zhang, Y., Courtois, P., Sener, A. & Malaisse, W.J. Dissimilar effects of D-mannoheptulose on the phosphorylation of alpha- versus beta-D-glucose by either hexokinase or glucokinase. *Int J Mol Med* **14**, 107-112 (2004).
276. Ramirez, R.*, et al.* Effects of D-mannoheptulose upon D-glucose metabolism in pancreatic B and non-B islet cells. *Int J Mol Med* **9**, 159-163 (2002).
277. Malaisse, W.J. Insulin release by pancreatic islets. in *Methods in Diabetes Research*, Vol. 1 147-152 (1984).
278. Leclercq-Meyer, V., Marchand, J., Woussen-Colle, M.C., Giroix, M.H. & Malaisse, W.J. Multiple effects of leucine on glucagon, insulin, and somatostatin secretion from the perfused rat pancreas. *Endocrinology* **116**, 1168-1174 (1985).
279. Alberti, K.G. & Zimmet, P.Z. Definition, diagnosis and classification of diabetes mellitus and its complications. Part 1: diagnosis and classification of diabetes mellitus provisional report of a WHO consultation. *Diabet Med* **15**, 539-553 (1998).
280. Diabetes, C.*, et al.* The effect of intensive treatment of diabetes on the development and progression of long-term complications in insulin-dependent diabetes mellitus. *N Engl J Med* **329**, 977-986 (1993).
281. Shapiro, A.M., Pokrywczynska, M. & Ricordi, C. Clinical pancreatic islet transplantation. *Nature reviews. Endocrinology* **13**, 268-277 (2017).
282. Robertson, R.P. Islet transplantation as a treatment for diabetes - a work in progress. *N Engl J Med* **350**, 694-705 (2004).
283. Shapiro, A.M., Pokrywczynska, M. & Ricordi, C. Clinical pancreatic islet transplantation. *Nature reviews. Endocrinology* (2016).
284. Gruessner, R.W. & Gruessner, A.C. The current state of pancreas transplantation. *Nature reviews. Endocrinology* **9**, 555-562 (2013).
285. Farney, A.C., Sutherland, D.E. & Opara, E.C. Evolution of Islet Transplantation for the Last 30 Years. *Pancreas* **45**, 8-20 (2016).

286. Rajab, A. Islet transplantation: alternative sites. *Curr Diab Rep* **10**, 332-337 (2010).
287. Scharp, D.W.*, et al.* Results of our first nine intraportal islet allografts in type 1, insulin-dependent diabetic patients. *Transplantation* **51**, 76-85 (1991).
288. Shapiro, A.M.*, et al.* International trial of the Edmonton protocol for islet transplantation. *N Engl J Med* **355**, 1318-1330 (2006).
289. Barton, F.B.*, et al.* Improvement in outcomes of clinical islet transplantation: 1999-2010. *Diabetes care* **35**, 1436-1445 (2012).
290. Sakata, N.*, et al.* Strategy for clinical setting in intramuscular and subcutaneous islet transplantation. *Diabetes Metab Res Rev* **30**, 1-10 (2014).
291. Virostko, J.*, et al.* Bioluminescence imaging in mouse models quantifies beta cell mass in the pancreas and after islet transplantation. *Mol Imaging Biol* **12**, 42-53 (2010).
292. Chen, X., Zhang, X., Larson, C.S., Baker, M.S. & Kaufman, D.B. In vivo bioluminescence imaging of transplanted islets and early detection of graft rejection. *Transplantation* **81**, 1421-1427 (2006).
293. Eriksson, O.*, et al.* Positron emission tomography in clinical islet transplantation. *Am J Transplant* **9**, 2816-2824 (2009).
294. Crenier, L., Courtois, P. & Malaisse, W.J. Uptake of tritiated D-mannoheptulose by liver, pancreatic exocrine and endocrine cells. *Int J Mol Med* **8**, 155-157 (2001).
295. Lu, Y.*, et al.* Long-term monitoring of transplanted islets using positron emission tomography. *Mol Ther* **14**, 851-856 (2006).
296. Kim, S.J.*, et al.* Quantitative micro positron emission tomography (PET) imaging for the in vivo determination of pancreatic islet graft survival. *Nat Med* **12**, 1423-1428 (2006).
297. Evgenov, N.V.*, et al.* In vivo imaging of immune rejection in transplanted pancreatic islets. *Diabetes* **55**, 2419-2428 (2006).
298. Maillard, E.*, et al.* Perfluorocarbon emulsions prevent hypoxia of pancreatic beta-cells. *Cell Transplant* **21**, 657-669 (2012).
299. Liang, S.*, et al.* In vivo and ex vivo 19-fluorine magnetic resonance imaging and spectroscopy of beta-cells and pancreatic islets using GLUT-2 specific contrast agents. *Contrast Media Mol Imaging* **11**, 506-513 (2016).
300. Ahrens, E.T. & Zhong, J. In vivo MRI cell tracking using perfluorocarbon probes and fluorine-19 detection. *NMR Biomed* **26**, 860-871 (2013).
301. Helfer, B.M.*, et al.* Functional assessment of human dendritic cells labeled for in vivo (19)F magnetic resonance imaging cell tracking. *Cytotherapy* **12**, 238-250 (2010).
302. Lutz, J., Kettemann, M., Racz, I. & Noth, U. Several methods utilized for the assessment of biocompatibility of perfluorochemicals. *Artif Cells Blood Substit Immobil Biotechnol* **23**, 407-415 (1995).
303. Hitchens, T.K.*, et al.* 19F MRI detection of acute allograft rejection with in vivo perfluorocarbon labeling of immune cells. *Magn Reson Med* **65**, 1144-1153 (2011).
304. Yumoto, K., Berry, J.E., Taichman, R.S. & Shiozawa, Y. A novel method for monitoring tumor proliferation in vivo using fluorescent dye DiD. *Cytometry A* **85**, 548-555 (2014).
305. Honig, M.G. & Hume, R.I. Fluorescent carbocyanine dyes allow living neurons of identified origin to be studied in long-term cultures. *J Cell Biol* **103**, 171-187 (1986).
306. Boutonnat, J.*, et al.* PKH26 probe in the study of the proliferation of chemoresistant leukemic sublines. *Anticancer Res* **18**, 4243-4251 (1998).
307. Lacy, P.E., Hegre, O.D., Gerasimidi-Vazeou, A., Gentile, F.T. & Dionne, K.E. Maintenance of normoglycemia in diabetic mice by subcutaneous xenografts of encapsulated islets. *Science* **254**, 1782-1784 (1991).
308. Sakata, N.*, et al.* MRI assessment of ischemic liver after intraportal islet transplantation. *Transplantation* **87**, 825-830 (2009).
309. Dionne, K.E., Colton, C.K. & Yarmush, M.L. Effect of hypoxia on insulin secretion by isolated rat and canine islets of Langerhans. *Diabetes* **42**, 12-21 (1993).
310. Reekmans, K.*, et al.* Spatiotemporal evolution of early innate immune responses triggered by neural stem cell grafting. *Stem cell research & therapy* **3**, 56 (2012).

311. Kerby, A., Bohman, S., Westberg, H., Jones, P. & King, A. Immunoisolation of islets in high guluronic acid barium-alginate microcapsules does not improve graft outcome at the subcutaneous site. *Artif Organs* **36**, 564-570 (2012).
312. Kawakami, Y.*, et al.* Modified subcutaneous tissue with neovascularization is useful as the site for pancreatic islet transplantation. *Cell Transplant* **9**, 729-732 (2000).
313. Juang, J.H., Bonner-Weir, S., Ogawa, Y., Vacanti, J.P. & Weir, G.C. Outcome of subcutaneous islet transplantation improved by polymer device. *Transplantation* **61**, 1557-1561 (1996).
314. Pileggi, A.*, et al.* Reversal of diabetes by pancreatic islet transplantation into a subcutaneous, neovascularized device. *Transplantation* **81**, 1318-1324 (2006).
315. Golocheikine, A.*, et al.* Cooperative signaling for angiogenesis and neovascularization by VEGF and HGF following islet transplantation. *Transplantation* **90**, 725-731 (2010).
316. Veriter, S.*, et al.* The impact of hyperglycemia and the presence of encapsulated islets on oxygenation within a bioartificial pancreas in the presence of mesenchymal stem cells in a diabetic Wistar rat model. *Biomaterials* **32**, 5945-5956 (2011).
317. Shivaswamy, V.*, et al.* Hyperglycemia induced by tacrolimus and sirolimus is reversible in normal sprague-dawley rats. *Endocrine* **37**, 489-496 (2010).
318. Dewitte, H.*, et al.* Design and evaluation of theranostic perfluorocarbon particles for simultaneous antigen-loading and (1)(9)F-MRI tracking of dendritic cells. *J Control Release* **169**, 141-149 (2013).
319. Wolfs, E.*, et al.* Optimization of multimodal imaging of mesenchymal stem cells using the human sodium iodide symporter for PET and Cerenkov luminescence imaging. *PLoS One* **9**, e94833 (2014).
320. Malaisse, W., Malaisse-Lagae, F. & Wright, P.H. A new method for the measurement in vitro of pancreatic insulin secretion. *Endocrinology* **80**, 99-108 (1967).
321. Hsu, S.M., Raine, L. & Fanger, H. Use of avidin-biotin-peroxidase complex (ABC) in immunoperoxidase techniques: a comparison between ABC and unlabeled antibody (PAP) procedures. *The journal of histochemistry and cytochemistry : official journal of the Histochemistry Society* **29**, 577-580 (1981).
322. Unger, R.H. Diabetic hyperglycemia: link to impaired glucose transport in pancreatic beta cells. *Science* **251**, 1200-1205 (1991).
323. Matsumoto, S., Tomiya, M. & Sawamoto, O. Current status and future of clinical islet xenotransplantation. *J Diabetes* **8**, 483-493 (2016).
324. Ricordi, C. & Strom, T.B. Clinical islet transplantation: advances and immunological challenges. *Nature reviews. Immunology* **4**, 259-268 (2004).
325. Bulte, J.W. Hot spot MRI emerges from the background. *Nature biotechnology* **23**, 945-946 (2005).
326. Zhang, H. Perfluoro-15-crown-5 ether-labeled dendritic cells. in *Molecular Imaging and Contrast Agent Database (MICAD)* (Bethesda (MD), 2004).
327. Schirra, C.B., D.; Keupp, J.; Razavi, R.; Schaeffter, T.; Kozerke, S. Compressed Sensing for Highly Accelerated 3D Visualization of 19F-Catheters. in *Proc. Intl. Soc. Magn. Reson. Med.* (2009;17:4405).
328. Liu, E.T. & Temlyakov, V.N. The Orthogonal Super Greedy Algorithm and Applications in Compressed Sensing. *Ieee T Inform Theory* **58**, 2040-2047 (2012).
329. Needell, D. & Tropp, J.A. CoSaMP: Iterative signal recovery from incomplete and inaccurate samples. *Appl Comput Harmon A* **26**, 301-321 (2009).
330. Candes, E.J., Wakin, M.B. & Boyd, S.P. Enhancing Sparsity by Reweighted l(1) Minimization. *J Fourier Anal Appl* **14**, 877-905 (2008).
331. Huang, X.L., Liu, Y.P., Shi, L., Van Huffel, S. & Suykens, J.A.K. Two-level l(1) minimization for compressed sensing. *Signal Process* **108**, 459-475 (2015).
332. Kim, Y.C., Narayanan, S.S. & Nayak, K.S. Accelerated three-dimensional upper airway MRI using compressed sensing. *Magn Reson Med* **61**, 1434-1440 (2009).
333. Haldar, J.P., Hernando, D. & Liang, Z.P. Compressed-sensing MRI with random encoding. *IEEE Trans Med Imaging* **30**, 893-903 (2011).
334. Wu, B., Millane, R.P., Watts, R. & Bones, P.J. Prior estimate-based compressed sensing in parallel MRI. *Magn Reson Med* **65**, 83-95 (2011).
335. Feng, L.*, et al.* Golden-angle radial sparse parallel MRI: combination of compressed sensing, parallel imaging, and golden-angle radial sampling for fast and flexible dynamic volumetric MRI. *Magn Reson Med* **72**, 707-717 (2014).

336. Block, K.T., Uecker, M. & Frahm, J. Undersampled radial MRI with multiple coils. Iterative image reconstruction using a total variation constraint. *Magn Reson Med* **57**, 1086-1098 (2007).
337. Holland, D.J.*, et al.* Compressed sensing reconstruction improves sensitivity of variable density spiral fMRI. *Magn Reson Med* **70**, 1634-1643 (2013).
338. Seeger, M., Nickisch, H., Pohmann, R. & Scholkopf, B. Optimization of k-space trajectories for compressed sensing by Bayesian experimental design. *Magn Reson Med* **63**, 116-126 (2010).
339. Bilgic, B., Goyal, V.K. & Adalsteinsson, E. Multi-contrast reconstruction with Bayesian compressed sensing. *Magn Reson Med* **66**, 1601-1615 (2011).
340. Gudbjartsson, H. & Patz, S. The Rician distribution of noisy MRI data. *Magn Reson Med* **34**, 910-914 (1995).
341. Liang, S.L., K.; Holvoet, B.; Verbeke, R.; Manshian, B.; Malaisse, W J.; Sener, A.; Lentacker, I.; Himmelreich, U. . Tri-modal in vivo imaging of the rodent pancreatic islets transplanted in the subcutaneous site. in *Proc. Intl. Soc. Magn. Reson. Med.*, Vol. 23 4681 (2015;23:4681).
342. Amiri, H.*, et al.* Cell tracking using (19)F magnetic resonance imaging: technical aspects and challenges towards clinical applications. *European radiology* **25**, 726-735 (2015).
343. Malaisse, W.J. Insulin release by pancreatic islets. . in *Methods in Diabetes Research.* (1984;1(B):147-152).
344. Tropp, J.A. & Wright, S.J. Computational Methods for Sparse Solution of Linear Inverse Problems. *P Ieee* **98**, 948-958 (2010).
345. Gerding, D.N. Clostridium difficile infection prevention: biotherapeutics, immunologics, and vaccines. *Discovery medicine* **13**, 75-83 (2012).
346. Magill, S.S.*, et al.* Multistate point-prevalence survey of health care-associated infections. *N Engl J Med* **370**, 1198-1208 (2014).
347. Louie, T.J.*, et al.* Fidaxomicin versus vancomycin for Clostridium difficile infection. *N Engl J Med* **364**, 422-431 (2011).
348. Lowy, I.*, et al.* Treatment with monoclonal antibodies against Clostridium difficile toxins. *N Engl J Med* **362**, 197-205 (2010).
349. Giannasca, P.J.*, et al.* Serum antitoxin antibodies mediate systemic and mucosal protection from Clostridium difficile disease in hamsters. *Infection and immunity* **67**, 527-538 (1999).
350. Ashford, M. & Fell, J.T. Targeting drugs to the colon: delivery systems for oral administration. *Journal of drug targeting* **2**, 241-257 (1994).
351. Yang, M.*, et al.* A novel pH-dependent gradient-release delivery system for nitrendipine II. Investigations of the factors affecting the release behaviors of the system. *International journal of pharmaceutics* **286**, 99-109 (2004).
352. Khan, M.Z., Prebeg, Z. & Kurjakovic, N. A pH-dependent colon targeted oral drug delivery system using methacrylic acid copolymers. I. Manipulation Of drug release using Eudragit L100-55 and Eudragit S100 combinations. *J Control Release* **58**, 215-222 (1999).
353. Matsumoto, M.*, et al.* Impact of intestinal microbiota on intestinal luminal metabolome. *Scientific reports* **2**, 233 (2012).
354. Yoshida, M.*, et al.* Neonatal Fc receptor for IgG regulates mucosal immune responses to luminal bacteria. *The Journal of clinical investigation* **116**, 2142-2151 (2006).
355. Goto, T.*, et al.* Pharmaceutical design of a novel colon-targeted delivery system using two-layer-coated tablets of three different pharmaceutical formulations, supported by clinical evidence in humans. *J Control Release* **97**, 31-42 (2004).
356. Tuleu, C.*, et al.* A scintigraphic investigation of the disintegration behaviour of capsules in fasting subjects: a comparison of hypromellose capsules containing carrageenan as a gelling agent and standard gelatin capsules. *European journal of pharmaceutical sciences : official journal of the European Federation for Pharmaceutical Sciences* **30**, 251-255 (2007).
357. Pedersen, P.B., Bar-Shalom, D., Baldursdottir, S., Vilmann, P. & Mullertz, A. Feasibility of capsule endoscopy for direct imaging of drug delivery systems in the fasted upper-gastrointestinal tract. *Pharmaceutical research* **31**, 2044-2053 (2014).
358. Christmann, V., Rosenberg, J., Seega, J. & Lehr, C.M. Simultaneous in vivo visualization and localization of solid oral dosage forms in the rat gastrointestinal tract by magnetic resonance imaging (MRI). *Pharmaceutical research* **14**, 1066-1072 (1997).

359. Ai, H. Layer-by-layer capsules for magnetic resonance imaging and drug delivery. *Adv Drug Deliv Rev* **63**, 772-788 (2011).
360. Terreno, E., Castelli, D.D., Viale, A. & Aime, S. Challenges for molecular magnetic resonance imaging. *Chem Rev* **110**, 3019-3042 (2010).
361. Nasongkla, N.*, et al.* Multifunctional polymeric micelles as cancer-targeted, MRI-ultrasensitive drug delivery systems. *Nano letters* **6**, 2427-2430 (2006).
362. Nakada, T., Kwee, I.L., Griffey, B.V. & Griffey, R.H. 19F 2-FDG NMR imaging of the brain in rat. *Magn Reson Imaging* **6**, 633-635 (1988).
363. Fidler, J.L., Fletcher, J.G., Bruining, D.H. & Trenkner, S.W. Current status of CT, magnetic resonance, and barium in inflammatory bowel disease. *Seminars in roentgenology* **48**, 234-244 (2013).
364. Saphier, S., Rosner, A., Brandeis, R. & Karton, Y. Gastro intestinal tracking and gastric emptying of solid dosage forms in rats using X-ray imaging. *International journal of pharmaceutics* **388**, 190-195 (2010).
365. Worsoe, J.*, et al.* Gastric transit and small intestinal transit time and motility assessed by a magnet tracking system. *BMC gastroenterology* **11**, 145 (2011).
366. Wempe, M.F.*, et al.* Pharmacokinetics of letrozole in male and female rats: influence of complexation with hydroxybutenyl-beta cyclodextrin. *The Journal of pharmacy and pharmacology* **59**, 795-802 (2007).
367. Som, P.*, et al.* A fluorinated glucose analog, 2-fluoro-2-deoxy-D-glucose (F-18): nontoxic tracer for rapid tumor detection. *J Nucl Med* **21**, 670-675 (1980).
368. Naressi, A., Couturier, C., Castang, I., de Beer, R. & Graveron-Demilly, D. Java-based graphical user interface for MRUI, a software package for quantitation of in vivo/medical magnetic resonance spectroscopy signals. *Computers in biology and medicine* **31**, 269-286 (2001).
369. Kircher, M.F., Gambhir, S.S. & Grimm, J. Noninvasive cell-tracking methods. *Nature reviews. Clinical oncology* **8**, 677-688 (2011).
370. Caruthers, S.D.*, et al.* In vitro demonstration using 19F magnetic resonance to augment molecular imaging with paramagnetic perfluorocarbon nanoparticles at 1.5 Tesla. *Investigative radiology* **41**, 305-312 (2006).
371. Colotti, R.*, et al.* Characterization of perfluorocarbon relaxation times and their influence on the optimization of fluorine-19 MRI at 3 tesla. *Magn Reson Med* **77**, 2263-2271 (2017).
372. Flaim, S.F. Pharmacokinetics and side effects of perfluorocarbon-based blood substitutes. *Artif Cells Blood Substit Immobil Biotechnol* **22**, 1043-1054 (1994).
373. Gutberlet, M.*, et al.* Free-breathing Dynamic 19F Gas MR Imaging for Mapping of Regional Lung Ventilation in Patients with COPD. *Radiology*, 170591 (2017).

Curriculum Vitae

Personal Information

Name:	Sayuan Liang (Wade)
Address:	Louizastraat 36, 2000 Antwerpen
Email:	liangsayuan@msn.com/ sa.yuan.liang@philips.com
Mobile No.:	0032488512116 / 008613626664617
Date of birth:	17/06/1987
Nationality:	China

Education Background

2009-2010:	Postgraduate Studies of Advanced Medical Imaging (Passed Cum Laude, KU Leuven, Belgium)
2008-2009:	Master of Intelligent Electronics (Passed Cum Laude, GroepT KU Leuven, Belgium)
2005-2009:	Bachelor of Telecommunications (Exchange Program, Beijing Jiaotong University, China)
2006-2008:	Bachelor of Electronics (Passed Cum Laude, GroepT KU Leuven, Belgium)

Work Experience

08/2017:	Senior Scientist, MRI, Imaging and Clinical Applications (Philips Research, Shanghai, China)
07/2015-07/2017:	MR Physicist/ Engineer (Bio-Imaging Lab, University of Antwerpen, Belgium)
11/2014-06/2015:	Research Assistant (MRI unit, MoSAIC, KU Leuven, Belgium)
11/2010-10/2014:	Ph.D. Candidate (MRI unit, MoSAIC, KU Leuven, Belgium)
07/2010-10/2010:	Intership Student (IMEC, Leuven, Belgium)

09/2009-06/2010:	Master Thesis Student
	(University Hospital of Leuven, Belgium)
09/2008-06/2009:	Master Thesis Student
	(NXP, Leuven, Belgium)

Honors & Awards

2017:	Outstanding Self-Financed Student Abroad Award (Nominated)
2015:	Travel Grant (32nd ESMRMB Annual Meeting)
2015:	Summa Cum Laude Award (23rd ISMRM Annual Meeting)
2015:	Magna Cum Laude Award (23rd ISMRM Annual Meeting)
2015:	Student Stipend (23rd ISMRM Annual Meeting)
2015:	Broad Your Horizontal Travel Grant (KU Leuven)
2010-2014:	ViBRANT Doctoral Grant (EC-FP7-NMP-2008, KU Leuven)
2006-2009:	Full Scholarship (GroepT, KU Leuven)
2005-2006:	First Class Study Scholarship (Beijing Jiaotong University)

Academic & Social Activity

2015-2016:	Abstract Reviewer (European Molecular Imaging Meeting)
2015-2017:	Abstract Reviewer (ISMRM Benelux chapter)
2013-2017:	Trainee Member (ISMRM, ESMRMB, EMIM)
2007-2011:	Key Member and President (Chinese Student and Scholar Association Leuven)

Scientific Contributions

1. ***Liang S.,*** *Dresselaers T., Louchami K., Zhu C., Liu Y., Himmelreich U. (2017). "Comparison of different compressed sensing algorithms for low SNR 19F MRI application - imaging of transplanted pancreatic islets and cells labeled with perfluorocarbons." NMR in Biomedicine, 11, 24-31.*
2. ***Liang S.,*** *Louchami K., Kolster H., Jacobsen A., Zhang Y., Thimm J., Sener A., Thiem J., Malaisse W., Dresselaers T., Himmelreich U. (2016). "In vivo and ex vivo 19-fluorine magnetic resonance imaging and spectroscopy of beta-cells and pancreatic islets using GLUT-2 specific contrast agents." Contrast Media & Molecular Imaging, 11, 506-513.*

3. *R. Xiong, F. Joris, **S. Liang,** J. Demeester, A. Skirtach, K. Raemdonck, U. Himmelreich, S. De Smedt, K. Braeckmans. (2016) "Cytosolic delivery of nano-labels by photoporation prevents their asymmetric inheritance and enables extended quantitative in vivo cell imaging." Nano Lett (Epub ahead of print)*
4. *Staelens D.*, **Liang S.*,** Appeltans B., Van de Wouwer M., Van den Mooter G., Van Assche G., Himmelreich U.*, Vande Velde G*. (2016). "Visualization of delayed release of compounds from pH-sensitive capsules in vitro and in vivo in a hamster model." Contrast Media & Molecular Imaging, 11, 24-31. (* Authors contributed equally)*
5. *Q. Xia, Y. Feng, T. Yin, Y.Liu, **S. Liang,** J. Liu, L. Tong, G. Huang, J. Yu, Y. Jiang, U. Himmelreich, R. Oyen, Y. Ni. (2016) A multifunctional contrast dye for morphological research. Microscopy Research Technique. 79(2): 111-21.*
6. *Dewitte, H., Geers, B., **Liang, S.,** Himmelreich, U., Demeester, J., De Smedt, S., Lentacker, I. (2013) "Design and evaluation of theranostic perfluorocarbon particles for simultaneous antigen-loading and 19F-MRI tracking of dendritic cells." Journal of Controlled Release, 169 (1-2), 141-149.*
7. ***Liang S.,** Louchami K., Holvoet B., Verbeke R., Deroose C., Manshian B., Lentacker I., Himmelreich U. "Tri-modal in vivo imaging of pancreatic islets transplanted subcutaneously in mice." Mol Imaging Biol (Manuscript in Submission)*
8. *Mannheim J., Kara F., Doorduin j., Fuchs K., Reisch G., **Liang S.,** Verhoye M., Gremse F., Mezzanotte L., Huisman M. (2017) "Standardization of small animal imaging – current status and future prospects" Mol Imaging Biol.(Accepted)*
9. ***Liang S.,** Himmelreich U. "19F MRI as a tool for preclinical research" Manuscript in Submission*

Poster and Abstracts at International Conference

1. ***Liang, S.,** Kolster, H., Louchami, K., Dresselaers, T., Malaisse, WJ., Sharma, S., Himmelreich, U. (2013). In vitro and in vivo 19-fluorine magnetic resonance imaging (MRI) of beta-cells and pancreatic using GLUT-2 specific contrast agents. Proc. International Society for Magnetic Resonance in Medicine: vol. 21. International Society for Magnetic Resonance in Medicine, Salt lake City, 20-26 April 2013, 1505. (Poster)*
2. *K. Louchami, **S. Liang,** E. Hupkens, WJ. Malaisse, J. Thimm, A. Sener and U. Himmelreich (2013). 19F-mannoheptuloses as tools for the non-invasive imaging of GLUT2-expressing cells: ex vivo and in vivo studies. 49th Annual Meeting of the European Association for the Study of Diabetes, Barcelona, 23-27 September 2013. (Poster)*
3. *K. Louchami, **S. Liang,** A. Sener, A. Rzajeva, M. Aswendt, E. Gianolio, S. Aime, U. Himmelreich (2014). Gadolinium chelate (Gd-DO3A-GAD) new contrast agent for non-invasive quantification of beta cell mass. 50th Annual Meeting of the European Association for the Study of Diabetes, Vienna, 15-19 September 2014. (Poster)*
4. ***Liang, S.,** Louchami, K., Verbeke, R., Manshian, B., Malaisse, W., Sener, A., Lentacker, I., Himmelreich, U. (2014). Dual-modal in-vivo imaging of the rodent pancreatic islets transplanted in the subcutaneous site. World Molecular Imaging Congress, Seoul, 17-20 September 2014. (Poster)*
5. ***Liang, S.,** Louchami, K., Holvoet, B., Verbeke, R., Manshian, B., Malaisse, W., Sener, A., Lentacker, I., Himmelreich, U. (2015). Tri-modal imaging platform for transplanted rodent pancreatic islets. European Molecular Imaging Meeting, Tubingen, 18-20 March 2015. (Oral)*

6. ***Liang, S.,*** *Staelens, D., Appeltans, B., Van de Wouwer, M., Van den Mooter, G., Van Assche,G., Vande Velde, G., Himmelreich, U. (2015). Combined 19F MRI and CT imaging for the visualization of delayed release of compounds using pH-sensitive polymers coated capsules in vitro and in a hamster animal model. Proc. International Society for Magnetic Resonance in Medicine: vol. 23. International Society for Magnetic Resonance in Medicine, Toronto, 30 May-06 June 2015, 0386. (Oral, Summa Cum Laude Award)*
7. ***Liang, S.,*** *Liu,Y., Dresselaers, T,. Louchami, K,. Sabine Van Huffel, S., Himmelreich, U. (2015) Comparison of different compressed sensing algorithms for low SNR 19F application --- imaging of transplanted pancreatic islets with PFCE labeled. Proc. International Society for Magnetic Resonance in Medicine: vol. 23. International Society for Magnetic Resonance in Medicine, Toronto, 30 May-06 June 2015, 0693. (Oral, Magna Cum Laude Award)*
8. ***Liang, S.,*** *Louchami, K., Holvoet, B., Verbeke, R., Manshian, B., Malaisse, W., Sener, A., Lentacker, I., Himmelreich, U. (2015). Tri-modal in vivo imaging of the rodent pancreatic islets transplanted in the subcutaneous site. Proc. International Society for Magnetic Resonance in Medicine: vol. 23. International Society for Magnetic Resonance in Medicine, Toronto, 30 May-06 June 2015, 4681. (Electronic Poster)*
9. ***Liang, S.,*** *Liu,Y., Dresselaers, T,. Sabine Van Huffel, S., Himmelreich, U. (2015) Compressed Sensing as a valuable tool for visualization of low SNR signal in 19F MRI. Proc. European Society for Magnetic Resonance in Medicine and Biology, Edinburgh, 1-3 October 2015. (Oral)*
10. ***Liang, S.,*** *Kolster, H., Himmelreich, U. (2015). Comparison of different surface coils for imaging the iris of the mouse eye. Proc. European Society for Magnetic Resonance in Medicine and Biology, Edinburgh, 1-3 October 2015. (Poster)*
11. *Saini S., Korf H.,* ***Liang S.,*** *Verbeke R., Lentacker I., Mathieu C., De Smedt S., Himmelreich U. (2015). Immune cell labeling and biodistribution profile study on cationic 19F emulsion: a step towards insight of T1D pathogenesis. DiabImage presymposium on Diabetes Imaging. Stockholm,Sweden, 13 September 2015. (Oral)*
12. *Saini, S., Poelmans, J.,* ***Liang, S.,*** *Verbeke, R., Korf, H., Lentacker, I., Stefaan, D., Himmelreich, U. (2017). Dynamic in vivo comparison of immune cell infiltration in immunocompromised Aspergillus lung infection models using 19F MRI. World Molecular Imaging Congress, Philadelphia, 13-16 September 2017. (Poster)*